THE DYNAMICS OF TURBULENT PREMIXED FLAMES: MECHANISMS AND MODELS FOR TURBULENCE-FLAME INTERACTION

by
Adam M. Steinberg

A dissertation submitted in partial fulfillment
of the requirements for the degree of
Doctor of Philosophy
(Aerospace Engineering)
in The University of Michigan
2009

Doctoral Committee:

Professor Steven L. Ceccio, Co-Chair
Professor James F. Driscoll, Co-Chair
Professor Werner J. A. Dahm
Professor Volker Sick
Assistant Professor Matthias Ihme

To my Family and Friends for Life and Happiness

ACKNOWLEDGEMENTS

Perhaps it is surprising that after writing several hundred pages of a technical dissertation, I find myself wondering how to approach the seemingly simple task of acknowledging the people that made that dissertation possible. Then again, perhaps not; the cause and effect relationships in turbulent-flame interactions may be easier to understand than those in person-person interactions. Then again, perhaps not.

Lacking anywhere else to start, I will revert to the technical leanings of an engineer and provide a definition:

Symbiosis (n): any interdependent or mutually beneficial relationship between two persons, groups, etc.

If anyone ever asked me what to look for in a research advisor, the answer would be symbiosis. If asked if I had it, the answer would be (hopefully) yes. From my perspective, the benefits came in sage advice when needed, a free reign when appropriate, and all the resources I could ask for (oh yeah, there was some money in there too). As for exactly what exactly Professors Driscoll and Ceccio got, you will have to ask them. I'm pretty sure I came out on top.

Then again, there are some non-symbiotic relationships involved in the doctoral process (though I will not go so far as to call them parasitic). To wit, the effort and time put forth by the doctoral committee in reviewing and critiquing several hundred pages of dissertation. To Professors Dahm, Ihme, and Sick, thank you for

your time and consideration.

And now a story. In the autumn of 2004, a young(ish) Canadian man headed south of the border to Michigan. After exploring the town of Ann Arbor for a while, he arrived at a building called the FXB. He was then introduced to two people, one from a place called Ohio and one from a place called Tennessee. The trio was then placed in a 2.5 m x 5.5 m x 2.5 m box and told to spend the next four or five years there. Perhaps a difficult situation. Now what if I told you that, when the group were occasionally released from this box, they would often end up in the same general location, imbibing libations (while of course thinking about turbulence) or just generally engaged in whatever was happening at the time. Hard to believe, no? Well it happened. So to Alex (a.k.a. Stefan, Aquel, Psycho) and Danny (a.k.a. CVD, the Spin King) thanks. Whomever ends up stuck in an office with me next has a lot to live up to.

Let us now expand the box outwards to encompass the entire FXB. In it we would find Andy (Pinch) Lapsa, Erin (Keebs) Farbar, and Kristina (Lemmer) Lemmer. Heck, we'll even allow us to move through time to find Prashant (Heavy P) Patel. I have sometimes asked myself: why don't I have a lot of friends outside of the Aerospace Engineering department? The answer: there was never a need. So from emergency Thursday night competitions involving fancy tables and cheap cups, to unexpected trips up and (especially) down stairs, to the strangest Jenga set ever created, thanks for not making me look far for interesting friends. Oh yeah, Matt and Evan. Wow. Enough said.

And yet we cannot yet even leave the FXB. There are both old and new players that must be accounted for. First the old. To Jeff, Chad, Sulabh, and Zac, thank you for your example (and occasional counter-example). There is a reason that people

keep coming to Michigan and you were no small part of it. Speaking of people who keep coming to Michigan, the fate of many an experiment now lies in the hands of one Jacob (5$ $\leftrightarrow$) Temme. Good luck, you'll be fine. The same goes for Shab and Nick, who must also continue the on-ice broomball domination. To Tom, Eric, Dave, Chris, and Terry (who really isn't in the FXB, but whatever), nothing around here would get done without you guys, so thank you. To Denise, remember that if you have to try and get along without us, we also have to try and manage without you.

Finally! There is world outside the FXB that must be explored! It seems almost criminal that I've gotten to this point without mentioning one Hyacinth (Hyce, Tang) Schumaker. Hyce is one of those rare people who, just by being their friend, you immediately earn other friends. Not in the standard sense of you are friends with her friends. People actually want to be friends with you so they can get an in with her (we cannot discount the influence of certain baked goods in this though). We will have to figure out the logistics of shipping cookies oversees. And speaking of shipping food internationally, I happen to recall a certain Pizza^2 that was delivered to one Elena Spatoulas. I'm pretty sure I'll need an occasional large pepperoni, bacon, and mushroom in Germany, so plan on making some trips to Windsor. Merci d'avoir un sens de l'humeur. To Ellie, merci pour l'enseignement-moi un sens de l'humor.

Hmmmmm, who remains? Ah yes, the family. I have often been told that I am curt with my family; that I do not appreciate them. While the first, I sadly admit may be true, the second is completely false. The greatest thing about family is that no matter what, they support you. Never once in my life have I found myself needing anything, material or immaterial, that was not provided without question or hesitation. In fact, the question was never even necessary. Everything has been offered without prompting and often before I even realized its value. It always amazes

me how I can return from being away for spans of a year and be included without missing a beat. I guess that's family.

TABLE OF CONTENTS

LIST OF FIGURES

Figure

LIST OF TABLES

Table

LIST OF APPENDICES

Appendix

NOMENCLATURE

Symbol	Description
a_t	Tangential strain rate exerted on flame
A	Flame surface area
b	Various modeling constants
c	Reaction progress variable
c^*	Reaction progress variable at iso-surface representing the flame
c_k	Kolmogorov constant
C	Flame surface curvature
d	Diameter
D	Diffusivity
$\vec{e}$	Eigenvector
E	Energy spectrum
f	Space curve defining the flame
$\underline{G}$	Level-set variable for flame tracking
h	Pao correction
H	LES filter kernel
I_0	Flame speed stretch rate factor
k	Turbulence kinetic energy or wave number
Ka	Karlovitz number
l	Length

ℓ	Markstein length
L	Integral length scale
Le	Lewis number
$\dot{m}$	Mass flow rate
$\underline{m}$	Representative flame surface orientation in LES model of Ref. [51]
$\vec{M}$	Representative filtered flame surface orientation in LES model of Ref. [51]
Ma	Markstein number
$\hat{n}$	Flame surface normal vector
N	Number of data samples
p	Pressure
P	Perimeter of a turbulent structure or probability
q	generic variable for derivations
r	Characteristic length scale in flame-vortex interactions
Re	Reynolds number
s	Flame speed
$\underline{S}$	Fluid dynamic strain rate tensor
Sc	Schmidt number
St	Stokes number
t	Time
T	Temperature
$\vec{u}$	Velocity
u, v, w	Velocity components
v_r	Characteristic velocity in flame-vortex interactions
V	Volume
w_r	Local volumetric reaction rate of flamelet

$\vec{w}$	Flame surface velocity in lab fixed frame
(x, y, z)	Cartesian coordinates
(x_f, y_f, z_f)	Flame space curve (f) components
X	Mole fraction
Y	Mass fraction

Greek

α	Thermal diffusivity of resolution factor
β	Model constant
χ	Correlation coefficient
δ	Flame thickness
Δ	LES filter width
ϵ	Restriction parameters for 2D measurements
ε	Kinetic energy dissipation rate
γ	Heat release factor
Γ	Stretch or strain efficiency function
λ	Turbulence length micro-scale
κ	Flame total stretch rate
κ_c	Flame curvature stretch rate
Λ	Characteristic wavelength for hydrodynamic instability
μ	Dynamic viscosity
ν	Kinematic viscosity
ω_r	Volumetric reaction rate
$\vec{\omega}$	Vorticity
$\underline{\Omega}$	Rotation rate tensor

ϕ	Equivalence ratio
Φ	Stretch efficiency transfer function
φ	Distance along flame surface
Ψ	Turbulent burning velocity function
ρ	Density
ς	Growth rate of hydrodynamic instability
Σ	Flame surface density
τ	Time scale
θ	Parametrization of flame space curve (f)
Υ	Wrinkling transfer function
$\vec{\xi}, \vec{\zeta}$	Parameter sets
Ξ	Flame wrinkling factor
ζ	Eigenvalue

Subscript	**Description**
a	Regarding strain rate
b	Burnt gas property
c	Chemical property
C	Co-flow fluid property
f	Property defined along the flame surface
k	Kolmogorov scale property
l	Laminar flame property
L	Integral scale property
O	Diagnostics with respect to OPCS-PIV system
p	Vortex pair property

sg	Subgrid scale property
s	Turbulent structure property
t	Turbulent flame property
M	Main-flow fluid property
T	Taylor scale property
u	Unburnt gas property
Δ	Resolved scale property in LES
κ	Regarding stretch rate
ν	Viscous scale property
$\prime$	Fluctuation

Superscript	**Description**
0	Unstretched flame property
a	Regarding a_t
c	Regarding C or κ_c

Mathematical

δ_{ij}	Kronecker delta function
ϵ_{ijk}	Levi-Civita tensor
ρ	Auto-correlation function
σ	Standard deviation
$\langle\cdot\rangle$	Spatial average
$(\bar{\cdot})$	Temporal or ensemble average
$(\tilde{\cdot})$	Filter operation
$(\hat{\cdot})$	Density weighted filter operation

$\breve{(\cdot)}$	Flame surface conditional filtering
$\check{(\cdot)}$	Level-set representation of a filtered quantity
$(\cdot)'$	Fluctuation

Acronyms

CFD	Computational fluid dynamics
CS-PIV	Cinema-stereoscopic particle image velocimetry
DNS	Direct numerical simulation
FFT	Fast Fourier transform
JPDF	Joint probability density function
LES	Large eddy simulations
OPCS-PIV	Orthogonal-plane cinema-stereoscopic particle image velocimetry
PDF	Probability density function
PIV	Particle image velocimetry
PLIF	Planar laser induces fluorescence
RANS	Reynolds averages Navier-Stokes simulations
RMS	Root mean square

CHAPTER I

Introduction and Theory

1.1 Motivation

The use of combustion engines to generate power has steadily increased over the past century [41]. As such engines have become increasingly pervasive, they have consequentially come under increased scrutiny. The two major critiques of these engines are fairly obvious: a) they burn a non-renewable fuel source and b) they emit the products of this combustion as harmful pollutants. Nevertheless, for the foreseeable future combustion will remain the primary energy source for transportation and power generation. The desirable advancements in combustion technology are therefore equally obvious: a) burn fuel more efficiently and b) reduce pollutant emissions. However, simultaneously achieving these goals while maintaining safety and reliability standards is a difficult task. To do so requires complex systems and advanced tailoring of the combustion process to an extent that has not been previously necessary. Consequentially, the extensive experimentation programs typically employed in the design process have become progressively more expensive. In order to mitigate such costs, increasing design work is performed using computational fluid dynamics (CFD). However, a better understanding of many fundamental combustion processes must be developed for such simulations to be a sufficiently accurate

engineering tool.

For example, increasingly stringent standards have mandated the reduced emission of various oxides of nitrogen (NO_x) [35]. One of the most promising methods of achieving this is to employ lean premixed flames. This is the combustion method used in advanced gas turbine engines such as the GENx [76]. In such an engine, fuel is mixed with excessive oxidizer relative to the stoichiometric requirement. This results in a lower flame temperature. By keeping the flame temperature below about 1800 K, the thermal and prompt mechanisms of NO_x production are greatly reduced [29, 63].

However, using premixed flames presents many design challenges. Unlike non-premixed combustion where the reactions occur where fuel and oxidizer mix, premixed reactions occur in thin sheets that are free to move in the fluid. The position and behavior of these sheets are dictated by the details of the incoming fluid and the physical constraints. In almost all practical applications, the premixed flame is propagating into a turbulent flow. The interaction between the flow field and the flame creates a highly convoluted interface between the reactants and products. Details of this interface control many of the important design considerations such as flame length and shape, flame kernel growth, flash back and blow out limits, acoustic instabilities, and noise. Hence, understanding the propagation of a premixed flame in a turbulent flow is an important task.

1.2 Outline

The focus of this dissertation is to develop an improved understanding for the manner in which turbulence interacts with a premixed flame. Of particular interest are the mechanisms with which turbulence generates flame surface area. The flame

area is fundamental in determining the rate at which the overall turbulent flame propagates, and consequentially controls many aspects of the flame surface dynamics associated with turbulence. As mentioned above, CFD is becoming a more prevalent engineering design tool for combustion devices. Hence, the analysis is geared to develop both a mechanistic understanding of turbulence-flame interactions, as well as models that are appropriate for modern simulations.

The dissertation is arranged as follows:

1. **Introduction and theory** - The remainder of the first Chapter discusses the relevant turbulence and combustion theory necessary for the subsequent Chapters. A brief review of premixed turbulent combustion is provided. Previous methods of simulating flames in the thin flamelet regime are discussed and the physical consequences of the employed submodels analyzed. This analysis indicates several issues that must be addressed for the models to accurately reflect real turbulence-flame interaction.

2. **Experimental approach** - This Chapter introduces the experiment, test conditions, diagnostics, and general experimental approach to the problem. Two diagnostic techniques were developed for this research, which are described and evaluated. The first technique, Cinema-Stereoscopic Particle Image Velocimetry (CS-PIV), provides temporally resolved, highly accurate planar measurements of turbulence-flame interaction processes. The second, Orthogonal-Plane Cinema-Stereoscopic Particle Image Velocimetry (OPCS-PIV), provides reconstructed pseudo-3D measurements of these processes. The roles of these diagnostics in the subsequent analysis are discussed. Data processing and reduction techniques are also described.

3. **Characterization of the flow and flames** - A detailed characterization of the test conditions is provided. This includes relevant inflow parameters and global mean results. These are necessary to produce and evaluate computational simulations of this configuration.

4. **The mechanisms of flame strain and wrinkling** - This Chapter utilizes the CS-PIV measurements to develop phenomenological descriptions of the straining and wrinkling processes in a turbulent premixed flame. It is first shown that the typical image of stretching by turbulent vortices does not accurately describe the turbulence-flame interactions. Hence, a new mechanism that explicitly distinguishes the roles of different types of turbulent structures is developed based on both experimental results and theoretical analysis. This is shown to better describe real turbulence-flame interactions. Numerical considerations and the relationship between 2D and 3D measurements are also presented.

5. **The geometry of turbulence-flame interactions** - In this Chapter, the 3D measurements of turbulence-flame interactions are utilized. Three-dimensional structures in non-reacting turbulence are first discussed and compared with direct numerical simulations (DNS). The interaction of such structures with the flame surface are then presented along with statistics characterizing the interaction geometry. From the complex geometry of these interactions, it is argued that model development must not be based on a particular canonical geometry. This is in conflict with previous theories.

6. **Modeling subgrid terms for LES** - First, a new analysis procedure for studying turbulence-flame interactions is presented. This procedure is designed to reflect the physical processes occurring at the subgrid scales of a Large

Eddy Simulation (LES). Hence, the results produced should be ideal for developing subgrid models. Various models for the subgrid strain rate, curvature stretch rate, and turbulent burning velocity previously employed in simulations are then evaluated. It was found that these models do not accurately predict the measured results due to many simplifying assumptions. However, the general modeling paradigms employed could often be expanded to reflect the real turbulence-flame interaction. These new paradigms are presented and used to develop more accurate models for the various subgrid terms.

7. **Conclusions** - The results of this dissertation are summarized, conclusions are drawn, and appropriate future research is indicated.

1.3 Review of flamelet regimes of turbulent premixed combustion

It has long been observed that a turbulent premixed flame occupying the same mean volume as a laminar flame will consume reactants at a much greater rate [68]. This increase in burning rate is caused by the interaction of the turbulent flow with the flame. Hence, the mechanisms with which turbulence affects the flame must be understood.

A common assumption in the description of turbulent premixed combustion is that the reactions occur in thin propagating sheets called 'flamelets'. Such cases exist when the chemical time scale (τ_c) is less than the turbulence integral time scale (τ_L). The chemistry is then assumed to be sufficiently fast for the flow to consist of only two phases: the unburnt reactants and the burnt products. These are separated by the reacting flamelets.

Further classification of these flamelets may be made by considering the turbulence and chemical length scales. If the smallest turbulence length scale, which for now

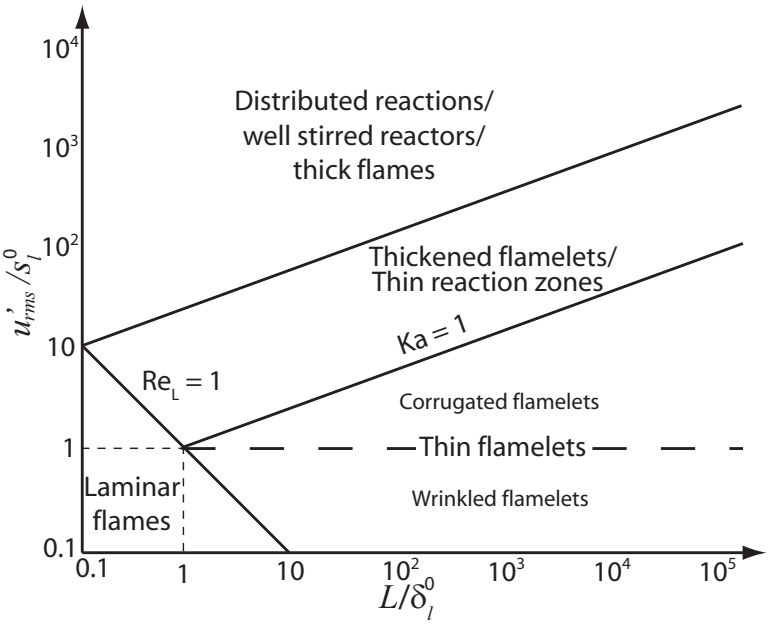

Figure 1.1: Regimes of turbulent premixed combustion

will be associated with the Kolmogorov scale (λ_k) is larger than the laminar flame thickness (δ_l^0), the inner structure of the flamelet is assumed to be that of an unsteady stretched laminar flame or a 'thin flamelet'. If this length scale is smaller than the flame thickness, micro-scale eddies may penetrate and modify the flame structure, creating a 'thickened flamelet'.

To distinguish the different regimes of turbulent premixed combustion, it is common practice to construct a regime diagram. Such a diagram is given in Fig. 1.1. The ordinate is u'_{rms}/s_l^0, where u'_{rms} is the root-mean-squared velocity fluctuations and s_l^0 is the unstretched laminar flame speed. The abscissa represents the turbulence length scale, characterized by the integral scale L, relative to the flame thickness. While there is considerable variation in theoretically predicted regimes and transitions (e.g. Refs. [85, 90]), the presented diagram demonstrates the important features.

In the lower left corner, the turbulence is weak and small scale. For a turbulent

Reynolds number:

$$\mathrm{Re}_L = \frac{u'_{rms} L}{\nu} = \left(\frac{u'_{rms}}{s_l^0}\right)\left(\frac{L}{\delta_l^0}\right) \tag{1.1}$$

less than unity, the flame is essentially laminar. The relationship between the kinematic viscosity, ν, and the flame properties will be shown in §1.4. In the lower right exists the thin flamelet regime. This is sometimes further divided into 'wrinkled flamelets' where no pocket formation is expected and 'corrugated flamelets' where the flame front is convoluted to the point that isolated pockets of fresh and burnt gasses are formed. The division is along the line $u'_{rms}/s_l^0 = 1$. Above this is the thickened flamelets regime, with the division lying along the line $\mathrm{Ka} = 1$, where Ka is the Karlovitz number. This can be expressed as [85]:

$$\mathrm{Ka} = \frac{\tau_c}{\tau_k} = \left(\frac{L}{\delta_l^0}\right)^{-\frac{1}{2}} \left(\frac{u'_{rms}}{s_l^0}\right)^{\frac{3}{2}} \tag{1.2}$$

where τ_k is the Kolmogorov time scale. Farther above this is a regime in which broadly thickened flames or distributed reactions may exists.

Of the different possible effects of turbulence on the flame, only the importance of increasing flame surface area is known with certainty. The ability of eddies smaller than the flame thickness to significantly modify the flamelet structure is uncertain since the lifetime of these eddies in very short. The existence of distributed reactions is generally only observed in cases of rapid compression ignition; the fast and uniform temperature rise due to compression caused homogenous reaction, not the turbulence [36]. However, the existence of the thin flamelet regime is well established and represents a wide range of conditions having practical importance [40, 50, 106]. Hence, this class of turbulent premixed combustion is the focus of this work.

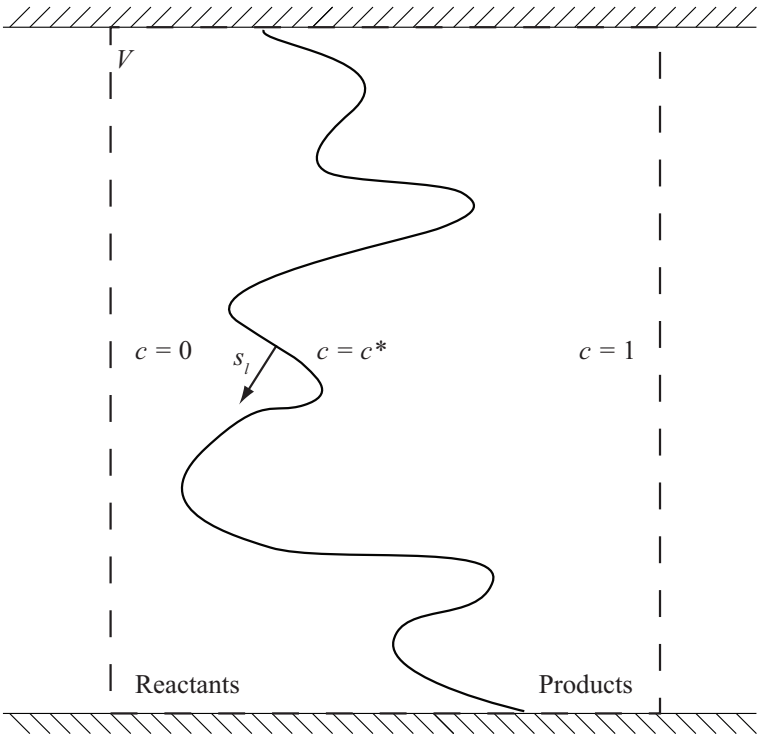

Figure 1.2: Instantaneous turbulent flame surface.

1.4 The thin flamelet regime

Within the thin flamelet regime, flamelets have the structure of unsteady, stretched laminar flames. Hence, they exist in thin sheets separating the fresh reactants from the burnt products. These two states are distinguishable by the reaction progress variable:

$$c = \frac{T - T_u}{T_b - T_u} \tag{1.3}$$

where T is the temperature, u indicates the unburnt reactants, and b indicates the burnt products. Hence, $c = 0$ and 1 in these states respectively. A particular value, $c = c^*$, is used to identify the flame surface.

Consider the wrinkled turbulent flame shown in Fig. 1.2. The instantaneous flame surface is everywhere propagating normally to itself at the local flame speed, s_l. This propagation speed is, in general, different from the unstretched laminar flame speed

s_l^0. A control volume (V) containing the flame surface may be created as shown. The instantaneous mass flow rate of reactants ($\dot{m}_r$) through the flame in V can be written as:

$$\frac{\dot{m}_r}{V} = \rho_u \langle s_l \rangle \frac{A_t}{V} = \rho_u \langle s_l \rangle \Sigma \tag{1.4}$$

where A_t is the flame surface area in V and ρ_u is the density of the unburnt gas. The term Σ represents the flame surface density, which is the flame surface area per unit volume. Spatial averaging is denoted by $\langle \cdot \rangle$ and $\langle s_l \rangle$ is the mean propagation speed of the flamelet in V.

From Eq. 1.4, the two mechanisms associated with turbulence that affect the reaction rate are apparent:

1. **The flame surface density is altered.** A turbulent flame is stretched due to the interaction between velocity gradients in the reactants and the propagating flame front. This results in an increase in the flame surface area per unit volume and the total reaction rate of the flame.

2. **The local reaction rate of the flame surface is altered.** As turbulence interacts with the flame, the curved streamlines and flame front cause unequal diffusion of heat and different reactants. This in turn causes the local reaction rate to change. The net effect alters the mean reaction rate, or equivalently the mean propagation speed [64].

Hence, in order to properly model turbulent premixed flames, it is essential to understand the mechanisms that control these two effects. However the increase in flame surface area is by far the dominant of the pair. Increases in turbulent flame speeds over laminar ones have been reported as high as factors of about five, while changes in the propagation speed of stretched flames are generally on the

order of 10% [36]. In practical application, the majority of turbulent combustion simulations consider the increase in burning velocity to be nearly a purely flame surface area effect. Variations in the local propagation speed are often ignored or treated using simple laminar theory [22, 28, 51, 84]. Thus it is apparent that an accurate description of the mechanisms responsible for the generation of flame surface area is critical. Such a description is the focus of this work.

1.4.1 Properties of a laminar flamelet

Before moving on, a brief discussion of laminar flame properties is required. In the above analysis, two flame properties were employed: the laminar flame speed and the laminar flame thickness. A typical definition of the unstretched laminar flame thickness is set by the unstretched flame speed and the thermal diffusivity of the unburnt mixture (α_u):

$$\delta_l^0 = \frac{\alpha_u}{s_l^0} \tag{1.5}$$

This thickness is about one order of magnitude smaller than the thermal thickness of the flame and approximately represents the width of the reaction zone. An equivalent stretched flame thickness, δ_l, can be defined using an appropriate stretched flame speed (i.e. s_l). Note that the thermal diffusivity in typical fuel-air mixtures is approximately equal to the kinematic viscosity and Eq. 1.1 therefore represents a Reynolds number.

However, the aforementioned stretched flame speed is a much more complicated property. In general, flame speeds can be defined in two ways: displacement speeds that measure the speed of a particular flame iso-surface, and consumption speeds that are integrated through the flame front and represent the rate of reactant consumption. In the case of an unstretched flame, these speeds are essentially equivalent

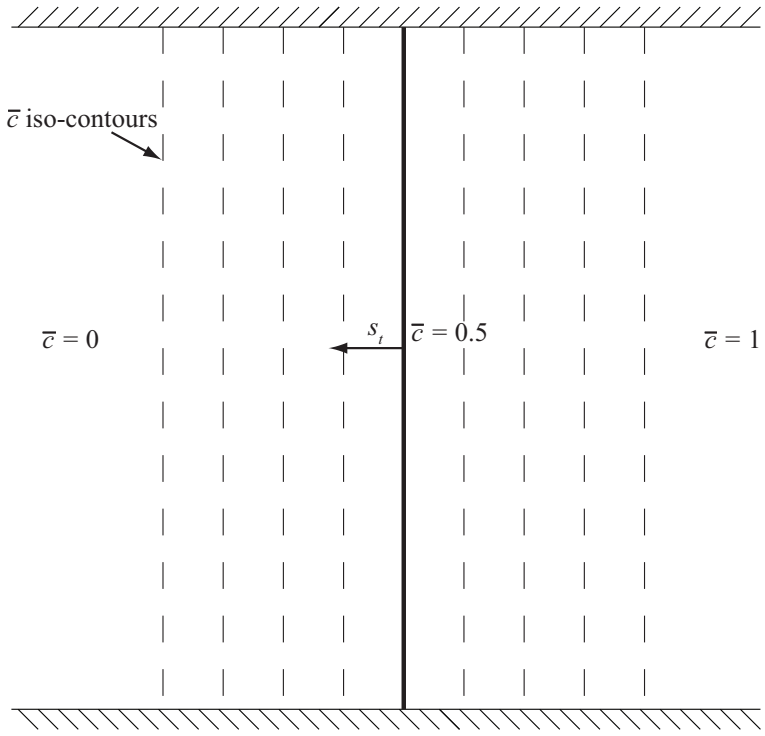

Figure 1.3: Mean progress variable field of a turbulent premixed flame.

as all iso-surface move with the same speed.

However, as a flame is stretched the iso-surfaces move relative to each other. Hence, the displacement speed is very dependant on the specific iso-surface considered. For the purposes of this dissertation, flame speeds will be considered as consumption speeds. This is essentially the propagation speed of the overall wave. That is,

$$s_l = -\frac{1}{\rho_u} \int_{-\infty}^{\infty} \dot{w}_r d\hat{n} \tag{1.6}$$

where $\dot{w}_r$ is the local volumetric reaction rate of the flamelet and $\hat{n}$ is the flame surface normal direction. This is the definition most consistent with that of a standard laminar flame speed.

1.5 The area of a turbulent flame

In 1940, Damköhler [32] postulated that the primary effect of turbulence at a scale larger than the flame thickness is to increase the reactive flame surface area; the turbulence causes the flame surface to wrinkle. Such a wrinkled flame is shown in Fig. 1.2 and the reactant mass flux is given by Eq. 1.4. The temporal average of this instantaneous equation may be taken to determine the mean reaction rate in the volume.

Alternatively, the mean reaction progress variable can be considered. In the mean, $\overline{c}$ is distributed over space as shown in Fig. 1.3. The flame is considered to lie on a particular $\overline{c} = \overline{c}^*$ iso-surface, typically taken as $\overline{c}^* = 0.5$. Hence, it is smoother than the instantaneous flame surface, possesses an area of $\overline{A}_l < A_t$, and propagates at a turbulent burning velocity $s_t > s_l$. In either view the mean reaction rate is equal, yielding:

$$\overline{\dot{m}}_r = \overline{\langle s_l \rangle A_t} \rho_u = s_t \overline{A}_l \rho_u \tag{1.7}$$

Hence, the increase in the consumption speed of the flame caused by turbulence is given by:

$$\frac{s_t}{s_l^0} = I_0 \frac{A_t}{\overline{A}_l} = I_0 \Xi \tag{1.8}$$

The factor I_0 represents differences in the local propagation speed of the actual flamelet from that of the unstretched flamelet. This factor will be discussed further in §1.5.2. The flame wrinkling factor is denoted by Ξ. This represents the projection of the flame surface area onto the direction of mean propagation and is related to the flame surface density by [22]:

$$\overline{\Sigma} = \overline{\Xi} |\nabla \overline{c}| \tag{1.9}$$

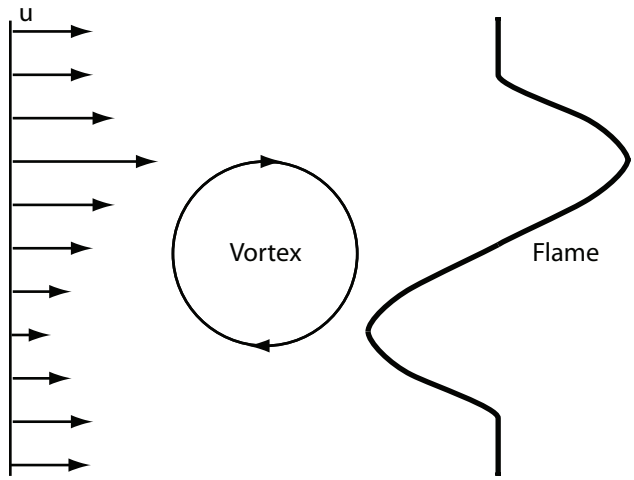

Figure 1.4: Schelkin's concept of flame wrinkling by a vortex.

It is therefore clear that the increase in burning rate of a turbulent flame relative to a laminar flame is characterized by the increase in flame surface area. Hence, the two common methods of determining the turbulent flame area are described below.

1.5.1 Geometric descriptions

To describe the change in flame surface area caused by turbulence, Schelkin considered the interaction between a simple rotating vortex with the flame as shown in Fig. 1.4 [98]. In this configuration, there are equal regions in which the velocity is lower and higher than the mean. It was postulated that such turbulence would produce a pair of conical wrinkles, the area of which could be related to the vortex strength relative to the laminar flame speed. From the geometry of these cones, a relationship for the turbulent burning velocity was derived:

$$\frac{s_t}{s_l^0} = \left[1 + \left(\frac{2u'_{rms}}{s_l^0}\right)^2\right]^{1/2} \tag{1.10}$$

This equation reproduces the general trend experimentally observed for moderately intense turbulence. That is, the turbulent burning velocity (and hence flame area) increases in a somewhat linear manner with $\frac{u'_{rms}}{s_l^0}$. However, there is consider-

able scatter in experimentally measured and computationally determined values of $\frac{s_t}{s_l^0}$ when correlated with Eq. 1.10 [36, 85].

In an attempt to correct this, there have been many attempts to fit the turbulent burning velocity to a more general equation of the form:

$$\frac{s_t}{s_l^0} = 1 + b_1 \left(\frac{u'_{rms}}{s_l^0} \right)^{b_2} \tag{1.11}$$

where b_1 and b_2 may depend on the turbulence parameters [1]. However, there does not appear to be any form of Eq. 1.11 that can reproduce the experimental results; the relationship between the turbulent burning velocity and the turbulence intensity appears to be highly geometry and case dependant even in simple laboratory configurations [85]. Furthermore, the turbulent burning velocity does not increase monotonically with the turbulence intensity, but exhibits a leveling off or 'bending' at high u'_{rms}. At even higher turbulence intensities, the burning velocity may begin to decrease. These trends are associated with flamelet quenching and merging, are highly geometry dependent, and are difficult to predict using simple correlations [36, 90].

A variety of other approaches have also been attempted to derive a general correlation between the turbulent burning velocity and properties of the turbulence. These include modeling the flame as a fractal surface [47, 48] or using theoretical analysis based on Renormalization Group Theory [89, 114]. However, there is no current method that can accurately predict the turbulent burning velocity based on an algebraic relationship with the turbulence parameters for a variety of geometries [36]. The reason for this and further aspects of modeling the turbulent burning velocity are discussed in §1.9.

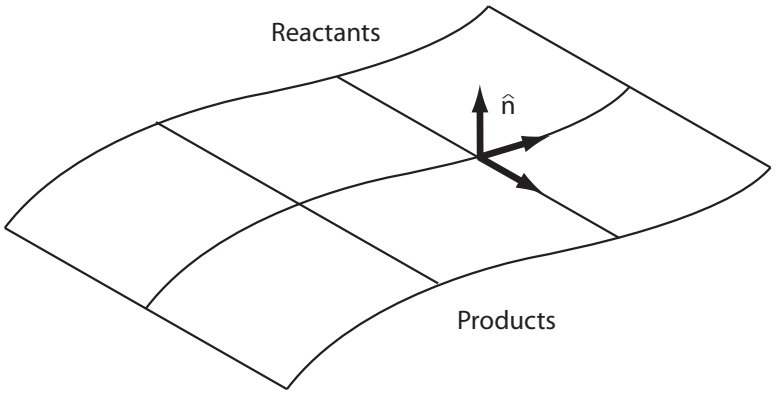

Figure 1.5: Material surface subjected to stretch rates

1.5.2 Flame stretch

From the above discussion, it appears that simple correlations for the turbulent flame speed or flame surface area are unlikely to be sufficiently accurate to describe the complex processes in turbulence-flame interactions. In order to create a more accurate model for the flame surface area, it is necessary to understand the mechanisms with which turbulence changes the area of a flamelet.

In the flamelet regime the flame surface is treated as a propagating interface between reactants and products. Hence, an equation is required for the change in incremental area (δA) with time for such a surface in a turbulent flow. This change in area is defined as the stretch rate (κ) and given by:

$$\kappa = \frac{1}{\delta A}\frac{D(\delta A)}{Dt} \tag{1.12}$$

The equation relating the stretch rate to turbulence parameters has been derived in various forms [17, 71]. To do so, we consider a surface given by $A(t)$ with a unit normal direction denoted by $\hat{n}$ as shown in Fig. 1.5. For consistency with the standard definition of curvature, $\hat{n}$ will be taken to point into the reactants. The surface is propagating at a velocity $\vec{w}$ in the laboratory frame.

For any vector quantity, the rate of change its flux across the surface ($\vec{q}$) can be

written using the transport relation for a surface as:

$$\frac{D}{Dt}\int_{A(t)} \vec{q}\cdot\hat{n}dA = \int_{A(t)}\left[\frac{\partial\vec{q}}{\partial t} + \vec{w}\cdot\nabla\vec{q} - \vec{q}\cdot\nabla\vec{w} + \vec{q}\nabla\cdot\vec{w}\right]\cdot\hat{n}dA \tag{1.13}$$

For the case of $\vec{q} = \hat{n}$, Eq. 1.13 yields:

$$\frac{D}{Dt}\int_{A(t)} dA = \int_{A(t)}\left[\frac{\partial\hat{n}}{\partial t} + \vec{w}\cdot\nabla\hat{n} - \hat{n}\cdot\nabla\vec{w} + \hat{n}\nabla\cdot\vec{w}\right]\cdot\hat{n}dA \tag{1.14}$$

Since $\hat{n}$ is a unit normal vector,

$$\frac{\partial\hat{n}}{\partial t}\cdot\hat{n} = \frac{1}{2}\frac{\partial|n|^2}{\partial t} = 0 \tag{1.15}$$

$$(\vec{w}\cdot\nabla\hat{n})\cdot\hat{n} = \vec{w}\cdot\frac{1}{2}\nabla|n|^2 = 0 \tag{1.16}$$

and hence,

$$\frac{D}{Dt}\int_{A(t)} dA = \int_{A(t)}\left(-\hat{n}\cdot(\hat{n}\cdot\nabla)\,\vec{w} + \nabla\cdot\vec{w}\right)dA \tag{1.17}$$

Thus, for a differential surface element, δA, over which the argument on the right remains constant, an expression for the stretch rate is obtained:

$$\kappa = \frac{1}{\delta A}\frac{D(\delta A)}{Dt} = -\hat{n}\cdot(\hat{n}\cdot\nabla)\,\vec{w} + \nabla\cdot\vec{w} \tag{1.18}$$

To gain insight into the terms comprising κ, it is useful to decompose the propagation speed of the surface in the laboratory frame ($\vec{w}$) into its flow and flame propagation components. That is,

$$\vec{w} = \vec{u} + s_l\hat{n} \tag{1.19}$$

where $\vec{u}$ is the fluid velocity field. Recall that the surface normal points into the reactants.

Substituting Eq. 1.19 into Eq. 1.18 and simplifying yields:

$$\kappa = (-\hat{n}\cdot(\hat{n}\cdot\nabla)\,\vec{u} + \nabla\cdot\vec{u}) + s_l\nabla\cdot\hat{n} \tag{1.20}$$

$$= (\delta_{ij} - n_i n_j)\frac{\partial u_i}{\partial x_j} + s_l\frac{\partial n_i}{x_i} \tag{1.21}$$

$$= a_t + \kappa_c \tag{1.22}$$

The first term on the right side of Eq. 1.21 is associated with velocity gradients at the flame surface and represent the tangential strain rate exerted on the flame by the flow (a_t). The second term represents changes in the flame area due to propagation of the curved wave (κ_c). This can be seen clearly since $\nabla \cdot \hat{n}$ is the curvature (C) of the surface. With the surface normal defined as above, a positive curvature is convex towards the reactants. This corresponds to a center of curvature in the products, an outwardly propagating wave, and hence an increasing flame surface area. The converse is true for a negatively curved flame, which is concave towards the reactants.

The relationship between the stretch rate and the flame surface area is further elucidated by the flame surface density. The transport equation for Σ was originally formulated based on heuristic arguments by Marble and Broadwell for the Coherent Flamelet Model [69]. It has since been derived from more rigorous mathematical arguments by a variety of authors [17, 92, 108, 110]. First we define the flame surface density as $\Sigma = \delta A / \delta V$. The rate of change of any volumetric property, q, within a surface, $S(t)$, moving with the flame is:

$$\frac{D}{Dt}\int_{V(t)} q dV = \int_{V(t)} \frac{\partial q}{\partial t} dV + \int_{S(t)} q\vec{w} \cdot \hat{n} dA \tag{1.23}$$

Considering the rate of change of the volume itself as the surface is stretched, $q = 1$ and:

$$\frac{D}{Dt}\int_{V(t)} dV = \int_{S(t)} \vec{w} \cdot \hat{n} dA = \int_{V(t)} \nabla \cdot \vec{w} dV \tag{1.24}$$

For a differential volume element this becomes:

$$\frac{1}{\delta V}\frac{D\left(\delta V\right)}{Dt} = \nabla \cdot \vec{w} \tag{1.25}$$

Combining this with Eqs. 1.19 and 1.22 and expanding the substantiative derivative

as:

$$\frac{D}{Dt} = \frac{\partial}{\partial t} + \vec{w} \cdot \nabla \tag{1.26}$$

yields a final transport equation for Σ:

$$\frac{\partial \Sigma}{\partial t} + \nabla \cdot \left[\left(\vec{u} + s_l \hat{n} \right) \Sigma \right] = \left(-\hat{n} \cdot \left(\hat{n} \cdot \nabla \right) \vec{u} + \nabla \cdot \vec{u} \right) \Sigma + \left(s_l \nabla \cdot \hat{n} \right) \Sigma = a_t \Sigma + \kappa_c \Sigma \tag{1.27}$$

The terms on the left represent the combined effects of advection, convection, and normal propagation of the flame surface. The right side represents the mechanisms that create and destroy Σ, namely the stretch rates. An additional term is often subtracted from the right side to represent destruction phenomena not accounted for in the above analysis. These include effects such as flamelet annihilation due to quenching and merging. However, these phenomena did not occur in the present experiment and are therefore not considered.

From Eq. 1.27, it is apparent that turbulence affects the flame area both by straining the flame surface and generating wrinkles (i.e. curvature). However the physical processes responsible for these two mechanisms are very complex. That is, the turbulence affects the topography of the flame, changing both the strain rate exerted and contributing stretch through curvature. The flame also greatly affects the turbulence by both attenuating and generating velocity gradients. This further alters the stretch rate. Hence, the physics of the turbulence-flame interaction must be considered when describing the stretching of a flame surface.

1.5.3 The stretched flame propagation speed

The stretch rate is also a central parameter in determining deviations in the flame speed from the unstretched value. The traditional laminar model states [85]:

$$s_l = s_l^0 - \ell \kappa \tag{1.28}$$

where ℓ is the Markstein length. This can be recast in terms of the dimensionless Markstein number, $\mathrm{Ma} = \ell/\delta_l^0$, and Karlovitz number, $\mathrm{Ka} = \kappa\delta_l^0/s_l^0$, as:

$$\frac{s_l}{s_l^0} = I_0 = 1 - \mathrm{MaKa} \tag{1.29}$$

However, this relationship does not appear to completely account for the effect of stretch rate on the flame speed. In particular, strain rate and curvature stretch rate appear to cause different responses [24, 25]. Also, the flame speed cannot increase monotonically to infinity; at some stretch rate (either positive or negative depending on Ma) it begins to decrease. To account for these effects, more complex models have also been proposed [64, 72]. However, such models are not the focus of this dissertation and the qualitative relationship of Eq. 1.29 is sufficient.

1.6 Turbulent combustion simulations

From the above discussion, it is apparent that accurate models for κ and/or s_t/s_l^0 are required to predict the flame surface area and the consequential behavior of turbulent premixed flames. However, before discussing previous modeling methodologies for these terms, it is useful to discuss how they are employed in turbulent combustion simulations. This will be done in the context of Large Eddy Simulations (LES).

In an LES, the large scales of the turbulence are explicitly resolved and the small scale effects are modeled in the subgrid. That is, the flow field is filtered at some scale, Δ, and fluctuations below this scale are not directly computed. In combustion simulations, the flame is also too thin for explicit resolution. Hence, some form of filtered flame front also must be considered. Simulations posses the filtered velocity field, flame front position, and some other flow field properties such as the temperature and composition. However, the small scale details of the flame and flow are

not resolved. Hence, any turbulence-flame interaction processes occurring at subgrid scales must be modeled.

LES methods for turbulent premixed combustion generally fall under three classification: models that employ a transport equation for the filtered reaction progress variable (flame surface density methods), models that artificially thicken the flame front, and models that attempt to track the filtered flame front location (G-equation methods). All of these employ the laminar flamelet paradigm and face somewhat similar challenges. A brief description of each is provided below. Further details are provided by Pitch [88].

1.6.1 Flame surface density methods

Methods that employ the filtered reaction rate equation have been proposed by Boger et al. [4] and Hawkes and Cant [51, 52]. Such methods require modeling of the flame surface density at the subgrid scales. That is, the transport equation for the filtered reaction progress variable is [52]:

$$\frac{\partial \tilde{\rho}\tilde{c}}{\partial t} + \frac{\partial \tilde{\rho}\hat{u}_i\tilde{c}}{\partial x_i} = \frac{\partial}{\partial x_i}\left(\frac{\tilde{\rho}\nu_t}{\mathrm{Sc}_{sg}}\frac{\partial \tilde{c}}{\partial x_i}\right) + \rho_u s_l \Sigma_{sg} \tag{1.30}$$

where Sc_{sg} is a subgrid scale Schmidt number. The notation $(\tilde{\cdot})$ indicates an LES filtering operation and $(\hat{\cdot})$ indicates a density weighted filtering operation. That is, for any field quantity, $q(\vec{x})$, and filter kernel, $H(\vec{x}-\vec{x}')$, on a domain F:

$$\tilde{q}(\vec{x}) = \int_F q(\vec{x}')H(\vec{x}-\vec{x}')d\vec{x}' \tag{1.31}$$

$$\hat{q}(\vec{x}) = \int_F \frac{\rho(\vec{x})}{\langle\rho\rangle} q(\vec{x}')H(\vec{x}-\vec{x}')d\vec{x}' \tag{1.32}$$

In Eq. 1.32, the filter kernel must be normalized such that:

$$\int_F \frac{\rho(\vec{x})}{\langle\rho\rangle} H(\vec{x}-\vec{x}')d\vec{x}' = 1 \tag{1.33}$$

Closure of Eq. 1.30 requires a model for the subgrid flame surface density (Σ_{sg}). To do so, Hawkes and Cant [51, 52] employ the subgrid filtered equivalent of the flame surface density transport equation (Eq. 1.27), which takes the form:

$$\frac{\partial \Sigma_{sg}}{\partial t} + \frac{\partial}{\partial x_i}\left[\left(\hat{u}_i + \left(\left(\tilde{u}_i\right)_f - \hat{u}_i\right) + \widetilde{s_l n_i}\right)\Sigma_{sg}\right] = \tilde{a}_t \Sigma_{sg} + \widetilde{s_l \frac{\partial n_k}{\partial x_k}}\Sigma_{sg} \tag{1.34}$$

here $(\cdot)_f$ indicates that the property is conditioned on the flame surface. Note that some properties $(a_t, s_l, \hat{n})$ are only defined on the flame and hence the subscript f is unnecessary. This equation has several unclosed terms; any terms involving flame front conditioned properties cannot be resolved by the LES and must be modeled.

To do so, models are generally derived based on RANS paradigms such as those in Refs. [17, 38]. In Refs. [51, 52], the strain rate was broken into three parts representing the effect of the resolved flow ($a_{t,\Delta}$), subgrid turbulence ($a_{t,sg}$), and choice of c^* ($a_{t,c}$). The terms representing the effect of the turbulence on the flame were then modeled as:

$$a_{t,\Delta} = (\delta_{ij} - m_{ij})\frac{\partial \hat{u}}{\partial x_j} \tag{1.35}$$

$$a_{t,sg} = \Gamma\left(\vec{\xi}\right)\frac{\sqrt{k}}{\Delta} \tag{1.36}$$

where m_{ij} is representative of the filtered flame surface normal (analogous to $n_i n_j$ in Eq. 1.21), Γ is a stretch efficiency function parameterized by $\vec{\xi}$, and k is the turbulence kinetic energy.

The subgrid curvature stretch rate was also decomposed into the contribution from the resolved and subgrid turbulence and modeled as:

$$\kappa_{c,\Delta} = \frac{\partial}{\partial x_i}\left(s_l(1+\gamma c^*)M_i\right) + s_l(1+\gamma c^*)\frac{\partial M_i}{\partial x_i} \tag{1.37}$$

$$\kappa_{c,sg} = -\alpha\beta s_l \frac{\Sigma_{sg}}{1-\tilde{c}} \tag{1.38}$$

where $\vec{M}$ is representative of a filtered flame orientation, γ is a heat release parameter, α is a resolution factor, and β is a constant.

Further details of the model terms can be found in Refs. [51, 52]. However, two important features of the subgrid scale models must be highlighted. It is first noted that α, β, s_l, Γ, k, and Σ_{sg} are all positive quantities and that $\tilde{c}$ varies between zero and one. Hence, the subgrid scale strain rate is exclusively positive and characterized by the stretch efficiency function. This function is very important and will be discussed in detail below. Also, the model implies that subgrid scale flame curvature is exclusively negative and proportional to the flame surface density. The accuracy of these assumptions will also be analyzed.

1.6.2 Thickened flame models

Flame surface density models, while being a physically attractive solution, possess one particular difficulty: they attempt to track the propagation of the reaction progress variable, c. However, changes in the c-field between reactants and products occur over too short of a distance to be resolved on an LES grid; the flame is thinner than the size of a cell. While various methods have been proposed to overcome this, they are generally quite complex and expensive, involving explicit filtering or adaptive meshes. An alternative solution has been proposed in which the flame front is artificially thickened such that it can be resolved on a standard LES grid, while leaving the laminar flame speed unaltered [22, 28]. This is done by proportionally increasing the molecular and thermal diffusivity. In such a formulation, the thickened flame can be explicitly tracked. However, the physics of the turbulence-flame interactions are significantly altered.

For this approach, the effect of the turbulence-flame interaction must be modified such that the net influence of the turbulence on the thickened flame is similar to

what would occur in a real flame. That is, the propagation speed (or reaction rate) of the thickened flame must reflect increases is the subgrid flame surface that no longer appear. This essentially reduces to determining the subgrid scale turbulent burning velocity or the subgrid flame surface area.

To do so, Charlette et al. [22] employ the subgrid wrinkling factor, Ξ, which is linked to the subgrid turbulent burning velocity by:

$$\frac{s_t}{s_l^0} = \frac{A_{T\Delta}}{\Delta^2} = \Xi \tag{1.39}$$

They then apply flame surface density ideas in the subgrid to determine Ξ. That is, instead of using the subgrid flame surface density to close the $\tilde{c}$ transport equation, it was used to derive an estimate for the subgrid enhancement of the flame speed that is not reflected by the wrinkling of the thickened flame. However, the transport equation itself was not solved. Instead, a balance between the subgrid production and destruction of Σ was assumed. The subgrid strain rate was then modeled in a similar fashion to Eq. 1.36, setting:

$$a_{t,sg} = \Gamma\left(\vec{\xi}\right)\frac{u'_\Delta}{\Delta} = -\kappa_{c,sg} \tag{1.40}$$

where u'_Δ is the subgrid root-mean-square velocity fluctuations. They then postulate a relationship between the subgrid wrinkling factor and the subgrid curvature, yielding an equation of the form:

$$\frac{s_t}{s_l^0} = \Xi = \left(1 + \min\left[\frac{\Delta}{\delta_l^0}, a_{t,sg}\right]\right)^\beta \tag{1.41}$$

where β may be allowed to vary.

Despite the differences between the Σ and thickened flamelet models, both approaches include a few similar assumption: the strain rate is positive and related to the stretch efficiency function, the curvature is negative. In the former method

the curvature is related to the subgrid flame surface density while in the latter it is related to the strain rate. The validity of these assumptions is an important aspect of these models that needs to be evaluated. Also, the assumption that the strain rate and curvature locally balance must be assessed.

1.6.3 G-equation methods

An alternative approach that avoids the problems caused by the thinness of the physical flame is to employ an artificial scalar field, typically referred to as G [112]. The flame is represented by a particular isosurface of the G-field, $G(\vec{x}, t) = G_0$. The reactants are identified by $G < G_0$ and the products by $G > G_0$. Since G is an artificial scalar, it can be smooth on the LES grid. Furthermore, G only has physical meaning at the flame surface; as long as the dynamics of this surface are accurately prescribed, the dynamics of the remainder of the G field are unimportant.

The equation for the transport of G has been derived by several authors [58, 85, 87, 112]. Pitsch [87] proposes the following form:

$$\frac{\partial \breve{G}}{\partial t} + \breve{\vec{u}}_u \cdot \nabla \breve{G} = (\breve{s}_{lu} + s_{tu}) |\nabla \breve{G}| \tag{1.42}$$

In this equation, $\breve{(\cdot)}$ represents a conditional averaging operation along the flame surface. That is, $\breve{\vec{u}}_u$ represents the mean gas velocity at the filtered flame front on the unburnt side of the flame. Hence, it is the velocity field into which the flame is propagating. Similarly, $\breve{s}_{lu}$ is the mean laminar flame speed on the unburnt side of the flame. The subgrid turbulent burning velocity relative to the unburnt gas is given by s_{tu}. This describes the increase in the propagation speed of the flame due to the subgrid turbulence and, in the laminar flamelet regime, represents the increase in subgrid flame surface area. Note that $\breve{G}$ does not designate a filtering operation applied to the G-field, but simply the level-set representation of the filtered flame

front; G is smooth on the grid. If proper values are used for $\breve{\vec{u}}_u$, $\breve{s}_{lu}$, and s_{tu}, the G-field at $\breve{G} = G_0$ accurately mimics the dynamics of the real filtered flame.

These terms must therefore be properly modeled. The mean laminar burning velocity along the filtered flame can be computed using models such as Eq. 1.29 or another appropriate correlation. However, the $\breve{G}$ transport equation still requires models for the subgrid turbulent burning velocity and conditional velocity field on the flame.

For the subgrid turbulent burning velocity, Pitsch suggested using an algebraic relationship that recovers the Damköler limits at appropriate turbulence levels [87, 88]. However, as was discussed in §1.5.1, such relationships are unlikely to be sufficiently general for an accurate model in the flamelet regime; they do account for transport of flame surface area and are geometry dependent. Appropriate models for the turbulent burning velocity will be discussed in §1.9. For the conditional velocity on the flame surface, a density weighted filtering of the velocity field was proposed, however this term will not be evaluated herein [87].

1.7 Previous models for the stretch rate

As can be deduced from the above discussion, accurately predicting the flame surface area is essential to accurately simulating turbulent premixed combustion. Models for the stretch rate are intrinsically necessary for flame surface density methods and may be necessary for G-equation methods if algebraic relationships for the turbulent burning velocity fail. Such models are typically derived based on a similar paradigm. A characteristic stretch rate for the turbulence is determined based on standard modeling variables. For example, using the turbulence kinetic energy and kinetic energy dissipation rate (ε), a characteristic stretch rate for the large scale

turbulence is given by ε/k or, equivalently, by u'_{rms}/L. A characteristic stretch rate for the small scale turbulence is $\sqrt{\varepsilon/\nu}$. In LES, different characteristic stretch rates can be defined based on a combination of these parameters and the LES filter scale. This characteristic stretch rate is then multiplied by constants or a function that attempts to simulate the turbulence-flame interaction. Early models used a simple constant or a combination of constants and global turbulence parameters such as Re_L [90]. However, DNS of two-dimensional vortex pairs impinging on a laminar flame showed that the relationship between turbulence and stretch rate was more complex than could be captured by these simple methods [74]. In particular, it was observed that the stretch rate exerted by small vortices was less than expected based purely on consideration of the velocity gradient magnitudes. These discrepancies have been attributed to a variety of effects involving the evolution of the vortices and geometric effects of the finite flame thickness.

The difference in the effectiveness of different scales in stretching the flame front led to development of the Intermittent Turbulence Net Flame Stretch (ITNFS) model [74]. Since then, the philosophy behind the model has remained largely unchanged with some modifications being made to the detailed formulation in various implementations [22, 28]. At present, it is the only modeling paradigm available that explicitly takes into account the physics of the turbulence-flame interactions.

The concept follows two basic steps:

1. Determine the effective stretch rate exerted by a canonical configuration of vortices impinging on a flame front at a variety of different strengths and scales. Use these to determine the stretch efficiency as a function of scale.

2. Determine the distribution of stretch rate over the range of scales in a turbulent flow. The net effective stretch rate can then be computed by integrating over

these scales.

This procedure results in the stretch efficiency function for a turbulent flow that consists of flame-vortex interactions in the canonical configuration. This is the stretch efficiency function used in the aforementioned LES methods.

However, the ITNFS model relies on many simplifying assumptions that produce and unrealistic image of the turbulence and the turbulence-flame interaction. These assumptions are inherent to the fundamental building block of the model. That is, the geometry, evolution, and characterization of the turbulence-flame interaction at a given scale are extremely simplified and do not accurately reflect real turbulence. These aspects of the model and the inherent problems are discussed below.

1.7.1 The stretch efficiency of scale r in the ITNFS model

The ITNFS model was developed based on DNS of a simple, canonical turbulence-flame interaction [74, 91]. The configuration involved the interaction between a two-dimensional counter-rotating vortex pair characterized by a scale (r) and a speed (v_r), and a planar laminar premixed flame front characterized by the flame speed and thickness as shown in Fig. 1.6. The length scale was designated as the distance between the vortex cores and the velocity scale was defined as the maximum velocity difference relative to s_l^0. Details of the exact numerical configuration can be found in Ref. [91].

The effectiveness of turbulence at a given scale at stretching a flamelet was expressed using a stretch-efficiency transfer function, Φ. This was defined as a function of r/δ_l^0 such that:

$$\kappa = \Phi\left(\frac{r}{\delta_l^0}\right)\frac{v_r}{r} \tag{1.43}$$

The characteristic stretch rate of the vortices was assumed to be v_r/r. To estimate

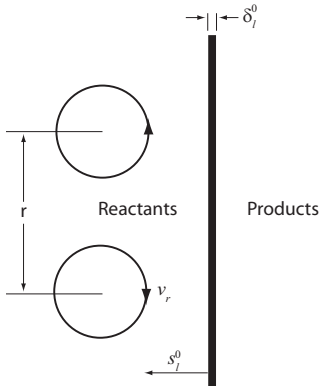

Figure 1.6: Canonical configuration for DNS of flame vortex interactions

Φ, the rate of increase in the total reaction rate over the computational domain was determined. This was equated with the rate of increase in flame surface area. Hence, the stretch efficiency transfer function was calculated to account for both the strain and curvature components of the stretch rate simultaneously.

The data and curve fit from Ref. [74] are reproduced in Fig. 1.7. The curve was fitted by the function:

$$\Phi\left(\frac{r}{\delta_l^0}\right) = 10^{-\frac{0.545}{s+0.364}} \tag{1.44}$$

where

$$s = \log_{10}\left(\frac{r}{\delta_l^0}\right) \tag{1.45}$$

As can be seen, there is considerable vertical scatter around the curve fit, particularly at low r/δ_l^0. Hence, it is apparent that another parameter is significant in this relationship or the characteristic strain rate of the vortices was incorrectly defined.

Colin et al. [28] considered an additional parameter, setting:

$$\kappa = \Phi\left(\frac{r}{\delta_l^0}, \frac{v_r}{s_l^0}\right)\frac{v_r}{r} \tag{1.46}$$

Based on the same methodology as above, they proposed the following fit for their

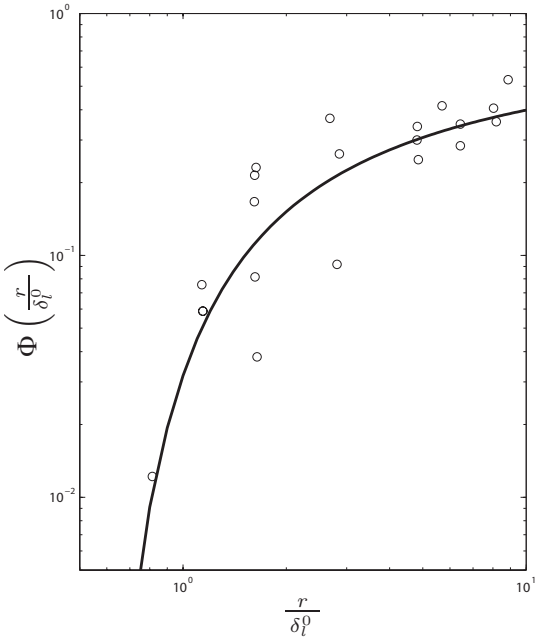

Figure 1.7: Stretch efficiency transfer function of Meneveau and Poinsot [74].

Φ:

$$\Phi\left(\frac{r}{\delta_l^0}, \frac{v_r}{s_l^0}\right) = \frac{1}{2}\left[1 + \mathrm{erf}\left(0.6\left(\ln\left(\frac{r}{\delta_l^0}\right) - \left(\frac{v_r}{s_l^0}\right)^{-1/2}\right)\right)\right] \tag{1.47}$$

Charlette et al. [22] use a similar approach to Colin et al. [28], adding an additional cutoff scale for weak vortices. That is, they do not allow vortices with a characteristic strength of $v_r/s_l^0 < 1/2$ to stretch the flame. However, this cutoff is fairly arbitrary. In fact, it should be completely accounted for in a properly formulated transfer function as described by Eq. 1.47.

Despite these modifications, there are several fundamental issues in the determination of Φ not accounted for in any of these studies. Firstly, this simple model for the turbulence geometry may not be sufficient. Turbulence does not occur solely in isolated counter rotating vortex pairs but is very complex, consisting of coherent structures of various size, shape, orientation, and grouping. Attempting to model the turbulence-flame interaction using a single 'building block' turbulent structure is a

large simplification and likely inadequate for a proper description; it is unlikely that the strain rate exerted by geometrically different turbulent structures would be the same even if they possessed a few similar characteristic properties. Furthermore, the canonical geometry assumes that the only effect of turbulence is to generate extensive (positive) strain and negative curvature. However, several studies have shown that both negative strain rate and positive curvature often occur. Secondly, there is no inherent reason that the stretching of a flame surface should be characterized entirely by vortices. Vorticity is only one quantity of importance in a turbulent flow. Hence, characterizing the turbulence-flame interaction solely based on vortex properties could lead to inaccurate results. Thirdly, vorticity in this simple configuration does not evolve in the same manner as a complete three-dimensional turbulent flow field. For example, it does not allow for vortex line stretching. Fourthly, treating the strain rate and curvature stretch rate as a single entity may lead to inaccuracies. These processes are fundamentally different and may be related to different properties of the turbulence. Finally, the use of preconceived vortices requires an *a priori* decision of the vortex scales and strengths to be considered. While these can be varied over a considerable range, they may not properly represent the turbulence in a given flow.

1.7.2 The effect of a range of scales in the ITNFS model

Despite the problems with the fundamental building block of the ITNFS model, the stretch efficiency transfer function thus devised can be used to model the effects of a turbulent flow containing a range of scales on the flame front. To do so, the efficiency of the individual scales is integrated across the scales present in the flow.

This yields a net stretch efficiency function, Γ, such that:

$$\kappa = \Gamma \kappa^* \tag{1.48}$$

where κ^* is some characteristic stretch rate of the flow. Three methods for performing the integration have been proposed based on various descriptions of the turbulence. However, in all cases the final stretch efficiency function followed the same general trend.

Meneveau and Poinsot [74] employed an intermittent model for the turbulence. A multi-fractal description of the intermittency was used to relate the local dissipation at scale r with the mean dissipation. From this and Φ, the distribution of velocity and the mean stretch rate at r was determined. This was then integrated to provide a stretch efficiency function associated with turbulence scales below Δ:

$$\Gamma_{MP} = \left(\frac{\Delta}{L}\right)^{2/3} \frac{c_v}{\ln 2} \int_{p_{min}}^{p_{max}} \Phi\left(e^{-p}\frac{L}{\delta_l^0}\right) e^{p(2/3-\mu/9)} dp \tag{1.49}$$

where $p = \ln(L/r)$ and $\mu \approx 0.25$ is the intermittency exponent. The constant c_v was included to match the model to experimental data and was set to 0.28.

Colin et al. [28] realized that the final changes brought about by considering the intermittency of turbulence were minor. That is, the intermittency only contributes a deviation of $\mu/9 \approx 0.028$ relative to $2/3$ in the integrand of Eq. 1.49. With this in mind, they utilized the standard Kolmogorov cascade, yielding:

$$\Gamma_{Co} = \left(\frac{\Delta}{L}\right)^{2/3} \frac{c_v}{\ln 2} \int_{p_{min}}^{p_{max}} \Phi\left(e^{-p}\frac{L}{\delta_l^0}, e^{-p/3}\left(\frac{L}{\Delta}\right)^{-1/3}\frac{u'_\Delta}{s_l^0}\right) e^{2p/3} dp \tag{1.50}$$

As an alternative to using the velocity distribution, Charlette et al. [22] choose to use the relationship between the strain rate and energy spectrum for homogeneous turbulence. That is, they propose that

$$\kappa^2 = (\Gamma_{Ch}\kappa_c)^2 = \left(\frac{\pi}{L}\right)^3 \int_1^\infty \Phi\left(\frac{r(k)}{\delta_l^0}, \frac{v_r(k)}{s_l^0}\right)^2 k^2 E_{11}(k) dk \tag{1.51}$$

Here, the turbulence scale is given as the non-dimensional wave number $k = L/r$.

The one-dimensional longitudinal energy spectrum, $E_{11}(k)$, was assumed to follow the Pao spectrum:

$$E_{11}(k) = \frac{18}{55}\left(\frac{\pi}{L}\right)^{-5/3} c_k \varepsilon^{2/3} k^{-5/3} h(k, \mathrm{Re}_L) \tag{1.52}$$

The universal Kolmogorov constant, c_k was taken to be 1.5. The function $h(k, \mathrm{Re}_L)$ represents the Pao correction for the viscous cutoff:

$$h(k, \mathrm{Re}_L) = \exp\left(-\frac{3}{2} c_k (k\pi)^{4/3} \mathrm{Re}_L^{-1}\right) \tag{1.53}$$

From this, they derive a stretch efficiency function given by:

$$\Gamma_{Ch}^2 = \frac{18}{55} c_k \pi^{4/3} \int_1^\infty \Phi\left(\frac{1}{k}\frac{\Delta}{\delta_l^0}, \frac{1}{k^{1/3}}\frac{u'_\Delta}{s_l^0}\right)^2 k^{1/3} h(k, \mathrm{Re}_\Delta) dk \tag{1.54}$$

The stretch efficiency function of Charlette et al. [22] is presented in Fig. 1.8 for various Δ/δ_l^0. As larger scales are included in the subgrid, the stretch efficiency of the subgrid turbulence increases. This indicates that the large scales are more effective at stretching the flame. This trend is identical to those produced by the other methods [28, 74].

1.7.3 Problems with the ITNFS model

As mentioned above, there are significant problems both with this model for the stretch rate and its implementation in combustion simulations. Namely, the geometric configuration of the turbulence-flame interaction is over simplified, the stretch rate may not be properly characterized, the turbulence does not evolve properly, and the straining and wrinkling of the flame are treated simultaneously. Furthermore, despite the fact that the ITNFS model computes a *stretch* efficiency function, it is typically employed as a *strain* efficiency function.

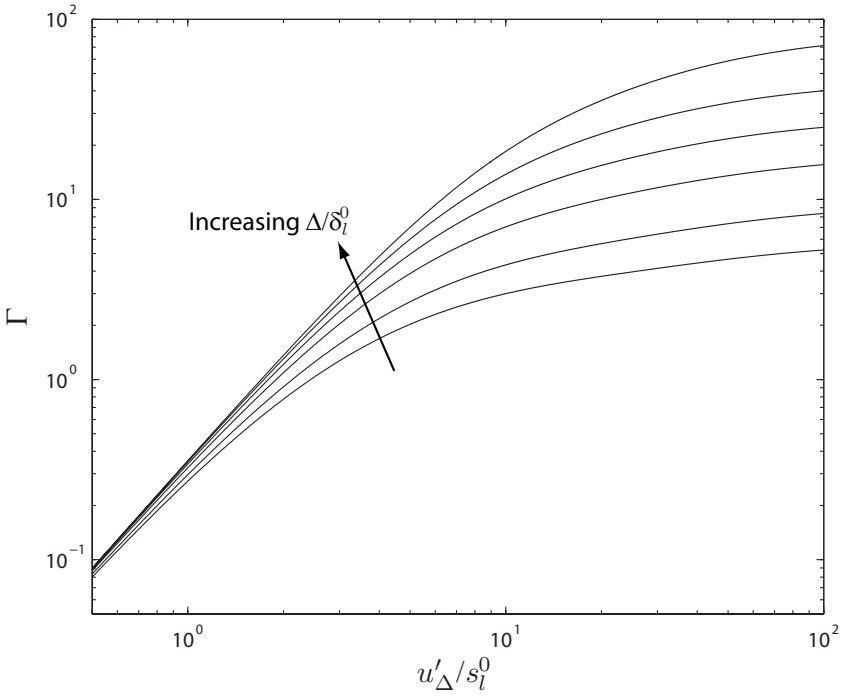

Figure 1.8: Stretch efficiency function of Charlette et al. [22].

Fundamentally, using such a model for the turbulence-flame interaction implies that the sole effect of the turbulence is to produce extensive (positive) strain rate on the flame and generate negative curvature wrinkles; it is the only possibly allowed by the canonical configuration. In reality this is not the case. A variety of studies have measured the probability density functions (PDFs) of the flame curvature using Planar Laser Induced Fluorescence (PLIF) and Mie scattering techniques [7, 42, 43]. Limited measurements of the instantaneous strain rate on a flame have also been made using Particle Image Velocimetry (PIV) [42]. Similar PDFs have been constructed using DNS [18, 24, 97, 116]. In all cases, the results indicated a distribution of strain rate and curvature that was both positive and negative. For the most part, the mean strain rate has been positive while the mean curvature has been near zero, though in some cases the mean strain rate was negative and the mean curvature was positive [116]. This indicates that the effect of turbulence on a flame surface cannot

be described by the canonical flame-vortex interaction of Fig. 1.6.

1.8 Previous models for the curvature stretch rate

As described above, the stretch efficiency function describes the total stretch rate on the flame surface. However, in modeling applications it is typically used to describe only the strain rate. Separate models are used for the curvature stretch rate. For example, Eq. 1.40 postulates that a balance exists between the strain rate and curvature stretch rate, whereas Eq. 1.38 assumes that the curvature stretch rate is negative and proportional to the flame surface density. The latter may be conceptually related to the canonical flame-vortex interaction of Fig. 1.6 which creates solely negative curvature.

1.8.1 Problems with the models

The assumption that the curvature stretch rate is everywhere balanced by the strain rate implies that there is no transport of flame surface area. That is, the generation of flame surface area is equaled by the destruction everywhere. This model possesses the same faults that are made in algebraic models for the turbulent burning velocity and is discussed in §1.9.1.

Other models are based on a geometric argument: in order for the flame surface area in a given volume to increase, the flame must become more wrinkled and therefore more curved. However, this argument ignores the fact that an unwrinkled flame still has flame surface density. Furthermore, a wrinkled flame contains regions of both positive and negative curvature. As the flame becomes more wrinkled both of these increase. Hence, models for the total curvature stretch rate should reflect this balance and how it changes with increased wrinkling.

1.9 Previous models for the turbulent burning velocity

As mentioned in §1.5.1, the original goal of studying turbulence-flame interactions was to determine a general relationship for the overall turbulent burning velocity of an apparatus as a function of global turbulence parameters. In the thin flamelet regime, such correlations generally take the form of Eq. 1.11. However, experimental and computational results have indicated that obtaining such a global correlation is likely impossible; the results are highly geometry dependent [36, 85]. Upon further reflection, the reasons for this are obvious: the correlation attempts to relate the global flame speed of an entire apparatus to certain characteristic properties of the turbulence. However, these properties may be varying in space and time. The relationship between the overall flame speed and turbulence will therefore depend on the relationship between the spatial and temporal history of the turbulence at the flame, which is particular to given experiment or simulation.

To avoid this issue, one may attempt to relate the local turbulent burning velocity to the local turbulence. That is, one might create correlations that are not based on overall properties of an apparatus, but location by location along the flame. This is the methodology employed by Charlette et al. [22, 23], Knusden and Pitsch [58], Peters [85], and Pitch, [87].

As described in §1.6.2, Charlette et al. [22, 23] relate the turbulent burning velocity directly to the area of the wrinkled flames. They then devise a model for the flame wrinkling factor based on the subgrid flame surface density. However, they do not employ the Σ or Ξ transport equations. Instead they assume that a local balance exists between the subgrid strain rate and curvature stretch rate and then employ the stretch efficiency function. They therefore relate the flame wrinkling to

the local, instantaneous turbulence via the modeled strain rate. A dynamic exponent, β, is employed to add adaptability to the model.

Models for the turbulent burning velocity also have been developed for the level set paradigm. Peters [85] derived such an algebraic equation by assuming equilibrium production and destruction of flame area and employing various submodels. Pitsch [87] derives the equation based on the subgrid flame brush thickness, once again employing various submodels. In both cases the models are designed to recover the Damköhler limits for large and small scale turbulence. The forms of these models are similar, and in the notation of Pitsch [87] given by:

$$\frac{s_t}{s_l} = -\frac{b_3^2}{2b_1 \mathrm{Sc}_t}\frac{\nu_t}{\alpha_u}\frac{s_l}{u'_\Delta} + \sqrt{\left(\frac{b_3^2}{2b_1 \mathrm{Sc}_t}\frac{\nu_t}{\alpha_u}\frac{s_l}{u'_\Delta}\right)^2 + \frac{b_3^2 \nu_t}{\mathrm{Sc}_t \alpha_u}} \tag{1.55}$$

where the b_i are model constants.

Knudsen and Pitsch [58] have also proposed a dynamic model for the turbulent burning velocity. This is based on the requirement that the overall flame propagation be independent of the filter used. From this, they develop a dynamic model in which a parameter, α, is set by the filter and physical properties of the problem. However, the turbulent burning velocity was once again related only to the local turbulence. Analysis of this model was performed using DNS of a propagating material surface in a constant density, isotropic, homogenous turbulent flow. It was shown that at least a dynamic model is necessary to predict the turbulent burning velocity.

1.9.1 Problems with the models

From the earliest studies (§1.5.1) to the modern models described above, all algebraic descriptions of the turbulent burning velocity possess a common assumption: the local turbulent burning velocity can be related to the local turbulence. However this is not the case. The local wrinkling of a turbulent flame has a 'memory' of

the previous wrinkling that it has undergone. Such a memory is clearly apparent in turbulent Bunsen flames. These flames become significantly more wrinkled near the tip, despite the fact that the turbulence intensity decreases in this region [42]. A relationship for the local turbulent burning velocity based entirely on the local turbulence intensity would predict the opposite: as the turbulence decayed downstream, the flame wrinkling and turbulent burning velocity would decrease. As a further example, if a highly wrinkled flame in a region of intense turbulence propagated into a region of weak turbulence, it would still be wrinkled. These wrinkles may naturally shrink due to kinematic restoration (Huygen's principle) or grow due to an instability. However, in either case, there would exist a time where a turbulent burning velocity relation based on the local turbulence would in no way reflect the actual geometry of the flame.

It therefore appears that algebraic relations such as Eqs. 1.11, 1.40, and 1.55 are unlikely to be accurate. The turbulent burning velocity, flame surface area, or flame wrinkling at a particular location is not only related to the local turbulence, but to all the wrinkling of the flame that has happened previously and transported to that location. Similarly, the local curvature stretch rate is not only related to the local strain rate as postulated in §1.6.2.

1.10 The structure and dynamics of turbulence

The above discussion has focused on various aspects of the interaction between turbulence and a premixed flame. As such, properties characterizing the structure and behavior of the flame surface have been described. Little has been said however regarding the turbulent flow itself; the only turbulence explicitly mentioned has been simple vortices used for the canonical studies. Despite this, the details of the

turbulent flow obviously play a key role in the dynamics of the flame. Hence, a brief discussion of turbulence is in order.

A turbulent flow can, as like any other continuum flow, be described by the Navier-Stokes equations. However, at high Reynolds number the non-linear inertial term in these equation dominates the linear viscous diffusion term. This results in the equations being non-deterministic; infinitesimal changes in the initial or boundary conditions will result in completely different flow fields.

To describe the dynamics of a turbulent flow, it is common practice to decompose the velocity gradient tensor into its symmetric and anti-symmetric components:

$$\begin{aligned} \nabla \vec{u} &= \frac{\partial u_i}{\partial x_j} = \frac{1}{2}\left(\frac{\partial u_i}{\partial x_j} + \frac{\partial u_j}{\partial x_i}\right) + \frac{1}{2}\left(\frac{\partial u_i}{\partial x_j} - \frac{\partial u_j}{\partial x_i}\right) \\ &= S_{ij} - \Omega_{ij} \end{aligned} \tag{1.56}$$

Here, $\underline{S}$ is the fluid dynamic strain rate tensor and $\underline{\Omega}$ is the rotation rate tensor. The components of $\underline{\Omega}$ are the various vorticity components:

$$\vec{\omega} = \nabla \times \vec{u} \tag{1.57}$$

The transport equation for the vorticity in a reacting flow has been previously derived and is given by [31, 77]:

$$\frac{D\omega_i}{Dt} = S_{ik}\omega_k + \nu \frac{\partial^2 \omega_i}{\partial x_k \partial x_k} + \frac{1}{\rho^2}\left(\epsilon_{ijk}\frac{\partial p}{\partial x_j}\frac{\partial \rho}{\partial x_k}\right) + \xi \tag{1.58}$$

where ϵ_{ijk} is the Levi-Civita tensor, and ξ represents the effects of viscosity gradients. The flame front manifests itself in this equation by both the baroclinic torque (third term on right side) and ξ. It has been shown that the baroclinic torque acts to attenuate vorticity in the reactants and generate oppositely signed vorticity in the products, while viscosity gradient effects are small [77].

The transport equation for strain rate has been derived in a non-reacting flow [81], and can be extended to a reacting flow (see Appendix A):

$$\begin{aligned} \frac{DS_{ij}}{Dt} &= S_{ik}S_{kj} - \frac{1}{4}\left(\omega_i\omega_j - \delta_{ij}\omega_k\omega_k\right) + \nu\frac{\partial^2 S_{ij}}{\partial x_k \partial x_k} \\ &- \frac{1}{\rho}\frac{\partial^2 p}{\partial x_i \partial x_j} + \frac{1}{2\rho^2}\left(\frac{\partial p}{\partial x_i}\frac{\partial \rho}{\partial x_j} + \frac{\partial p}{\partial x_j}\frac{\partial \rho}{\partial x_i}\right) + \zeta \end{aligned} \tag{1.59}$$

where ζ represents the effects of viscosity gradients. While the influence of the terms in this equation has not yet been studied, it is apparent that the flame affects the strain rate field through at least the density gradient (fifth term on right side).

It is noted that the strain rate may also be represented by a diagonal matrix or vector comprised of the eigenvalues of $\underline{S}$. In this representation, the eigenvalues represent the principal strain rates and the corresponding eigenvectors represent the directions in which they are applied.

Consistent with the concept of the vortices in the canonical turbulence-flame interactions studies, it is common practice to consider coherent structures in the turbulence. For the purpose of this study, a turbulent structure at a particular threshold value will be defined as a connected volume in which a specific turbulence variable is above that value. For example, a region of concentrated vorticity is a vortical structure while one of concentrated strain rate is a strain-rate structure. Obviously, such a definition requires the use of an arbitrary threshold. To avoid this, some studies of turbulence have used local criteria to seek out vortex tubes and/or sheets (e.g. Refs. [30, 53]); a binary criterion was used to determine if a particular point in the flow is part of a structure and a structure was defined as a collection of such points. These local methods have the advantage of providing a mathematically rigorous definition of the turbulent structure that does not require the arbitrary threshold. However, the threshold method also has many advantages. Firstly, it

allows any geometry of structure to be identified; it is not restricted to searching for vortex tubes or sheets. Also, by varying the threshold value, the geometry of different scales of the turbulence can be observed. At higher thresholds the fine scale (dissipative) structure is apparent, while at lower thresholds the intermediate scale (inertial) structure is observed. Thirdly, by thresholding a particular turbulence quantity, that quantity can be studied directly. Local methods do not generally study vorticity or strain-rate directly. Furthermore, a variety of studies have shown that the geometry of the vortical structures educed by the local methods and thresholding are very similar [21, 37].

A detailed review of the dynamics of Eqs. 1.58 and 1.59 which govern the behavior of these structures is beyond the scope of this work (see for example Refs. [75, 81]). However, a few simple observations can be made to aid in visualization of the fields. Firstly, high-intensity (fine scale) vorticity and strain-rate structures tend to be geometrically different. While vorticity tends to concentrate into 'tube'- or 'worm'-like structures at the small scale, strain-rate structures tend to be both amorphous ('blob'-like) and 'sheet'-like. Secondly, vorticity and strain-rate structures may be spatially distinct or may overlap. Hence, the same parcel of fluid may contain different information depending on how it is viewed and isolating the important turbulent structures is necessary. Thirdly, the flame affects both forms of turbulent structure as they pass through. In the case of vorticity, the baroclinic torque decreases the strength of the incoming vortical structures and may attenuate them completely. Furthermore, flame-generated vorticity of opposite sign to the incoming vortices may be generated in the products. As will be seen in Chapter IV, the flame also acts to attenuate strain-rate structures. However, there does not appear to be any flame-generated strain rate in the products. Studies of canonical

interactions between strain-rate structures and a flame front are needed to better understand the processes involved.

1.11 Stretch induced by the hydrodynamic instability

The stretching of the flame front has thus far been associated with velocity gradients manifesting themselves as turbulent fluctuations in the reactants. However, in turbulent premixed flames there is another source of velocity gradients: the flame front itself. The curved flame induces velocity gradients in the reactants due to continuity and thermal expansion requirements. These velocity gradients are the mechanism behind the hydrodynamic instability, which was first described independently by Darrieus [33] and Landau [61]. They predicted that an infinitely thin flame front would be unconditionally unstable to any wavelength perturbation.

A good physical interpretation of the mechanism causing this phenomenon is given by Williams [111]. Consider an infinitely thin planar flame propagating at s_l^0 into the reactants. As the unburnt gases pass through, they expand due to heat release. This expansion and the related acceleration occur in the direction normal to the flame front. If a small perturbation is made to the flame, as in Fig. 1.9, the acceleration remains entirely normal to the flame; the tangential component of velocity is conserved. Hence, as streamlines pass through the flame they deflect towards the flame normal direction. As perturbations in the streamlines must disappear far away from the flame (a stream tube of area A far upstream of the flame will have the same area far downstream due to continuity) streamlines must diverge and converge around the curved flame as shown. This results in a difference in reactant velocity upstream of the negatively and positively curved regions in such a fashion that the wrinkle amplitude grows. For a constant speed wave, the growth rate is proportional to the

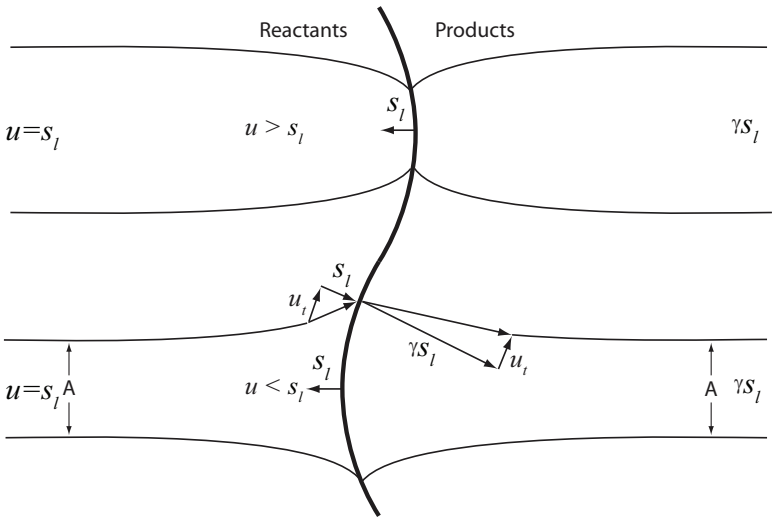

Figure 1.9: The hydrodynamic instability mechanism

difference between these velocities. The growth rate is therefore dependant on both the expansion (acceleration) across the flame and the curvature.

In the linear small perturbation limit, the curvature is unimportant and the growth rate (ς) of a disturbance with wave number k can be determined from a dispersion relationship as [33, 61]:

$$\varsigma = s_l^0 k \left[\frac{-\gamma + \sqrt{\gamma^3 + \gamma^2 - \gamma}}{\gamma + 1} \right] \tag{1.60}$$

where $\gamma = \rho_u / \rho_b$. Since $\gamma > 1$, the disturbance is unstable to all wave length perturbations. Obviously some effects are missing from this analysis as stable laminar flames are commonly created in laboratories. Hence, numerous modifications, extensions, and corrections to the theory have been made to account for a variety of effects, mostly associated with diffusion across curved streamlines (e.g. Refs. [27, 70, 73, 100]). These show that differential diffusion and buoyancy may stabilize perturbations.

In weakly turbulent flames, measurements and simulations have shown the hydrodynamic instability to be significant in setting the scale of flame cells, controlling

the turbulent burning velocity, and causing flame-generated vorticity [16, 83, 116]. Yuan et al. [116] showed that the turbulent burning velocity in such cases fluctuated in a periodic manner. As the turbulence intensity was increased, these fluctuations became more random; turbulence initiated the majority of flame surface area generation. However, even in such cases the mechanism responsible for the hydrodynamic instability is always present. Analytic work by Bychkov [15] has shown the significance of the hydrodynamic instability and turbulence working in concert for strongly corrugated flames. That is, as stronger turbulence creates larger corrugations in a flame surface, the hydrodynamic channeling of flow also increases. Hence, straining of the flame caused by this channeling may be significant over a considerable range of conditions.

From the phenomenological description of the hydrodynamic instability in Fig. 1.9, it is apparent that the growth of the disturbance can be interpreted in terms of the stretch rate. As the streamlines converge in the negatively curved region, they are applying a compressive (negative) strain rate to the flame. The converse it true in the positively curved regions. There is therefore a positive correlation between strain rate and curvature. The change in area of the disturbance can be seen as the negatively strained region being pushed into the products by the positively strained regions, and the resulting wrinkled flame propagating normally to itself.

Note that the flow pattern induced by the hydrodynamic instability must be irrotational; the flame is not a source of vorticity in the reactants. Hence, the velocity gradients causing strain due to this mechanism do not appear as vorticity; they must appear as fluid dynamic strain rate. There is therefore a source of fluid-dynamic strain rate associated with the flame that can manifest itself a distance from the front itself. It is suspected that this source is the pressure Hessian (fourth term

on the right of Eq. 1.59). All other terms appear to only effect the local fluid as it passes through the flame. However, the curved flame may send pressure waves into the reactants that generate fluid dynamic strain rate in the flow pattern shown in Fig. 1.9. However, this validity of this description is not analyzed in this work.

Regardless of the exact fluid dynamic mechanism, the significance of the hydrodynamic instability for generating flame surface area in a turbulent flame is still unknown. To date, there have been very few attempts to include this effect in turbulent combustion simulations. Paul and Bray [84] included a source of the form:

$$\kappa_{HD} = b_1 \left[1 - F\left(\frac{u'}{s_l^0}\right)\right] G\left(\gamma, \frac{u'}{s_l^0}, \frac{L}{\Lambda_n}\right) \frac{s_l^0}{\Lambda_n} \tag{1.61}$$

where b_1 is a constant and Λ_n is the neutral wavelength [16]. The function F was designed such that the significance of the hydrodynamic instability drops to zero as the turbulence intensity increases. The function G describes the instability and is related to the characteristic length scale of the wrinkling by:

$$G\left(\gamma, \frac{u'_{rms}}{s_l^0}, \frac{L}{\Lambda_n}\right) = \lim_{u'_{rms}/s_l^0 \to 0} \left(\frac{\Lambda_n}{\Lambda_c}\right) \tag{1.62}$$

where Λ_c is a characteristic wrinkle length scale.

As can be seen, this model treats the strain rate due to the hydrodynamic instability as a low turbulence intensity effect; both F and G are related to weak turbulence. However, as described above, large scale wrinkling associated with strong turbulence will increase the velocity gradients and strain rates associated with the hydrodynamic instability mechanism. Hence, it is unlikely that this model properly captures the straining due to this mechanism in stronger turbulence. The significance of this straining must be investigated to determine if it is an important source. This issue will be briefly addressed in this work.

1.12 Objectives

In this Chapter, a review has been presented of the turbulent premixed flame theory that is necessary for the remainder of the dissertation. The flames considered were those identified as thin flamelets in the regime diagram. The majority of the behavior for such flames is dictated by the increase in reactive surface area as they are stretched by the turbulence. Accurate descriptions are therefore required for the mechanisms that generate this area. However, it was also shown that present descriptions are unlikely to properly reflect the actual physical processes occurring in turbulent flames; they are based on extremely simplified vortex-flame interactions that do not reflect real turbulence. Hence, models and modeling paradigms based on these simple ideas are also unlikely to be accurate.

It is therefore apparent that measurements of real turbulence-flame interactions are necessary. This would allow the mechanisms with which turbulence effects the flame to be directly observed. However, to do so requires simultaneous temporally resolved measurements of a turbulent flow field and flame surface topography, which has not been previously accomplished. To do so, two new diagnostic techniques were developed: Cinema-Stereoscopic PIV (CS-PIV) and Orthogonal-Plane Cinema-Stereoscopic PIV (OPCS-PIV). These were employed in a turbulent slot Bunsen flame and represent the first application of temporally resolved diagnostics for the study of real turbulence-flame interactions; it is the first application of OPCS-PIV in general.

Using these diagnostics, the first objective of this dissertation was to evaluate the mechanistic description of turbulence-flame interactions that is predicted to occur if the canonical vortex-pair configuration is accurate. It was found that this configu-

ration did not accurately predict the effects of real interactions. A new description was therefore developed. This was based on analysis of the strain rate equation and confirmed from the measurements. Furthermore, the appropriateness of using any canonical turbulence geometry (or range thereof) to develop models was evaluated and found the be inadequate.

The second objective of the dissertation was to evaluate and develop models for the various unclosed terms in turbulent combustion simulations. Hence, a new method of investigating turbulence-flame interaction was developed that directly measures the subgrid processes that must be modeled in LES and does not stipulate an interaction geometry. Using this method, the models and modeling assumptions described above were tested against the measured data. It was found that the previous models possessed incorrect assumptions that made them inaccurate. Where appropriate, new models were developed that accurately describe real turbulence-flame interactions and fit the measured data. These new models can easily be implemented in various simulation algorithms and should provide a marked improvement in accuracy. However, in some cases the basic modeling assumptions were found to be inherently inaccurate. In these cases, the incorrect assumptions were explained and the consequences for various simulation methods described.

CHAPTER II

Experimental Approach

Investigation of turbulence-flame interactions requires simultaneous measurement of the temporally evolving turbulent flow field and flame surface topography. This has previously been accomplished in two-dimensional laminar flame/vortex experiments using simultaneous single-shot Particle Image Velocimetry (PIV) and Planar Laser Induced Fluorescence (PLIF) [77, 99]. Pseudo-temporal resolution was obtained by repeating the experiment and taking measurements at different times. The highly repeatable nature of the simple flow allowed construction of a time-sequence from instantaneous single-image measurements. Furthermore, the two-dimensionality of the flame and flow allowed all velocity components and the complete flame orientation to be deduced from two-component planar measurements. However, this approach is obviously impossible in real turbulence.

In turbulent flames, simultaneous measurements of the instantaneous velocity field and flame location have also been performed by combining PIV with PLIF and Rayleigh scattering techniques [26, 42, 86, 107]. However, temporally resolved measurements have not been obtained. To study the dynamics of real turbulent flames requires measurements to be taken at rates on the order of a kilohertz. This in turn requires lasers and cameras able to operate at these rates with sufficient

power and resolution respectively. Furthermore, efficient data processing algorithms and hardware are required to handle the volumes of data recorded by such systems. These problems are compounded by the need to address three-dimensional effects.

This dissertation presents the first temporally resolved measurements of turbulence-flame interactions and the associated straining and wrinkling processes in an actual turbulent flame. These were obtained by employing two separate diagnostics to a turbulent slot Bunsen flame. The first technique, Cinema-Stereoscopic PIV (CS-PIV), provided three-component vector fields in a plane parallel to the bulk flow direction. This diagnostic had high spatial and temporal resolution, along with a large field of view. The CS-PIV data were used for the majority of the phenomenological and statistical analysis. The second technique, Orthogonal-Plane Cinema-Stereoscopic PIV (OPCS-PIV), allowed reconstruction of the full three-dimensional velocity gradient field. This gave insight into the three-dimensional nature of the interactions. It also allowed evaluation of the error inherent in using the planar CS-PIV data to analyze 3D phenomena. However, the 3D data from the OPCS-PIV system were inappropriate for the majority of the quantitative interaction analysis due to inaccuracies inherent in the temporal reconstruction methodology (see §2.3). Furthermore, the OPCS-PIV diagnostic had lower spatial resolution and a smaller field of view than the CS-PIV. Hence, the high-accuracy, planar measurements were employed for detailed quantitative analysis. The lower-accuracy, pseudo-3D measurements were used for qualitative insight, to provide a link between the planar measurements and the true 3D fields, and to analyze instantaneous 3D statistics. In all cases the flame surface topography was measured from the gradient of the particle images. The details of the experiment along with these diagnostic techniques are provided below.

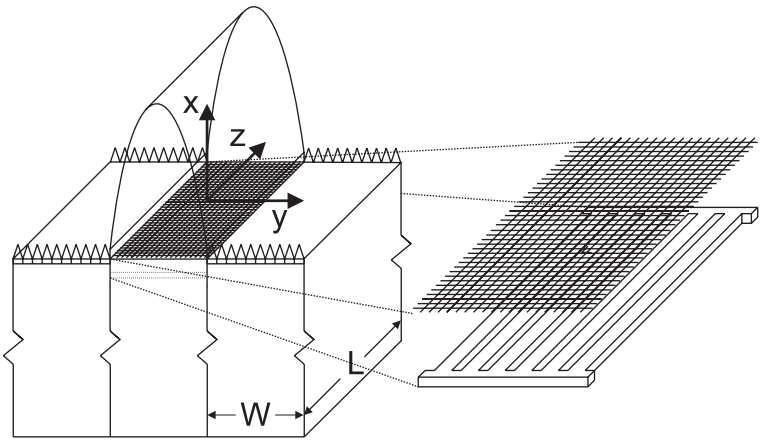

Figure 2.1: 2D slot Bunsen burner with side burners. W = 25mm, L = 50mm. The origin of the coordinate system is centered in the middle burner at the x-plane in which the flame is anchored.

2.1 Experimental Configuration

The flame studied was stabilized on the collection of three slot burners shown in Fig. 2.1. The Bunsen flame of interest was stabilized on the central burner. The bulk velocity and equivalence ratio of the center burner varied for the CS-PIV and OPCS-PIV test cases. Specific flow conditions are described in §2.2.1 and 2.3.1. However, in all cases the burner configuration was identical. The two outer burners stabilized short, grid flames and provided coflowing hot products. The flow rate through these burners was set such that the mean downstream velocity profiles of the products in both the central and side burners closely matched. This minimized the effects of shear on the flame dynamics. Furthermore, the equivalence ratio of the side burners was set to match the center burner, reducing gradients in composition and temperature. Flow rates were controlled using metered choked orifices and the experiment was conducted at approximately 295 K and 1 atm.

The primary turbulent fluctuations in the central burner were generated by means of a slot grating placed 1 cm upstream of the flame stabilization plane. A loose wire mesh was installed downstream of this grating to break up the large recirculation

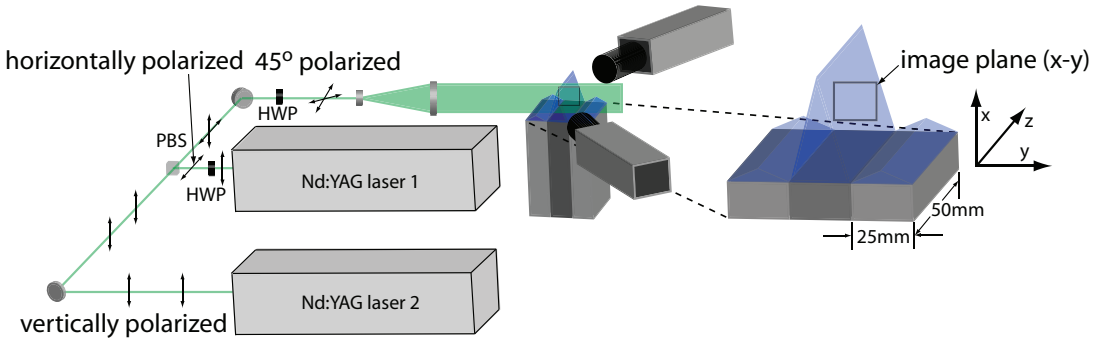

Figure 2.2: Experimental configuration containing CS-PIV system and burners. HWP - half wave plate, PBS - polarizing beam splitter.

zones and prevent flame stabilization on the grating. This combination provided strong fluctuations in all directions, with no mean out-of-plane velocity. Detailed characterization of the turbulent flow field is given in §3.1.

2.2 Cinema-Stereoscopic PIV

Temporally resolved planar velocity measurement have the potential to answer many open questions in fluid dynamics and combustion. For example, early cinema-PIV measurements by Upatnieks et al. studied the lift-off of turbulent jet flames [109]. Cinema-stereoscopic PIV measurements have been made by Ganapathisubramani et al. in a non-reacting flow to study the structure of turbulence [44, 45]. Recent work by Boxx et al. has used CS-PIV combined with OH-PLIF to observe the dynamics of a lifted turbulent jet flame [6]. However, this work represents the first use of such diagnostics for the study of flame dynamics, as well as a great improvement in spatial resolution and accuracy. Orthogonal-Plane Cinema-Stereoscopic PIV measurements (§2.3) previously have not been made.

Employing high-speed laser diagnostics for the detailed study of flame dynamics demanded a balance between conflicting requirements while achieving sufficient accuracy for all velocity components. That is, it was necessary to achieve a field of

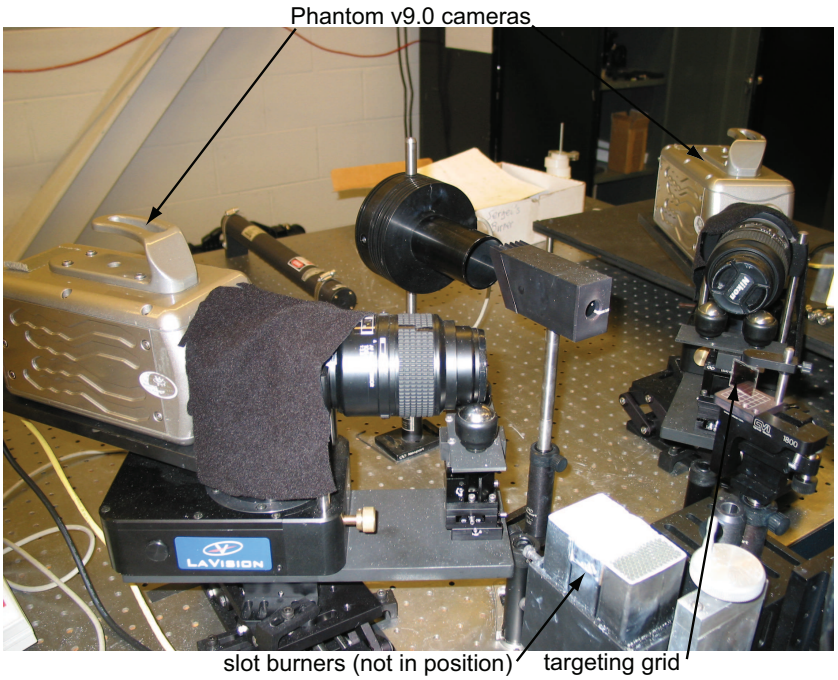

Figure 2.3: CS-PIV camera configuration.

view and frame rate sufficiently large to track the progress of the turbulence and capture the resulting flame motion, while obtaining sufficient resolution to identify the small scale turbulent structures. The signal quality was dependant on the particle image quality, and consequentially on the focus and light collection ability of the camera/lens system. This was greatly affected by the low pulse energy of the high-rep-rate lasers and the requirement to filter flame chemiluminescence. Hence, it was necessary to optimize several factors including camera resolution, camera and laser frame rate, magnification, flow speed, stereo configuration, sheet dimensions, and PIV particle properties.

The CS-PIV system is shown schematically in Fig. 2.2. The diagnostic was configured with the laser sheet parallel to the flow in the $x-y$ plane at $z=0$. This allowed the flame surface wrinkling to be captured and is analogous to the view in the canonical 2D studies.

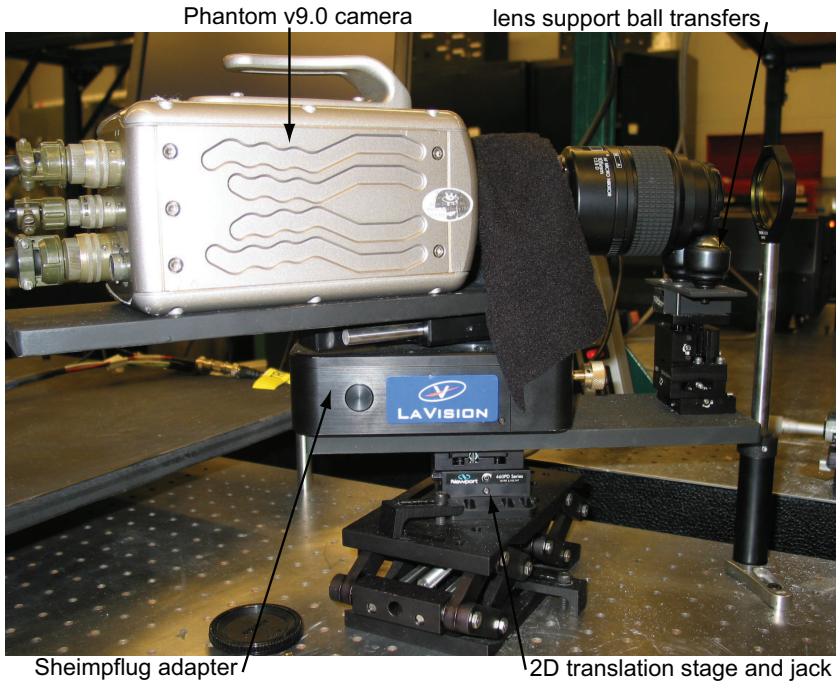

Figure 2.4: Individual CS-PIV camera translation system.

An angular stereoscopic camera arrangement was employed as shown in Fig. 2.3. The angle between the laser sheet normal and the lens axis was approximately 35°. However, in order to maintain focus across the laser sheet at the acute viewing angle the lens and camera planes could not be parallel; the object, lens, and camera planes needed to meet at a single point as dictated by the Scheimpflug criterion [94]. The different orientations of these planes created a perspective distortion across the field of view that had to be corrected. The required calibration was performed using the LaVision DaVis 7.0 software package and is described in §2.6.

The cameras were placed in a dual forward scatter configuration to increase light gathering and maximize the useful field of view [94]. Alignment of these fields of view was achieved by placing the Scheimpflug mounts on two axis translation stages and lab jacks (Fig. 2.4). This allowed the fields of view to be precisely aligned by translating the camera systems. Stabilization of the camera lenses was achieved by

supporting them with precision aligned ball transfers.

The two cameras used were Phantom v9.0s (Vision Research), which could capture images with a maximum resolution of 1632 x 1200 at frame rates of over 1 kHz. Higher frame rates are possible at lower resolution. A pair of ORC-1000 high-rep-rate Nd:YAG lasers (Clark-MXR), capable of producing 8 mJ per pulse of 532 nm light at several kilohertz, were used to create the light sheets. The beams from the two lasers were polarized orthogonally to each other and combined using a polarization based system. This avoided the high losses common to non-polarizing systems. To eliminate the difference in scattering from the S- and P-beams, the polarization was then rotated 45° by a half wave plate [14]. A sufficiently thin sheet was produced by first passing the laser beam through a 5x Galilean telescope. This provided sufficient vertical and horizontal expansion such that when the beam was subsequently contracted, a sheet with a full-width at half-maximum of approximately 300 μm and a usable height of 20 mm was created.

The flow was seeded with silica-coated TiO_2 particles (Huntsman A-PP2), which survived passage through the flame. This allowed vectors to be computed in the reactants and products simultaneously. Properties of these particles and the seed selection process are detailed in §2.7. During the experiment, the seed density was adjusted in real-time to provide an optimal balance between valid PIV vectors in the reactants and products. That is, the seed density was set to be slightly higher than optimal in the reactants, resulting in a slightly lower than optimal level in the products after expansion. This provided sufficient particles for accurate vector determination throughout the flow field. Scattered light from the particles was collected into the cameras using Micro-Nikkor 105 mm lenses operating at f/8.0. Narrow bandpass filters were placed in front of the lenses to remove chemiluminescence from

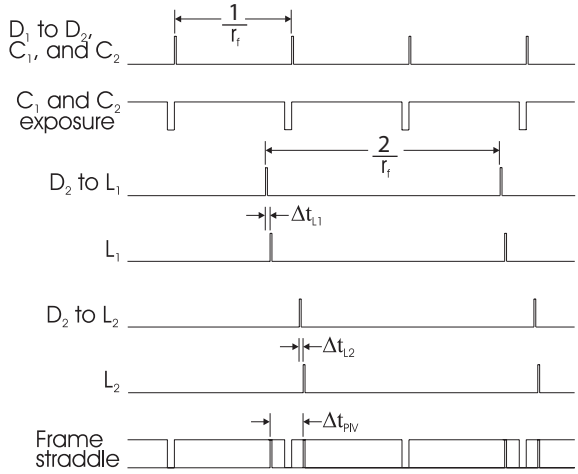

Figure 2.5: Timing diagram. D_i are delay generators, C_i are cameras, and L_i are lasers.

the flame.

A balance between field of view, frame rate, resolution, and flow speed was found with the cameras operating at a resolution of 672 x 1120 pixels and a frame rate (r_f) of 2222 Hz. Particle image pairs of a 12.8 mm x 18.2 mm field of view were obtained every 0.9 ms. With the long axis aligned with the principal flow direction, this allowed approximately 13 images of an eddy convecting at 1.5 m/s to be obtained. Frame straddling was employed and the time delay (Δt_{PIV}) between correlated particle images was set by the laser pulses as 40 μs. A timing diagram describing the operation of the system is provided in Fig. 2.5. Data was collected in spans of approximately 1 s, resulting in over 4000 images and 3.5 GB of data per run.

The spatial cross correlation and consequent velocity components were computed using the LaVision DaVis 7.0 software package. A multi-pass vector evaluation technique was employed with interrogation box sizes decreasing from 32 x 32 to 16 x 16 pixels with a 50% overlap. This resulted in a roughly cubical interrogation volume with a box size of approximately 280 μm and a vector spacing of approximately 140 μm. The adequacy of the dynamic range to accurately measure both reactant

Parameter	Value
Camera frame rate	2222 Hz
Temporal resolution	0.9 ms
Δt_{piv}	40 μs
Stereo angle	35°
Camera resolution	1120 px x 672 px ($x \times y$)
Field of view	18.2 mm x 12.8 mm ($x \times y$)
Interrogation box	280 μm
Vector spacing	140 μm
Seed material	silica coated TiO_2
Nominal seed diameter	0.15 μm

Table 2.1: CS-PIV parameters.

Case	ϕ	u'_{rms}/s_l^0	L/δ_l^0	Ma	Le
1	0.6	3.1	9.3	< 0	1.0
2	0.7	1.7	16	≈ 0	1.0
3	1.35	1.8	15	> 0	1.0

Table 2.2: CS-PIV test conditions

and product velocities was confirmed by systematically varying Δt_{PIV}. It was found that the flow statistics were unaltered by this parameter in the range of the selected value. The number of spurious vectors was less than 1.5% in both the reactants and products. A summary of the optimized CS-PIV parameters is given in Table 2.1.

2.2.1 CS-PIV test conditions

For the CS-PIV measurements, the center burner was provided with methane-air mixtures of various equivalence ratio at a bulk velocity of 1 m/s. The equivalence ratio was varied between 0.6 and 1.35. Specific conditions are given in Table 2.2, in which the flame speed and thickness are normalized by the root-mean-squared x-velocity fluctuation and turbulence integral scale determined below. By comparison with Fig. 1.1, the flames can be seen to fall within the thin flamelet regime.

The conditions were selected to highlight the different regimes of preferential diffusive instability associated with lean and rich methane-air flames and characterized by the Markstein number. As a flame is stretched, differential diffusion between the different reactants and/or heat causes certain flame segments to accelerate or decel-

erate. The correlation between the stretch rate and this distribution of flame speeds causes flame wrinkles to either grow or shrink. A negative value of Ma is associated with a diffusively unstable flame and vice versa. Case 2 (Ma ≈ 0) was selected such that the local flame speed remained essentially unchanged regardless of the stretch rate. The specific equivalence ratio for Case 3 was selected such that the unstretched laminar flame speed, as computed by Chemkin, was close to that of Case 2. The methane-air mixtures tested possessed Lewis numbers of approximately unity. This effectively eliminated the thermo-diffusive effects of stretch rate on the flame speed. Hence, variations in the flame speed were related to preferential-diffusive as opposed to thermo-diffusive imbalances.

When studying turbulent flows, it is important to consider the range of scales present. The largest scales of the turbulence are characterized by the integral length scale, defined as integral of the velocity autocorrelation. This correlation was determined from Laser Doppler Velocimetry measurements (described in §2.8) at the center of the burner, near the exit plane. Due to interference by the burner geometry, measurements could not be taken precisely at the exit. Hence, the measurements were taken 1.5 mm downstream ($(x, y, z) = (0, 0, 1.5)$). At this location, 2×10^5 data points were obtained over a time span of $\Delta t_{LDV} = 100$ s. The temporal autocorrelation:

$$\rho(\tau) = \frac{\overline{u'(t)u'(t+\tau)}}{\overline{u'(t)^2}} \tag{2.1}$$

was then calculated. This is shown in Fig. 2.6.

The longitudinal temporal integral scale in the x-direction was then calculated from the correlation. In the low Reynolds number limit, the integral scale can be

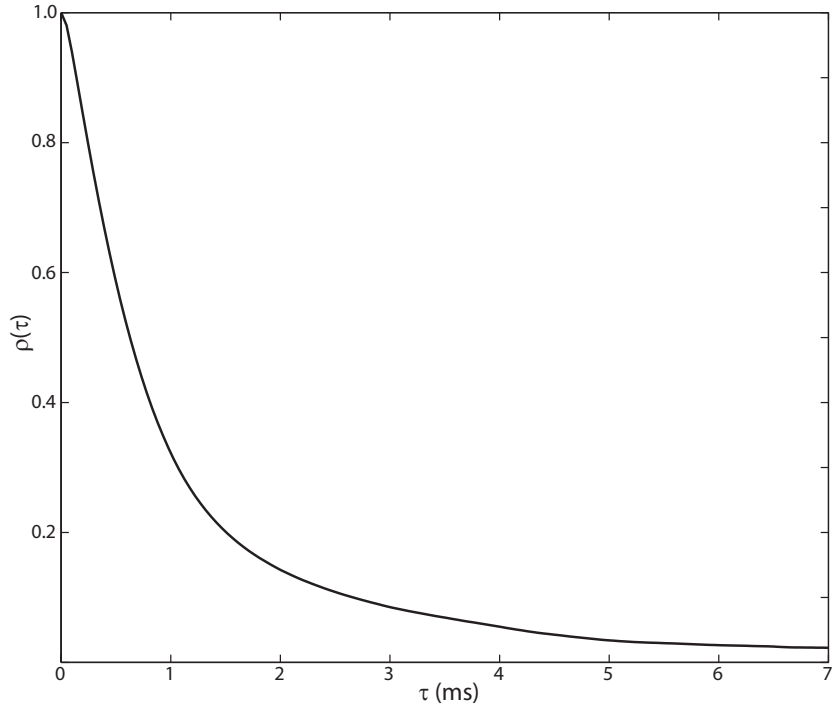

Figure 2.6: Temporal longitudinal velocity auto-correlation in the x-direction at the origin.

determined by integrating $\rho(\tau)$ or fitting it to a Gaussian of the form:

$$\rho(\tau) = e^{\frac{\pi}{4}\left(\frac{\tau}{\tau_L}\right)^2} \tag{2.2}$$

In the present data, $\rho(\tau)$ did not asymptote to zero as expected, but to approximately 0.02 (likely due to experimental noise). Hence, the integral would yield infinity. The integral scale was therefore calculated from Eq. 2.2. A least-squares fit was performed to the data, which yielded an integral time scale of $\tau_L = 1.8$ ms. The integral length scale was then calculated using the mean velocity at this location ($\overline{u} = 1.13$ m/s) such that:

$$L = \overline{u}\tau_L \tag{2.3}$$

This process mapped the temporal data to spatial data and yielded $L = 2.0$ mm.

Based on this, the integral scale Reynolds number at the exit was $\mathrm{Re}_L = 150$. This is lower than is typically considered for fully developed turbulence. However,

due to laser and camera limitations it was the largest Reynolds number that provided the desired spatial and temporal resolution as will be seen below.

The small scales of the turbulence can be characterized in several ways. The Taylor length scale is defined from the parabola with the same curvature as $\rho(\tau)$ at the origin:

$$\tau_T = \left(\frac{-2}{\left(\frac{d^2\rho(\tau)}{d\tau^2} \right)_{\tau=0}} \right)^{\frac{1}{2}} \tag{2.4}$$

Using the temporal autocorrelation, this yielded a temporal Taylor scale of $\tau_T = 0.81$ ms and Taylor length scale of $\lambda_T = 0.91$ mm. According to scaling arguments, the longitudinal Taylor scale is related to the integral scale by [34]:

$$\frac{\lambda_T}{L} \approx \sqrt{15}\sqrt{2}\,\mathrm{Re}_L^{-1/2} \tag{2.5}$$

With the above parameters, this yielded Taylor scale of approximately 0.89 mm, which is in good agreement with the measurement.

However, the Taylor scale is not representative of a particular physical scale in the turbulence. The smallest scales are represented by the Kolmogorov (λ_k) or viscous (λ_ν) length scale. The Kolmogorov scale is derived based on dimensional arguments and given by $\lambda_k = (\nu^3/\varepsilon)^{1/4}$. The dissipation rate is related to the mean turbulence by [93]:

$$\varepsilon = 30\nu \frac{\overline{u'^2}}{\lambda_T^2} \tag{2.6}$$

At the measurement location, $\overline{u'^2} = 0.11$ m^2/s^2 and $\varepsilon = 63$ m^2/s^3. This yielded a Kolmogorov scale of approximately 0.088 mm. The kinematic viscosity, ν, was taken to be that of air at the unburnt gas temperature, which was 1.5e-5 m^{2}s^{-1}

The viscous scale represents the viscous-diffusive balance that sets the smallest physical scales of the vortical structures. Buch and Dahm [12, 13] and Mullin and

L	λ_T	λ_ν	λ_k	Re_L
2.0 mm	0.91 mm	0.52 mm	0.088 mm	150

Table 2.3: CS-PIV turbulence scales at $(x, y, z) = (1.5, 0, 0)$.

Dahm [80] have shown this scale to be proportional to the Kolmogorov scale and approximately 5.9 times greater. This is consistent with the results of Jiménez et al. [55] and Ganapathisubramani et al. [45], who reported their smallest scale vortical structures as $6\lambda_k - 11\lambda_k$. Hence, $\lambda_\nu = 0.52$ mm at the measurement location.

The viscous scale can also be computed using the scaling relation [12, 13]:

$$\frac{\lambda_\nu}{L} \approx 11.2\,\mathrm{Re}_L^{-3/4} \tag{2.7}$$

This yields a viscous length scale of approximately 0.52 mm, which is in agreement with the previously calculated value. The turbulence scales are summarized in Table 2.3. It should be noted that the range of scales in this flow is less than one decade due to the low Reynolds number. While this issue does not affect the phenomenological results (Chapters IV and V), it does restrict the range of scales considered for model development (Chapter VI).

Using the Nyquist-Shannon sampling theorem, this turbulence field would be completely resolved by measurements with spacing of approximately 260 μm. While this is larger than the vector spacing in the present measurements, the velocity computations were made using an interrogation box window that was twice the vector spacing; the data set was twice over sampled. Hence it is possible that the smallest scale structures were not completely resolved by the present diagnostic. However, a variety of studies have shown that the smallest scales are not responsible for the majority of flame stretch [22, 28, 74]. This is likely due to their short life time, particularly in the vicinity of a flame front.

The smallest turbulent structures that were properly resolved by the CS-PIV

were determined by tracking small vortical structures in time. A typical measured turbulence field and the method for computing the vorticity are described in §2.2.2. The characteristic length of these structures was determined by computing the area (A_s) and perimeter (P_s) in which the vorticity remained greater that half the peak within the structure. The length scale was then determined as:

$$l_s = \frac{4A_s}{P_s} \tag{2.8}$$

If a structure was present for a minimum of two frames, it was considered to be properly resolved. The considered data set was restricted to cases where the structure existed in a region with out-of-plane velocity, $w < 0.05$ m/s. Hence, the structures could convect a maximum of 450 μm out of the measurement plane between frames. This largely eliminated erroneous disappearance of structures due to out of plane convection. It was found that structures with a characteristic size in the range of 560 μm (four data points) appeared in multiple frames for approximately 85% of the observed cases. The remaining 15% were either dissipated, passed out of the interrogation plane between frames, or were noise. It should also be noted that the size of the structures reported were only their image in the interrogation plane; the full 3D structure could have a different scale. To reduce this effect, care was taken to study vortical structures that appeared as isolated, roughly circular images. This was the profile expected of 'tube-like' viscous scale structures oriented normal to the plane.

2.2.2 CS-PIV data reduction and typical results

In order to acquire the desired information on turbulence-flame interactions, it was necessary to obtain images of the turbulent flow field, visualized in various manners and computed from the measured vector fields, interacting with the flame surface.

As mentioned previously, computation of the three-component velocity field from the particle images was performed using the LaVision DaVis 7.0 software package. The numerical process for this was internal to the software, typical for stereo-PIV, and not discussed in detail here (see eg. Ref [94]). The extraction of the flame surface topography from the particle images involved a complex numerical procedure. This is described in §2.5.

Post-processing of the measured data to obtain visualizations of the turbulence field involved taking various gradients of the vector fields. As described in §1.10, it is common to decompose the velocity gradient field into a rotational component, $\underline{\Omega}$, and irrotational component, $\underline{S}$. Recall that the elements of $\underline{\Omega}$ are the vorticity components. It will later be shown that turbulence manifesting itself as rotation or strain have distinct effects of the flame surface dynamics (§4.4). Hence, these quantities must be computed from the data.

From the planar measurements, only the out of plane component of vorticity (ω_z) could be measured. The in-plane normal and shear strains (S_{11}, S_{22}, and S_{12}) also were directly measurable. Furthermore, in regions away from the flame the continuity equation could be employed, allowing S_{33} to be determined from S_{11} and S_{22}. Note that the stereoscopic aspect of the diagnostic did not allow computation of any additional terms in either $\underline{\Omega}$ or $\underline{S}$. However, the third component was necessary for restricting the usable data to cases where 3D effects were minimal. This restriction is described in detail in §4.2.

For each of these quantities, various numerical schemes can be used to compute the required velocity derivatives. These include standard finite difference schemes, Richardson extrapolations, and least squares methods. However, physical insight into the quantities of interest can lead to numerical schemes that are more accurate

and possess less noise. These methods utilize the relationship between circulation, vorticity, and strain rate to determine ω_z, S_{12}, and S_{33}. Raffel et al. [94] have shown these methods to reduce both the noise and uncertainty in the computed quantities. Hence, circulation methods were used where applicable; the specific numerics are provided in Ref. [94]. The remaining normal strain rates, S_{11} and S_{22}, were computed using a standard second order central difference method. A 3 x 3 Gaussian filter was applied to all vector fields before computation of the vorticity and strain rate to reduce high frequency noise.

A typical time sequence of turbulence interacting with the flame surface is shown in Fig. 2.7. The turbulence is visualized both in terms of the vorticity (ω_z, 2.7(a)) and strain rate (S = resolved component of $(S_{ij}S_{ij})^{1/2}$, 2.7(b)). The flow is from bottom to top and the time between frames is 0.9 ms. In this sequence, the boxed region of turbulence contains two counter-rotating vortical structures and a single strain-rate structure. As the vorticity interacts with the flame, it is attenuated and vorticity with opposite sign is generated in the products. The strain rate structure also interacts with the flame and is attenuated. During these processes, the flame surface is strained and wrinkled. It should be noted that the flame front manifests itself in the S fields as a region of high strain due to the acceleration of the gas through the flame (i.e. $\nabla \cdot \vec{u} > 0$). However, this strain rate is not a result of the turbulence and hence not the focus of this work. Turbulence-flame interactions such as this will be studied in further detail in Chapter IV.

2.2.2.1 Experimental uncertainty

The measurement of interactions such as that shown in Fig. 2.7 are subject to experimental uncertainty from two sources, both of which are inherent to the PIV method of determining velocity fields. Firstly, there is an error associated with ac-

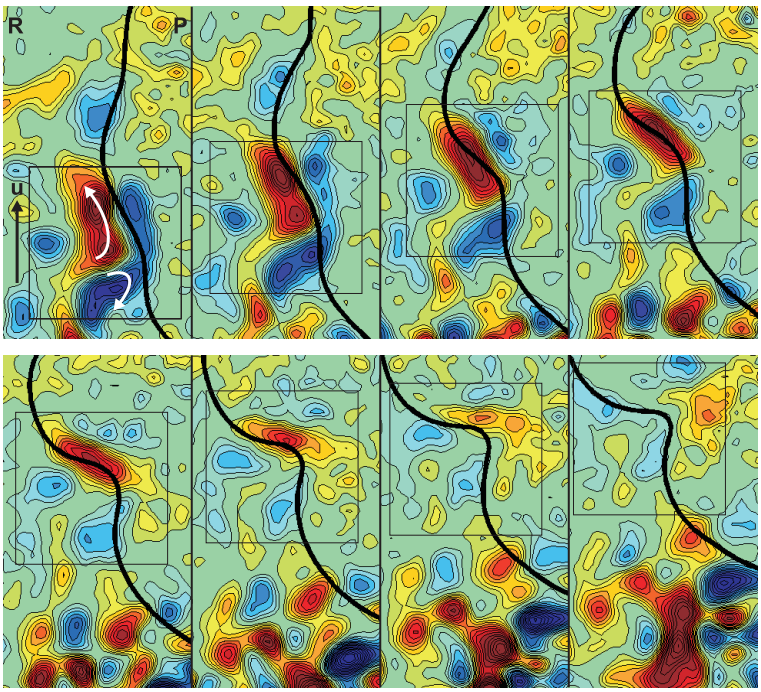

(a) ω_z contours between -700 s^{-1} (blue) and 700 (red) s^{-1}. The flame is the thick black line. The vortical structures in the boxed region are attenuated as they interact and flame generated vorticity is apparent in the final frame.

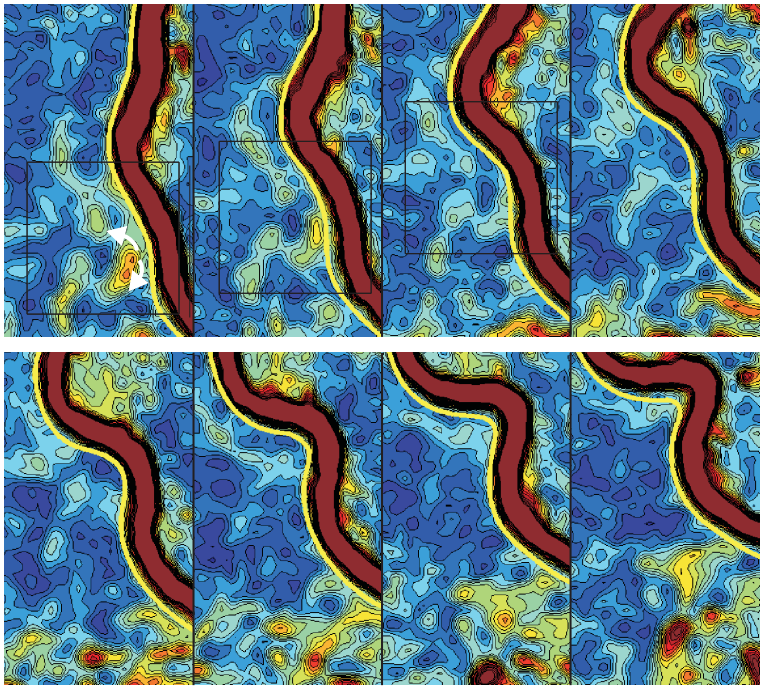

(b) S contours between 0 s^{-1} (blue) and 1000 s^{-1} (red). The flame is the thick yellow line. The strain rate structure in the boxed region is attenuated by the flame, which appears as a thick region of large S due to gas expansion.

Figure 2.7: Example time sequence of turbulence interacting with the flame surface from CS-PIV. Field of view is 5.9 mm x 10.5 mm. Reactants are on the left, the flow is from bottom to top, and the time between frames is 0.9 ms.

curately identifying and tracking individual particles. Such errors are caused by image abberations, inappropriate seeding, improper calibration, and loss of particles between frames. To ameliorate these issues, various aspects of the diagnostic were optimized. High quality particle images were obtained by using large focal length lenses at a relatively high f-stop (f/8.0). An adjustable flow bypass through the particle seeder, combined with an adaptive multi-pass interrogation scheme and optimized Δt_{PIV} provided good seed levels and minimized particle loss. The camera calibration and registration was carefully performed as described in §2.6. Under good experimental conditions such as these, Lawson and Wu [66] indicate that the root-mean-squared (RMS) measurement uncertainty should be around 1% and 4% for the in-plane and out-of-plane velocities respectively. Furthermore, modern PIV algorithms employ more sophisticated calibration and particle tracking methods than used in Ref. [66]. These should further reduce the uncertainty.

The second source of uncertainty is associated with averaging the velocity field across an interrogation box. The velocities calculated by PIV effectively represent the mean in an interrogation box and gradients internal the box are not resolved. This is of particular importance for turbulent scales on the order of the interrogation box width. Lavoie et al. [62] have performed a detailed study of the spatial resolution required for PIV measurements to accurately capture fine scale velocity gradients. For a spatial resolution of $0.5\lambda_\nu \approx 3\lambda_k$, they indicate that the gradients do not suffer from excessive smoothing. In particular, less than a 5% correction is needed to accurately capture both the energy and dissipation associated with λ_ν sized structures. This correction is significantly lower for larger structures. Hence, it is expected that spatial resolution limitations should produce an RMS error of less than 5% in a given velocity derivative. For dynamic turbulence quantities such as ω_i

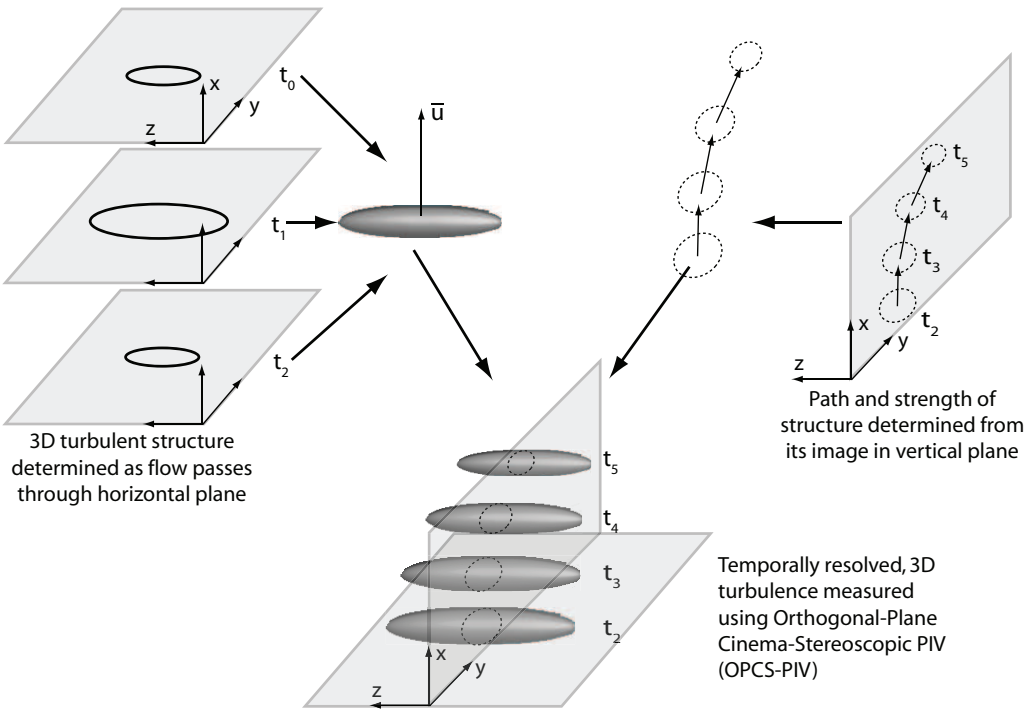

Figure 2.8: Concept of the Orthogonal-Plane Cinema-Stereoscopic PIV (OPCS-PIV) diagnostic.

and S_{ij}, the maximum RMS error would therefore be expected as less than 7%.

2.3 Orthogonal-Plane Cinema-Stereoscopic PIV

The OPCS-PIV diagnostic was designed to reconstruct temporally evolving 3D turbulence-flame interactions. The concept of the diagnostic is demonstrated in Fig. 2.8. Two orthogonal PIV planes were employed. In a plane perpendicular to the flow, temporally-resolved three-component velocity fields were measured. This allowed the entire velocity gradient tensor to be determined at this plane using a 'modified Taylor's hypothesis', which is described below. Turbulent structures could then be identified and their 3D geometry reconstructed from the temporally resolved slices. However, this plane did not provide any information about the structures after they passed through.

The second plane was oriented parallel to the flow and used to determine the

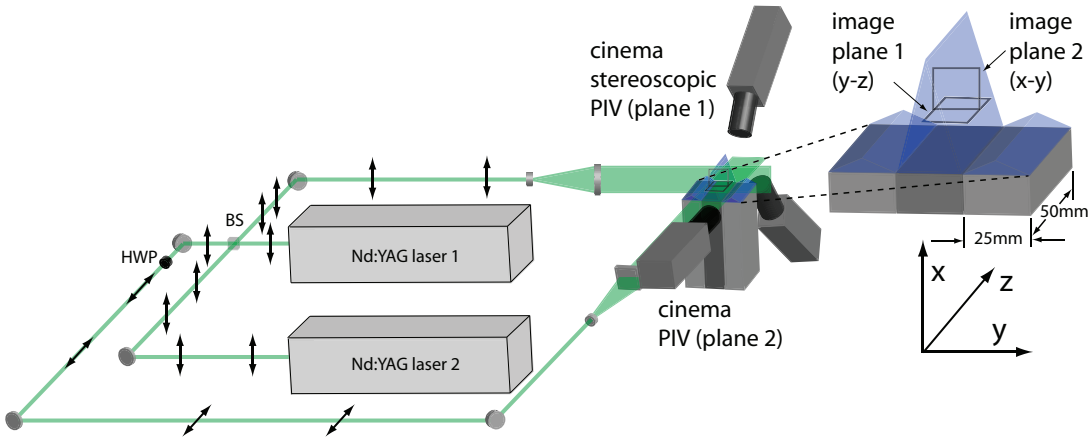

Figure 2.9: OPCS-PIV system layout with burners. HWP - Half wave plate. BS - Beam splitter. Arrows indicate polarization.

evolution of the turbulence as it progressed downstream. In this plane, temporally-resolved two-component velocity fields were measured. The 3D turbulent structures determined from the perpendicular plane had an image in this plane that evolved as the turbulence moved downstream. From this image, the path and strength of the structures could be deduced. Furthermore, each plane provided the instantaneous flame surface topography from the PIV particle density.

The system therefore consisted of two separate PIV system viewing mutually orthogonal planes as shown in Fig. 2.9. A Cinema-Stereoscopic PIV (CS-PIV$_0$) system was used to resolve the three velocity components in a plane perpendicular to the flow ($y-z$, image plane 1). The subscript O refers to diagnostics employed in the OPCS-PIV system. Note that when referencing the OPCS-PIV system, the CS-PIV$_0$ diagnostic was perpendicular to that employed in §2.2. A two velocity component Cinema-PIV (C-PIV$_0$) system was used to take measurements in an $x-y$ plane parallel to the flow (image plane 2). The image planes were arranged in an inverted T configuration with image plane 1 forming the base. That is, as the flow passed through image plane 1 it entered the field of view for image plane 2. From this data, temporally evolving 3D turbulence-flame interactions could be reconstructed. This

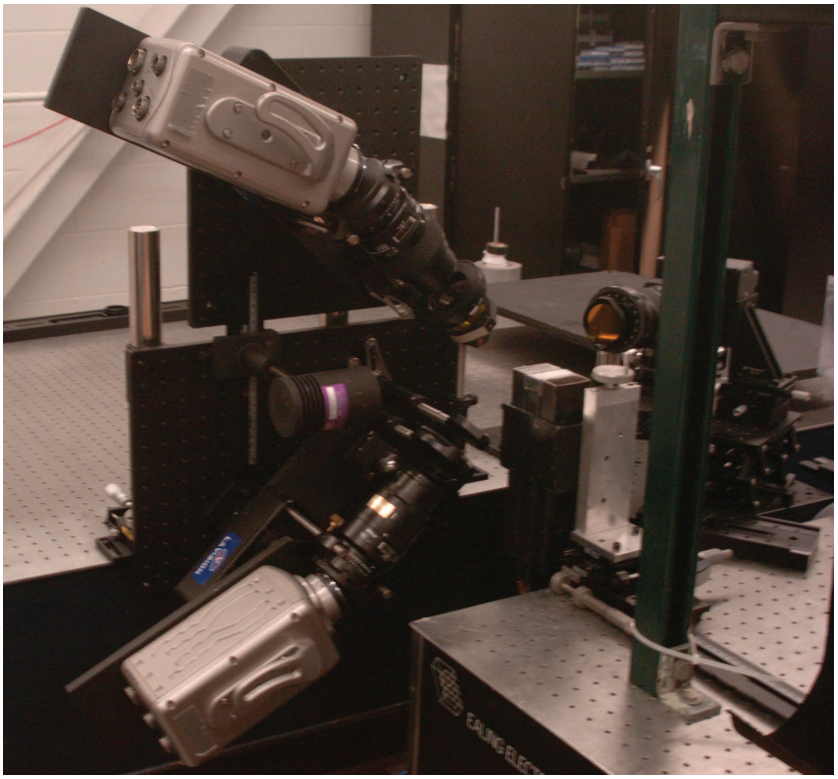

Figure 2.10: CS-PIV$_0$ camera configuration in OPCS-PIV system.

procedure is described in §2.4.

The CS-PIV$_0$ system used two Phantom v9.0 high-speed cameras, while the C-PIV$_0$ system used a Fastcam Ulima-APX (Photron). The CS-PIV$_0$ cameras were mounted vertically on optical panels (Fig. 2.10), which were able to translate in the y-direction. The cameras themselves were attached to two-axes translation stages. The C-PIV$_0$ camera was mounted to a lab jack and two-axis translation stage as shown in Fig. 2.11. Hence, all cameras could translate independently in three-directions, allowing them to be precisely aligned.

Both planes were illuminated by laser sheets generated from a pair of ORC-1000 (Clark-MXR) high-rep-rate Nd:YAG lasers. Each laser was operated at 3 kHz and produced about 6 mJ of 532 nm light per pulse. The pulses from one laser were set to lag the other by 30 μs, which determined the time between correlated particle

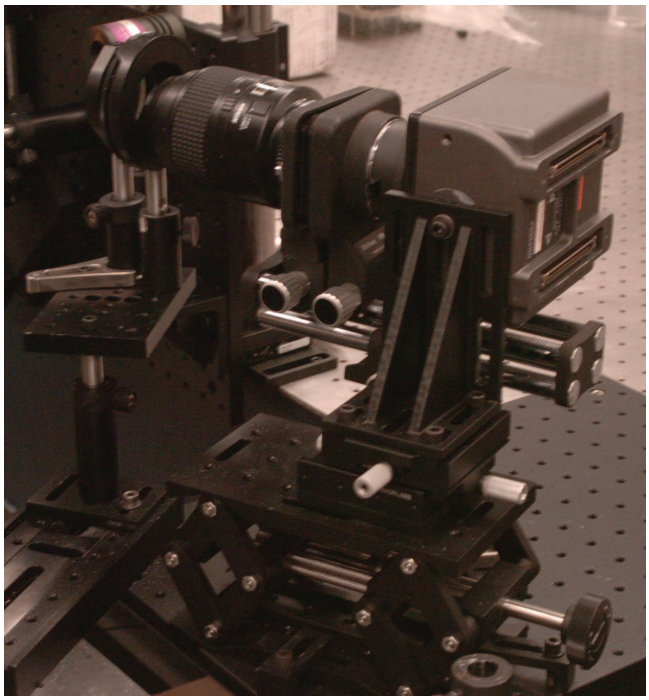

Figure 2.11: C-PIV$_0$ camera configuration in OPCS-PIV system.

images (Δt_{PIV}). The beams from the lasers were simultaneously combined and split as shown in Fig. 2.9. This resulted in two identical beams consisting of pairs of pulses separated by 30 μs and repeating at a rate of 3 kHz. Each beam was then expanded through a telescope before being contracted in one dimension to form the appropriate sheet. The full-width at half-maximum of both sheets was approximately 300 μm. In order to properly capture the correlated particle images, frame straddling was employed for each camera. The cameras were operated at 6 kHz and timed such that the correlated laser pulses straddled the inter-frame delay time. This resulted in vector fields being captured at 3 kHz or every 0.33 ms.

The flow was seeded with the same tracer particles as in §2.2. The scattered laser light from these particles was collected into the cameras using Micro-Nikkor 105 mm lenses. In order to obtain accurate vector fields, it was necessary to isolate the light scattered from each plane into the appropriate camera(s). Without isolation, light

scattered from particles in image plane 2 appeared as erroneous particle images for the cameras viewing image plane 1 (and vice versa). To separate the images, the method of Kim et al. [57] was used. The polarization state of one of the laser sheets was rotated 90° by means of a half wave plate. Hence, the scattered light from each plane had different polarizations. Linear polarization filters were placed in front of each camera lens and adjusted to minimize particle images from the unwanted sheet. Narrow band pass filters at the laser wavelength (532 nm) were used to remove flame chemiluminescence.

The specific configuration of the camera systems was dictated by light collection considerations. After splitting the beams from the lasers, each pulse consisted of approximately 3 mJ of light. This is considerably less than typically used for PIV. Furthermore, the chemiluminescence filters greatly reduced the light transmitted to the camera. Hence, all cameras were placed in the forward scatter configuration (similar to §2.2), increasing the amount of light directed towards them [94]. The CS-PIV$_0$ cameras were oriented at 45° from image plane 1. This resulted in a separation angle of 90° between the cameras, giving the theoretical maximum accuracy in computing the out-of-plane velocity component [65]. Normally, focusing problems caused by this high separation angle make it somewhat undesirable (hence the 35° of the standard CS-PIV system). However, due to the small field of view in these images (which aided in focusing) and the desire for an optimally resolved out-of-plane velocity (for the reconstruction procedure), the large separation angle was both feasible and desirable. The C-PIV$_0$ camera was oriented at 10° from image plane 2. While the angular orientation of the C-PIV$_0$ camera was not necessary from a purely vector computation standpoint, it was necessary both for light collection and to remove it from the laser path of image plane 1. However, in this configuration the field of view

of the lower CS-PIV$_0$ camera could be obstructed by the burner. This dictated the location of the measurement volume as described in §2.3.1.

The angular configuration of the PIV systems, particularly the stereoscopic system, once again created a strong perspective distortion. The calibration was performed using the LaVision software in the same manner as for the CS-PIV system and is described in §2.6.

The velocity vectors were computed from the spatial cross-correlation using the same software. At 6 kHz, the CS-PIV$_0$ system operated at a resolution of 432 x 554 pixels and imaged a 12.1 mm x 9.6 mm (y x z) field of view. The C-PIV$_0$ operated at 512 x 512 pixels and imaged a 12.3 mm x 13.4 mm (x x y) field of view. A multi-pass vector evaluation technique was employed for both systems with interrogation box sizes decreasing from 64 x 64 to 16 x 16 pixels. The resultant interrogation box sizes were approximately 390 μm for the CS-PIV$_0$ and 380 μm for the C-PIV$_0$. A 50% interrogation overlap was used resulting in vector spacings of 195 μm and 190 μm for the CS-PIV$_0$ and C-PIV$_0$ respectively. The resolution of the system with respect to the turbulence scales is addressed in §2.3.1.

To align the velocity fields from each plane, it was necessary to register the two image planes with respect to each other. This required identifying the z-location of image plane 2 in plane 1 and the x-location of image plane 1 in plane 2. Also, the respective y-axes had to be aligned. To do so, a knife edge was aligned with the intersection line of the two image planes. The knife edge was placed in a three-axis rotation stage and was able to translate in all three directions. This allowed precise alignment of the edge with the intersection line. Furthermore, the edge was translated such that a corner of the blade was in the field of view, providing a coincident point and two coincident lines in each cameras' field of view. The coordinates for each

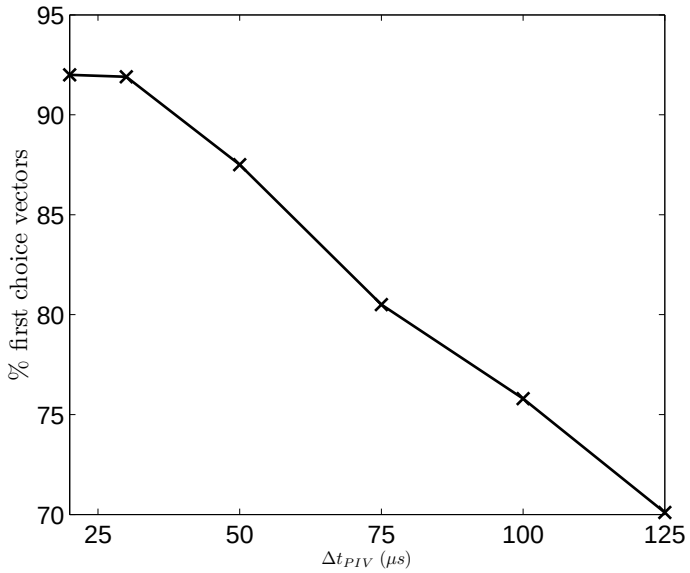

Figure 2.12: Variation of percent of first choice vectors with time between laser pulses (Δt_{PIV}). As Δt_{PIV} increased, the accuracy of the PIV cross-correlation decreased due to loss of particles through the sheet.

plane were then set such that the point and lines were coincident in the coordinate axes.

The appropriate Δt_{PIV} was set by various requirements in each image plane. In image plane 1, it was necessary that Δt_{PIV} be large enough that the particles traverse a sufficient distance in each direction for adequate vector computation. This is a standard requirement for PIV. However, it was also required that a sufficient number of particles remain in the sheet between laser pulses. With the flow traversing normal to image plane 1, this put a limitation on the maximum Δt_{PIV}. For image plane 2, only the first requirement applied and this did not provide any additional restriction. To determine the optimal value, data sets were taken with Δt_{PIV} ranging from 20 μs to 150 μs. The vector fields were computed and the percentage of first choice vectors compared. As can be seen from Fig. 2.12, the optimal value occurred for $\Delta t_{PIV} \leq 30$ μs. For higher Δt_{PIV}, excessive particles entered and left the sheet between laser

Parameter	CS-PIV$_0$	C-PIV$_0$
Camera frame rate	6 kHz	6 kHz
Temporal resolution	0.33 ms	0.33ms
Δt_{piv}	30 μs	30 μs
Stereo angle	45°	10°
Camera resolution	432 px x 544 px ($y \times z$)	512 px x 512 px ($x \times y$)
Field of view	12.1 mm x 9.6 mm ($y \times z$)	12.3 mm x 13.4 mm ($x \times y$)
Interrogation box	390 μm	380 μm
Vector spacing	195 μm	190 μm
Seed material	silica coated TiO_2	silica coated TiO_2
Nominal seed diameter	0.15 μm	0.15 μm

Table 2.4: OPCS-PIV parameters.

pulses. However, it was found that there was less noise in the y and z gradients at $\Delta t_{PIV} = 30$ μs relative to 20 μs. This is likely due to the greater accuracy in determining the relatively small in-plane velocities with the longer Δt_{PIV}. Hence, the time between laser pulses was set to 30 μs. The system attributes of the OPCS-PIV diagnostic are summarized in Table 2.4.

2.3.1 OPCS-PIV test condition

In order to avoid effects from the z-edges of the burner on the flow-field, it was desirable to perform measurements on the burner centerline (i.e. $z = 0$). In order to measure the strongest turbulence, it was desirable to perform measurements close to the burner exit (i.e. $x = 0$). However, interference from the burner geometry prevented these conditions from being simultaneously satisfied as shown in Fig. 2.13. Since the edge effects were inherent to the system, it was decided to move the measurement volume downstream. The location of image plane 1 was therefore set at 18 mm above the burner exit. In order to achieve turbulent fluctuations similar to those in §2.1 at this height, the bulk velocity was increased to 1.5 m/s (50% greater than those for the CS-PIV diagnostic) and an equivalence ratio of 0.6 was used. The location of image plane 2 was set 7.5 mm from the burner centerline. Laser Doppler velocimetry measurements showed that the velocity statistics at this location were

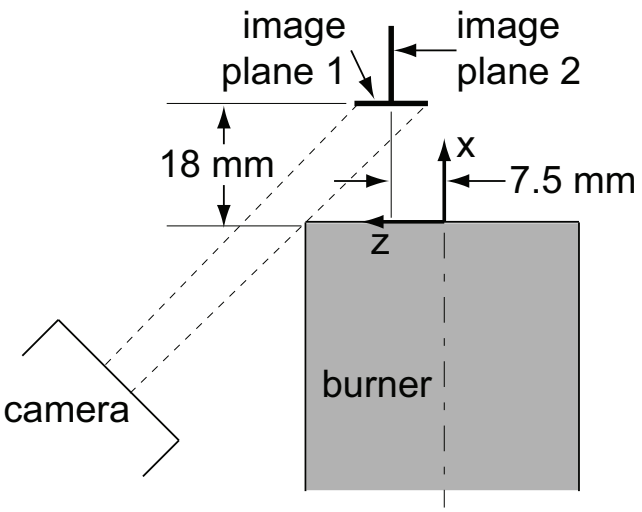

Figure 2.13: Geometric constraints on the field of view dictated by dual-forward scatter configuration of the CS-PIV$_0$ system.

L	λ_T	λ_ν	λ_k	Re_L
4.5 mm	0.93 mm	0.43 mm	0.074 mm	600

Table 2.5: OPCS-PIV turbulence scales at $(x, y, z) = (18, 0, 7.5)$.

within 5% of those along the centerline, indicating that edge effects were small. At $(x, y, z) = (18, 0, 7.5)$ mm, u'/s_l^0 was 2.2 and L/δ_l^0 was 19.6.

Once again, it is important to consider the range of scales present in the turbulent flow. At the location of image plane 1, $L = 4.7$ mm and $\mathrm{Re}_L = 600$. This Reynolds number is once again lower than typically considered for fully developed turbulence. Using Eq. 2.7, the smallest scale structures in the flow were expected to be approximately 0.43 mm. Such a turbulence field would be resolved by measurements with a frequency of 0.22 mm. This is slightly smaller than the resolution of the diagnostic, which is once again twice over sampled. Hence it is possible that the smallest scale structures were not resolved. However, as will be seen in §5.1, the diagnostic is capable of resolving 3D turbulent structures at the viscous scale. As mentioned previously, these structures are not a substantial contributor to the flame stretch.

2.4 OPCS-PIV reconstruction methodology and typical results

As previously described, the OPCS-PIV system was designed to reconstruct temporally evolving 3D turbulence flame interactions. This involved three steps:

1. Using the Cinema-PIV$_0$ data from the vertical plane (image plane 2), temporal segments that contained turbulence-flame interactions were identified.

2. The Cinema-Stereoscopic PIV$_0$ data during these time segments were then used to measure the three-dimensional velocity gradient tensors in the horizontal plane (image plane 1). A 'modified Taylor's hypothesis' was used to determine the out-of-plane velocity gradients. By convecting these planar slices downstream, the 3D structure of the turbulence was determined.

3. Using the Cinema-PIV$_0$ data (vertical plane), the strength and path of these structures were deduced as they interacted with the flame.

This process is detailed below.

2.4.1 Identification of turbulence-flame interactions from the cinema-PIV

The reconstruction of 3D turbulence-flame interactions first required identification of time segments in which these interactions occurred in a tractable manner. That is, it was necessary to isolate intervals in which:

1. **The interaction was contained in the measurement volume.** It was desired that the interaction begin near image plane 1 (at the bottom of image plane 2) to observe the entire interaction process.

2. **The interacting turbulent structures intersected image plane 2.** The flame surface topography in the x-direction was only available in image plane 2. Furthermore, the data from the C-PIV system, measured in image plane 2, were

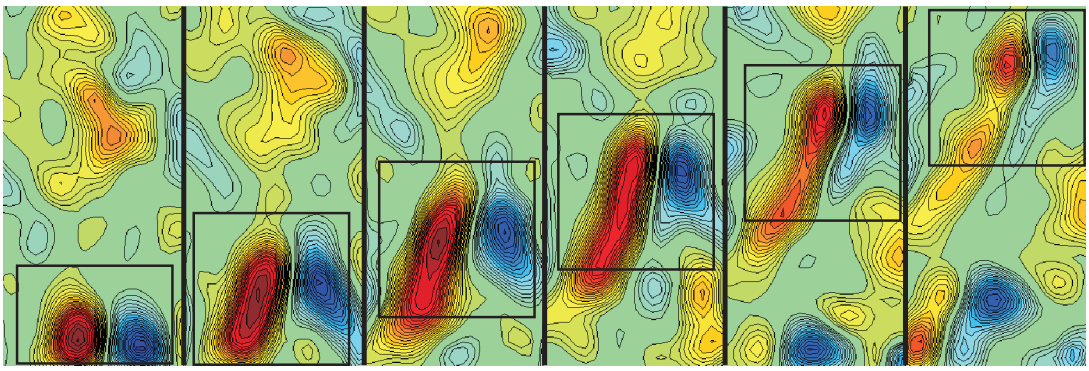

Figure 2.14: Measured vorticity from C-PIV$_0$. Structures decay with time and move to the right as they convect downstream. Contours of ω_z between -1200 s^{-1} (blue) and 1200 s^{-1} (red). Field of view is 4 mm x 8 mm. Every other frame is shown and the time between frames is 0.66 ms. Flow is from bottom to top.

used to evolve the turbulent structures (see §2.4.3). Hence, any turbulence-flame interaction studied had to intersect this plane.

3. **There was little convection in the z-direction.** Large convection in the z-direction would lead to incorrect evolution of the flame surface topography and/or the turbulence (§2.4.3). Hence, time segments were chosen in which $|w| < 0.05|\vec{u}|$. Under this restriction, the turbulence could convect less than λ_ν out of plane during an interaction.

To demonstrate the reconstruction process it is first useful to consider turbulence in the absence of the flame front. In order to keep the flow conditions (i.e. no mean shear) identical, non-reacting turbulent structures were studied in the reacting flow. The 'non-reacting' structures were extracted from locations far away from the flame front near the burner centerline ($y \approx 0$). For the purposes of this demonstration, structures of concentrated vorticity will be used. However, the method can be equally applied to any dynamic turbulence variable.

The evolution of a typical vorticity field measured from the C-PIV$_0$ is shown in Fig. 2.14. Contours of the resolved vorticity between -1200 s^{-1} (blue) and 1200 s^{-1} (red)

are shown, indicating clockwise and counter clockwise rotating fluid respectively. Every other frame is shown (Δt = 0.66 ms). This time sequence contained what appeared to be two counter-rotating vortical structures. As the flow progressed downstream, the structures decayed and their path deviated slightly to the right. This flow contained a tractable turbulence field for 3D extraction because it did not convect out of image plane 2 during the time sequence.

2.4.2 Reconstruction of the 3D turbulent structures

Once appropriate time segments such as that in Fig. 2.14 were identified, the corresponding 3D turbulence field could be reconstructed. Using Taylor's hypothesis, a first order reconstruction of the velocity gradient field can be performed using the CS-PIV$_0$ system. This process has been demonstrated by Ganapathisubramani et al. [44, 45] who constructed pseudo-volumes of 3D turbulent structures in a non-reacting jet. To do so, the velocity field in the interrogation plane was convected downstream at the local mean velocity. This produced frozen flow pseudo-volumes in which all velocity components were measured and from which the velocity gradient field could be calculated. They found that this method provided accurate reconstruction of the spatial structure of the velocity gradient field. However, the magnitude of the gradients exhibited some distinct errors [44]. Such errors may arise both from the application of Taylor's hypothesis and the inability of the frozen flow hypothesis to predict the downstream behavior of the turbulence.

For every time step Taylor's hypothesis states that the downstream spatial velocity derivative can be approximated from the temporal data as:

$$\frac{\partial u_i}{\partial x} \approx \frac{1}{\overline{u}_x}\frac{\partial u_i}{\partial t} \tag{2.9}$$

Physically, this can be interpreted as frozen fluid elements in the interrogation plane

convecting downstream at the local mean velocity, $\overline{u}_x$. From discrete temporal measurements, the derivatives are given by:

$$\frac{\partial u_i(0,y,z,t_0+\Delta t/2)}{\partial x} \approx \frac{1}{\overline{u}_x(0,y,z)} \frac{u_i(0,y,z,t_0) - u_i(0,y,z,t_0+\Delta t)}{\Delta t} \tag{2.10}$$

where Δt is the time between successive measurements. The frozen fluid element may be thought of as convecting a distance of $\overline{u}_x(0,y,z)\Delta t$ between these measurements. The local convective velocity therefore is decoupled from the local turbulence. This process can also be viewed as creating a frozen flow pseudo-volume of velocity data in which the data points at time $t_0+\tau$ are located at:

$$(x(t_0+\tau), y(t_0+\tau), z(t_0+\tau)) = (K\overline{u}_x(0,y,z)\Delta t, y_0, z_0) \tag{2.11}$$

where K is the number of time steps between $t=t_0$ and $t=\tau$. The spatial derivatives then can be computed directly from this volume and would most accurately represent the derivative between successive measurement points as indicated in Eq. 2.10.

However, decoupling the turbulence from the convection may not always be accurate. Various studies have investigated the effects of high turbulence intensity on the validity of Taylor's hypothesis with regards to spectral measurements [67, 113]. Under certain conditions, they suggest corrections to the spectra calculated from Taylor's hypothesis. However, these are statistical corrections and do not provide any improvement to the local instantaneous streamwise derivatives.

A simple correction that may provide increased accuracy is to locally convect the fluid elements at their particular velocities. The local turbulence is therefore not decoupled from the convection. In such a description, a fluid element in the measurement plane moves downstream a distance of $u_x(0,y,z,t)\Delta t$ between successive measurements (as opposed to $\overline{u}_x(0,y,z)\Delta t$). Hence, the streamwise velocity deriva-

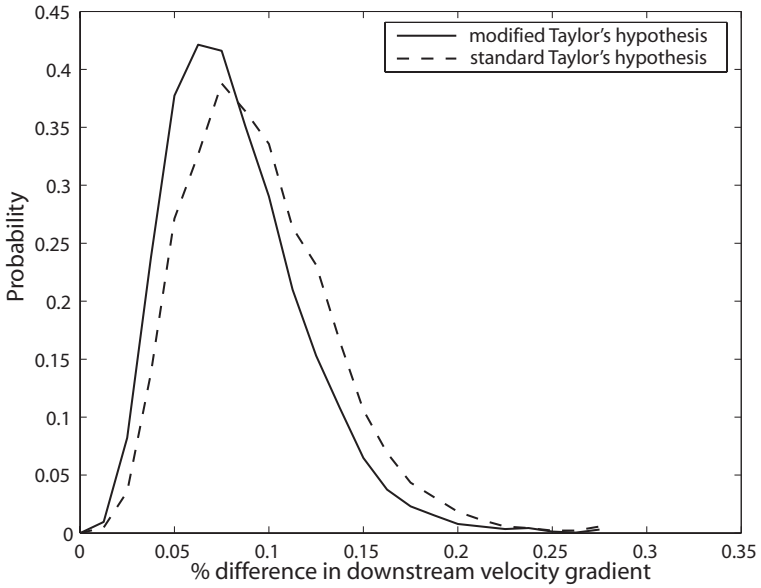

Figure 2.15: PDFs of the relative error in the downstream velocity derivatives computed from the CS-PIV$_0$ using the modified and standard Taylor's hypotheses relative to those directly measured from the C-PIV$_0$.

tives are given by:

$$\frac{\partial u_i(0,y,z,t_0+\Delta t/2)}{\partial x} = \frac{1}{dt}\frac{u_i(0,y,z,t_0)-u_i(0,y,z,t_0+\Delta t)}{u_x(0,y,z,t)} \tag{2.12}$$

Equation 2.12 will be referred to as the 'modified Taylor's hypothesis'.

A detailed evaluation of the accuracy of using CS-PIV$_0$ to determine the downstream velocity derivatives using the standard Taylor's hypothesis (Eq. 2.10) was conducted by Ganapathisubramani et al. [44]. They concluded that this technique was reasonably accurate (compared to other three component techniques) based on consideration of a variety of metrics. The conclusions of these analyzes are applicable to this diagnostic and are not replicated herein. Instead, the accuracy of Taylor's hypothesis and any improvements provided by the modified method of Eq. 2.12 for computing the streamwise derivatives were directly evaluated using the simultaneous C-PIV$_0$ data (the C-PIV$_0$ provided direct measurement of the streamwise derivatives in image plane 2). Coincident measurements were only available along the intersection line between image planes 1 and 2. Data from 5000 vector fields were used for

the statistics.

To determine the accuracy of each technique, probability distribution functions were computed of the relative error between the reconstructed streamwise velocity gradients (from CS-PIV$_0$) and those directly measured (from C-PIV$_0$). These PDFs are shown in Fig. 2.15. As can be seen, the relative error using both techniques was quite small, with the modified Taylor's hypothesis having lower mean error; the mean error for the modified and standard methods were approximately 8% and 9.5% respectively. Furthermore, the PDF for the modified method was more skewed towards smaller errors. This was due to its increased accuracy when the local, instantaneous velocity was significantly different than the mean. Due to this decrease in the mean and variation of the error, the modified Taylor's hypothesis was used for this study. Furthermore, it is expected that the relative difference between the modified and standard methods would increase as the turbulence intensity increased. However, either method provides a reasonably accurate reconstruction of the downstream velocity gradients. This further confirms the conclusions of Ref. [44] that CS-PIV$_0$ is a useful technique for the study of 3D turbulence.

The modified Taylor's hypothesis provided the streamwise velocity derivatives in image plane 1. The y- and z-derivatives in this plane were computed directly from the CS-PIV$_0$ data. Hence, the CS-PIV$_0$ provided temporally resolved slices of the 3D velocity gradient tensor as the flow passed through image plane 1. The measurement of these velocity gradient slices is demonstrated in Fig. 2.16. This figure shows slices of the 3D vorticity magnitude ($\omega = (\omega_i\omega_i)^{1/2}$) from image plane 1 (looking down on the flow) for the time segment leading into Fig. 2.14; the flow in Fig. 2.16 is entering Fig. 2.14. As the flow progressed through the plane, a coherent toroidal region of vorticity could clearly be seen. That is, what appeared to be two separate

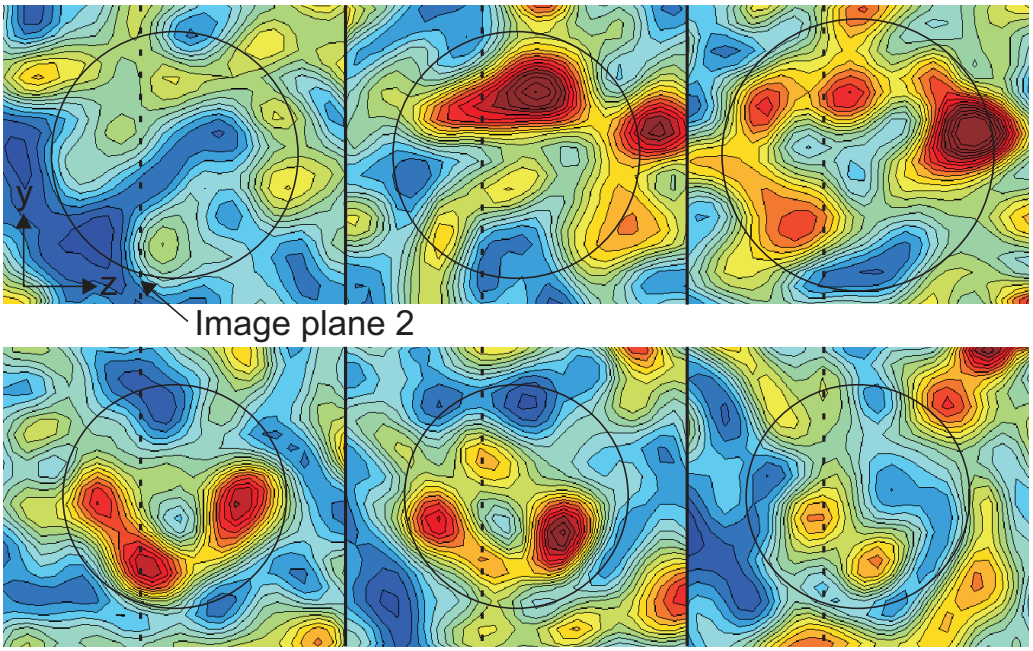

Figure 2.16: View from the top of image plane 1 (horizontal plane) as turbulence passes through. Contours of 3D vorticity magnitude between 0 s^{-1} (blue) and 1200 s^{-1} (red) have been reconstructed using the modified Taylor's hypothesis and the CS-PIV$_0$ data. The measurement corresponds to the times immediately before Fig. 2.14. What appeared to be two vortical structures in the vertical plane appeared as a single connected structure in this plane. The field of view is 5 mm x 4 mm.

counter-rotating vortical structures in the vertical cut actually possessed a connected structure in the third dimension. This toroidal structure is discussed more below.

From these reconstructed velocity gradient slices, the 3D geometry of the turbulence was determined by convecting the gradients downstream. That is, the slices were used to construct a volume in which the data points were located as given by Eq. 2.11, the x-velocity derivatives were given by Eq. 2.12, and the y- and z-derivatives were computed directly from the horizontal plane data. Hence, turbulence in this pseudo-volume has the same spatial structure as would be found in the standard Taylor's hypothesis, but with a more accurate approximation for the velocity gradient field.

A typical pseudo-volume of frozen turbulence is shown in Fig. 2.17. Isosurfaces of the vorticity magnitude are shown at a value of 1000 s^{-1}. This represents some of the most intense vorticity in the flow.

A planar cut of the reconstructed turbulence corresponding to the flow measured in Fig. 2.14 is shown in Fig. 2.18. As can be seen, the reconstruction accurately deduced the correct spatial structure and strength of the turbulence in the vicinity of image plane 1 (bottom of the image). However, this reconstruction does not include the evolution of the turbulence as it moves downstream. That is, the real turbulence moved to the right and decayed, while the frozen reconstructed turbulence did not. In the study of turbulence-flame interactions this evolution is very important and it will be treated in §2.4.3.

Once the spatial structure of the turbulence was reconstructed, the 3D structures of interest could be isolated from the flow. The isolation of particular structures was necessary in order to allow for their evolution as described in §2.4.3. To extract a 3D structure, the point corresponding to the maximum vorticity magnitude in the

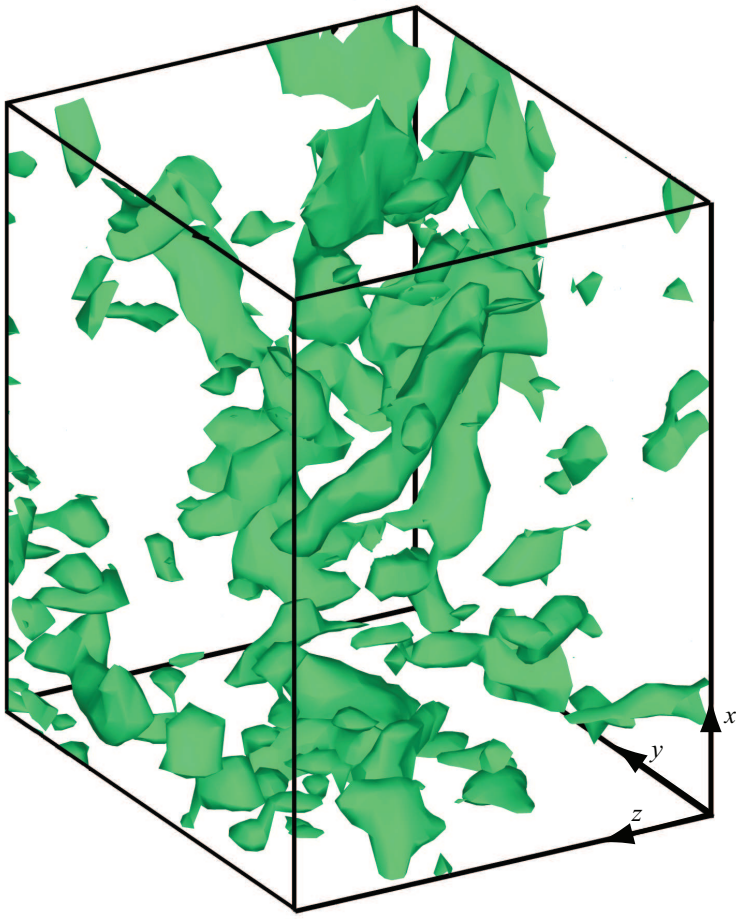

Figure 2.17: Vorticity structures measured using the CS-PIV$_0$ and modified Taylor's hypothesis. Isosurfaces of $\omega = 1000$ s^{-1}. The volume is 13 mm x 11 mm x 9 mm (x, y, z) and the flow is from bottom to top.

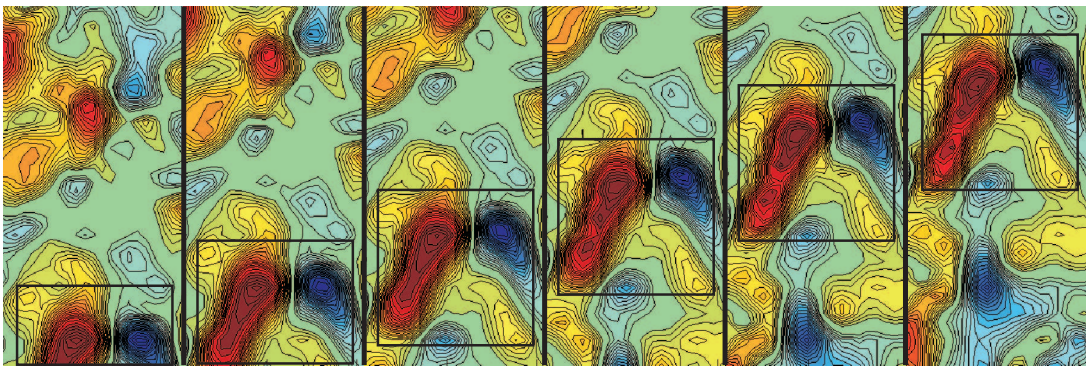

Figure 2.18: Reconstructed ω_z from CS-PIV$_0$ for the same time sequence as in Fig. 2.14. Structure strength and path are frozen. Contours of z-vorticity between -1200 s^{-1} (blue) and 1200 s^{-1} (red). Field of view is 4 mm x 8 mm. Every other frame is shown and the time between frames is 0.66 ms. Flow is from bottom to top.

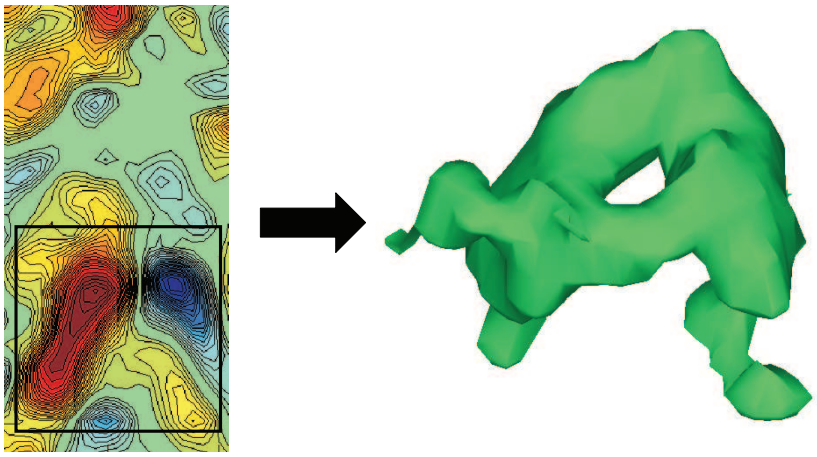

Figure 2.19: A toroidal vortex reconstructed from the CS-PIV$_0$ system. Isosurface of $\omega = 900$ s^{-1} shown. Time corresponds to the third frame of Figs. 2.14 and 2.18.

structure from the 2D slice was selected. From this point, a connected volume was sought in which the magnitude of the vorticity remained above the threshold being investigated.

The three-dimensional turbulence structure extracted from the data in Figs. 2.16 and 2.18 is shown in Fig. 2.19. As indicated by the horizontal plane data, the 3D turbulence consisted of a single toroidal structure. This is in contrast to the two separate structures indicated from the vertical plane data.

2.4.3 Evolution of the turbulence

In the final step of the reconstruction, the extracted 3D turbulent structures were convected and evolved. As a turbulent flow moves downstream it evolves under its own influence. Energy is transferred from the large to small scales where it is dissipated, vortex lines are stretched, and structures align with particular characteristics of the strain rate. In the presence of a flame front, this evolution is even more complex as the flame attenuates and generates velocity gradients. Hence, a method for evolving the turbulence as it interacts with the flame was necessary. This was done by utilizing the path and strength of the directly measured turbulence from the C-PIV$_0$. The path of a 3D structure was set by forcing the planar centroid of the structure in the $z = 0$ plane to follow the path of the centroid of the equivalent structure measured directly from the C-PIV$_0$. Additionally, the strength of the 3D structure was evolved by forcing its mean strength in the $z = 0$ plane to equal the mean strength of the structure from the C-PIV$_0$. This allowed the path and strength of the 3D turbulent structures to be deduced as they interacted with the flame front. However, no modification to the geometric structure of the turbulence was made as it progressed downstream.

The modification of the structure path and strength relative to the frozen flow approximation is demonstrated in Fig. 2.20 for the time sequence in Fig. 2.18. The displacements have been proportionally increased to prevent the structures from overlapping in the images and highlight the effects of the correction. Figure 2.20(a) demonstrates the structure evolution under the frozen flow approximation. The structure convects downstream at the local mean velocity and does not change in strength. Conversely, the structure in Fig. 2.20(b) evolves as dictated by the C-PIV$_0$ data; its path curves and its strength attenuates. By comparison with Fig. 2.14,

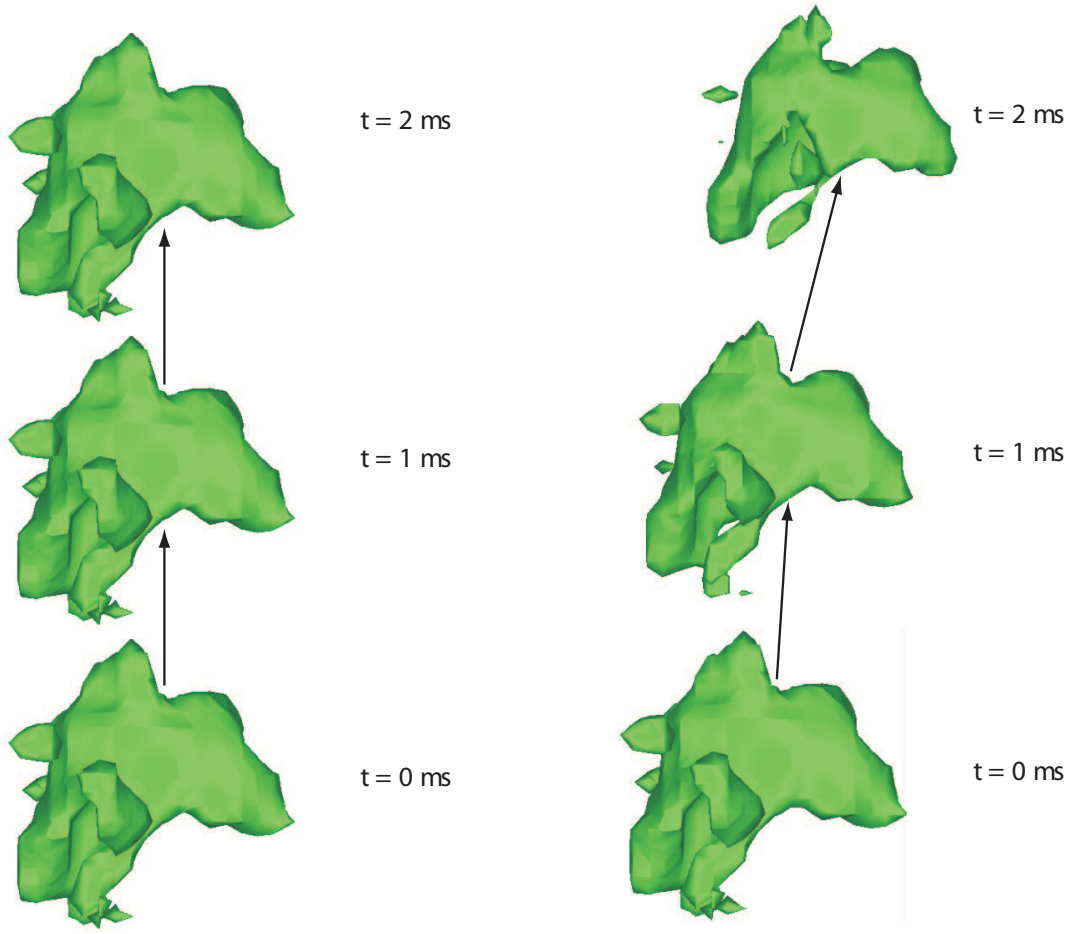

(a) Frozen flow - Path and structure strength fixed at t = 0.

(b) Using C-PIV$_0$ - Path and structure strength corrected from image plane 2 data.

Figure 2.20: Evolution of toroidal structure using frozen flow and C-PIV$_0$ corrected methods. Displacements are proportionally increased to avoid structure overlap and the emphasize correction.

this modified path and strength is seen to better reflect the behavior of the actual physical structure than the frozen flow approximation.

2.5 Flame front location and description

In order to observe the interaction between eddies and the flame, the instantaneous flame front position had to be determined. Simultaneous measurements of the velocity field and premixed flame properties have been performed by combining PIV with PLIF and Rayleigh scattering techniques [26, 42, 86, 107]. However the use

of these methods is difficult in high-rep-rate applications due to laser limitations. Therefore, a method to determine the flame front location from the particle images was developed and its accuracy evaluated.

Flame front location was accomplished by measuring the dilatation of the gas from the gradient of seed particle number density. Typical methods of mapping a flame front from seed density have generally involved threshold techniques [86, 102]. However, these techniques rely on an ad hoc threshold value and are constrained by the spatial filter selected, which is typically isotropic. These problems are greatly compounded when using solid seed; the particles survive the flame, creating a gradient of number density instead of a sharp cutoff. However, this gradient itself can be used to accurately identify the flame surface. That is, the flame surface can be associated with an iso-contour of particle image density gradient. Here, the maximum gradient contour is used as this was the most easily identified.

However, the highly non-uniform nature of the particle field made accurate determination of these gradients from a raw image very difficult; isolated seed density variations and high-frequency noise appeared as false expansion contours in the reactants. Therefore, a two-step method was used, which is illustrated in Fig. 2.21. First, an initial predictor step with a standard filter scheme was applied along with an adaptive threshold technique, the result of which was a binary image and approximate flame front as shown in Fig. 2.21(b). The second step repositioned the flame to coincide with the center of the local high gradient region using an edge finding filter aligned normal to the flame boundary predicted in the first step (Fig. 2.21(c)). As the density gradient curve had an S-shaped profile, this corresponded to the location of the maximum gradient. This two-step procedure effectively eliminated noise due to variations in particle seed density as shown in Fig. 2.21(d).

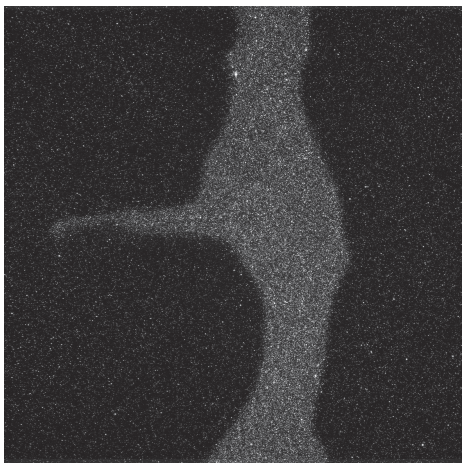

(a) Mie-scattering image

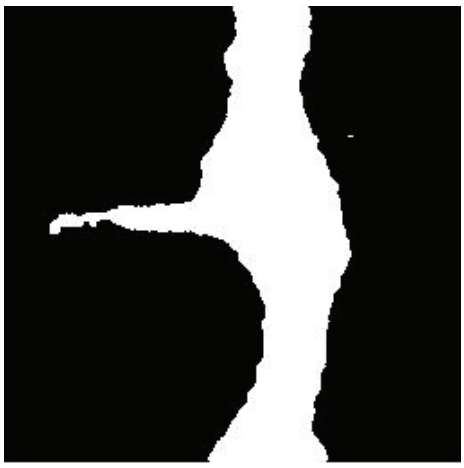

(b) Step 1 - Threshold based flame front

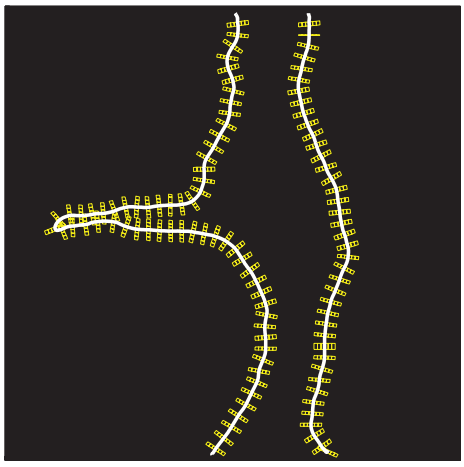

(c) Step 2 - Filter along local normal (every 20th location shown)

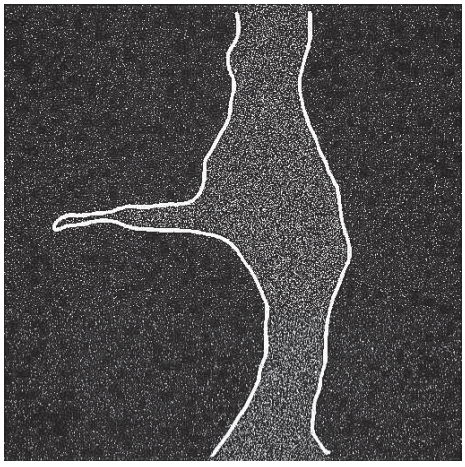

(d) Maximum particle gradient contour

(e) Correspondence with CH-layer location

Figure 2.21: Particle gradient based flame finding method.

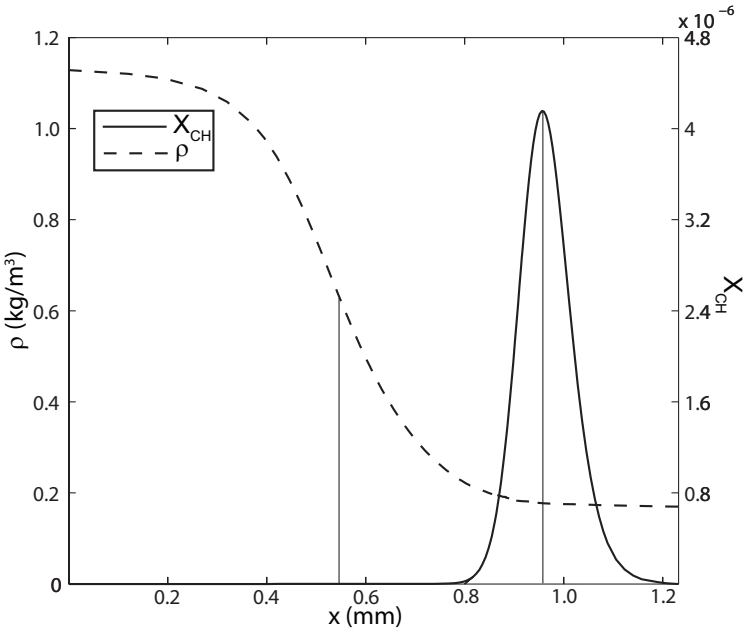

Figure 2.22: Location of maximum density gradient with respect to CH layer in a simulated, stoichiometric methane-air flame. The simulation was conducted using Chemkin and the GRIMech 3.0 chemical mechanism.

In order to quantify the accuracy of this method, comparisons were made between flame fronts found from the particle density gradient with those corresponding to the center of the CH-layer. This was done using simultaneous Mie scattering/CH-PLIF images originally taken by Filatyev et al[42]. This experiment was performed in a stoichiometric methane-air flame. As can be seen from Fig. 2.21(e), the particle gradient contour is slightly offset from the CH-layer towards the reactants. The mean offset from the center of the CH-layer was 415 μm and the standard deviation was 50 μm. The relatively high standard deviation was caused by local thickening of the CH layer due to out-of-plane curvature. In regions where the CH layer thickness was within 25% of the mean, the mean offset was 405 μm with a standard deviation of 25 μm.

This difference between the location of the particle image flame front and the CH-layer was expected. The particle density should be proportional to the gas density.

Therefore, the center of the high particle density gradient region should correspond to that of the high gas density gradient region. However, differences may occur due to particle lag from acceleration or thermophoretic effects within the flame front[104]. Chemkin simulations of a stoichiometric methane-air flame using the GRIMech 3.0 mechanism indicated that the maximum density gradient should occur approximately 390 μm upstream of the center of the CH-layer (Fig. 2.22). Thus it was concluded that the location of the measured maximum particle gradient contour corresponded well to the maximum gas density gradient contour.

For this experiment the flame front was regarded as an infinitely thin contour separating reactants and products at the location of maximum density gradient. Numerically, this interface can be described parametrically as:

$$f(\vartheta) = x_f(\vartheta)\hat{i} + y_f(\vartheta)\hat{j} + z_f(\vartheta)\hat{k} \tag{2.13}$$

As the parameter ϑ increases, $x_f(\vartheta)$, $y_f(\vartheta)$, and $z_f(\vartheta)$ trace out the flame surface. In the CS-PIV interrogation plane, $z_f(\vartheta) = 0$ and the remaining functions define the flame contour. For the OPCS-PIV measurements in image plane 1 (horizontal plane) $x_f(\vartheta) = 0$, while in image plane 2 (vertical plane) $z_f(\vartheta) = 0$.

Derivatives of any quantity involving the flame surface, q, with respect to a spatial coordinate, x_i, can be recast in terms of ϑ as:

$$\frac{\partial q}{\partial x_i} = \frac{\partial q}{\partial \vartheta}\frac{\partial \vartheta}{\partial x_i} = q'\frac{\partial \vartheta}{\partial x_i} \tag{2.14}$$

where $(')$ denotes differentiation with respect to ϑ.

The curvature (C) can be written in terms of derivatives with respect to ϑ as:

$$C = \frac{\left|\vec{f}' \times \vec{f}''\right|}{\left|\vec{f}'\right|^3} \tag{2.15}$$

which, in two-dimensions equates to:

$$C = \frac{x_f{}'y_f'' - x_f''y_f'}{\left(x_f'^2 + y_f'^2\right)^{3/2}} \tag{2.16}$$

2.6 Camera calibration

The angular configuration of the diagnostics created a strong perspective distortion across the field of view. That is, in order to maintain focus across the laser sheet at an acute viewing angle, the object, lens, and camera planes had to meet at a single point as described by the Scheimpflug criterion [94]. The differences in orientation between these planes resulted in varying distances between the laser sheet and camera sensor. This resulted in non-uniform magnification across the field of view. To calibrate the cameras for this, a target was placed in the light sheet and imaged at various z-locations.

A specially designed target was required, as standard targets were found to cause unacceptable errors due to two system attributes. The dual-forward scatter configuration required simultaneous imaging from opposite sides of the target. Additionally, the high resolution of this system required high magnification collection optics, resulting in a very low depth of field. Standard two-sided targets created noticeable translation and focusing errors due to their thickness. Transparent targets marked on a single side caused similar errors due to light bending effects in the target medium as described in Appendix B.

To avoid these errors, a thin, translucent, symmetric calibration target was used. This was comprised of a thin film, marked with 300 μm crosses on a 750 μm grid. The film was produced by taking photographs of a grid with known dimensions at a known magnification. The camera film was then developed, producing a miniaturized translucent grid with known properties. The grid was sandwiched between 100 μm

thick glass flats. This created small but equal in-plane image shifts for both cameras and out-of-plane shifts an order of magnitude smaller than the depth of field. This design was pioneered by Mullin [79], and adapted to the specific requirements of these diagnostics.

The distorted images from the cameras (Figs. 2.23(a)-2.23(b)) were corrected to a normal coordinate system (Figs. 2.23(c)-2.23(d)) and registered using the pinhole camera model in the commercial DaVis software package by LaVision. This process mapped equivalent pixels from each camera to the same physical position in the measurement plane. Minute adjustments were made to ensure proper registration of the cameras using the DaVis stereoscopic self calibration method, which ensures that simultaneous particle fields from both cameras contain identical information.

2.7 Flow seeding

Selection of the seed material was constrained by numerous requirements. Firstly, the seed material required a melting temperature sufficiently high to allow passage through the flame front. Additionally, the seed needed to possess a sufficiently low Stokes number (St) to accurately follow the turbulent fluctuations. The Stokes number is defined as:

$$\mathrm{St} = \frac{\tau_p}{\tau_f} \tag{2.17}$$

where τ_p is the fluid dynamic response time of the particle and τ_f is the characteristic time scale of the flow feature to be tracked.

The particle response time can be determined from the Stokes drag as:

$$\tau_p = \frac{\rho_p d_p^2}{18\mu} \tag{2.18}$$

where ρ_p and d_p are the density and diameter of the particle. The dynamic viscosity, μ, is that of the surrounding fluid.

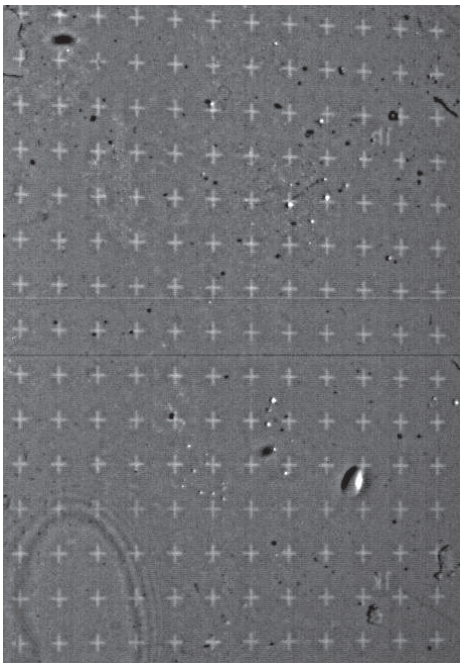

(a) Distorted image - camera 1

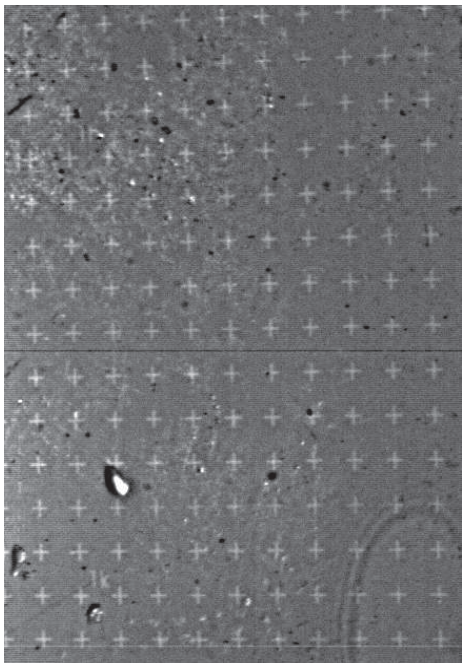

(b) Distorted image - camera 2

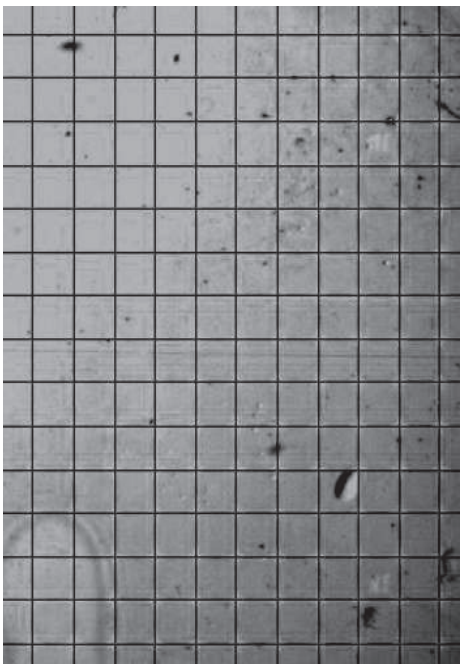

(c) Corrected image - camera 1

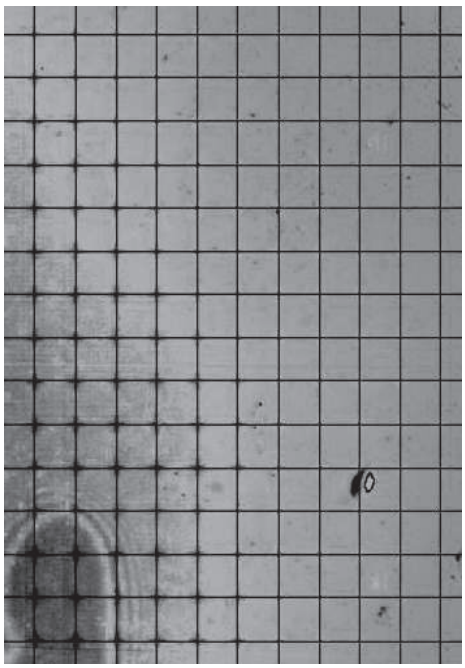

(d) Corrected image - camera 2

Figure 2.23: Calibration images for CS-PIV.

Seed	Material	d_p (μm)	St_{5d_p}
Huntsman A-PP2	TiO_2	0.15	0.036
Kenmira UV Titan	TiO_2	0.03	0.0014
Microgrit GB	Al_2O_3	0.10	0.015
Electron Microscopy Sciences DX	Al_2O_3	0.05	0.0038

Table 2.6: Seed properties.

A particle with Stokes number considerably less than unity is expected to follow the velocity gradients with negligible lag. In order to properly track the fine scale turbulence, the appropriate fluid dynamic time scale is the Kolmogorov time, τ_k. Assuming homogeneous, isotropic turbulence, this can be determined from the Kolmogorov scaling and the dissipation rate as:

$$\tau_k = \sqrt{\frac{\nu}{\varepsilon}} = \frac{1}{\sqrt{30}} \frac{\lambda_T}{u'_{rms}} \tag{2.19}$$

Hence, at the location of the LDV measurements in §2.2.1, $\tau_k = 0.50$ ms.

With appropriate materials restricted by the thermal requirement, the Stokes number restriction amounted to a restriction in particle diameter. However, the seed needed to be large enough to scatter a detectable amount of light from the low pulse energy, high rep-rate laser sheets. Furthermore, it was desired that the particle size be relatively uniform. That is, the seed crystals should not agglomerate into large clusters. Such large clusters prevented accurate evaluation of the velocity vectors and resulted in a path of erroneous data across a time sequence.

Two appropriate materials were apparent, alumina (Al_2O_3) and titanium dioxide (TiO_2). For each material, two brands were investigated, the properties of which are given in Table 2.6. All four of the brands investigated possessed sufficiently low Stokes number and high scattering to be used in this experiment. Stokes numbers were calculated based on a mean agglomerated particle size of five times the nominal crystal diameter [95].

However, the agglomeration properties of the TiO_2 were found to be superior to

those of alumina. Agglomeration properties were investigated directly from particle images. Seeded flow fields were imaged using the exact laser and camera configuration of the CS-PIV system. Seed densities were set to be low to avoid particle image overlap, which would appear erroneously as an agglomeration. Sample particle images are shown in Fig. 2.24. The images were binarized using a local (particle by particle) threshold and the area of the particles determined. This allowed the probability density functions of particle image area for each seed type to be computed. These are shown in Fig. 2.25. Any particle images with an area greater than 16 pixels were considered large and grouped together. As can be seen, all seeds possessed a similar distribution of sizes. However, the titanium dioxide seeds, in particular the Huntsman A-PP2, did not agglomerate into large clusters. Hence, the Huntsman seed was selected for this experiment.

2.8 Laser doppler velocimetry

At various times in the above discussion, laser Doppler velocimetry (LDV) measurements were utilized for velocity correlation statistics. This diagnostic can provide highly accurate, single point velocity measurements with temporal resolution far exceeding that of the PIV systems. Hence it is useful for single point statistics. As LDV is a well established diagnostic (e.g. Durst et al. [39]) a detailed description of the system is not needed; a brief description will be given.

The LDV system employed an Innova 90 (Coherent) argon laser operating at 514.5 nm. The beam from this laser was split and the subsequent two beams converged in the measurement volume, setting up a Doppler fringe pattern. The volume diameter was estimated as less than 0.5 mm from burn measurements. The flow was seeded with the same TiO_2 seed as in the PIV studies. As the seed passed through the fringe

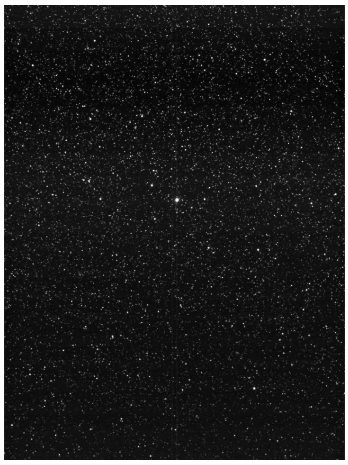

(a) Huntsman A-PP2

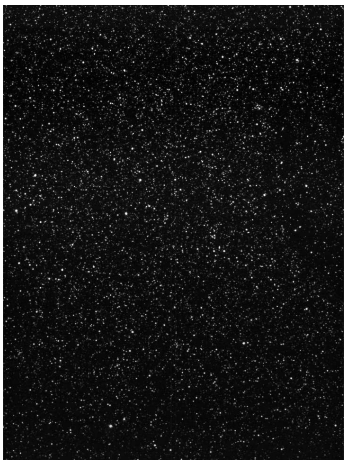

(b) Kenmira UV Titan

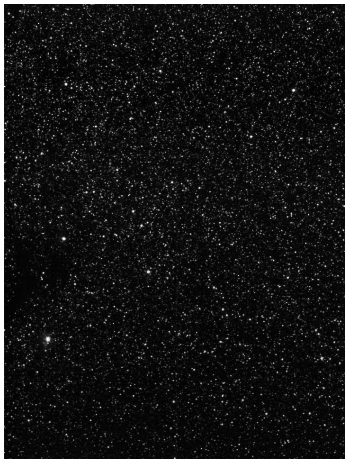

(c) Microgrit GB

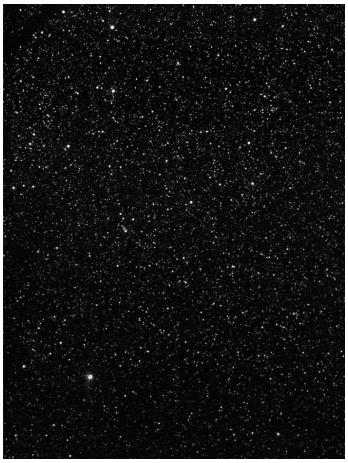

(d) EMS DX

Figure 2.24: Sample binary particle images for determination of seed properties.

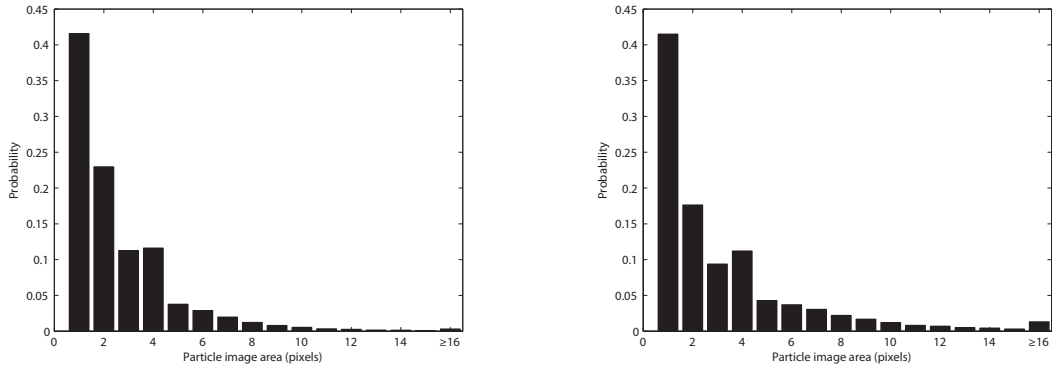

(a) Huntsman A-PP2

(b) Kenmira UV Titan

(c) Microgrit GB

(d) EMS DX

Figure 2.25: Probability density functions of particle image area for various flow seeds.

pattern, it scattered pulses of light. The frequency of these pulses was representative of the velocity. This light was collected and processed by a digital burst correlator (TSI IFA 655), which provided the desired temporal history of velocity data.

CHAPTER III

Characterization of the Flow and Flames

In this Chapter, the flow and flame properties are characterized. This is broken down into three parts. First, the exit flow conditions of the center burner are characterized using LDV measurements. Mean and fluctuation statistics are presented as well as the turbulence energy spectrum. Secondly, the flames are characterized in terms of progress variable, flame surface density, and velocity statistics. This characterization was performed using the CS-PIV. Finally, the co-flowing hot products are characterized. The flat, grid flames stabilized by the side burners did not allow for a detailed characterization of the exit conditions; the short, randomly flickering and moving flames prevented any useful diagnostic from being implemented at the exit. Details of the co-flow products downstream of these flames are presented in §3.3. It is these conditions in the products that should be matched for simulation purposes.

3.1 Characterization of the center burner exit flow

Characterization of the center burner exit conditions was made using LDV in the reacting flow. The reacting flow was used so that the mean shear profile was that of the actual tests. In a non-reacting case, the co-flow and main flow would not have the same downstream velocity profile and the mean shear would affect the velocity statistics. However, since the bulk velocity (volumetric flow rate) remained

unchanged for all CS-PIV test conditions, a single characterization was made using Case 2 ($\phi = 0.7$). Due to interference by the burner geometry, LDV measurements could not be made exactly at the burner exit plane. Hence, all exit flow characteristics were obtained at $x = 1.5$ mm.

The velocity profile was taken across the burner width (in the y-direction) at $z = 0$. Approximately 3×10^4 data points were taken at each location over a time span (Δt_{LDV}) ranging from 12 s to 30 s. The number of statistically independent data points (N) was given by:

$$N = \frac{\Delta t_{LDV}}{2\tau_L} \tag{3.1}$$

Hence, the 3×10^4 measurements provided between 3.3×10^3 and 8.3×10^3 independent data points.

Figure 3.1 shows the profile of the mean downstream velocity and its root-mean-squared fluctuations. As can be seen, the mean velocity profile was not a perfect top-hat shape. There were noticeable boundary layers and a non-uniform profile outside of the boundary layers. This non-uniformity was due to the slot grating used to generate the velocity fluctuations, which created distinct high- and low-speed regions 10 mm upstream of the exit plane. These regions had not completely been mixed by $x = 1.5$ mm. The rms velocity fluctuations also had a slightly non-uniform pattern, which closely resembled that of the mean velocity.

The one-dimensional energy spectrum (E_{11}) was calculated at based on the 2×10^5 data point set used to calculate the autocorrelation in §2.2.1. The LDV signal was first over-sampled and interpolated to a uniform data spacing, allowing it to be transformed to frequency space using a Fast Fourier Transform (FFT). The FFT of $u'(t)$ was then calculated, yielding $u'(k)$ where k is the wave number. This was then

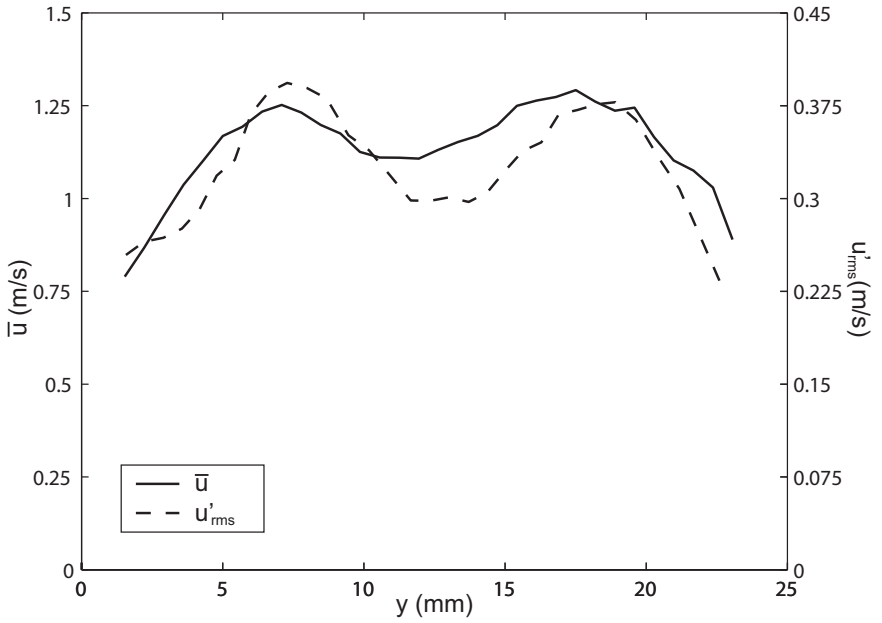

Figure 3.1: Velocity profiles across the burner in the y-direction at $x = 1.5$ mm, $z = 0$ mm taken using LDV.

multiplied by its complex conjugate ($u'^*(k)$) to yield the energy spectrum:

$$E_{11}(k) = u'(k)u'^*(k) \tag{3.2}$$

The spectrum is shown in Fig. 3.2. The energy has been normalized by $\varepsilon^{1/4}\nu^{5/4}$ according to its Kolmogorov scaling. As can be seen, the spectrum follows the shape that is typically measured and predicted [34]. However, due to the relatively low Reynolds number, the range of scales is small; there is only about one order of magnitude between the outer and inner scales. Furthermore, this limited range of scales practically eliminates the Kolmogorov inertial range in which the -5/3 scaling between energy and wave number occurs. Nevertheless, the measured spectrum demonstrates the expected features for low Reynolds number turbulence.

3.2 Characterization of the flames

That data reported in §3.1 are necessary to set the input conditions for simulations. Shown in Figs. 3.3-3.4 are global statistics of the flame and reacting flow field

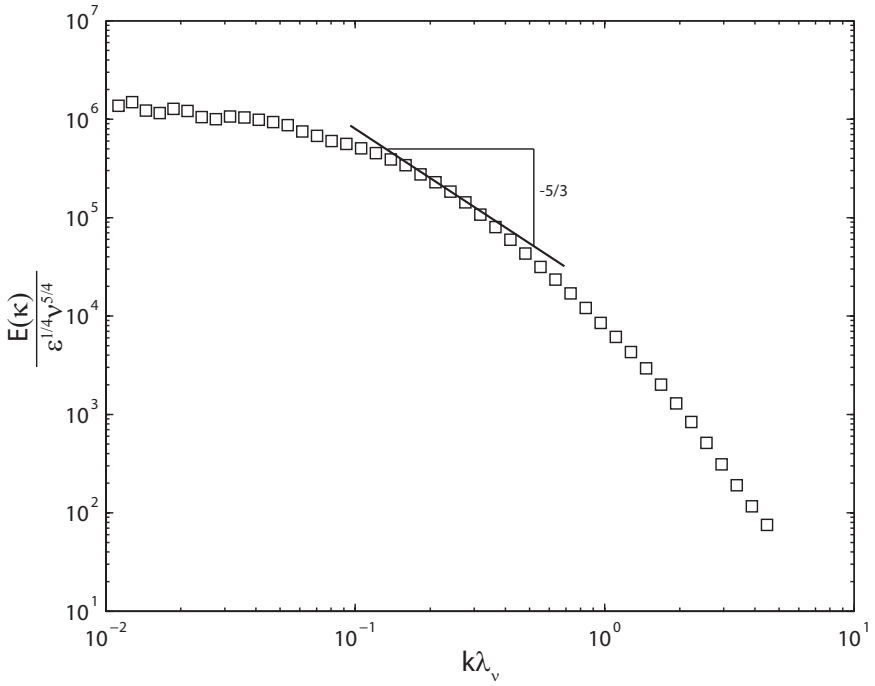

Figure 3.2: Longitudinal 1D energy spectrum at $(x, y, z) = (1.5, 0, 0)$ taken using LDV. Due to the low Reynolds number, the region exhibiting a -5/3 slope (the inertial range) is small.

necessary for validation of such simulations. These were obtained from 1000 CS-PIV images. The mean progress variable ($\overline{c}$) was calculated based on an infinitely thin flame assumption. That is, $c(t)$ was unity in the products and zero in the reactants, with the interface defined from as density gradient contour described in §2.5. The mean flame surface density was defined as the mean flame surface area per unit volume. For a two-dimensional measurement with an infinitely thin flame, $\overline{\Sigma}$ is the mean flame length per unit area. This was calculated by first dividing the domain into cells. In each cell, the mean flame length per unit area when the flame was in the cell was determined. This was then multiplied by the probability of the flame being in the cell to determine $\overline{\Sigma}$. Bell et al. [3] suggest the 2D method under-predicts $\overline{\Sigma}$ by 25% to 33%.

As can be seen in Fig. 3.3, the $\phi = 1.35$ flame was considerably taller than the $\phi = 0.7$ flame despite both possessing equal laminar flame speeds. This indicates

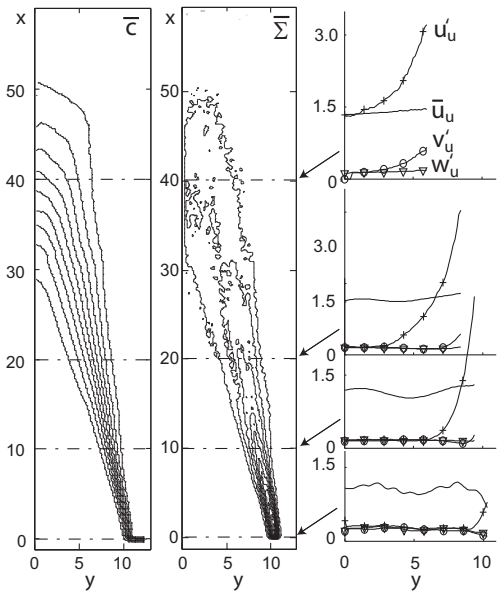

(a) Case 1 - $\phi = 0.6$

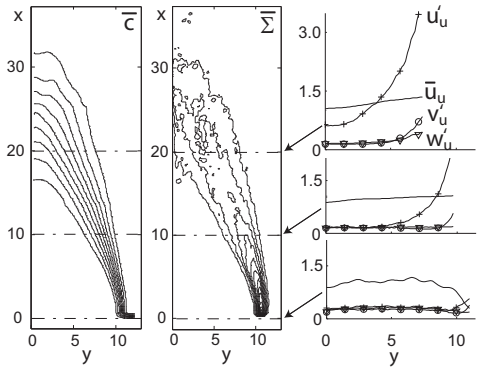

(b) Case 2 - $\phi = 0.7$

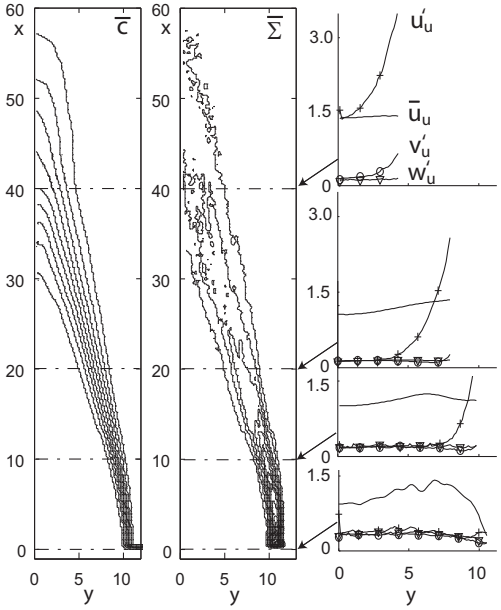

(c) Case 3 - $\phi = 1.35$

Figure 3.3: Mean reactedness ($\overline{c}$) contours are from 0.1-0.9 in 0.1 increments. Flame surface density ($\overline{\Sigma}$) contours range from 0.1 mm^{-1} to 1.2 mm^{-1} in 0.1 mm^{-1} increments. Velocity statistics are conditioned on the reactants. $(-) - \overline{u}_u$, $(+) - u'_u$, $(\circ) - v'_u$, $(\triangledown) - w'_u$. Velocities are in m/s. Positions are in mm.

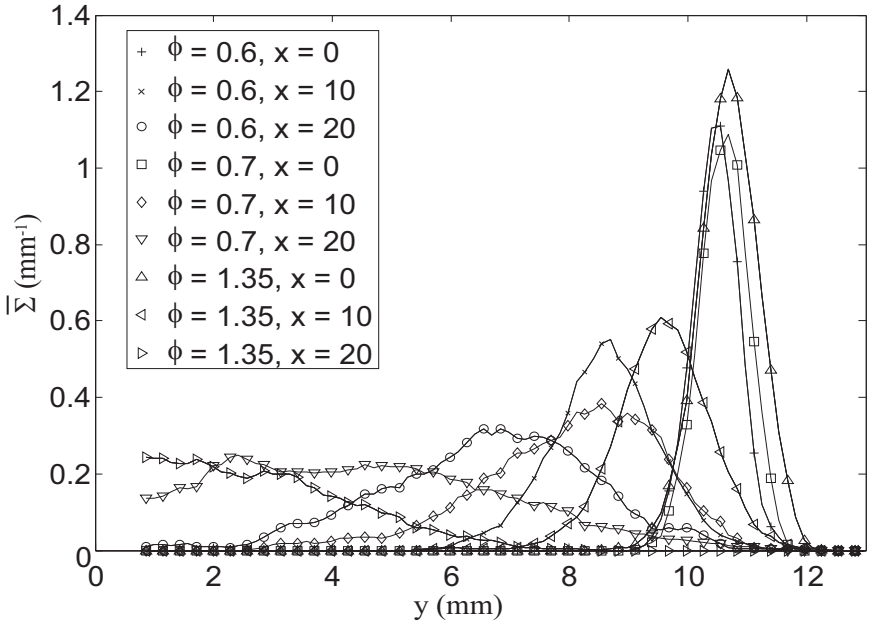

Figure 3.4: Profile of flame surface density at different downstream locations. The flame brush spreads at different rates for each flame.

that the diffusively stable nature of the rich flame significantly reduced the wrinkling and hence the turbulent burning velocity. The diffusively unstable ($\phi = 0.6$) flame was shorter than the $\phi = 0.7$ one despite having a significantly lower laminar flame speed. This further confirms that the details of the correlation between local burning rates and stretch are important in determining the global flame properties.

The velocity statistics shown in Fig. 3.3 were conditioned on the instantaneous unburnt reactants and reported for $\overline{c} < 0.9$. The average z velocity was found to be zero, indicating the flow was two-dimensional in the mean. The turbulence became isotropic a short distance downstream of the exit plane. As the flow proceeded into the flame brush, the fluctuations of the downstream component increased due to local acceleration from gas expansion.

Profiles of the flame surface density were taken in the transverse (y) direction at the heights (x) indicated in Fig. 3.4. Near the base of the flame, the brush was thin for all cases with a full width at half maximum ranging from 1 mm to 1.1 mm. At

Case	ϕ	u'/s_l^0	s_t (m/s)	s_t/s_l^0
1	0.6	3.1	0.25	2.4
2	0.7	1.7	0.39	2.1
3	1.35	1.8	0.29	1.5

Table 3.1: CS-PIV turbulent burning velocities.

downstream locations, the flame brush spread and the flame surface was distributed over a greater volume than at upstream locations.

The turbulent burning velocity for all cases was computed from the $\overline{c} = 0.5$ contour. Filatyev et al. [42] showed that the turbulent burning velocity, defined in terms of the global consumption speed, can be determined from the mean planar measurements as:

$$\overline{s}_t = \frac{\dot{m}_u}{\rho_u \overline{A}_f} \tag{3.3}$$

where $\overline{A}_f$ is the area of the $\overline{c} = 0.5$ contour. This can be approximated from the flame perimeter in the planar measurements (P_f) as:

$$\overline{A}_f = \overline{P}_f L_B \tag{3.4}$$

where L_B is the length of the burner.

The turbulent burning velocities computed using this method are presented in Table 3.1. As can be seen, the increase in burning velocity of the turbulent flame relative to the laminar flame is highly dependant on the equivalence ratio. This is true even at the same turbulence intensity level and in contrast to classical models that predict $s_t/s_l^0 = f(u'_{rms}/s_l^0)$ only. These differences are attributed to the differences in the response of the local flame speed to stretching, that is, preferential diffusion effects.

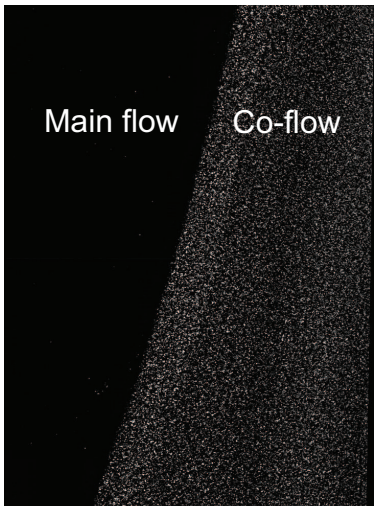

Figure 3.5: Sample particle image with co-flow stream seeded and main-flow stream unseeded. There is a sharp distinction at the interface between the fluids.

3.3 Characterization of the co-flow

The purpose of the co-flow was to reduce the shear between the products of the central burner and the surrounding air. Such a mean shear would generate additional turbulence and affect the flame dynamics. Hence, it was desired to closely match the downstream velocity in the products of the central burner to that of the co-flow burners. The co-flow burners stabilized short, grid flames that were flat in the mean. The flames were observed to have a mean height of less than 2 mm. Due to interference by the burner geometry, it was not possible to obtain accurate measurements in the reactants of these burners. However, it is the downstream profile in the products of these flames that should be matched in simulations.

To characterize the co-flow, the side burners were seeded and CS-PIV measurements made. The seed levels were such that there was optimal seeding in the products. For these tests the main flow was not seeded, enabling fluid from each source to be identified. A typical particle field is shown in Fig. 3.5. As can be seen, there was a clear distinction between fluid from the co-flow (seeded) and that from the center

burner (unseeded); there did not appear to be significant mixing of the streams at any instant or location. The location of the interface between the two fluids was determined by employing the flame finding method of §2.5; the maximum particle image gradient contour was identified. Once again, the profile of particle image density normal to this contour had a S-shaped curve and the maximum gradient occurred approximately where the particle image density dropped by 50% from the co-flow stream. To identify the mean location of the interface, all points on the co-flow side of the contour were assigned a value $\psi(t) = 1$ and all points on the main-flow side were assigned a value of $\psi(t) = 0$. The mean of 1000 images was taken to determine the mean mixing field ($\overline{\psi}$). These are presented in Fig. 3.6. In all cases, the mean contour, $\overline{\psi} = 0.5$, had a similar profile.

To characterize the relevant velocity field, the velocity statistics along these contours, conditioned on both the co-flow (subscript C) and main-flow (subscript M) fluids, were computed. Velocity statistics from the main-flow stream at $\overline{\psi} = 0.5$ were determined by removing the seed from the co-flow and heavily seeding the main-flow. Figure 3.7 shows these along with the contour shape for each case. As can be seen, the velocity profiles closely match. In some cases, the co-flow and main-flow profiles crossed. However, this agreement was the optimal that could be achieved with the employed geometry. Furthermore, there are some noticeable steps at certain locations in the velocity profiles. Since the flames were larger than the measurement field of view, the presented data is a composite image taken from different data sets at different downstream locations. The discontinuities are indicative of either non-converged statistics, slight misalignment of the fields of view, or minor changes in the overall flow-field between experimental runs. However, such discrepancies do not affect any of the subsequent analysis.

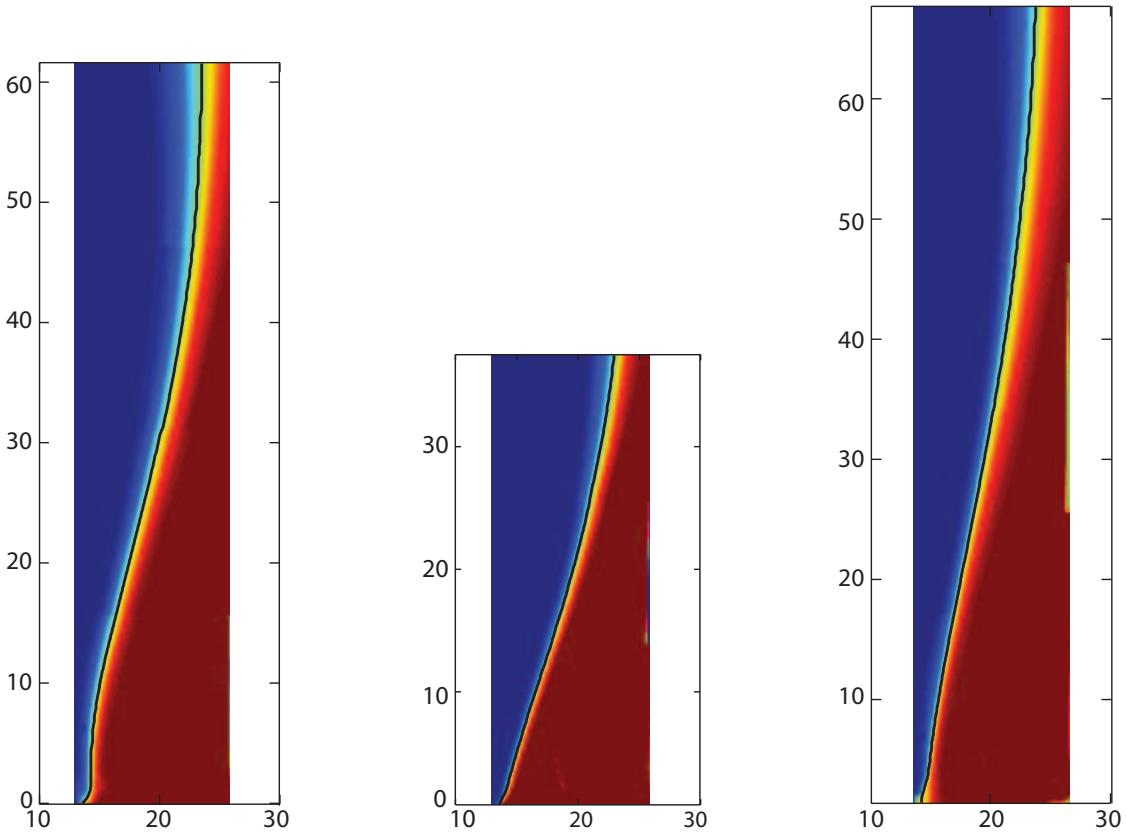

(a) Case 1 - $\phi = 0.6$ (b) Case 2 - $\phi = 0.7$ (c) Case 3 - $\phi = 1.35$

Figure 3.6: Mean mixedness ($\overline{\psi}$) fields for the CS-PIV test conditions with red indicating the co-flow ($\overline{\psi} = 1$) and blue indicating the main-flow ($\overline{\psi} = 0$). The mean contour ($\overline{\psi} = 0.5$) is shown by the thick black lines.

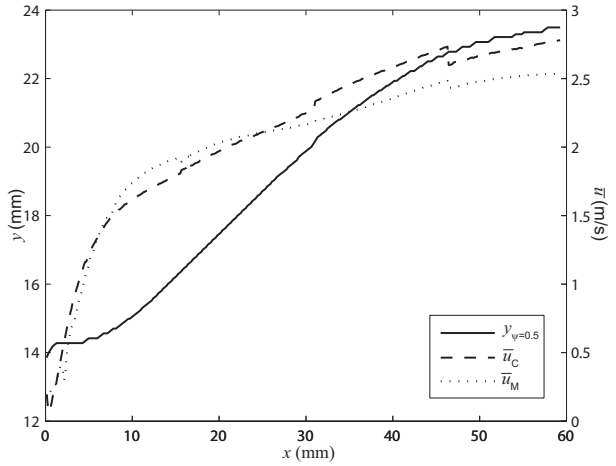

(a) Case 1 - $\phi = 0.6$

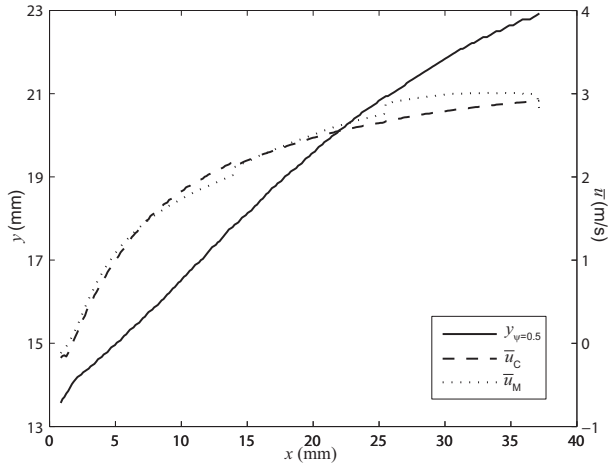

(b) Case 2 - $\phi = 0.7$

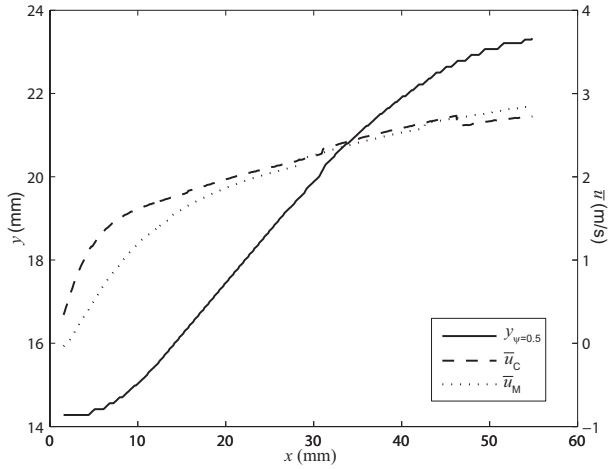

(c) Case 3 - $\phi = 1.35$

Figure 3.7: Mean downstream velocity profiles along the $\overline{\psi} = 0.5$ contour for the CS-PIV test cases, conditioned on the main-flow and co-flow. The shape of the $\overline{\psi} = 0.5$ contours is also plotted.

CHAPTER IV

The Mechanisms of Flame Strain and Wrinkling

In this Chapter, phenomenological descriptions of the straining and wrinkling processes in a turbulent premixed flame are presented. These descriptions were developed based on experimental measurements from the CS-PIV diagnostic and theoretical analysis. However, proper use of the experimental measurements required consideration of a number of factors.

One of the most important aspects of turbulence-flame interactions is that they exert tangential strain rates (a_t) on the flame, which generates flame surface area. Hence, accurate computation of this quantity is necessary. In the laminar flamelet regime the flame is considered to be an infinitely thin interface and the strain rate on a particular iso-surface representing the flame is required. This in turn requires accurate computation of the topography and velocity gradients at this surface. As seen in §2.5, the PIV particle images can be used to accurately measure the topography. However, the high gradients associated with the flame front can present significant problems for computation of the velocity derivatives. Hence, numerical considerations for these derivatives are first presented.

Another issue that had to be addressed was the relationship between 2D measurements and 3D phenomena. The CS-PIV diagnostic provided planar, three-

component measurements of turbulence-flame interactions that were, in reality, fully three-dimensional. These data were utilized for this analysis due to their higher accuracy, better resolution, and larger field of view. However, restrictions needed to be placed on the CS-PIV data such that only segments (spatial and temporal) were used in which 3D effects were expected to be small. These restrictions were developed based on theoretical considerations and the OPCS-PIV measurements at image plane 1. They are presented in §4.2.

With the numerical methods and restricted data set in hand, turbulence-flame interactions were first analyzed in the context of the canonical geometry; the turbulence field was characterized solely by 'vortices'. However, the vorticity field was found to be inadequate for predicting either a_t or the flame wrinkling. Hence, a theoretical analysis of the interaction between velocity gradients and the flame surface was conducted. This indicated that the fluid dynamic strain rate field is essential for describing turbulence-flame interactions. From this analysis, new phenomenological descriptions of the straining and wrinkling processes were developed based on both the $\underline{S}$ and $\vec{\omega}$ fields. These descriptions were confirmed by subsequent analysis of the measured data.

Finally, the statistics of the flame strain rate and curvature are presented. It is shown that these were distributed over a range of positive and negative values. Furthermore, the mean curvature was positive in many cases. Both of these observations are in conflict with standard modeling assumptions. Hence, the implications for modeling turbulent premixed flames are discussed.

Case	$\Delta\delta(mm)$
1	0.65
2	0.60
3	0.60

Table 4.1: Shift from maximum density gradient iso-contour to leading edge iso-contour based on Chemkin simulations.

4.1 Calculation of velocity derivatives on the flame front

Measurement of the tangential strain rate on the flame surface is essential for analysis of turbulence-flame interactions. It has been shown that the strain rate on the flame is given by the equation [17]:

$$a_t = -\hat{n} \cdot (\hat{n} \cdot \nabla)\, \vec{u} + \nabla \cdot \vec{u} \tag{4.1}$$

Hence, accurate computation of a_t required accurate computation of the velocity derivatives at the flame surface. However, obtaining these from experimental data required careful consideration. Inside the flame front, thermophoretic and acceleration effects caused significant lag in the PIV particles [104]. This lag introduced errors in the velocities computed within the flame front, which could translate to errors in the velocity derivatives and a_t. However, proper choice of the flame iso-surface at which the derivatives were calculated was used to minimized this effect.

In order to eliminate the effects of particle lag on the measured velocities, strain rate measurements were made at the leading edge of the flame where the accumulated particle lag due velocity and temperature gradients was small. Hence, strain rates were measured on a contour separated from the maximum density gradient contour by a set distance, $\Delta\delta$, towards the reactants in the normal direction. These distances corresponded to the distance between the location of maximum density gradient and the leading edge of the flame as computed by Chemkin using the GRIMech 3.0 mechanism for each of the flames. They are listed in Table 4.1.

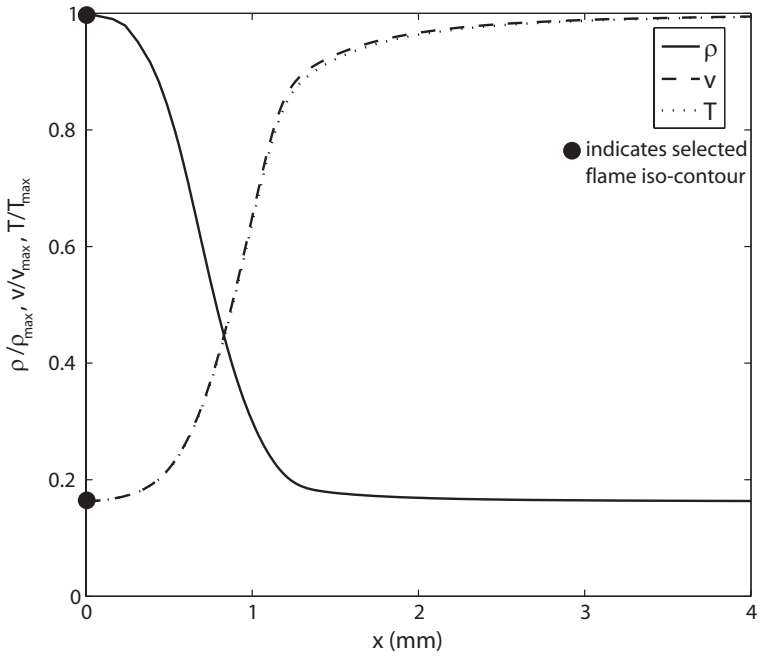

Figure 4.1: Profiles of density, velocity, and temperature for Case 2 ($\phi = 0.7$) as computed by Chemkin.

Profiles of the temperature, velocity, and density for Case 2 ($\phi = 0.7$) are presented in Fig. 4.1. These have been normalized by their maximum values. At the computed leading edge contour, the temperature and velocity gradients were both low relative to those within the flame. The accumulated particle lag due to thermophoretic effects at this location were too small to be treated with the classical analysis of Sung and Law [103, 104] and hence ignored. The velocity gradient was less than 25 s^{-1}, which is significantly less than those associated with the turbulence (see for example §4.5.1). Since the selected particles accurately followed the highest turbulent velocity gradients, they should also accurately follow the flow field at this flame location. Furthermore, this velocity gradient was associated with the divergence term in Eq. 4.1; it was associated with gas expansion through the flame. However, since it was considerably lower than the gradients associated with the turbulence, the divergence component of a_t was expected to be small.

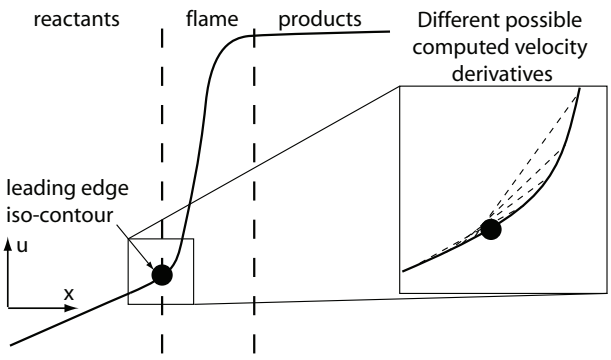

Figure 4.2: Errors induced in computed velocity derivatives at the leading edge caused by the proximity of the flame. As the downstream (product side) data point approaches the leading edge, the accuracy of the derivative improves.

The presence of the flame front also required careful design of the numerical method used to compute a_t. Velocity data were measured on a regular square grid, while the flame was defined freely in space. Hence, the velocities had to be interpolated to the flame surface. At the flame density iso-surface selected, neither gas acceleration due to expansion or thermophoretic particle lag affected the measured velocities. However, significant error to the numerical derivatives could be induced due to the proximity of this expansion related high acceleration region. The mechanism for this is demonstrated in Fig. 4.2. At the flame iso-surface selected, the numerical derivative computed using nodes well into the flame front would severely over predict the actual magnitude of the gradient.

It therefore was necessary to both interpolate velocities and construct derivatives using selected velocity nodes that often formed irregular patterns. Observation showed that the leading edge of the gas acceleration through the flame was always greater than 100 μm downstream of the selected flame surface. Hence, usable nodes on the product side were restricted to those within 100 μm. All points on the reactant side were usable. This irregular node pattern and freely defined flame required a triangular mesh on which to compute the velocity derivatives. These derivatives

were computed at the triangle node corresponding to the flame using a second order accurate inverse distance weighted method based on the gradients over the faces of the adjacent triangles[2].

4.2 The relationship between 2D and 3D measurements

As mentioned previously, the w-velocity component measured with the CS-PIV system did not provide any additional terms of $\underline{S}$ or $\vec{\omega}$. However, this component and its in-plane derivatives did allow restriction of the usable CS-PIV data set to cases when the unknown terms and other three dimensional effects were expected to be small. That is, for both the phenomenological and statistical analyzes, temporal and spatial segments of the data set were isolated in which the planar measurements were an accurate representation of the entire flow field. With these restrictions, the planar computation of the stain rate and curvature stretch rate were found to reflect their three-dimensional equivalents with acceptable.

4.2.1 Restriction of the CS-PIV data set

The first task was to eliminate data segments in which there was large out-of-plane convection. Such convection would appear as erroneous evolution of both the turbulence and flame shape. Hence, interaction events were selected during which $|w| < \epsilon_1 |\vec{u}|$. All ϵ_i factors are small numbers for which appropriate values will be determined below.

Additional restrictions were needed to reduce the effects of the out-of-plane velocity derivatives. These manifested themselves as unresolved terms in $\underline{S}$ and $\vec{\omega}$, namely S_{13}, S_{23}, ω_1, and ω_2. Furthermore, while $S_{33} = \frac{\partial w}{\partial z}$ could be inferred using the continuity equation, the equation for a_t includes a term of the form $n_3^2 S_{33}$. Since n_3 was unknown, the influence of this term was reduced if S_{33} was small.

To minimize the effects of the unresolved shear strain rates and vorticity, the measured in-plane derivatives of w were employed. For S_{i3}, the usable data set was restricted to cases where:

$$\left|\frac{\partial w}{\partial x_i}\right| < \epsilon_2 \, |\underline{S}| \tag{4.2}$$

For ω_i the restriction was based on:

$$\left|\frac{\partial w}{\partial x_j}\right| < \epsilon_2 \, |\vec{\omega}| \tag{4.3}$$

where $i = \{1, 2\}$ for $j = \{2, 1\}$. The same value of ϵ_2 was found to be sufficient for all parameters.

To limit the influence of S_{33}, the continuity condition was used. In the reactants and at the flame iso-surface selected (leading edge), there was nearly zero divergence of the velocity field. This allowed data segments with small S_{33} to be identified. That is, data segments were selected in which:

$$|S_{33}| = \left|\frac{\partial w}{\partial z}\right| = \left|\frac{\partial u}{\partial x} + \frac{\partial v}{\partial y}\right| < \epsilon_3 |\underline{S}| \tag{4.4}$$

It now remained to determine the appropriate ϵ_i such that the unresolved components of $\underline{S}$ and $\vec{\omega}$ were small compared to the resolved components. This was done using the OPCS-PIV measurements in image plane 1 (horizontal plane). The inaccuracies inherent to this system were largely associated with the downstream evolution of the turbulence. However, these errors did not effect this analysis as only the directly measured data at image plane 1 were used. Errors in these data were associated only with the modified Taylor's hypothesis and the PIV itself. The restriction process is described in detail only for S_{23}, but was identical for all terms. The statistics were based on approximately 1.5×10^6 data points.

The restriction parameter, ϵ_2, was based on the joint PDF of $\frac{S_{23}}{|\underline{S}|}$ and $\frac{\partial w/\partial y}{|\underline{S}|}$. This is shown in Fig. 4.3. As can be seen from 4.3(b), there is a distinct positive correlation

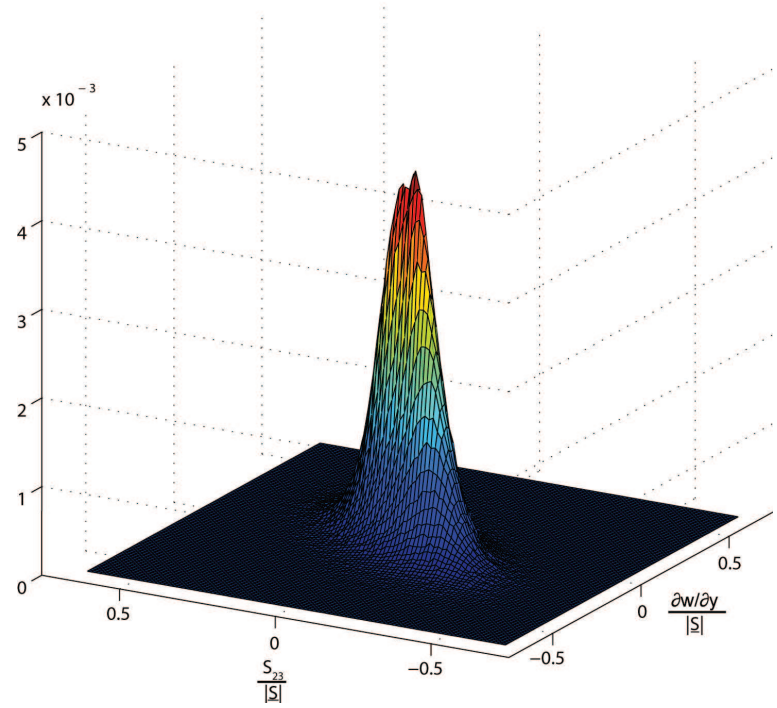

(a) JPDF

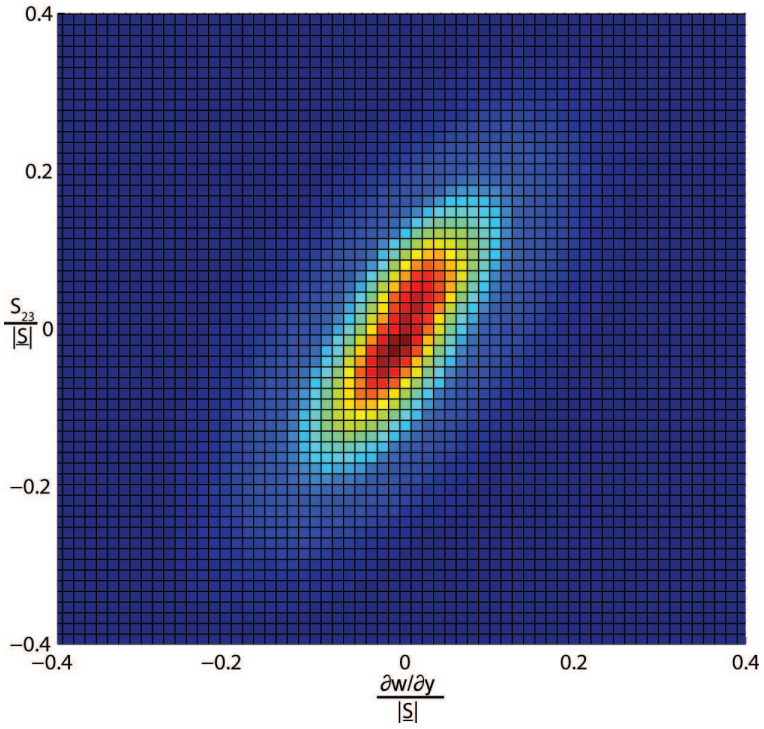

(b) Top view

Figure 4.3: Joint probability distribution function of the strain rate component S_{23} and velocity gradient $\frac{\partial w}{\partial y}$ normalized by strain rate magnitude $|\underline{S}|$. There is a positive correlation between the two quantities.

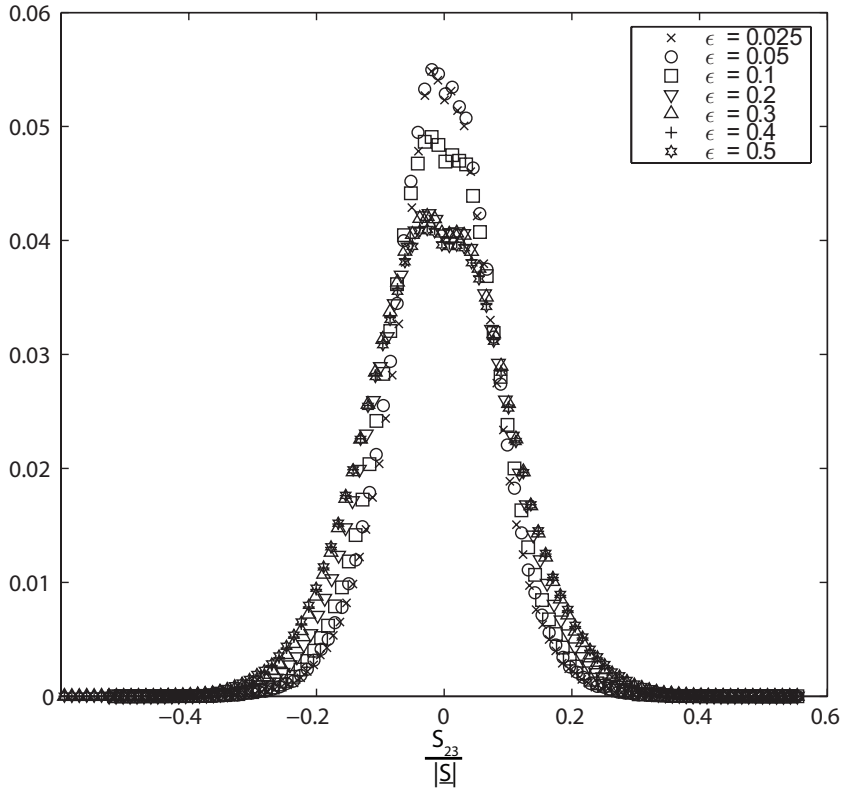

Figure 4.4: Conditional PDF of $P\left(\frac{S_{23}}{|S_{ij}|} : \left|\frac{\partial w}{\partial y}\right| < \epsilon\,|S_{ij}|\right)$ for various ϵ_2.

between the two quantities. Furthermore, as $\frac{|\partial w/\partial y|}{|\underline{S}|} \to 0$, the probability of having large $\frac{|S_{23}|}{|\underline{S}|}$ also decreases.

The appropriate ϵ_2 was selected by iteration. The conditional PDF:

$$P\left(\frac{S_{23}}{|\underline{S}|} : \left|\frac{\partial w}{\partial y}\right| < \epsilon_2 |\underline{S}|\right) \tag{4.5}$$

was constructed for a variety of ϵ_2. These are shown in Fig. 4.4. From these, the probability of $|S_{23}| < 0.05\,|S|$ and $|S_{23}| < 0.1\,|S|$ were plotted as a function of ϵ. As shown in Fig. 4.5, as ϵ decreased the probability of small $|S_{23}|$ increased. For $\epsilon = 0.05$, over 97% of the cases had $|S_{23}| < 0.1|\underline{S}|$ and about 80% had $|S_{23}| < 0.05|\underline{S}|$. At this value of ϵ_2, about 25% of the total data set was usable. Hence, a value of $\epsilon_2 = 0.05$ was used for S_{23}.

A similar process was performed for the other unresolved components of $\underline{S}$ and $\vec{\omega}$.

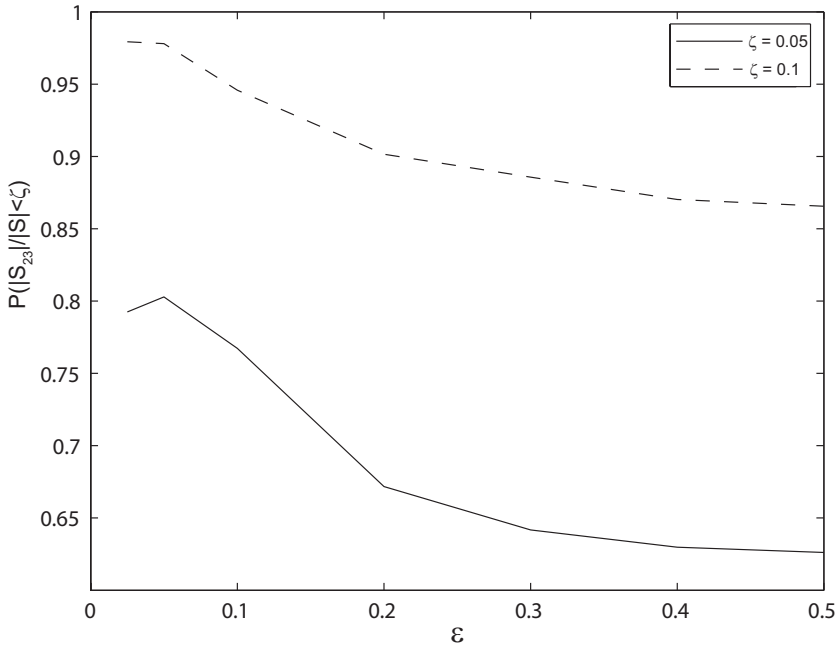

Figure 4.5: Probability of small $|S_{23}|$ versus ϵ_2.

Similar statistical results were found using $\epsilon_2 = \epsilon_3 = 0.05$ for all terms. Hence, this value was used to restrict the data set to cases with small out-of-plane contributions for $\underline{S}$ and $\vec{\omega}$.

It was also found that, since there was no mean out-of-plane velocity, regions with low gradients of w also equated to regions of low magnitude of w. Nevertheless, an additional restriction of $|w| < 0.1|\vec{u}|$ ($\epsilon_1 = 0.1$) was implemented. Under this constraint, the turbulent structures could convect a maximum of approximately 1.8 mm out-of-plane as they traversed the entire field-of-view. However, it was found that $|w| < 0.025|\vec{u}|$ in 75% of the data set adhering to the aforementioned velocity gradient restrictions. With the simultaneous implementation of all restrictions, approximately 10% of the recorded data set was usable.

4.2.2 Accuracy of using planar a_t and C measurements

Within the restricted data set, it was necessary to assess the influence of the three-dimensional terms on the planar measurements of the strain rate and curvature

stretch rate. For the strain rate, the influence of the 3D terms was reduced both by the limitations on the velocity gradients and by the natural orientation of the flame. Their influence on the curvature stretch rate was also somewhat reduced due to this orientation.

From Eq. 4.1, it is apparent that the strain rate was largely determined by the product of the flame surface normal vector and the velocity gradient tensor; at the leading edge isocontour the velocity field divergence was low (see §4.1). These product terms were of the form $n_i n_j \frac{\partial u_i}{\partial x_j}$. Hence, all out-of-plane velocity derivatives, which were unknown, were multiplied by the out-of-plane flame orientation, n_z. This out-of-plane orientation was also unknown. However, due to the geometry of the flame, n_z was considerably smaller than the other components of $\hat{n}$. That is, in the laminar case the flame studied would have $n_z = 0$; the slot burner would produce a 2D flame, invariant in the z-direction. Non-zero values in the turbulent flame were associated with regions out-of-plane curvature. Conversely, both n_x and n_y have mean values differing from zero. Throughout the turbulence-flame interactions, strain rates exerted by the fluid in these directions had a much more significant effect on the flame than those in the z-direction. Furthermore, there are terms in the equation for a_t that involve n_z (unresolved) and the in-plane derivatives of w (resolved). However, due to the above restrictions on the velocity gradient field the influence of these terms was significantly reduced.

The significance of $n_3$was assessed in the restricted data set using the OPCS-PIV data. The three component normal vector was calculated from the two perimetrically

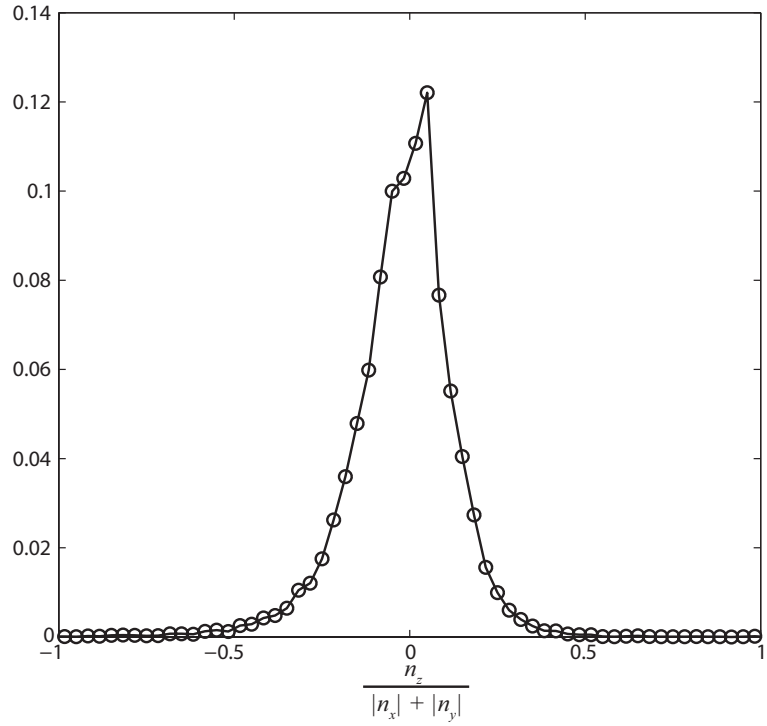

Figure 4.6: PDF of the out-of-plane flame orientation (n_z) for the restricted data set. n_z was considerably smaller than the remaining components.

defined space curves representing the flame in each image plane using the equations:

$$|\hat{n}| = \sqrt{n_x^2 + n_y^2 + n_z^2} = 1 \tag{4.6}$$

$$\frac{n_x}{n_y} = \frac{n_{1x}}{n_{1y}} \tag{4.7}$$

$$\frac{n_z}{n_y} = \frac{n_{2z}}{n_{2y}} \tag{4.8}$$

where $\hat{n}_1$ and $\hat{n}_2$ were the 2D normal vectors in image planes 1 and 2 respectively. Hence, the necessary information to reconstruct the three-component normal was only available at a single spatial location for each OPCS-PIV image. That is, there was only one location where the flame front contours crossed. This provided the full flame orientation at this point. Data from 20000 vector fields were used to compile the statistics. The restricted set contained approximately 2200 of these and all PDFs below were constructed using this set.

Presented in Fig. 4.6 is the PDF of $\frac{n_z}{|n_x|+|n_y|}$. As can be seen, n_z was distributed

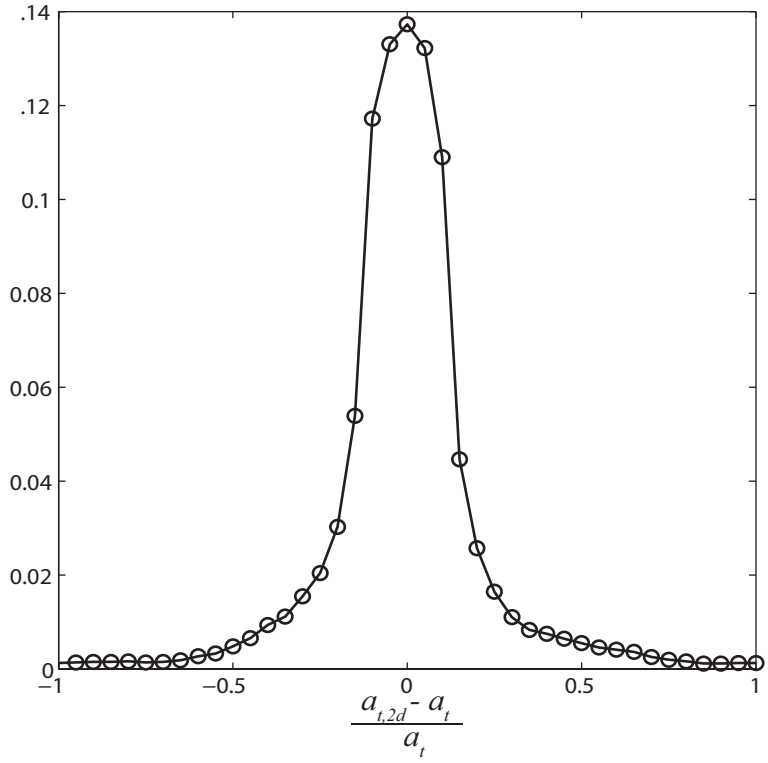

Figure 4.7: PDF of the strain rate that could be resolved using planar measurements relative to the full 3D measurements.

about zero. Furthermore, n_z was considerably less than the other components, with a mean relative magnitude of $\overline{\left(\frac{|n_z|}{|n_x|+|n_y|}\right)} = 0.15$.

To determine the influence of the velocity field restrictions and flame orientation on the strain rate, the PDF of $\frac{a_{t2D}-a_t}{a_t}$ was computed at the flame intersection point. Here, a_{t2D} represents the portion of a_t that would be computed using the planar CS-PIV measurements only. This PDF is shown in Fig. 4.7. Integrating the area under the PDF indicated that over 80% of the full 3D strain rate was captured by the planar measurements over 80% of the time. Hence, the planar measurements were found to accurately represent the strain rate on the flame.

The significance of the out-of-plane flame curvature was also assessed. The curvatures in image planes 1 (C_1) and 2 (C_2) at the intersection point were computed. For the majority of the curvature to be captured by the CS-PIV, it was desired that

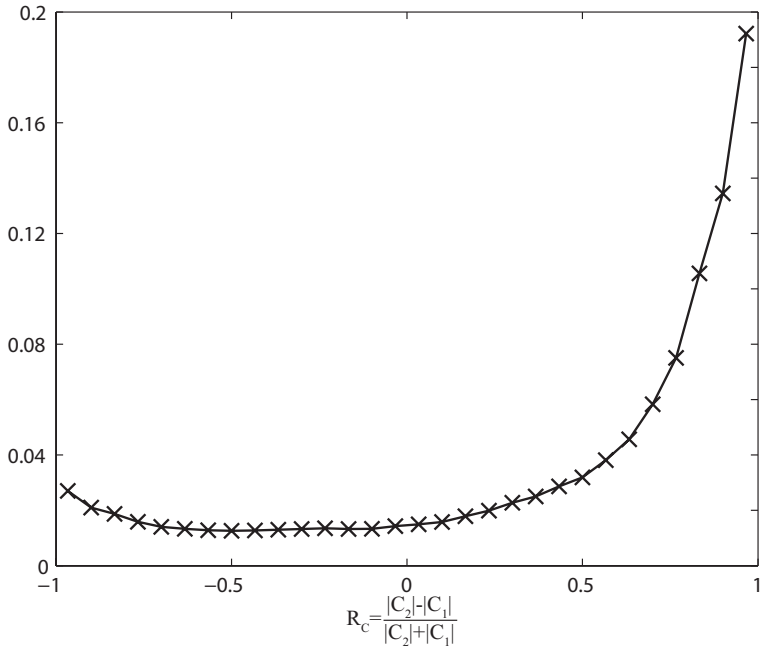

Figure 4.8: PDF of the horizontal curvature (C_2) relative to the vertical curvature (C_1) in terms of R_C. The horizontal was generally smaller than the vertical in the restricted data set.

$|C_2| \gg |C_1|$. This can be evaluated by considering the ratio:

$$R_C = \frac{|C_2| - |C_1|}{|C_2| + |C_1|} \tag{4.9}$$

Positive values of R_c indicate that the curvature was predominantly in the vertical plane. Negative values indicate predominantly horizontal plane curvature. The limits of positive and negative one indicate purely vertical and horizontal curvature respectively. The PDF of this ratio was computed and is shown in Fig. 4.8. As can be seen, the curvature in image plane 2 was generally greater than that in plane 1 for the restricted data set. The mean value was $\overline{R_C} = 0.44$, yielding $\overline{|C_2|} = 2.6\overline{|C_1|}$. The curvature stretch rate measured by the CS-PIV therefore captured the majority of the total. However, unlike the strain rate, there were still a number of cases where $|C_1|$ was equal to or larger than $|C_2|$.

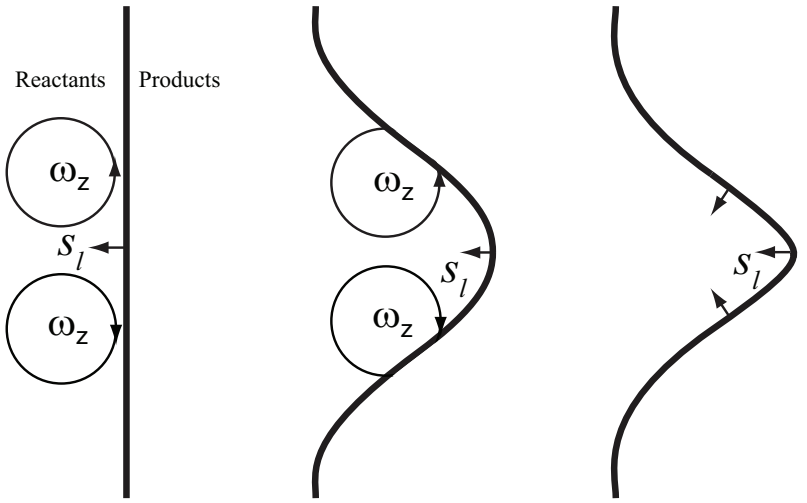

(a) t_0 (b) t_1 (c) t_2

Figure 4.9: Canonical flame-vortex interaction.

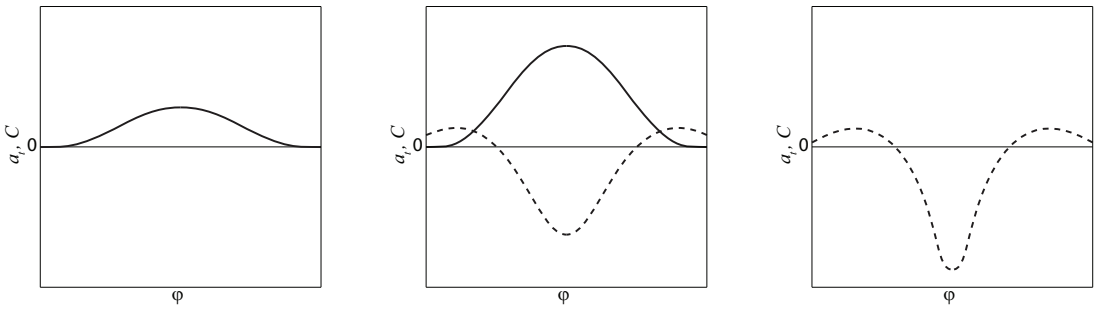

(a) t_0 (b) t_1 (c) t_2

Figure 4.10: Strain rate (–) and curvature (- -) profiles expected during the canonical flame-vortex interaction of Fig. 4.9.

4.3 Stretch characterized by vorticity

In order to investigate turbulence-flame interactions, Poinsot et al. [91] considered the configuration shown in Fig. 4.9 in which a pair of two-dimensional vortices (structures of concentrated vorticity) were impinged on a laminar flame. The expected profiles of the strain rate and flame curvature versus distance along the flame surface (φ) are shown in Fig. 4.10. As the vortex pair interacts with the flame, extensive strain rate is exerted and a negative curvature wrinkle forms. The wrinkle then forms a cusp due to kinematic resonation.

This configuration has been studied in great detail, both computationally and experimentally. Meneveau and Poinsot [74] analyzed interactions over a range of vortex sizes and strengths to deduce the net effect of an entire turbulent flow. Colin et al. [28] and Charlette et al. [22] extended this work by considering additional parameters and different methods of summing the scales. Furthermore, it is a popular configuration for the study of flame quenching, baroclinic effects on vorticity, and flame stability [77, 99]. Extensive reviews of the canonical flame-vortex interaction are provided by Renard et al. [96] and Kadowaki and Hasegawa [56].

Hence, to begin, turbulence-flame interactions were investigated in a manner consistent with the classical studies listed above. That is, the turbulence field was viewed in terms of the vorticity. In this view, coherent vortical structures interacted with the flame and the stretching was characterized by the properties of these structures.

For all data presented below, Case 2 ($\phi = 0.7$) was used. The Lewis number of the deficient reactant in this mixture is approximately unity, indicating equal diffusivity between the reactant and heat. While there is significant scatter in measured Markstein numbers, the $\phi = 0.7$ case falls within the commonly reported range of Ma ≈ 0 for methane-air flames, indicating that preferential diffusion effects were small[78]. Hence, the propagation speed of the flame was expected to remain relatively constant, irrespective of the local stretch rate.

A typical instantaneous vorticity field measured using the CS-PIV is shown in Fig. 4.11. Contours of ω_z are plotted between -1200 s^{-1} (blue) and 1200 s^{-1} (red). The flame is represented by the thick black line and the reactants are on the left. As can be seen, the vorticity field was very complex. It was both unfeasible and inappropriate to analyze the interaction of such a field with the flame in the context of the canonical geometry. Hence, isolated temporal and spatial segments were extracted from the

data set in which the local turbulence-flame interaction resembled the canonical configuration. That is, counter-rotating pairs of vortical structures exerting extensive strain on the flame were identified. These interactions were analyzed to evaluate the relevance of the canonical geometry to real turbulent flames.

4.3.1 Stretching by vortex pairs

A turbulence-flame interaction resembling the canonical configuration is presented in Fig. 4.12. In this time sequence, two counter-rotating vortical structures interacted with the flame, the flame was strained, and a negative curvature wrinkle was formed. Profiles of the instantaneous strain rate and curvature on the flame surface are shown in Fig. 4.13. As can be seen, the interaction was qualitatively very analogous to that expected from the canonical configuration shown in Figs. 4.9 and 4.10. However, there was one notable difference; the strain rate was exerted before the wrinkle formed. This indicates that the straining and wrinkling processes might be somewhat distinct. It is also noted that there was considerable strain rate exerted before the vortical structures appeared to interact and the maximum strain rate did not occur when the maximum vorticity was on the flame contour. Hence, the geometry of the vortical structures does not appear to characterize the strain rate on the flame.

Furthermore, analysis of multiple interactions indicated that the strength of the straining and wrinkling processes were not well characterized by the vorticity field. To demonstrate this, Figs. 4.14 and 4.15 present two further interactions resembling the canonical configuration. In all three cases it can be visually observed that the turbulent structures had similar strengths and scales. These will be further quantified below. However, it was also apparent that the interactions had very different effects on the flame; different sized wrinkles were produced.

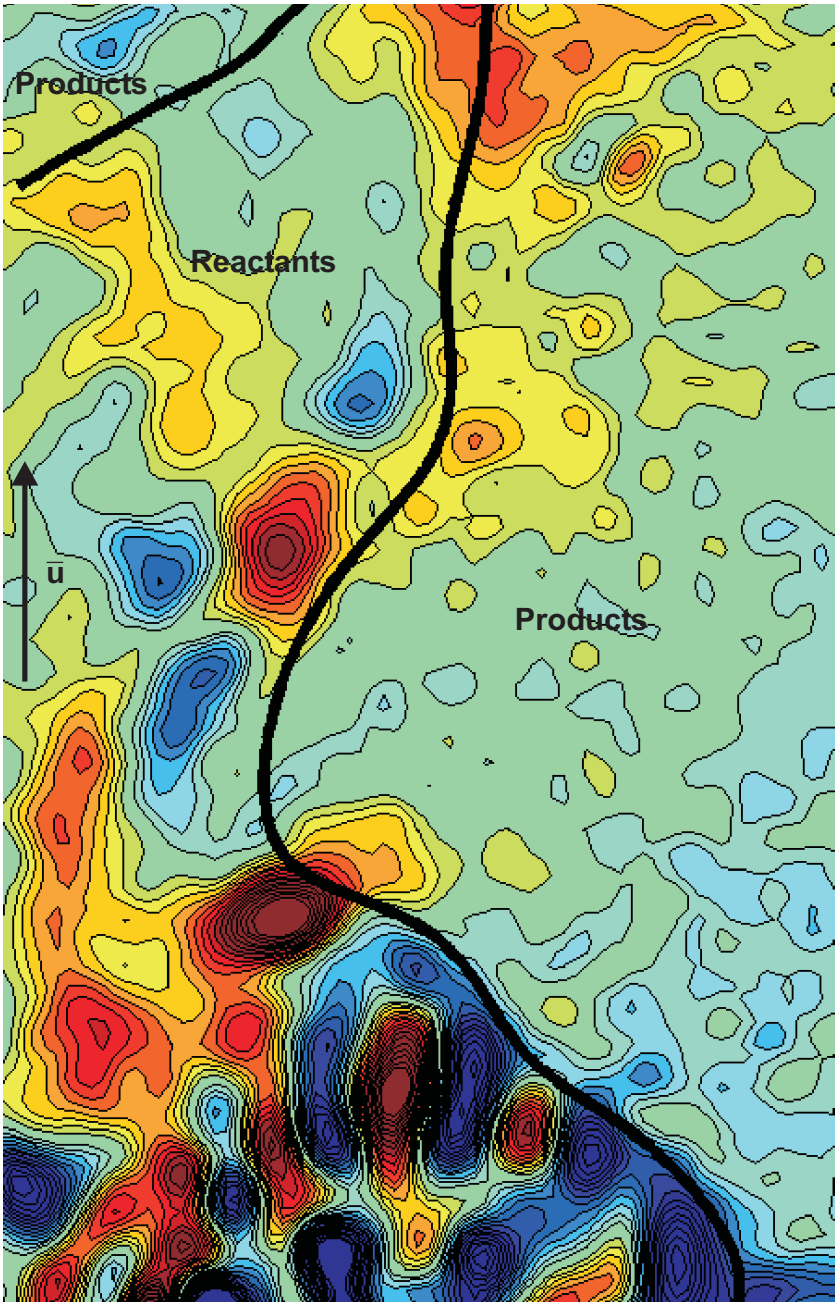

Figure 4.11: A typical vorticity field interacting with the flame surface. The vorticity has a complex geometry and cannot generally be analyzed in the context of the canonical configuration. Contours of vorticity between -1200 s^{-1} (blue) and 1200 s^{-1} (red). Flame is represented by the thick black line. Flow is from bottom to top and the field of view is 11 mm x 17 mm.

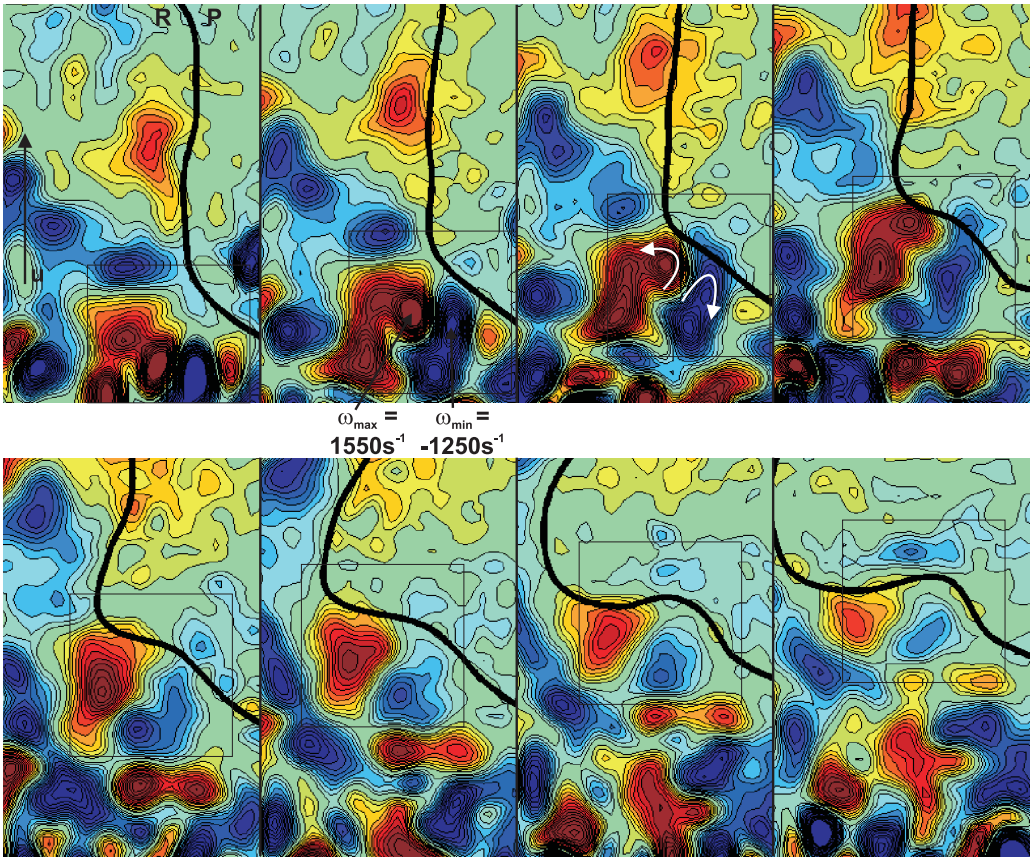

Figure 4.12: Interaction of a counter rotating pair of vortical structures with the flame. A negatively curved wrinkle is created. Contours of vorticity between -1200 s^{-1} (blue) and 1200 s^{-1} (red). Flame is represented by the thick black line. Flow is from bottom to top, reactants are on the left, the field of view is 6 mm x 9.5 mm, and the time between frames is 0.9 ms.

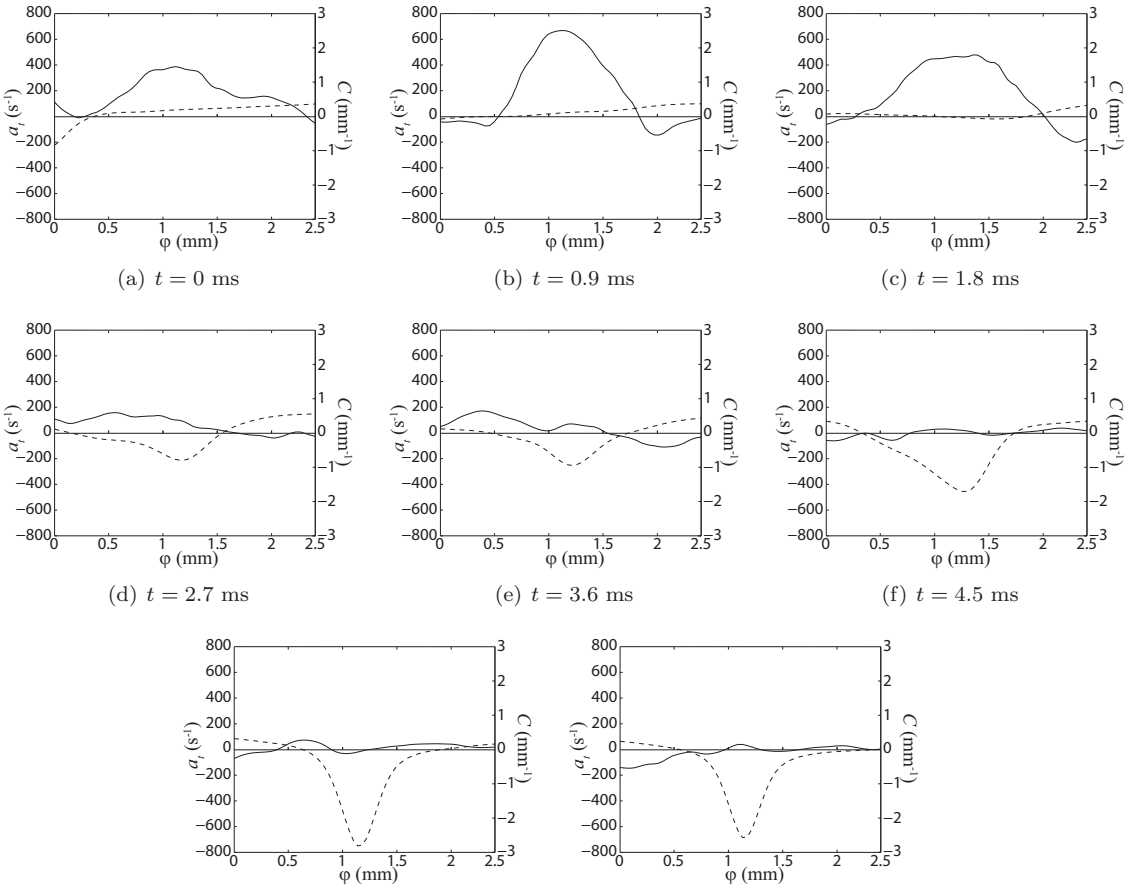

(a) $t = 0$ ms (b) $t = 0.9$ ms (c) $t = 1.8$ ms

(d) $t = 2.7$ ms (e) $t = 3.6$ ms (f) $t = 4.5$ ms

(g) $t = 5.4$ ms (h) $t = 6.3$ ms

Figure 4.13: Profiles of the strain rate (–) and curvature (- -) along the flame surface in the vicinity of the turbulence flame interaction in Fig. 4.12.

To investigate these differences, the strain rate exerted on the flame during each interaction was calculated. These were found to vary widely. Figure 4.16 presents profiles of the strain rate on the flame and flame curvature taken at the time when the maximum strain rate occurred for each interaction. The distance along the flame surface has been normalized by the length of flame surface being strained (l_f). As can be seen, the maximum strain rate varied widely from interaction to interaction. The interaction in Fig. 4.12 exerted approximately twice as much as those in Figs. 4.14 and 4.15. It is therefore apparent that the peak strain rate was not characterized by the vorticity field.

Furthermore, despite the similarity in peak strain rate, the interaction in Fig. 4.14 formed a wrinkle while that in Fig. 4.15 did not. The interaction in Fig. 4.12 created a negatively curved wrinkle of similar size to Fig. 4.14 despite having twice the peak strain rate. Hence, the net flame surface generated is not characterized by the peak strain rate as presented in Fig. 4.16; the integral over time and space during the interaction must be considered.

To investigate such interactions further, forty turbulence-flame interactions resembling the canonical configuration were studied. These involved vortical structures over a range of scales and strengths. For each interaction, the temporal history of the strain rate was calculated both in terms of the maximum and spatial average exerted on the flame. To do so, the area of the flame that was being strained was first identified. At each time step, the profile of $a_t(t, \vartheta)$ (recall that the flame is defined as a space curve parameterized by ϑ) along the flame surface was calculated (similar to Fig. 4.16). From this, the peak strain rate in the vicinity of the vortical structures was identified. This was defined as $a_{t,max}(t)$. From $a_{t,max}(t)$, the region in which the strain rate remained above half the peak was identified. The strain rate

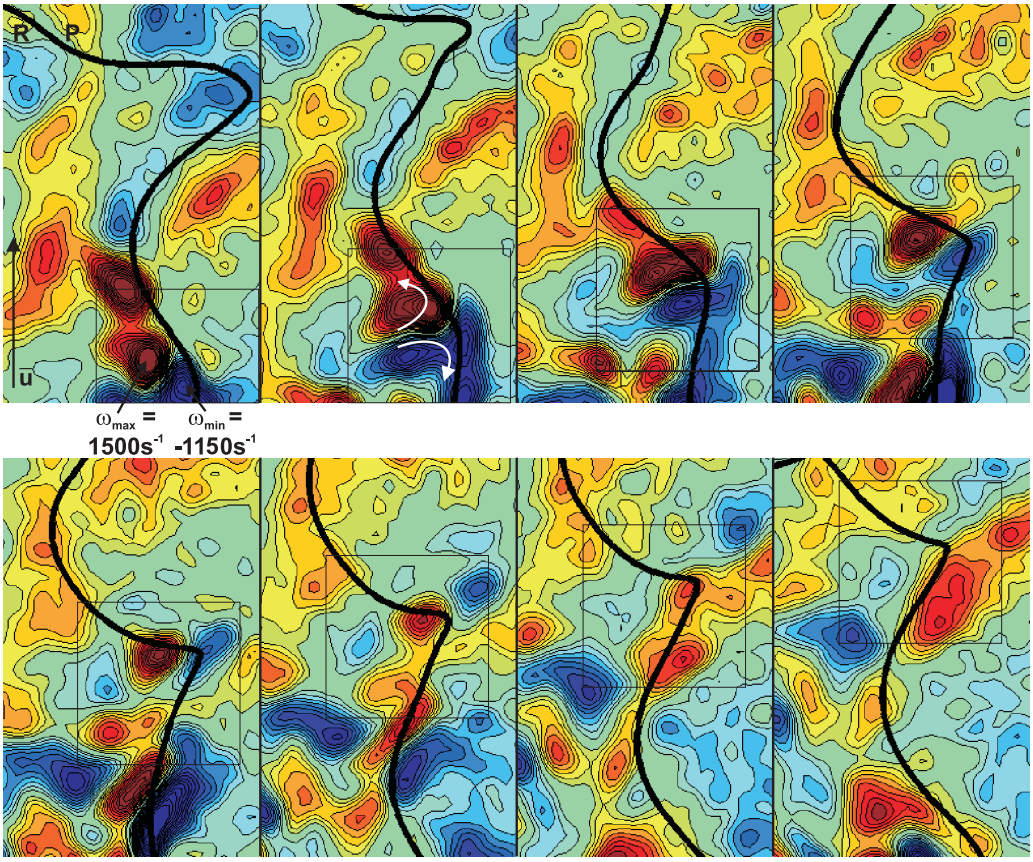

Figure 4.14: Interaction of a counter rotating pair of vortical structures with the flame. A negatively curved wrinkle is created. Contours of vorticity between -1200 s^{-1} (blue) and 1200 s^{-1} (red). Flame is represented by the thick black line. Flow is from bottom to top, reactants are on the left, the field of view is 6 mm x 9.5 mm, and the time between frames is 0.9 ms.

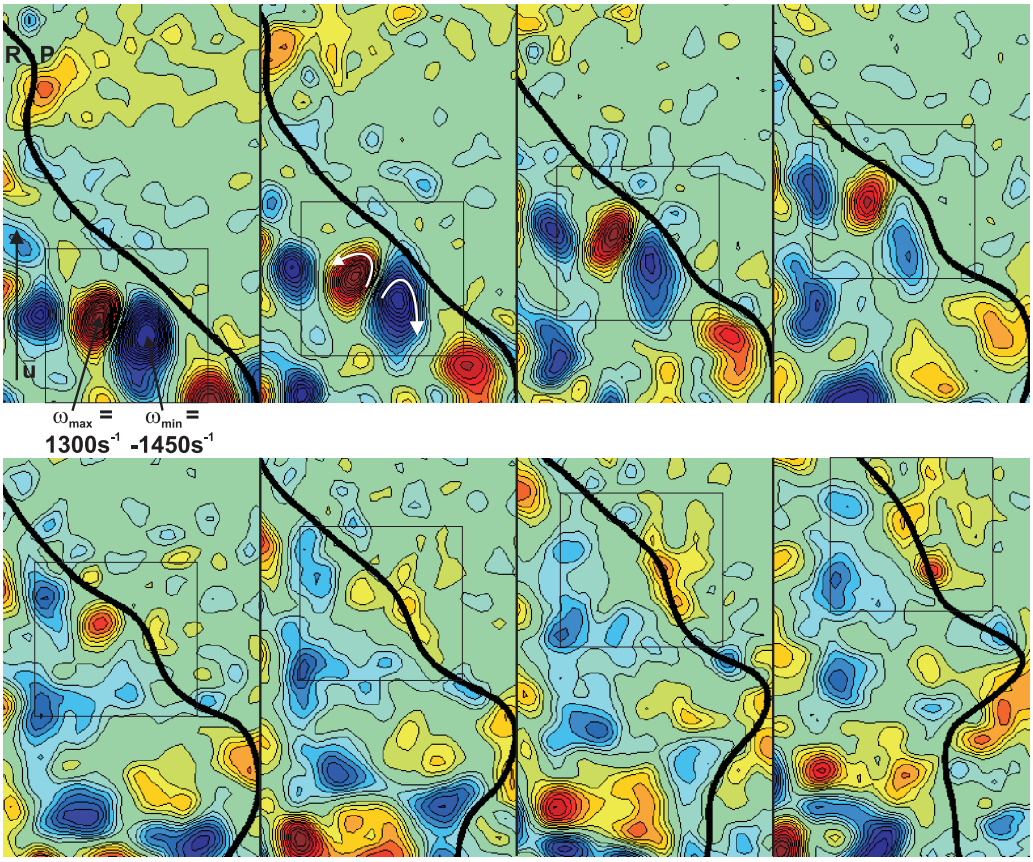

Figure 4.15: Interaction of a counter rotating pair of vortical structures with the flame. There is very little wrinkling of the flame surface. Contours of vorticity between -1200 s^{-1} (blue) and 1200 s^{-1} (red). Flame is represented by the thick black line. Flow is from bottom to top, reactants are on the left, the field of view is 6 mm x 9.5 mm, and the time between frames is 0.9 ms.

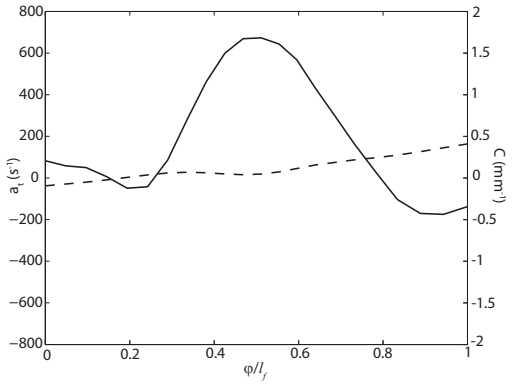

(a) Profiles corresponding to Fig. 4.12. A peak strain rate of approximately 700 s^{-1} is exerted on the flame and a negatively curved wrinkle forms (at a later time).

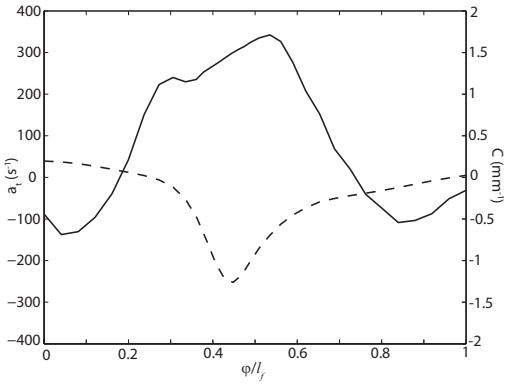

(b) Profiles corresponding to Fig. 4.14. A peak strain rate of approximately 350 s^{-1} is exerted on the flame and a negatively curved wrinkle forms.

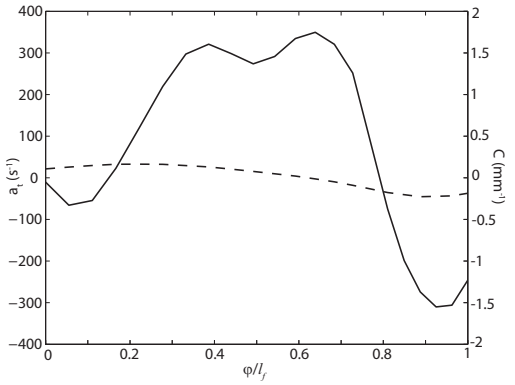

(c) Profiles corresponding to Fig. 4.15. A peak strain rate of approximately 350 s^{-1} is exerted on the flame but no wrinkle forms.

Figure 4.16: Profiles of the strain rate (–) and flame curvature (- -) in the vicinity of the turbulence-flame interaction shown in Figs. 4.12-4.14. The profiles are taken at the time of maximum strain rate.

was then spatially averaged over this region to obtain $\langle a_t(t) \rangle$. The beginning of the interaction (t_0) was defined as the first time a peak of strain rate was apparent on the flame surface. This was generally 2-3 time steps before the peak strain rate was exerted on the flame.

The strength of the interactions were characterized in two ways. Firstly, the maximum vorticity magnitude in each structure was computed. The interaction was then characterized by the mean of these two values (ω_{max}). This is analogous to the characterization in the canonical studies. Secondly, the half maximum contour for each structure was computed. The spatial average of the vorticity magnitude within these contours was then calculated ($\langle |\omega| \rangle$). This characterization accounts for differences in the vorticity distribution not accounted for in the maxima. It is noted that the canonical studies typically characterized the strength of the interaction by a rotational velocity. However, such a velocity was difficult to define in real turbulence; the structures were not circular in cross-section and convecting at different velocities. However, the vorticity definition employed can be related that of the canonical studies since the precisely defined velocity field in the latter stipulates the vorticity field.

The scale of the interaction was also important. As demonstrated by Meneveau and Poinsot [74], the effectiveness of vortices to stretch a flame is scale dependant. The scales were also characterized in two ways. Firstly, the distance between the vorticity peaks was used (l_p). Once again, this is analogous to the canonical studies. Secondly, the size of the structures was used. Each structure had a characteristic size defined from the area and perimeter of its half maximum region given by Eq. 2.8. The mean size of the two structures was used to characterize the pair (l_s). All vortex characteristics were taken at at the time when the peak strain rate was exerted on the flame.

Table 4.2 lists the interactions studied and their characteristics. The interactions were grouped by similarly sized (in terms of l_s) structures. Within these groups, they were sorted by their strengths (ω_{max}). If the vorticity field properly characterized the interaction, the straining of the flame surface for similar interactions should have been similar. However, this was found to not be the case.

To demonstrate this, Figs. 4.17 - 4.19 present temporal profiles of the strain rate for all the interactions. Figures 4.17 and 4.18 present profiles of both $a_{t,max}(t)$ and $\langle a_t(t) \rangle$ for the interactions of Group V1. In each plot, the strain rate is normalized by one of the vortex strength metrics. Furthermore, the temporal axis is normalized by one of two characteristic time scales for the interaction. These are given by

$$\tau_i = \frac{l_i}{s_l^0} \tag{4.10}$$

where $l_i = l_p$ (Fig. 4.17) or l_s (Fig. 4.18). As can be seen, the vorticity field does not properly characterize the strain rate exerted on the flame regardless of the normalization. Even for vorticity fields of similar strength and scale, there was a wide range of computed strain rates. Furthermore, the normalized duration over which the strain rate was exerted varied greatly between interactions regardless of the time scale. Hence, for interaction groups V2-V4, only the profiles of $\frac{a_{t,max}(t)}{\omega_{max}}$ are provided, with time normalized by τ_s (Fig. 4.19).

As can be seen, regardless of the scale, strength, and normalization, the strain rate exerted on the flame was not characterized by the vorticity field. This was true both for the magnitude of the strain rate and the duration over which it was exerted. However, it is noted that the normalized interaction times were on the order of unity, indicating that $\frac{l_i}{s_l^0}$ may be the proper form for τ_i; a proper length scale for the interaction is needed.

Group	Interaction	l_p (mm)	l_s (mm)	ω_{max} (s^{-1})	$\langle\|\omega\|\rangle$ (s^{-1})	Marker
V1	v1	0.8	1.0	1.1E+03	7.8E+02	×
	v2	0.9	0.7	1.0E+03	8.0E+02	+
	v3	0.9	1.0	1.2E+03	9.1E+02	○
	v4	0.9	1.1	1.3E+03	9.4E+02	□
	v5	0.9	0.7	1.4E+03	1.0E+03	▽
	v6	0.9	1.0	1.6E+03	1.1E+03	△
	v7	1.0	1.3	8.7E+02	6.3E+02	*
	v8	1.0	0.9	1.0E+03	7.4E+02	◇
	v9	1.0	1.3	1.1E+03	7.8E+02	·
	v10	1.0	1.8	1.2E+03	8.4E+02	◁
	v11	1.0	1.3	1.2E+03	9.0E+02	▷
V2	v12	1.1	1.4	8.9E+02	6.5E+02	×
	v13	1.1	1.3	9.2E+02	6.8E+02	+
	v14	1.1	1.2	9.2E+02	6.7E+02	○
	v15	1.1	1.2	9.6E+02	6.8E+02	□
	v16	1.1	1.3	9.6E+02	6.7E+02	▽
	v17	1.1	1.9	1.0E+03	7.1E+02	△
	v18	1.1	1.5	1.1E+03	8.3E+02	*
	v19	1.1	2.5	1.3E+03	9.2E+02	◇
	v20	1.1	1.0	1.3E+03	9.2E+02	·
	v21	1.1	1.2	1.6E+03	1.2E+03	◁
V3	v22	1.2	2.0	7.3E+02	5.2E+02	×
	v23	1.2	1.7	7.5E+02	5.2E+02	+
	v24	1.2	1.8	8.0E+02	5.9E+02	○
	v25	1.2	1.3	8.5E+02	6.2E+02	□
	v26	1.2	1.5	9.2E+02	6.4E+02	▽
	v27	1.2	1.7	9.5E+02	6.8E+02	△
	v28	1.2	1.2	1.0E+03	7.4E+02	*
	v29	1.2	2.7	1.1E+03	8.2E+02	◇
	v30	1.2	1.9	1.2E+03	8.6E+02	·
	v31	1.2	1.7	1.2E+03	8.5E+02	◁
	v32	1.2	1.8	1.3E+03	9.3E+02	▷
V4	v33	1.3	1.6	7.9E+02	5.8E+02	×
	v34	1.3	2.3	9.3E+02	6.8E+02	+
	v35	1.3	1.3	9.9E+02	7.2E+02	○
	v36	1.3	2.1	1.2E+03	8.4E+02	□
	v37	1.3	3.0	1.4E+03	9.9E+02	▽
	v38	1.4	1.6	8.2E+02	6.0E+02	△
	v39	1.4	1.5	9.2E+02	6.5E+02	*
	v40	1.5	2.4	8.6E+02	6.4E+02	◇

Table 4.2: Characteristics of turbulence-flame interactions in terms of vorticity.

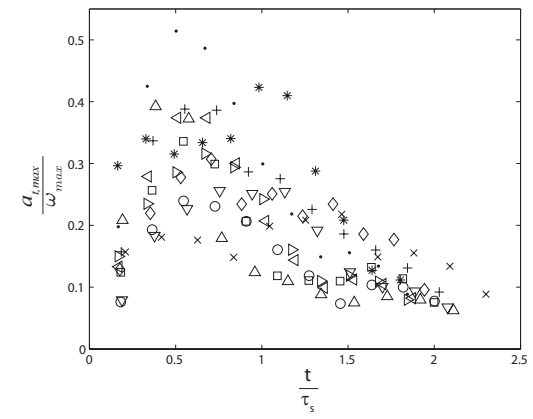

(a) Normalization of $a_{t,max}$ by ω_{max}

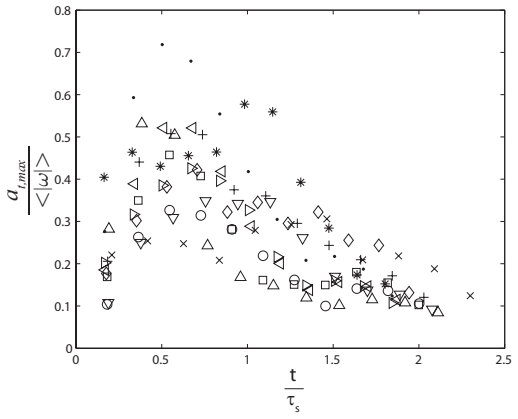

(b) Normalization of $a_{t,max}$ by $\langle|\omega|\rangle$

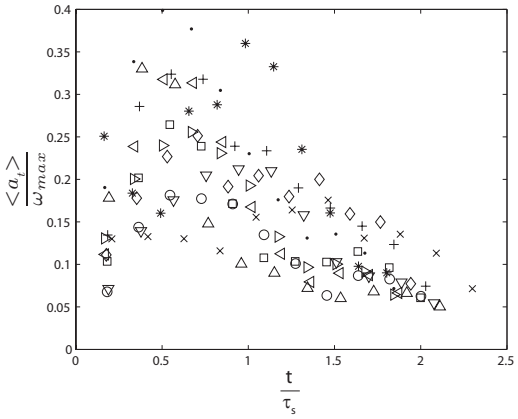

(c) Normalization of $\langle a_t \rangle$ by ω_{max}

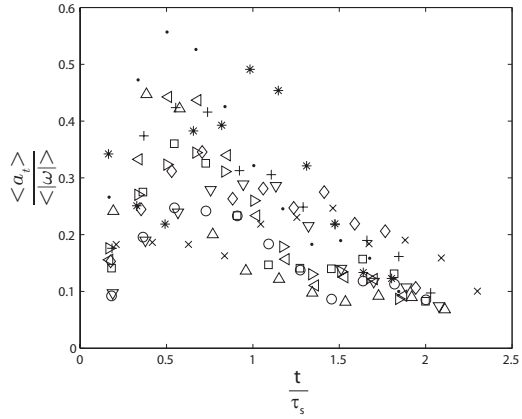

(d) Normalization of $\langle a_t \rangle$ by $\langle|\omega|\rangle$

Figure 4.17: Temporal evolution of the strain rate exerted on the flame, characterized by the vorticity and normalized in various manners. Time is normalized by τ_s. Interactions of Group V1 (see Table 4.2 for the symbols).

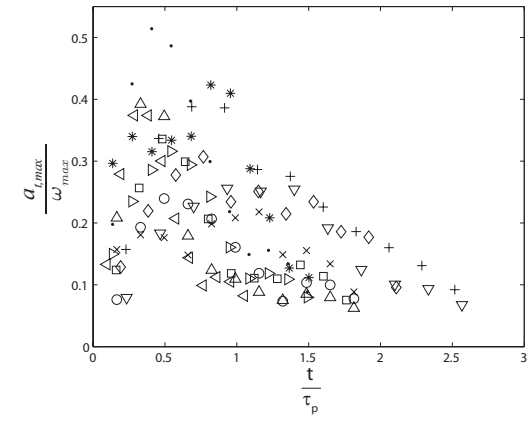

(a) Normalization of $a_{t,max}$ by ω_{max}

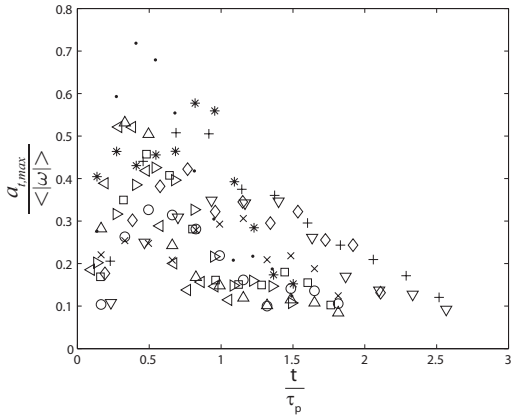

(b) Normalization of $a_{t,max}$ by $\langle|\omega|\rangle$

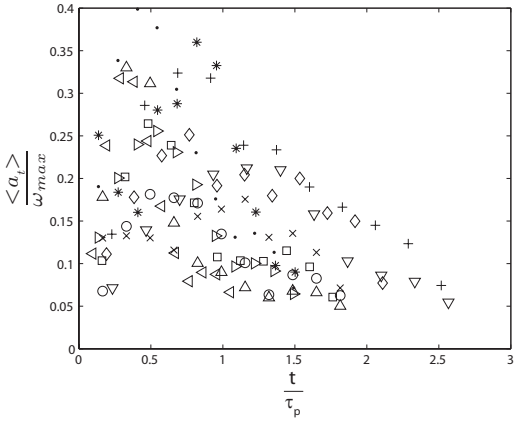

(c) Normalization of $\langle a_t \rangle$ by ω_{max}

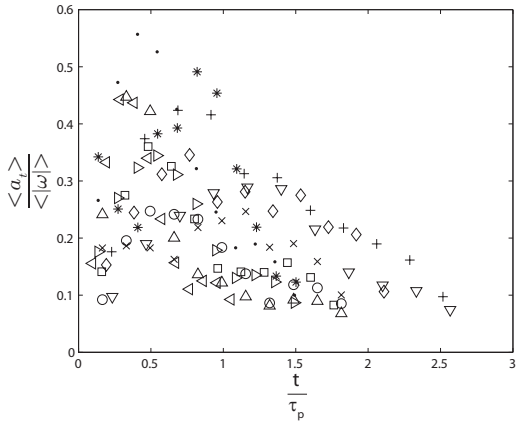

(d) Normalization of $\langle a_t \rangle$ by $\langle|\omega|\rangle$

Figure 4.18: Temporal evolution of the strain rate exerted on the flame, characterized by the vorticity and normalized in various manners. Time is normalized by τ_p. Interactions of Group V1 (see Table 4.2 for the symbols).

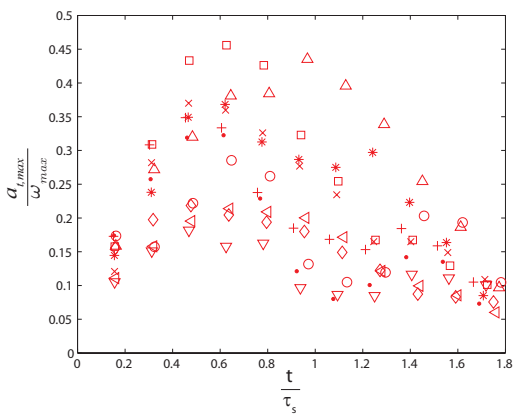

(a) Group V2

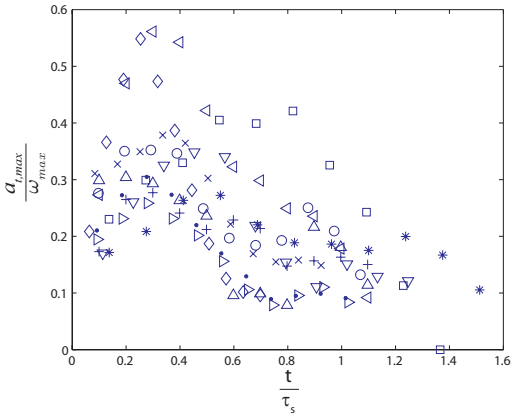

(b) Group V3

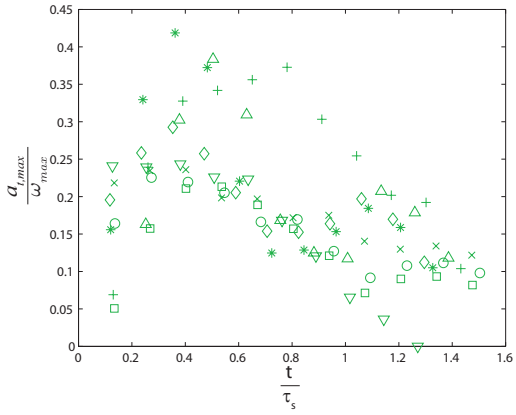

(c) Group V4

Figure 4.19: Temporal evolution of $a_{t,max}$, characterized by vorticity and normalized by ω_{max}. Interactions of Groups V2-V4 (see Table 4.2 for the symbols).

4.3.2 More complex interactions

From the above discussion, it is apparent that the vorticity field in a turbulent flame does not characterize a_t for interactions resembling the canonical counter-rotating vortex configuration. Furthermore, this simple configuration was not typical of the interactions that occur. Instantaneous images containing an interaction of this geometry occurred in less than 20% of the recorded data. Within these frames, the canonical geometry only accounted for a portion of the total turbulence-flame interaction.

Interactions between more complex turbulence fields and the flame were found to cause a significant amount of flame wrinkling. For example, Figs. 4.20 and 4.21 show interactions between several vortical structures and the flame. In each case, wrinkles were generated in the flame surface by configurations different than the canonical one. In Fig 4.20, a single wrinkle forms around a large group of vortical structures. Additional structures (to the lower right of the boxed region) do not contribute to the wrinkling. Partially through the process, another group of structures interact with the flame, but do not cause an additional wrinkle. Based on the canonical description, each vortex pair should create a wrinkle in the flame. In Fig. 4.21 the negative vorticity structure interacts with the flame while paired with two different positive vorticity structures at subsequent (and overlapping) times, creating a single wrinkle. These time sequences further indicate that the canonical counter-rotating vortex configuration is not sufficient to describe turbulence-flame interactions.

4.4 The mechanisms of flame strain and wrinkling

Since the interaction of a vorticity field with the flame does not properly characterize the straining of the flame surface, an alternative description was sought.

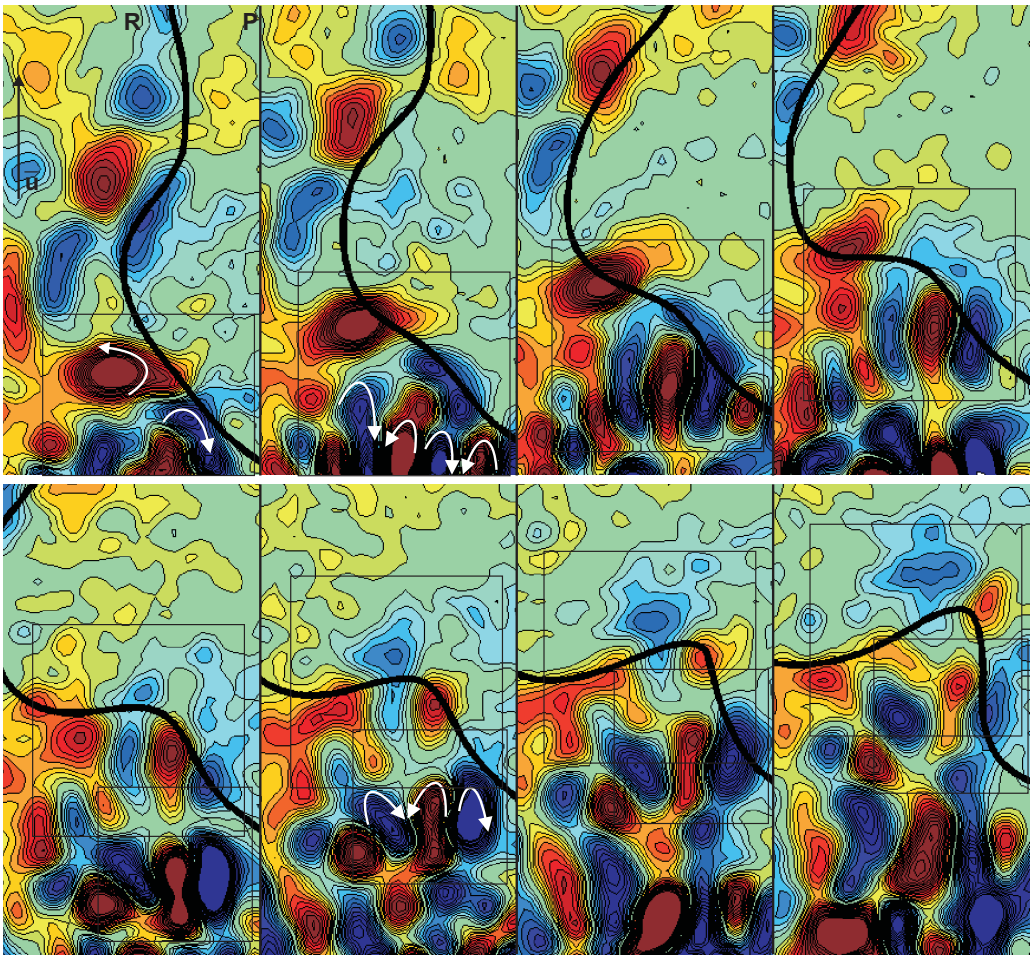

Figure 4.20: Interaction of a complex vorticity field with the flame, creating a negatively curved wrinkle. The wrinkle forms around a group of four vortical structures, with some others being excluded. The later group of structures does not create an additional wrinkle. Contours of vorticity between -1200 s^{-1} (blue) and 1200 s^{-1} (red). Flame is represented by the thick black line. Flow is from bottom to top, reactants are on the left, the field of view is 6 mm x 11.5 mm , and the time between frames is 0.9 ms.

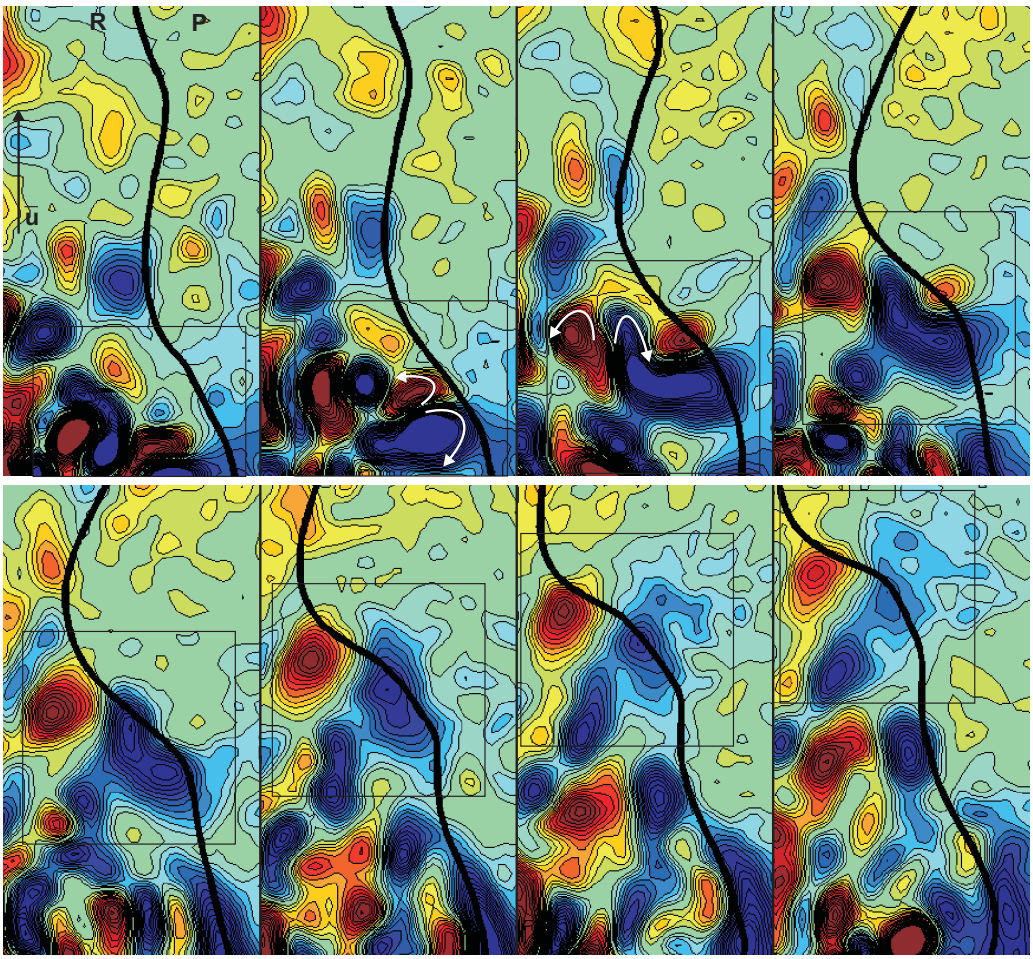

Figure 4.21: Interaction of a complex vorticity field with the flame, creating a negatively curved wrinkle. The negative vorticity structure interacts with two positive vorticity structures at subsequent and overlapping times. Contours of vorticity between -1200 s^{-1} (blue) and 1200 s^{-1} (red). Flame is represented by the thick black line. Flow is from bottom to top, reactants are on the left, the field of view is 6 mm x 11.5 mm, and the time between frames is 0.9 ms.

Consider the strain rate defined by Eq. 4.1. The velocity gradient tensor can be decomposed into $\underline{S}$ and $\underline{\Omega}$ according to Eq. 1.56. Hence:

$$a_t = -\hat{n} \cdot (\hat{n} \cdot \underline{S}) + \hat{n} \cdot (\hat{n} \cdot \underline{\Omega}) + \nabla \cdot \vec{u} \tag{4.11}$$

However, the antisymmetry of the rotation rate tensor means that $\hat{n} \cdot (\hat{n} \cdot \underline{\Omega}) = 0$ and the strain rate induced on the flame can be written as:

$$a_t = -\hat{n} \cdot (\hat{n} \cdot \underline{S}) + \nabla \cdot \vec{u} = (\delta_{ij} - n_i n_j) S_{ij} \tag{4.12}$$

Hence, the strain rate exerted on the flame does not involve vorticity, but is directly related to the fluid strain rate tensor. This indicates that velocity gradients appearing as fluid dynamic strain rate generate flame surface area through strain and a flow containing only vorticity should not strain the flame.

Thus is is apparent that the image of rotating 'vortices' straining the flame to generate area is misconceived. These *a priori* decided upon structures are not a proper representation of the structures responsible for straining the flame surface. Furthermore, attempting to associate a characteristic strain rate with a radius and rotational velocity of the vortical structures may lead to misinterpreted results. We must then ask: what turbulent structures lead to the generation of flame surface area? The answer is regions of concentrated fluid dynamic strain rate (strain-rate structures). That is, a turbulent flow consists of an evolving velocity gradient field in which their are coherent volumes both of high vorticity (vortices) and high fluid dynamic strain rate (strain-rate structures). It is these latter regions that are responsible for the generation of flame surface area through strain.

The importance of strain-rate structures in non-reacting turbulence has been studied by many authors [5, 59, 81, 75]. Also, the effect of the strain-rate field on scalar gradients in a turbulent flame has been investigated [20, 105]. However, the role of

coherent strain-rate structures in the generation of flame surface area has not yet been studied.

4.4.1 Strain-rate structures in the canonical vortex configuration

To understand the relationship between the canonical counter-rotating vortices and the strain rate structures, the complete flow field associated with a pair of Burgers' vortices was computed. These are the most commonly investigated vortex tubes [34]. In a Burgers' vortex, the vorticity vector points along the vortex axis and has the form:

$$\vec{\omega} = \frac{\Gamma_0}{4\pi\nu} e^{-(r/\lambda)^2} \hat{k} \tag{4.13}$$

where Γ_0 is the circulation and λ is a characteristic length of the structure. For this demonstration, the pre-exponential coefficient and λ were set to unity.

Two such vortices were superimposed on a quiescent flow field as shown in Fig. 4.22(a). From this vorticity field, the resultant velocity field was calculated using the Biot-Savard law. That is, at every point in the domain, $\vec{u}$ was calculated as:

$$\vec{u}(\vec{x}) = \frac{1}{4\pi} \int \frac{\vec{\omega}(\vec{x'}) \times (\vec{x} - \vec{x'})}{|\vec{x} - \vec{x'}|^3} d\vec{x'} \tag{4.14}$$

The accuracy of this method was confirmed by computing the vorticity from the resultant velocity field. This is shown in Fig. 4.22(b). As can be seen, this vorticity field is nearly identical to the original. The slight deviations were likely due to the limited resolution used.

From the velocity field, the two dimensional strain-rate tensor was constructed at each point in the domain. Figure 4.23 shows the strain rate field associated with the flow, where the contours are of $S = (S_{ij}S_{ij})^{1/2}$. As can be seen, there are two structures of concentrated strain-rate associated with the leading and trailing regions

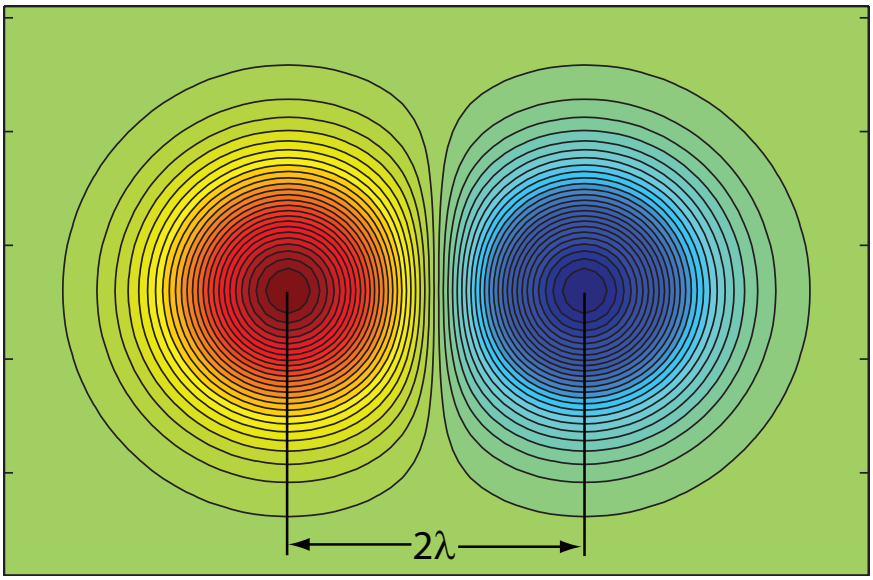

(a) Original Burgers' vortex pair

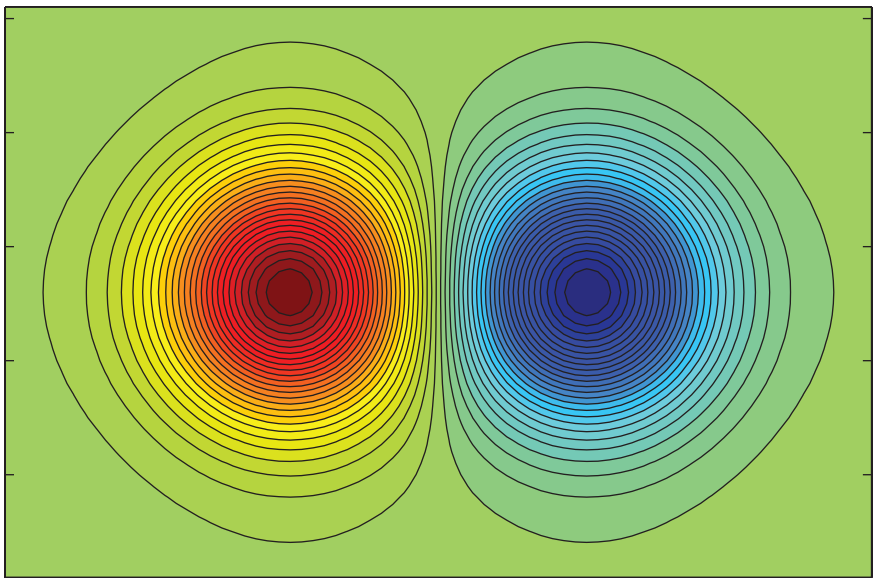

(b) Burgers' vortex pair reconstructed from Biot-Savard velocity field

Figure 4.22: Burgers' vortex pair representing the canonical geometry. Contours of ω_z.

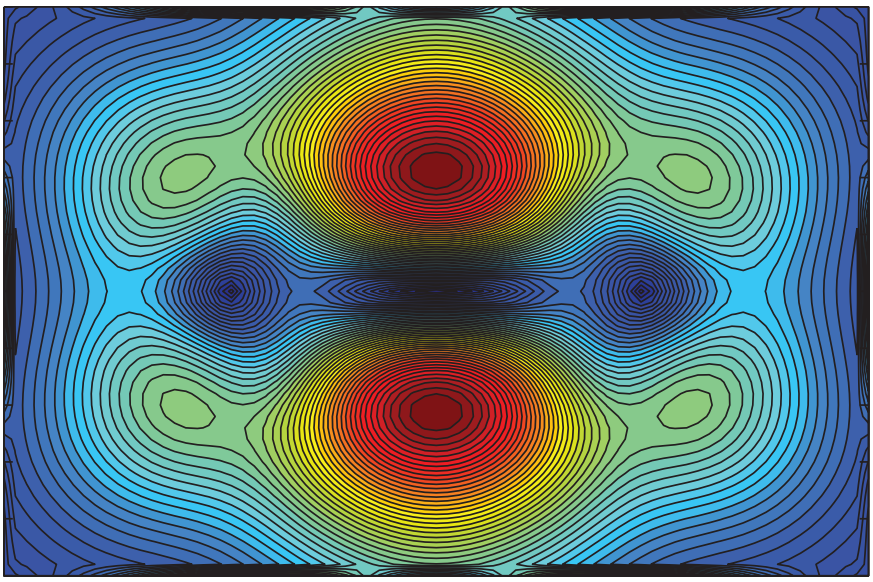

Figure 4.23: Strain rate field associated with the canonical geometry of Fig. 4.22. Contours of $S = (S_{ij}S_{ij})^{1/2}$.

of the vortices. If the flame propagated without changing shape over this strain field, the net change in surface area would be zero; the upper and lower structures would counteract. In reality, the flame wrinkles due to the vorticity and the structures attenuate as they evolve. Hence there is a net strain exerted.

Using strain-rate structures to describe a_t avoids many of the issues associated with the traditional counter-rotating vortices. Firstly, the restrictive building block of an *a priori* constructed geometry is eliminated. Instead of counter-rotating vortices in a head-on configuration, individual strain-rate structures that may be of any orientation, configuration, or geometry may be considered. This negates the need to consider strain rate patterns associated with different vortex configurations. Secondly, it allows for proper characterization of the size and strength of the important turbulent structures. Instead of a vortex radius and rotational velocity, parameters associated with the strain-rate structure should be used. Finally, it allows many more interactions to be studied in real turbulence. The requirement for counter-rotating vortical structures greatly restricted the interactions that could be considered. When

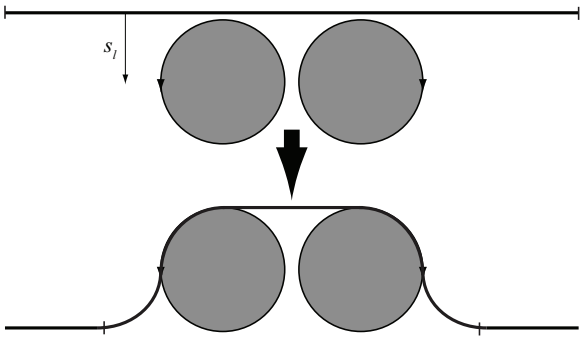

(a) Solid body rotations. A wrinkle forms but no flame surface is generated.

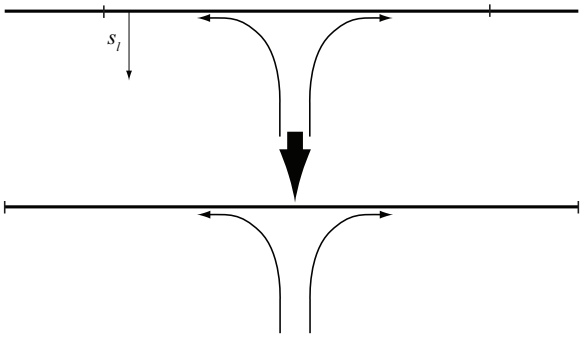

(b) Straining structure (counterflow). No wrinkle forms, but flame surface is generated.

Figure 4.24: Interactions between different forms of turbulent structure and the flame.

individual strain-rate structures are considered, these restrictions to not apply.

4.4.2 The roles of $\underline{\underline{S}}$ and $\vec{\omega}$

Consider the effect of a pure vortical or pure strain rate flow field interacting with a flame. The former corresponds to a solid body rotation, while the latter commonly occurs in a counterflow geometry. The flame front is considered to be an infinitely long propagating surface. Hence the interaction is analogous to a local turbulence-flame interaction in a much larger flame. The solid body rotations (Fig. 4.24(a)) are configured in the canonical (vortex pair) manner. As they pass through the flame, a wrinkle is formed. However, this is a process of simply wrapping up existing flame surface and no additional area is created; the length between the hashes does not change. Conversely, the straining flow field does not create a flame wrinkle, but

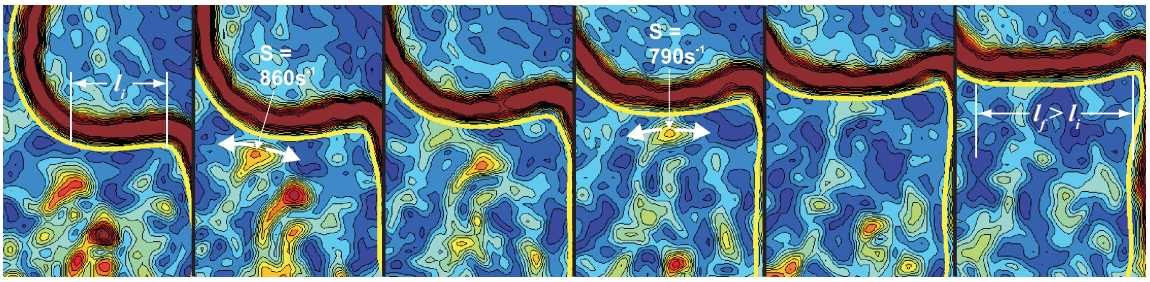

(a) Contours of strain rate (S) between 0 s^{-1} and 1200 s^{-1}. Flame contour in yellow.

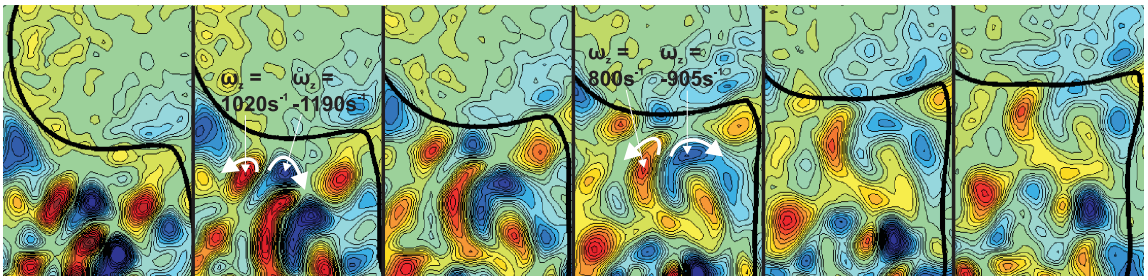

(b) Contours of vorticity (ω_z) between -1200 s^{-1} (blue) and 1200s^{-1} (red). Flame contour in black.

Figure 4.25: Strain-rate structures elongating a flat flame segment. Flame surface area is generated without a wrinkle begin formed. Field of view is 6 mm x 9 mm, time between frames is 0.9 ms. Reactants on left.

produces a flat flame with greater surface area as shown in Fig. 4.24(b); the hash marks move apart. Hence, the interaction between a turbulent flow field and a flame front is a combined process of strain-rate structures generating flame surface area and vortical structures redistributing it into wrinkles. Furthermore, both processes require the flame surface and turbulent structures to be oriented in such a manner that the velocity gradients are effective. This is clearly seen for the strain rate components in Eq. 4.12; if $\hat{n}$ is not properly oriented, the $\underline{S}$ components have no effect on a_t. Similarly, if the solid body rotations in Fig. 4.24(a) encountered a flame segment already wrinkled in the final configuration, no additional wrinkling would occur.

Using the CS-PIV measurements, it was possible to confirm these ideas. While the straining and wrinkling processes in the real flame were continuously and simultaneously occurring, it was possible to largely isolate each mechanism to observe their

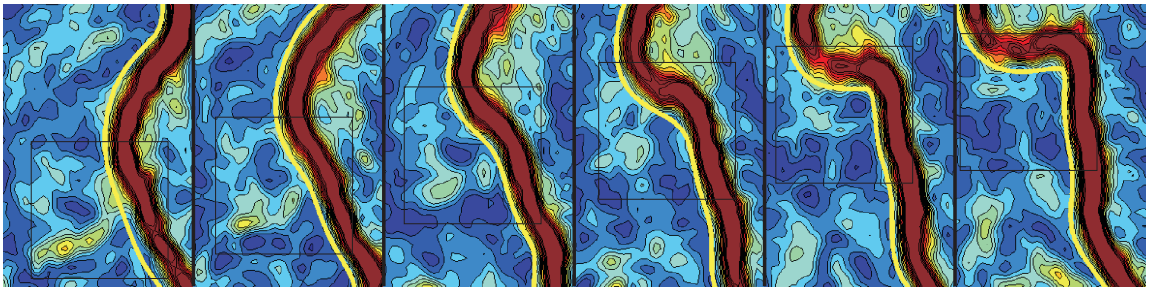

(a) Contours of strain rate (S) between 0 s^{-1} and 1200 s^{-1}. Flame contour in yellow.

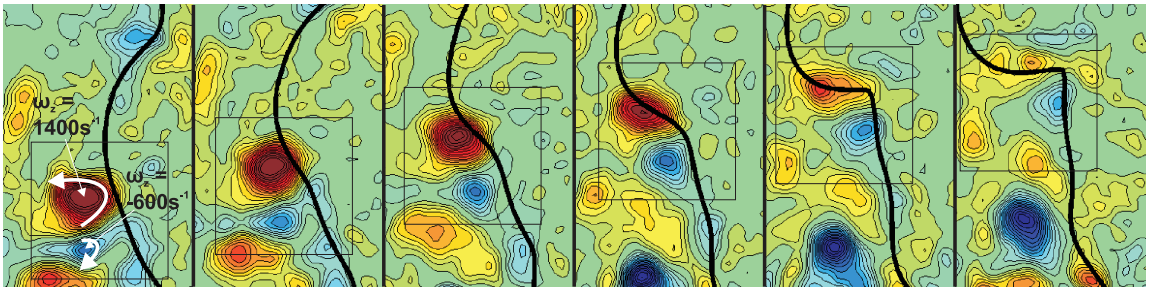

(b) Contours of vorticity (ω_z) between -1200 s^{-1} (blue) and 1200s^{-1} (red). Flame contour in black.

Figure 4.26: A strong vortical structure wraps existing flame surface around it. Little flame surface area is generated. Field of view is 6 mm x 9 mm, time between frames is 0.9 ms. Reactants on left.

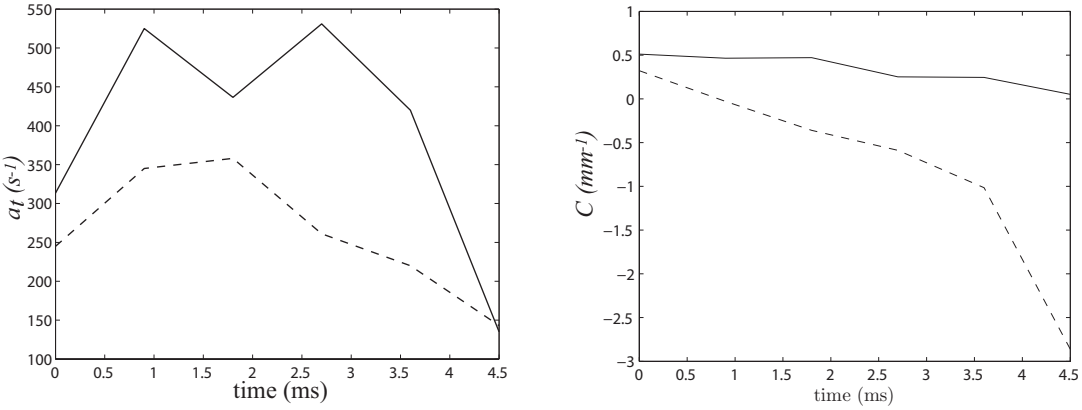

(a) Strain rate.

(b) Flame curvature.

Figure 4.27: Temporal evolution of the maximum strain rate and flame curvature the interactions in Figs. 4.25 (–) and 4.26 (- -).

distinct effects. Interactions demonstrating these mechanisms are shown in Figs. 4.25 and 4.26 in terms of both the vorticity and fluid dynamic strain rate fields. The vorticity fields are visualized in the same manner as in §4.3. For the strain rate fields, contours of the strain rate (S = resolved component of $(S_{ij}S_{ij})^{1/2}$) between 0 and 1200 s^{-1} are plotted. The flame contour is represented by the thick yellow line. It should be noted that the flame front manifests itself in the S fields as a region of high strain due to the acceleration of the gas through the flame (i.e. $\nabla \cdot \vec{u} > 0$). However, this strain rate is not a result of the turbulence and hence not the focus of this work. Nevertheless, the high acceleration region is an indicator of the flame thickness and the accuracy of the leading edge isocontour. Temporal profiles of the $a_{t,max}$ and maximum flame curvature (C_{max}) resulting from these interactions are shown in Fig. 4.27.

Figure 4.25 shows the interaction between two strain-rate structures and the flame front. The vortical structures in this interaction were configured such that no flame wrinkle was produced; the flame surface was already oriented around the overall vorticity group. However, the extensively straining structures still exerted strain on the flame surface, generating surface area and resulting in a longer flat flame contour. This is confirmed by Fig. 4.27. In Fig. 4.27(a), two pulses of a_t are exerted on the flame corresponding to the two strain-rate structures. However, the turbulence does not generate a wrinkle. Figure 4.27(b) shows that the initial slightly positive curvature is stretched out, resulting in a flatter flame front. This process is analogous to the counterflow geometry of Fig. 4.24(b).

Conversely, Fig. 4.26 shows a vortex pair interacting with the flame. The structure with positive vorticity is considerably stronger than its counterpart. The strain rate structure is also weak. As the positive vortex encounters the flame, existing flame

surface is wrapped around it; the flame to the upper right is pulled around the vortex. The weaker, negative vortex does not significantly influence the flame and a asymmetric wrinkle is formed. Due to the weak strain rate structure, the a_t exerted on the flame is relatively low throughout the interaction as shown in Fig. 4.27(a). Hence, the high negative curvature wrinkle seen in Fig. 4.27(b) is formed without significant straining of the flame surface.

These ideas, combined with the geometry of the vortical and strain-rate structures in the canonical configuration (Figs. 4.22 and 4.23) show why the strain rate may lead the wrinkling as occurred Figs. 4.12 and 4.13. If the strain-rate structure interacted first, it would generate flame surface area. This would subsequently be wrapped into the wrinkle as the vortical structures interacted. The different locations of the vortical and strain-rate structures in this interaction will be demonstrated in §4.5.1.

Recognizing that different turbulent structures have different roles in the interaction, it is important to understand the relationship between the strain rate and vorticity fields. The transport equations for the vorticity and strain rate in a reacting flow are given by Eqs. 1.58 and 1.59. From these equations it is apparent that the vorticity and strain rate fields are mutually interacting. However, the existence of a particular local vorticity field at a given time does not imply that a particular local strain rate field must exist or vice versa. The evolution and influence of the entire flow to that point effect the local turbulence. Hence, while the deterministic relationship between the rotational structures in Fig. 4.22 and the strain rate structures of Fig. 4.23 is valid for the simple canonical flow, it should not be viewed as a unique relationship.

4.5 The interaction of strain-rate structures and the flame

With this new understanding of how a flame surface is stretched, the turbulence-flame interactions from §4.3 can be reanalyzed to determine if they are better understood and characterized by the properties of their strain-rate structures.

4.5.1 Strain-rate structures associated with counter-rotating vorticity

Firstly, the strain rate fields for the three interactions shown in Figs. 4.12-4.15 are presented in Figs. 4.28-4.30. As can be seen, while the vortical structures in each case were very similar, the strain-rate structures were quite different.

The strain-rate structure in Fig. 4.28 was considerably stronger than in either Figs. 4.29 or 4.30. Hence, the peak strain-rate exerted on the flame was considerably higher as was shown in Fig. 4.16. However, the structure attenuated much more quickly than in Fig. 4.28. The net generation of flame surface area and flame wrinkling between these two interactions was therefore similar. Furthermore, the strain rate structure in Fig. 4.28 interacted before the vortical structures in Fig. 4.12. This led to the lag between straining and wrinkling of the flame surface seen in Fig. 4.13. Conversely, the vortical and strain-rate structures in Figs. 4.14 and 4.29 interacted simultaneously. Hence, the straining and wrinkling were simultaneous as seen in Fig. 4.16(b).

Furthermore, in Figs. 4.29 and 4.30, the strain-rate structures had approximately the same strength. However, the structure in Fig. 4.29 interacted with the flame for considerably longer. Hence, while the peak strain in each interaction was approximately equal (Figs. 4.16(b) and 4.16(c)), the first interaction produced more surface area. This area was then wrapped into the wrinkle by the vortical structures.

From the above interactions it appears that the analysis of §4.4 is accurate: the

strain rate on the flame is characterized by the fluid dynamic strain rate. To further demonstrate this, the interactions listed in Table 4.2 were reanalyzed under this new interpretation; they were characterized in terms of the strength and size of the strain-rate structure. These characteristics are listed in Table 4.3. Note that with this characterization there is only one relevant length scale (there is no distance between structures). Furthermore, the interactions had to be regrouped. Interactions with similarly sized vortical structures did not necessarily have similarly sized strain-rate structures.

Figure 4.31 presents profiles of a_t versus time for the interactions of group S1. Once again, two measures of a_t are presented, $a_{t,max}$ and $\langle a_t \rangle$. These are normalized by either the maximum or average S in the structure, which are defined in the same manner as for the vortical structures. The temporal axis is normalized by τ_s defined by Eq. 4.10, where l_s is the characteristic length of the strain rate structure.

As can be seen, there is considerably less scatter in the data than when normalized by properties of the vorticity (Figs. 4.17-4.19). Furthermore, the scatter is relatively independent of the normalization. Hence, for groups S2-S4 only the profiles of $a_{t,max}$ normalized by S_{max} are presented (Fig. 4.32).

As can be seen, there is a much more distinct pattern to the curves when normalized by the strain-rate structure properties. The curves increase until about $t/\tau_s = 1$ and then descend. However, while the scatter in a_t is reduced compared to the vorticity normalization, it is still significant. To demonstrate this, the maximum strain rate occurring in each interaction was determined. For each interaction group, the standard deviation of these maxima was computed and normalized by the mean value. These were designated σ_m and are presented in Table 4.4. As can be seen, the S-normalization significantly reduced the scatter in the normalized a_t. However, the

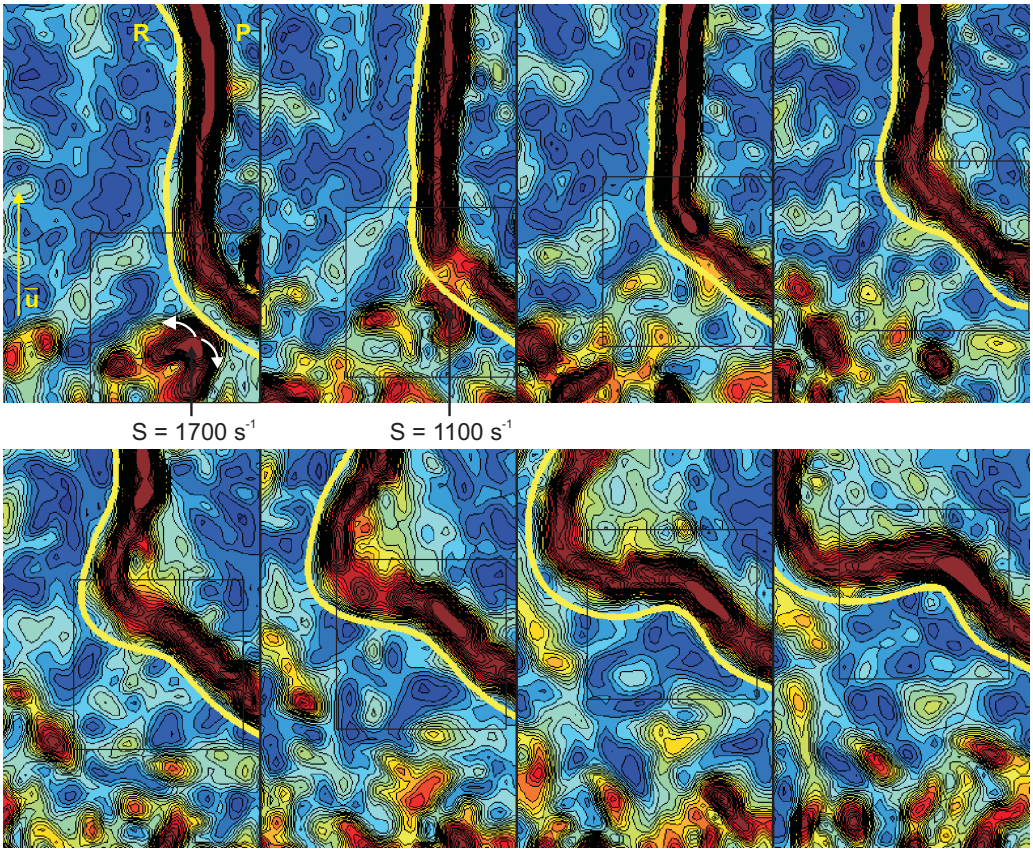

Figure 4.28: Interaction of the strain-rate structure with the flame. This time sequence corresponds to the vorticity fields in Fig. 4.12. The strain-rate is very strong when it interacts with the flame (stronger than either Figs. 4.29 or 4.30). The interaction time is less than in Fig. 4.29 and similar to Fig. 4.30. This results in similar sized wrinkle top that in Fig. 4.29. Contours of strain-rate magnitude between 0 s^{-1} (blue) and 1500 s^{-1} (red). Flame is represented by the thick yellow line. Flow is from bottom to top, reactants are on the left, the field of view is 6 mm x 9.5 mm, and the time between frames is 0.9 ms.

scatter was still significant. This was expected as the strain rate exerted on the flame surface depended on the relative orientations of $\hat{n}$ and $\underline{S}$. Nevertheless, it appears that the phenomenological description of flame stretch presented in §4.4 is accurate.

4.5.2 Strain-rate structures associated with complex vorticity fields

Since the straining of the flame is characterized by individual strain-rate structures, the complex turbulence-flame interactions that occur in real systems can be analyzed; the assumption that the turbulence exists as isolated counter-rotating vortex pairs is unnecessary. For example, consider the two complex interactions previ-

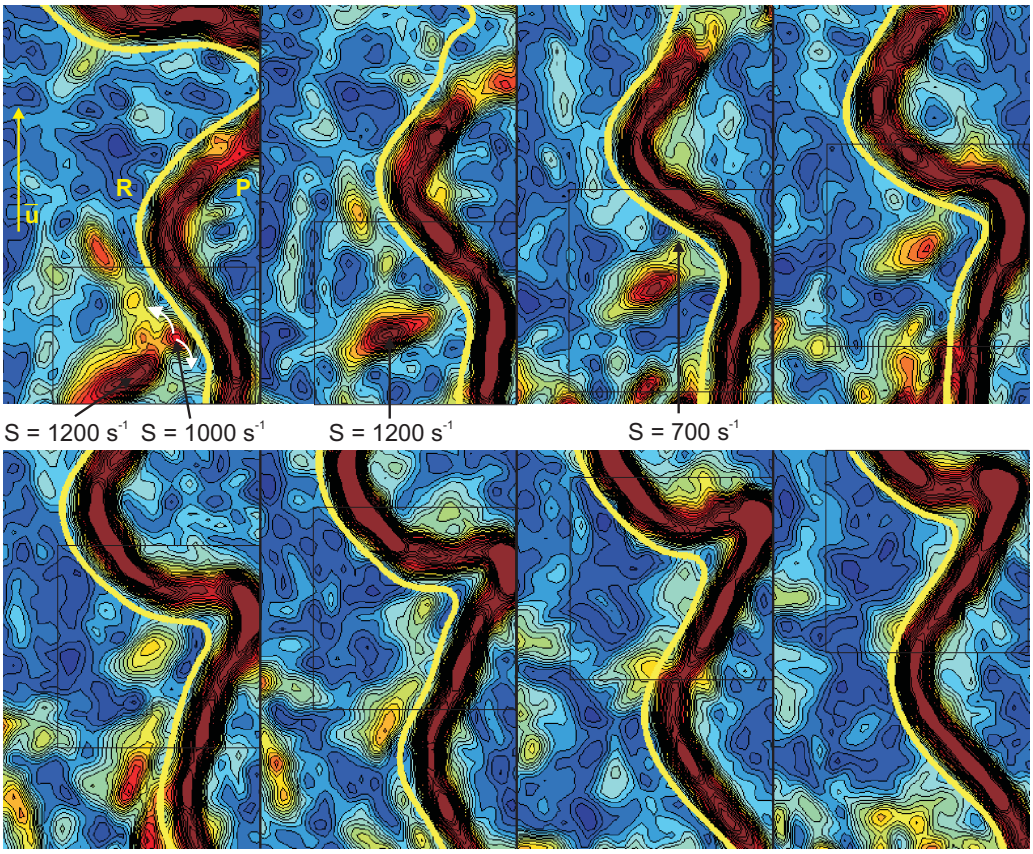

Figure 4.29: Interaction of the strain-rate structure with the flame. This time sequence corresponds to the vorticity fields in Fig. 4.14. The strain-rate is strong and interacts with the flame for a long time period. This produces significant flame surface area that is wrapped into a wrinkle by the vorticity. Contours of strain-rate magnitude between 0 s^{-1} (blue) and 1500 s^{-1} (red). Flame is represented by the thick yellow line. Flow is from bottom to top, reactants are on the left, the field of view is 6 mm x 9.5 mm, and the time between frames is 0.9 ms.

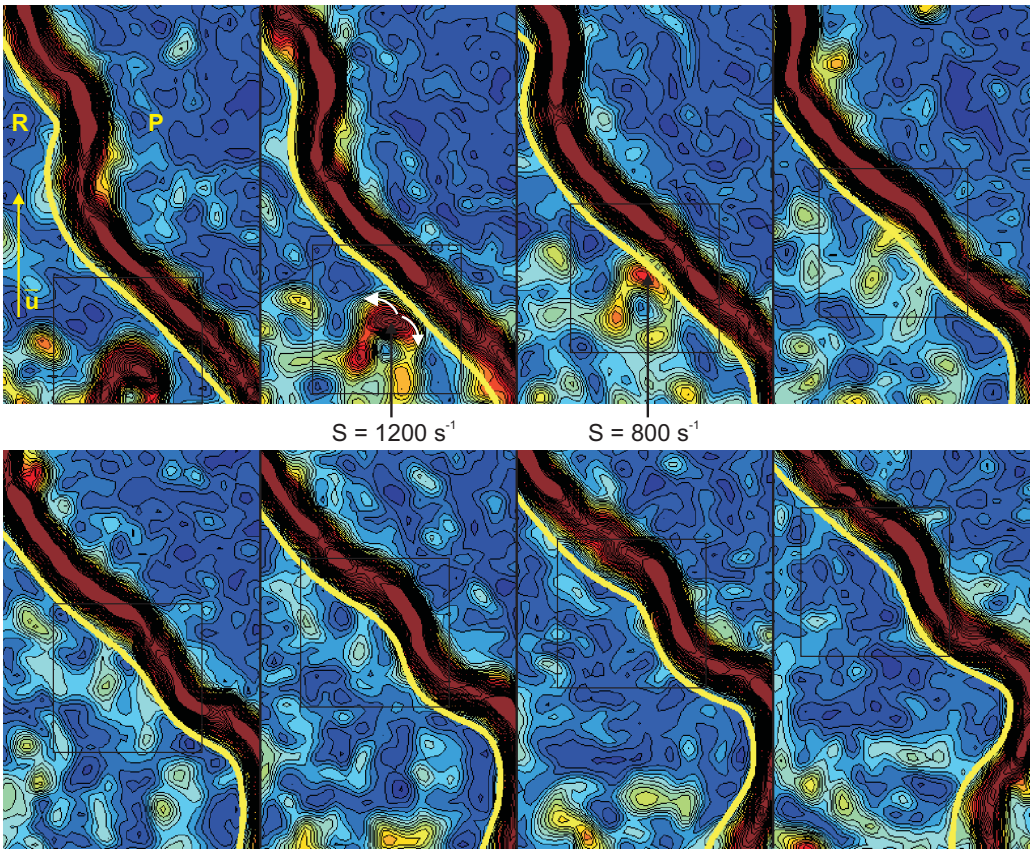

Figure 4.30: Interaction of the strain-rate structure with the flame. This time sequence corresponds to the vorticity fields in Fig. 4.15. The strain-rate is strong, but interacts with the flame for a shorter time period than in Fig. 4.29. Less flame surface is produced, resulting in a smaller wrinkle. Contours of strain-rate magnitude between 0 s^{-1} (blue) and 1500 s^{-1} (red). Flame is represented by the thick yellow line. Flow is from bottom to top, reactants are on the left, the field of view is 6 mm x 9.5 mm, and the time between frames is 0.9 ms.

Group	Interaction	l_s (mm)	S_{max} (s^{-1})	$\langle S \rangle$ (s^{-1})	Marker
S1	s1	0.4	7.7E+02	7.0E+02	$\times$
	s2	0.5	5.6E+02	4.1E+02	$+$
	s3	0.5	5.8E+02	5.7E+02	$\circ$
	s4	0.5	6.0E+02	4.4E+02	$\square$
	s5	0.5	6.1E+02	5.1E+02	$\triangledown$
	s6	0.5	9.9E+02	9.3E+02	$\triangle$
	s7	0.6	5.6E+02	3.9E+02	$*$
	s8	0.6	9.8E+02	7.8E+02	$\diamond$
S2	s9	0.8	6.0E+02	5.0E+02	$\times$
	s10	0.8	6.1E+02	4.9E+02	$+$
	s11	0.8	6.5E+02	5.1E+02	$\circ$
	s12	0.8	6.8E+02	5.5E+02	$\square$
	s13	0.8	7.5E+02	5.8E+02	$\triangledown$
	s14	0.8	7.7E+02	6.2E+02	$\triangle$
	s15	0.8	8.9E+02	6.8E+02	$*$
	s16	0.8	9.2E+02	8.1E+02	$\diamond$
	s17	0.8	1.1E+03	8.3E+02	$\cdot$
	s18	0.8	1.4E+03	8.9E+02	$\triangleleft$
S3	s19	0.9	7.9E+02	5.9E+02	$\times$
	s20	0.9	8.0E+02	6.1E+02	$+$
	s21	0.9	8.7E+02	6.8E+02	$\circ$
	s22	0.9	9.1E+02	7.0E+02	$\square$
	s23	0.9	1.0E+03	8.2E+02	$\triangledown$
	s24	0.9	1.8E+03	1.4E+03	$\triangle$
	s25	1.0	6.7E+02	5.3E+02	$*$
	s26	1.0	8.1E+02	6.8E+02	$\diamond$
	s27	1.0	8.2E+02	6.5E+02	$\cdot$
	s28	1.0	8.6E+02	5.9E+02	$\triangleleft$
	s29	1.0	9.8E+02	7.7E+02	$\triangleright$
S4	s30	1.0	9.9E+02	7.4E+02	$\times$
	s31	1.0	9.9E+02	7.7E+02	$+$
	s32	1.0	1.1E+03	8.0E+02	$\circ$
	s33	1.0	1.1E+03	8.7E+02	$\square$
	s34	1.1	6.5E+02	5.3E+02	$\triangledown$
	s35	1.1	8.0E+02	5.1E+02	$\triangle$
	s36	1.1	1.7E+03	1.2E+03	$*$
	s37	1.2	9.2E+02	7.1E+02	$\diamond$
	s38	1.3	1.0E+03	8.5E+02	$\cdot$
	s39	1.4	5.3E+02	3.6E+02	$\triangleleft$
	s40	1.4	8.6E+02	6.1E+02	$\triangleright$

Table 4.3: Characteristics of turbulence-flame interactions in terms of strain rate.

Group	V1	V2	V3	V4	S1	S2	S3	S4
σ_m	0.29	0.35	0.37	0.21	0.12	0.20	0.22	0.14

Table 4.4: Computed scatter in the measured strain rates for each interaction group.

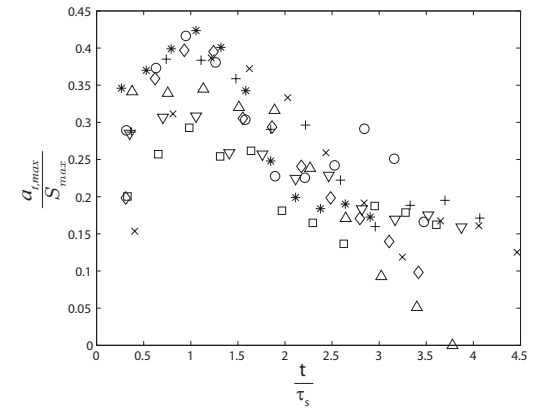

(a) Normalization of $a_{t,max}$ by S_{max}

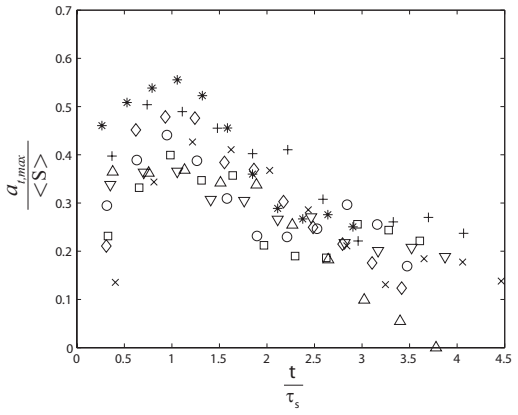

(b) Normalization of $a_{t,max}$ by $\langle S \rangle$

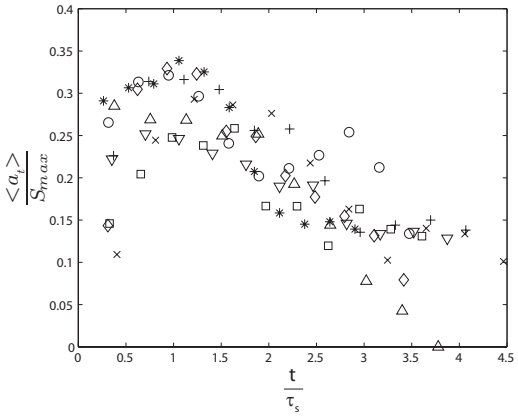

(c) Normalization of $\langle a_t \rangle$ by S_{max}

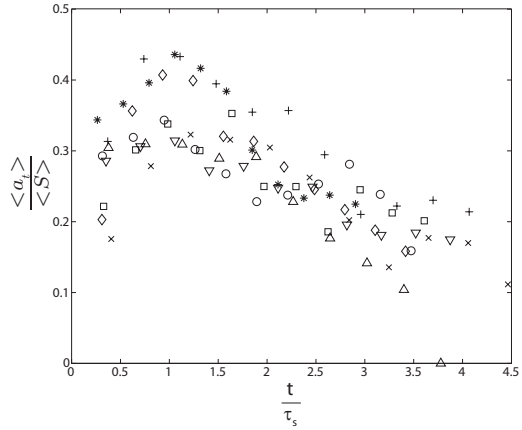

(d) Normalization of $\langle a_t \rangle$ by $\langle S \rangle$

Figure 4.31: Temporal evolution of the strain rate exerted on the flame, characterized by the fluid dynamic strain rate and normalized in various manners. Interactions of Group S1 (see Table 4.3 for the symbols).

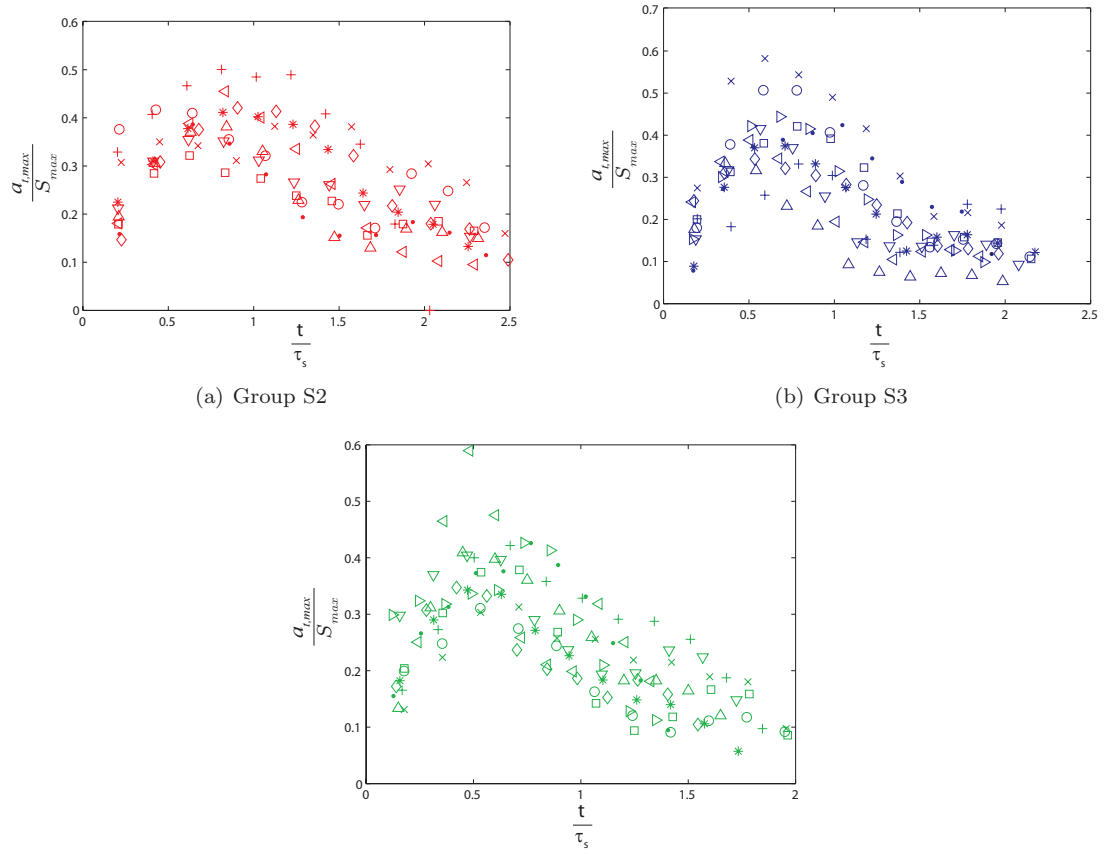

(a) Group S2

(b) Group S3

(c) Group S4

Figure 4.32: Temporal evolution of $a_{t,max}$, characterized by the fluid dynamic strain rate and normalized by S_{max}. Interactions of Groups S2-S4 (see Table 4.3 for the symbols).

ously shown in Figs. 4.20 and 4.21. In these interactions, there were several vortical structures interacting with the flame simultaneously. These geometries are not considered in the canonical configuration. However, when viewed in terms of strain rate, the interactions can be easily understood.

Firstly, the vorticity field in Fig. 4.20 contains a large number vortical structures. A wrinkle forms around four of these. After these structures pass through the flame, another series of structures interact. Exactly why a single wrinkle forms and the role of the several of the structures is unclear from the vorticity field. Based on the canonical interpretation this interaction should form multiple wrinkles, one around each vortex pair.

However, when viewed in terms of the strain rate field the interaction is easily understandable. This is shown in Fig. 4.33. In the first three frames, a structure exerts extensive strain on the flame in the upper portion of the boxed region. Similarly, in the second to fourth frame, another structure exerts extensive strain on the flame in the lower portion of the box. Flame surface is generated at these locations, which set the corners of the wrinkle. In frames 1 and 2, there is a weak structure that would exert compressive strain, but it does not interact with the flame. Similarly, in the sixth and seventh frame the extensively straining structure interacts while the compressively straining structure does not. By simultaneously considering the vorticity field (Fig. 4.33) it is clear why this latter interaction does not create an additional wrinkle: the flame surface is already oriented around the vorticity. Hence, by viewing the fluid dynamic strain rate field (i.e. strain-rate structures), the manner in which this complicated turbulence strains the flame is clear.

As another example, the vorticity field in Fig. 4.21 contains a single negative vorticity structure that interacts with the flame while paired with two positive vor-

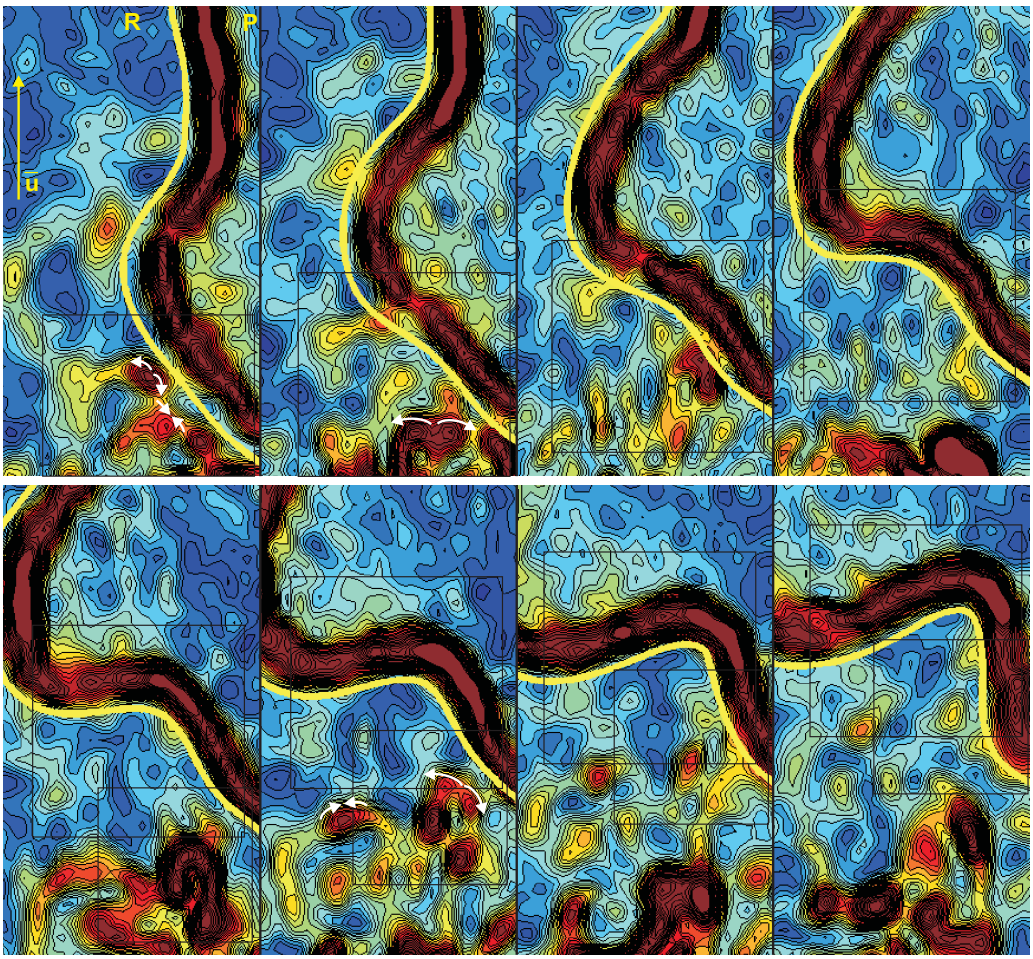

Figure 4.33: Interaction of several strain-rate structures with the flame. The time sequence corresponds to the complex vorticity field in Fig. 4.20. Flame surface is generated at the locations where the strong strain-rate structures interact with the flame, which sets the wrinkle boundaries. Contours of strain-rate magnitude between 0 s^{-1} (blue) and 1500 s^{-1} (red). Flame is represented by the thick yellow line. Flow is from bottom to top, reactants are on the left, the field of view is 6 mm x 10.5 mm, and the time between frames is 0.9 ms.

ticity structures at subsequent and overlapping times. The corresponding strain rate field is shown in Fig. 4.34. In this view, there are two clearly distinct strain-rate structures that interact with the flame to generate flame surface area. The flame surface thus generated is wrapped into the wrinkle by the vortical structures.

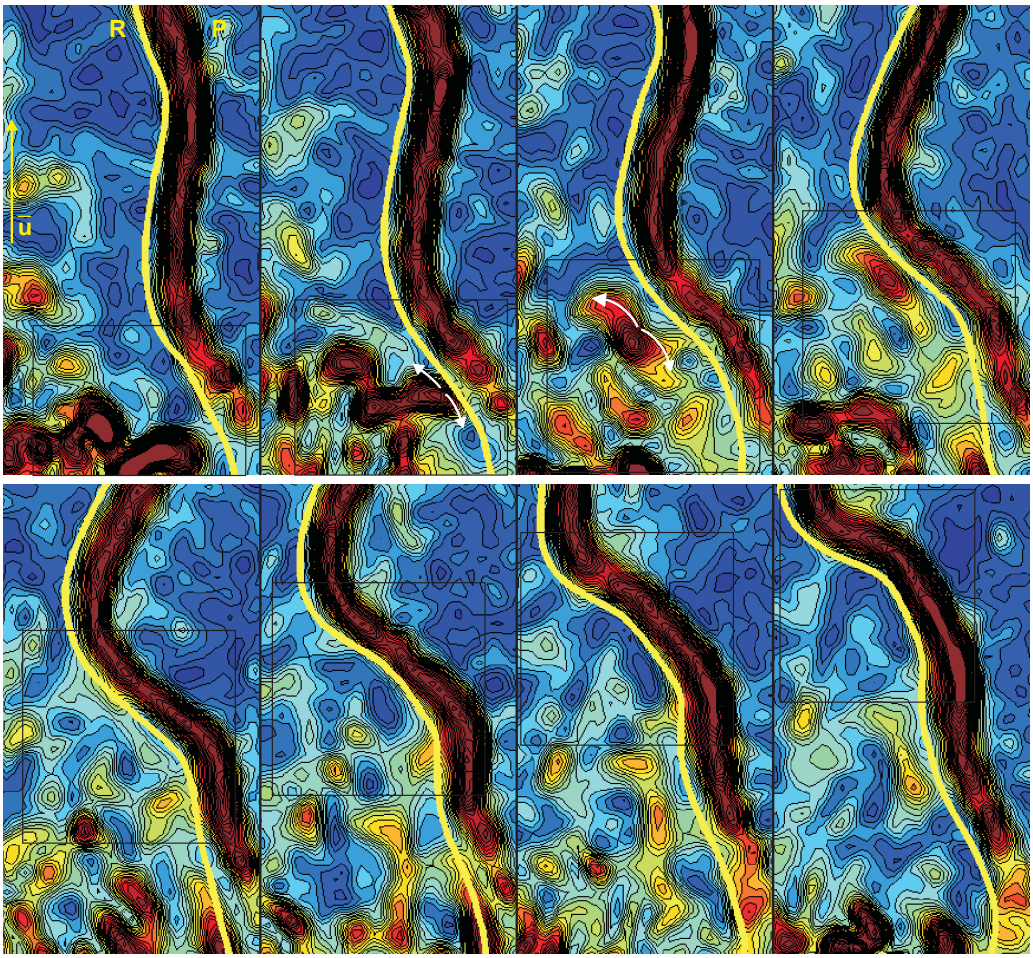

Figure 4.34: Interaction of two strain-rate structures with the flame. The time sequence corresponds to the complex vorticity field in Fig. 4.21. The complex vorticity field interactions is clarified by the strain rate field; flame surface is generated at the locations where the strain-rate structures interact. Contours of strain-rate magnitude between 0 s^{-1} (blue) and 1500 s^{-1} (red). Flame is represented by the thick yellow line. Flow is from bottom to top, reactants are on the left, the field of view is 6 mm x 10.5 mm, and the time between frames is 0.9 ms.

4.6 Positive curvature wrinkles

In the above discussion, turbulence-flame interactions have been considered in which extensive strain was exerted on the flame, producing flame surface area that was formed into wrinkles with negative curvature. Such interactions play an important role in the stretching of the flame and have been the basis for most previous studies. However, other interaction geometries also occur. In particular, the opposite process is important; turbulence that exerts compressive strain on the flame and generates wrinkles with positive curvature must be considered.

These interactions are especially important since positive curvature wrinkles tend to grow with time, while negative curvature wrinkles tend to shrink. When turbulence forms a positive curvature flame wrinkle, it propagates outwards into the reactants, increasing in area. It will continue to do so until it is further affected by the turbulence or encounters some boundary constraint. Negative curvature wrinkles (such as those considered above) tend to form cusps and shrink due to kinematic restoration (Huygen's principle). Hence, interactions that form positive curvature wrinkles are important for the generation of flame surface area.

The canonical picture of this process is shown in terms of the vortical structures in Fig. 4.35. Such an interaction measured using the CS-PIV is shown both as the vorticity field and strain-rate field in Figs. 4.36 and 4.37. As can be seen, there is very little compressive strain rate exerted on the flame; the strength of the strain rate structure is considerably less than in Figs. 4.12-4.14. This weak strain rate is somewhat intrinsic to this type of interaction as the positive curvature wrinkle tends to force the vortical structures apart and reduce the strength of the strain-rate structure. However, the vortical structures incite a positive curvature wrinkle

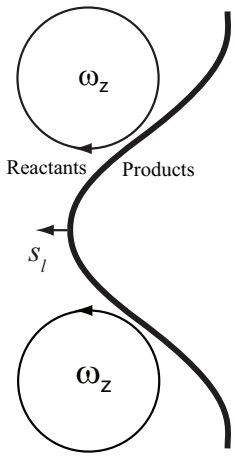

Figure 4.35: Schematic of an inwardly rotating pair of vortical structures creating a positive curvature flame wrinkle.

to form. The area of this wrinkle grows considerably due to propagation. Hence, interactions of this type are extremely important for the generation of flame surface area due to curvature stretch.

4.7 The statistics of strain-rate and curvature

The positive curvature wrinkle and compressive strain rate seen in Figs. 4.36 and 4.37 raise an important question: what is the distribution of strain rates and curvatures on the flame front? As mentioned previously, the canonical counter-rotating vortex geometry used to develop the stretch efficiency function states that the only effect of turbulence on the flame is to cause extensive strain rate and negative curvature [74]. The strain-rate and curvature submodels used in various LES implementations employ this paradigm [22, 52].

To analyze the validity of these assumptions, profiles of strain rate and curvature along the flame surface were calculated. These are shown in Fig. 4.38 for a few instants in the measured data. As can be clearly seen, both quantities vary between positive and negative values. While the strain-rate profiles have an essentially random shape, the curvature profile have some distinct characteristics. There are small

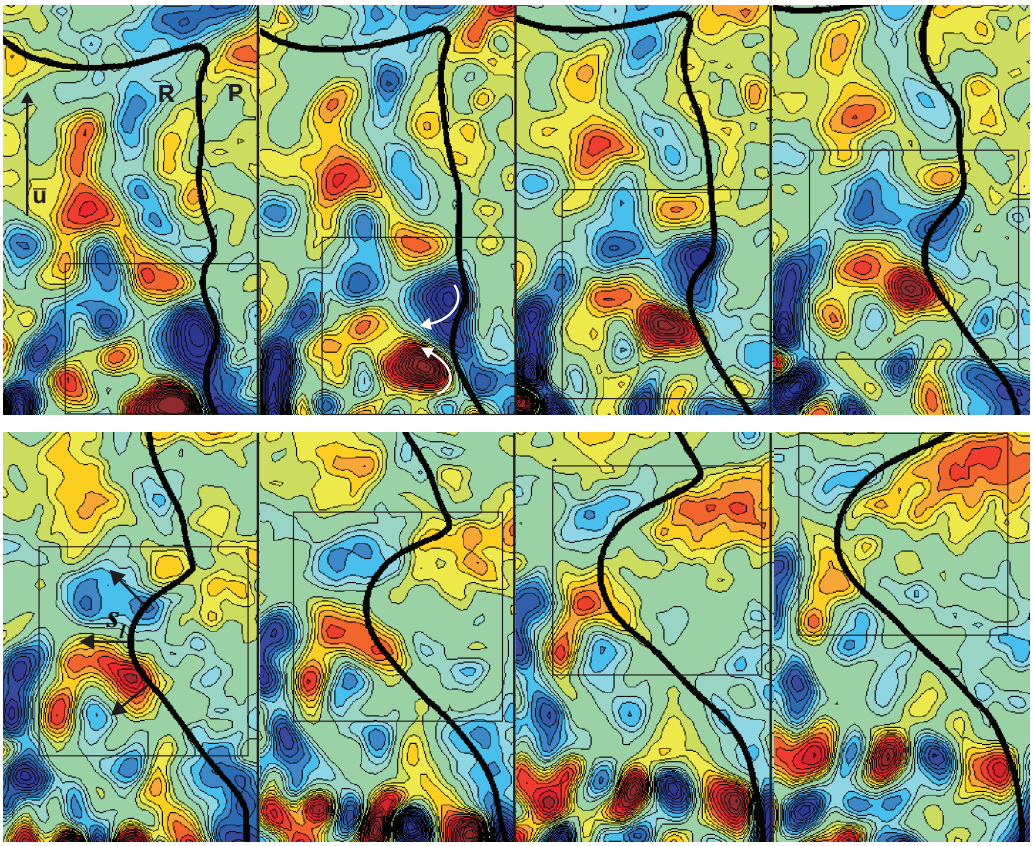

Figure 4.36: Measured interaction of an inwardly rotating pair of vortical structures creating a positive flame wrinkle. Due to the positive curvature, the wrinkle grows in size as it propagates. Contours of vorticity between -1200 s^{-1} (blue) and 1200 s^{-1} (red). Flame is represented by the thick black line. Flow is from bottom to top, reactants are on the left, the field of view is 6.5 mm x 10.5 mm , and the time between frames is 0.9 ms.

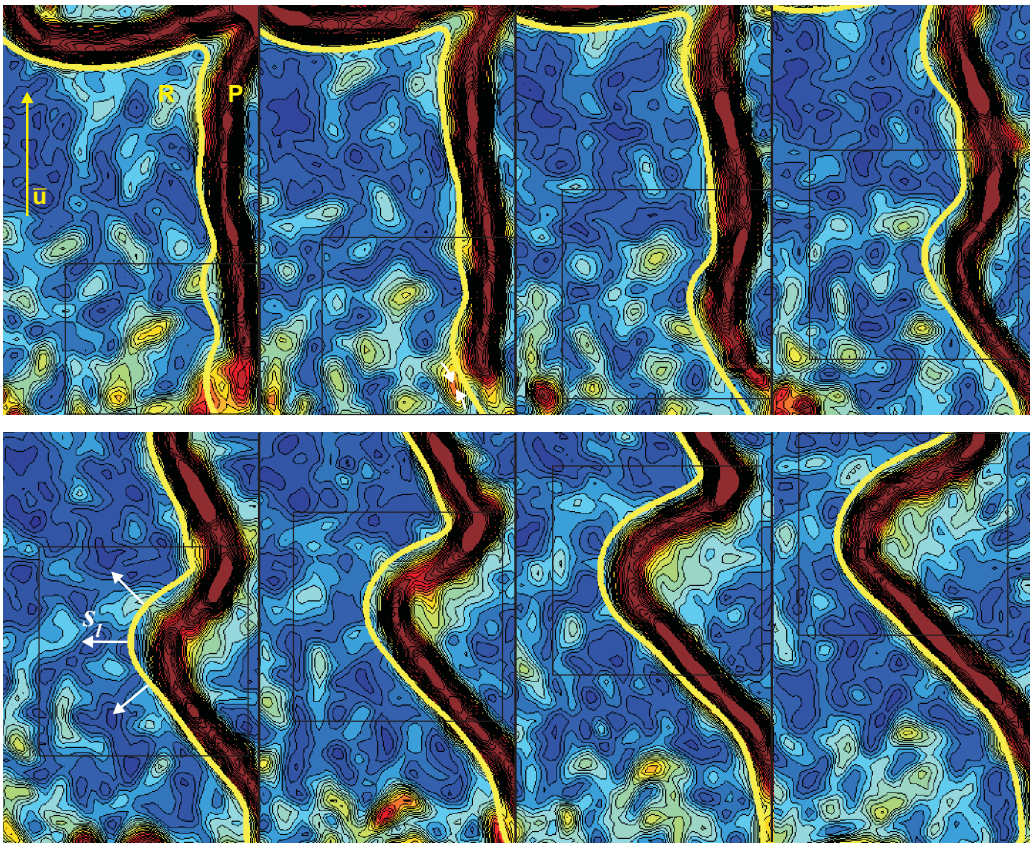

Figure 4.37: Strain rate field corresponding to Fig. 4.36. The strain-rate structure exerts weak compressive strain on the flame as the positive curvature wrinkle forms. Contours of strain-rate magnitude between 0 s^{-1} (blue) and 1500 s^{-1} (red). Flame is represented by the thick yellow line. Flow is from bottom to top, reactants are on the left, the field of view is 6.5 mm x 10.5 mm, and the time between frames is 0.9 ms.

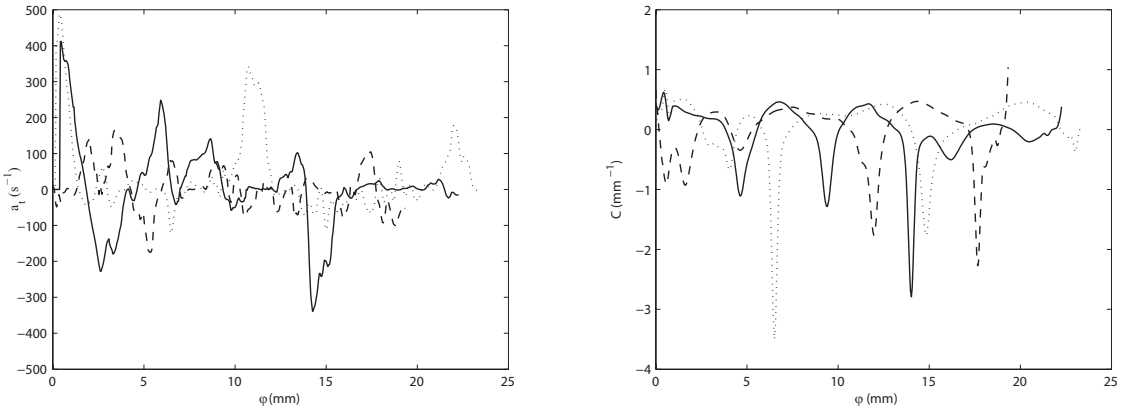

(a) Strain rate

(b) Curvature

Figure 4.38: Typical profiles of a_t and C versus distance along the flame surface (φ). The strain rate varies between positive and negative values. There are small regions of high negative curvature indicating cusps and larger regions of low positive curvature indicating expanding wrinkles. The different lines represent different instances in time.

regions of high negative curvature and larger regions of lower positive curvature. This is exactly the profile expected for a propagating curved wave. That is, regions of negative curvature tend to form cusps due to kinematic restoration. Regions of positive curvature tend to grow and, as they are doing so, reduce in curvature (consider an expanding laminar spherical flame).

The distribution of strain rate and curvature is further educed by their respective PDFs. To construct the PDFs, the x-coordinate was divided into bands of 1 mm. The strain rate and curvature statistics in each of these bands was then compiled. Division of the domain was necessary since the turbulence and flame wrinkling varied with downstream distance; the PDFs also varied. Data from approximately 10000 vector fields were used for each test case.

The PDFs of strain rate at various heights for each case are provided in Fig. 4.39. A few trends are clearly apparent. Firstly, the strain rates were distributed amongst positive and negative values. Near the base of the flame, the strain rate exhibited a distinct positive tendency. This diminished downstream, and at some point the PDFs appeared essentially symmetric. The positive skewness at the flame base varied slightly from case to case; Case 2 displayed the most positive strain rate, followed by Case 3 and Case 1. This is likely due to minor differences in the boundary conditions at the base. That is, the co-flow stream was set to minimize shear over the entire length of the flame. To do so, the conditions immediately at the base of the flame varied slightly. Nevertheless, the results show that the strain rates are not exclusively positive as dictated by the canonical vortex configuration.

However, the mean strain rate exerted on the flame was positive. This is shown by the downstream profiles in Fig. 4.40. As the downstream distance increased, the mean strain decreased. This was expected since the turbulence decayed downstream.

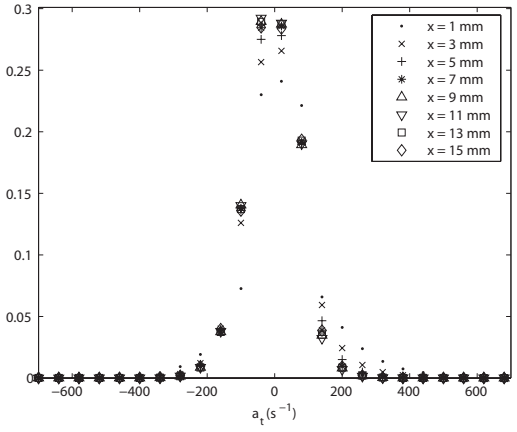

(a) Case 1 - $\phi = 0.6$

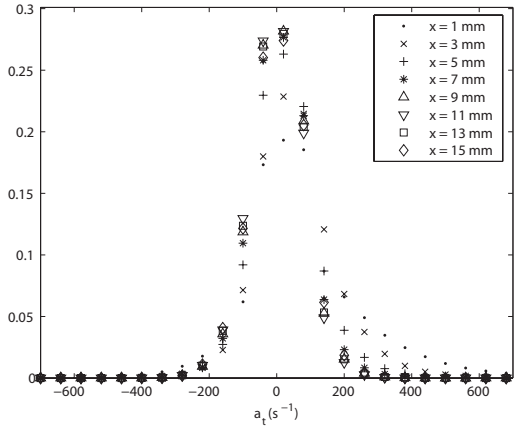

(b) Case 2 - $\phi = 0.7$

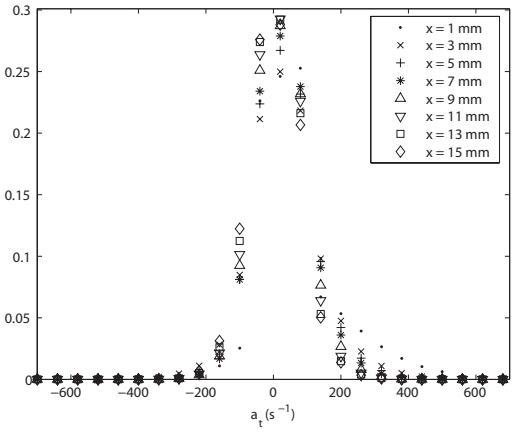

(c) Case 3 - $\phi = 1.35$

Figure 4.39: PDFs of a_t at various heights in the flames.

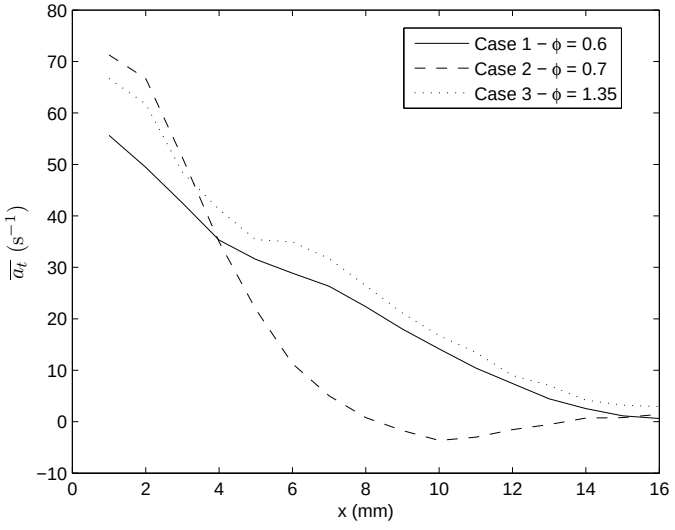

Figure 4.40: Downstream profiles of the mean strain rate on the flames.

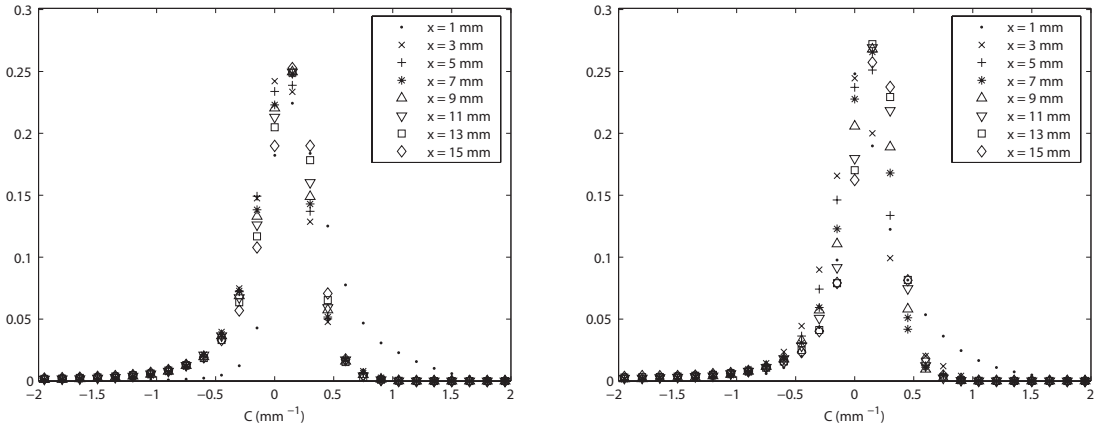

(a) Case 1 - $\phi = 0.6$

(b) Case 2 - $\phi = 0.7$

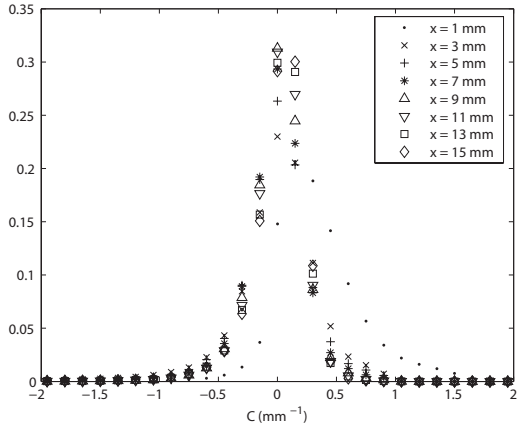

(c) Case 1 - $\phi = 1.35$

Figure 4.41: PDFs of C at various heights in the flames.

Additionally, there were distinct differences in the profiles of mean strain rate for the different cases. In particular, Cases 1 and 3 had similar profiles, while Case 2 differed. This was due to the difference in the mean position of the flames. As seen in §3.2, the flames in Cases 1 and 3 had similar heights, $\overline{c}$ contours, and $\overline{\Sigma}$ contours. Hence, they were similarly oriented and exposed to the flow. The flame in Case 2 was significantly shorter, oriented differently with respect to the flow, and exposed to different locations in the flow. The profile of mean strain rate was therefore different. Nevertheless, these profiles do indicate that the net effect of the strain rate exerted on the flame by turbulence was to increase the flame surface area.

The PDFs of curvature, shown in Fig. 4.41, also exhibited some interesting fea-

tures. Near the base of the flame, the mean curvature was positive for all cases, likely due to the specific boundary conditions of this geometry. At downstream locations, the PDFs became skewed towards larger negative curvatures; a negative tail appeared on the PDFs. The most likely curvature was slightly positive. Once again, this was expected based on the development of cusps and expanding regions as described above.

The downstream profiles of the mean and most expected curvature, shown in Fig. 4.42, further demonstrate the trends listed above. The mean curvature for all cases was positive at the base and quickly approached zero. This indicates a near balance between effects of the small regions of high negative curvature and large regions of low positive curvature for all flames. The most probable C, $[C]$, was dependant on the manner in which the curvature data was binned. Hence, the width of these bins is indicated by the error bars in the figure. The most likely curvature was positive or zero throughout, confirming the significance of the outwardly expanding portions of the wrinkles. It should also be noted that the base of the flame is a region of both positive strain rate and curvature stretch rate. Hence, flame surface area is produced at this location. The implications of this are discussed in greater detail below.

4.8 Implications for modeling

The phenomenological and statistical information expounded above have significant implications for the modeling of turbulent premixed flames, both in terms of submodels and balance assumptions. Firstly, current formulations for the subgrid strain rate and curvature stretch rate are incomplete. Secondly, the assumption of balance between these terms appears to be inaccurate and transport of flame surface is significant. If transport is significant, algebraic formulations for the local turbu-

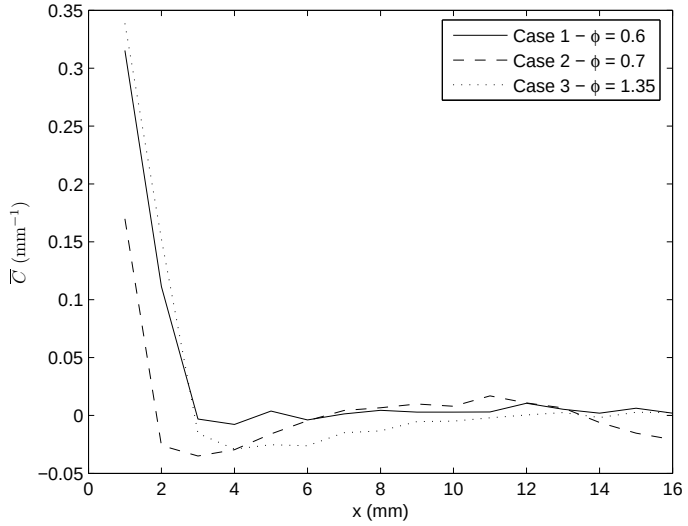

(a) Mean curvature

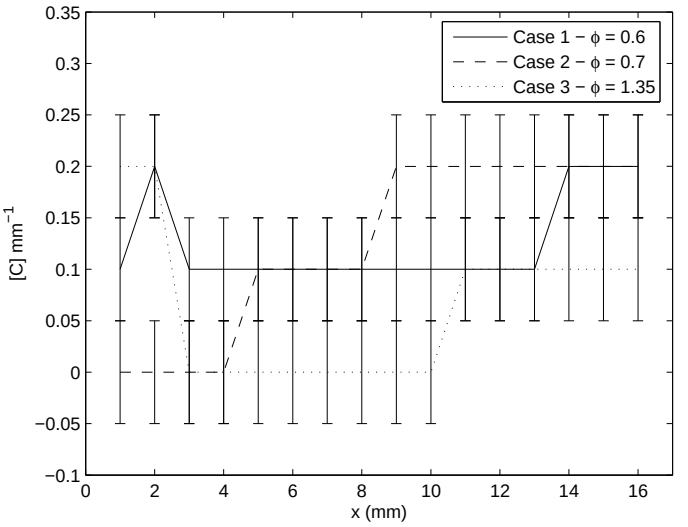

(b) Expected curvature

Figure 4.42: Downstream profiles of the mean and most expected curvature of the flames. The error bars on the most expected curvature indicate the width of the bins.

lent burning velocity would not accurately describe the local increase in flame surface area.

Current models for the strain rate typically relate a_t to the stretch efficiency function (see §1.6). This implies that the strain rate is completely described by vortex pair-flame interactions and that the strain rate is always positive. Furthermore, the efficiency functions are derived based on characterizing the interaction by properties of vortices. However, both of these attributes have been shown to be incorrect. Firstly, the interaction between turbulence and the flame is not described by counter-rotating vortices. Very few vortex pair interactions were observed and much more complex arrangements of turbulent structures caused significant strain and wrinkling. Even within the few interactions resembling the canonical configuration, the strain rate exerted on the flame was not characterized by the vortices; it was the fluid dynamic strain rate field that described the interaction. It was also observed that negative strain rates were often exerted on the flame. Hence, relating the total strain rate to a sum of extensively straining events would greatly over predict a_t. Modeling the strain rate based on counter rotating vortices is therefore inappropriate.

Models for the flame curvature make the incorrect assumption that the mean is always negative. In Refs. [51, 52], C is negative and proportional to the flame surface density. In Refs. [22, 23], it is negative and equal in magnitude to the strain rate (which is positive as described above). In either case, the results of §4.6 and §4.7 indicate flaws with these models. Large positive curvature wrinkles were found to be created by the turbulence. Since such wrinkles propagate outwardly, they tend to grow with time while reducing in curvature magnitude. Negatively curved wrinkles tends to shrink with time while increasing in curvature magnitude. The statistics indicate that the mean curvature is often around zero, and the most expected cur-

vature positive. Near the base of these flames, the mean was also positive. Hence, the assumption that the curvature stretch rate is negative appears incorrect.

Beyond the consequences for specific submodels, the above two observations have a significant implication regarding the transport of flame surface: it must be considered. In a turbulent premixed flame, there are regions in which flame surface is created and regions in which it is destroyed. In a statistically stable flame, the net production must balance the net destruction over the entire flame. However, these processes do not need to be overlapping. In the current flames, production of flame surface area took place near the base where the mean strain rate and curvature were positive. The flame surface thus produced convected downstream and was eventually destroyed. In a Bunsen flame, the destruction location is obviously the tip of the flame. This is a highly negatively curved region that acts as a sink for the flame surface produced below. The dynamics of the tip are very complex, but must be such that they balance the local transport of flame surface. This includes local propagation along with the convection, generation, and destruction.

The local balance between production and destruction of flame surface that is assumed in some models is therefore not generally correct. Of course, there can be situations where there is no mean transport. This would be the case in flames that are statistically stationary in space and time. For example, a planar flame propagating steadily into homogeneous turbulence would have no mean transport of flame surface to different locations. Algebraic balance relationships for the flame surface density may work in such scenarios [19]. However, in complex systems (though even as simple as Bunsen flames) the transport is important. It is noted that Refs. [22, 23] assume a balance between *subgrid* strain rate and curvature. However, this is based on a older RANS assumption for the global balance and there is no further justification

given [11]. There does not appear to be any intuitive reason why it should hold in the subgrid, but this will be addressed in Chapter VI.

The importance of flame surface transport also has implications for models of the turbulent burning velocity. If flame surface is transported, the local flame surface area and hence turbulent burning velocity is not based solely on the local turbulence. It is instead influenced by all of the wrinkling that has happened previously and has been transported to that location. This is another way of regarding the winkling 'memory' apparent in Bunsen flames that was discussed in §1.9.1. Algebraic relationships such as those discussed in §1.9 are unable to account for flame surface transport and may produce inaccurate results. While they may perform well in statistically stationary situations as described above, they will be unlikely to do so in more complex situations (or even Bunsen flames). This would cause problems for G-equation methods that employ such relations to determine the propagation speed of the $G = G_0$ surface. Instead, such simulations may require a subgrid model that include a transport equation for the flame surface density or flame wrinkling. These quantities could then be related to the turbulent burning velocity. All of these considerations will be discussed further in Chapter VI.

4.9 An aside: the hydrodynamic instability

Throughout this Chapter, the stretching of the flame surface has been considered to be a result of velocity fluctuations in the reactants associated with turbulence. That is, the fluctuations were generated by some form of shear between the flowing gas and either the apparatus or fluid at a different speed. There is however an additional source of velocity gradients in the reactants of a turbulent premixed flame: the flame front itself. These velocity gradients are associated with the hydrodynamic

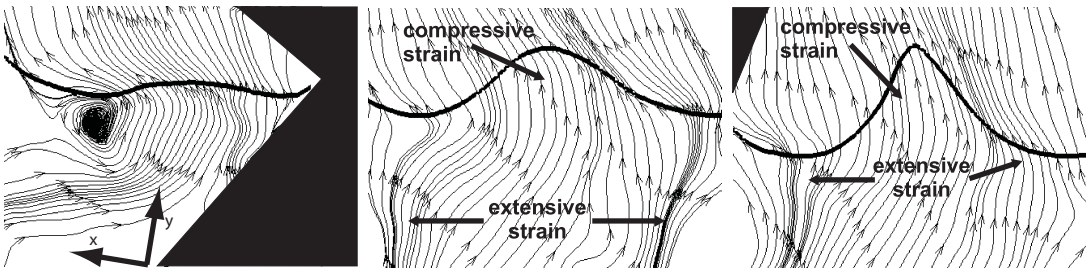

(a) t = 0 ms (b) t = 6.3 ms (c) t = 12.6 ms

Figure 4.43: Measured development of a wrinkle due to the hydrodynamic instability. Streaklines shown relative to mean downstream velocity in the reactants. Diverging and converging streaklines show extensive and compressive strain respectively. Black regions are outside the field of view.

instability and can be described phenomenologically by continuity and gas expansion as shown in §1.11. The flow pattern associated with this process consists of streamlines that converge in negatively curved regions of the flame and diverge in positively curved regions. This causes a velocity difference that promotes wrinkle growth.

This phenomenon was apparent in the current measurements as demonstrated in Fig. 4.43. In this Figure, the flow field has been rotated such that the wrinkle growth is in the vertical direction. Instantaneous velocity streaklines are shown in a reference frame moving at the mean reactant velocity. These streaklines were computed by tracing the path of hypothetical fluid elements following the instantaneous velocity field. At $t = 0$ ms, a perturbation in the flame front was generated. This caused velocity gradients to form in the reactants. At $t = 6.3$ ms, the predicted pattern of diverging streamlines at the positively curved regions and converging streamlines in the negatively curved region was evident (c.f. Fig. 1.9). At $t = 12.6$ ms a large wrinkle had been formed. At this point, competition between wrinkle growth due to the hydrodynamic instability and stabilization due to Huygens principle determined the behavior of the wrinkle.

It is therefore apparent that the hydrodynamic instability mechanism does occur in turbulent premixed flames and can cause significant flow patterns and wrinkle

growth. Hence, this mechanism should be considered as a source of flame surface area in models. Unfortunately, the current experiment was not well suited to derive a detailed description of such a source term. This is because the hydrodynamic instability is much more significant in apparatuses where the maximum hydrodynamic length scale is orders of magnitude larger than any flame length scale [15]. While the hydrodynamic instability was apparent in the current measurements, the length scales were not large enough to truly develop strong wrinkling from this mechanism. Furthermore, any description must include the effects of varying the apparatus size, which was not done. Nevertheless, it was apparent that the hydrodynamic instability flow pattern did develop and could cause significant changes in the reactant velocities.

CHAPTER V

The Geometry of Turbulence-Flame Interactions

In the previous Chapter, it was shown that the canonical geometry of counter-rotating vortex pairs is inadequate to describe the interaction of a turbulent flow field with the flame. The planar measurements taken using the CS-PIV showed complex vorticity and strain rate fields interacting with the flame, generating surface area and creating wrinkles. The geometries of these interactions were not encompassed by the canonical configuration. Furthermore, the turbulence was found to generate significant negative strain and positive curvature. Such effects are not accounted for by the canonical geometry.

In this Chapter, the geometry of turbulence-flame interactions is further studied using the three-dimensional OPCS-PIV measurements. To begin, the structure of non-reacting turbulence is investigated and the resultant geometries compared to predictions from DNS. Typical interactions of such 3D structures with the flame are then presented. These illustrate the complex geometry of three-dimensional turbulence and how planar measurements can be misleading. Finally, the orientation of the vorticity and strain rate fields with respect to the flame surface is discussed. These orientations are compared to those stipulated by the canonical flame-vortex interaction and found to encompass a much wider breadth of possibilities. From these

observations, it is argued that developing models for the strain rate or curvature based on simple, *a priori* turbulence configurations is inadequate.

5.1 The geometry of turbulence

The appearance of the toroidal vortical structure in Fig. 2.19 begs the question: what is the structure of turbulence? This is a question that has garnered much debate and at present there is no consensus answer; there is not even a consensus on what a turbulent structure is. Nevertheless, it is interesting to compare the structures measured using the OPCS-PIV diagnostic to those computed using high resolution DNS.

Two types of vortical structures are commonly identified. High intensity (threshold) vorticity tends to concentrate into fine scale structures that are longer in one dimension than the others. These are the taxonomical 'tube'- or 'worm'- like structures. At lower threshold levels, both bundles of tubes and 'sheet'-like structures have been identified [10, 75]. These types of structure were abundant in the present measurements. For example, Fig. 5.1 shows a vortical structure at two different threshold levels: $\omega = 700$ s^{-1} (Fig. 5.1(a)) and $\omega = 1000$ s^{-1} (Fig. 5.1(b)). At the lower threshold, the structure appeared as a connected bundle of interwoven tubes. As the threshold was increased, the individual tubes became apparent. The longest dimension of the tube-bundle was about 6.2 mm. This is larger than the turbulence integral scale. However, since the integral scale is an average quantity, it is not surprising that one dimension of an instantaneous structure exceeds this. The radial dimension of the tube-like structures at $\omega = 1000$ s^{-1} ranged from about 0.4 mm to 1.1 mm. The smallest of these corresponded well to the predicted viscous cutoff scale λ_ν.

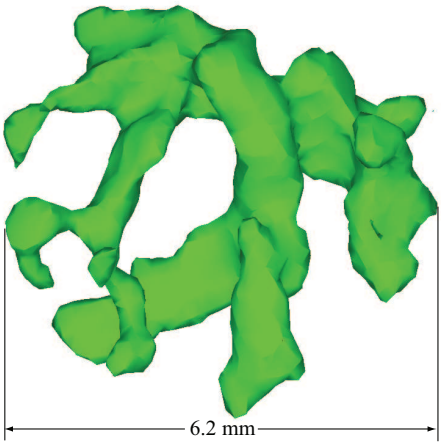

(a) Bundle of vortex tubes at $\omega = 700$ s^{-1}

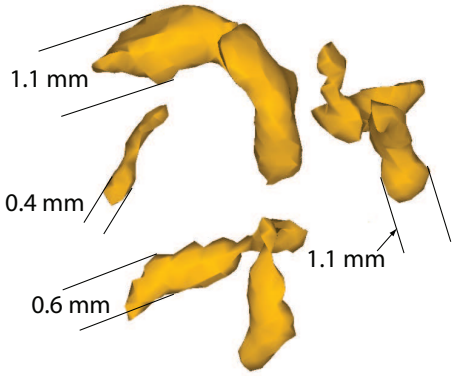

(b) Individual vortex tube structures at $\omega = 1000$ s^{-1}

Figure 5.1: Tube-like vortical structures at different threshold levels.

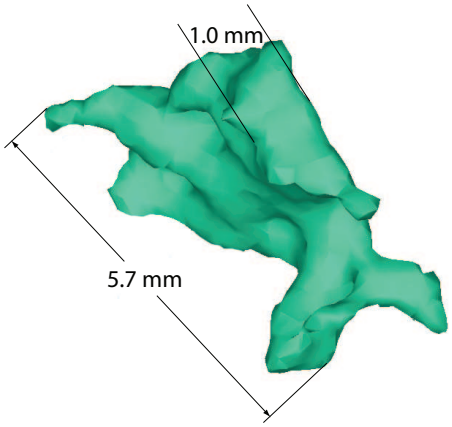

Figure 5.2: Sheet-like vortical structure at a threshold of $\omega = 700$ s^{-1}.

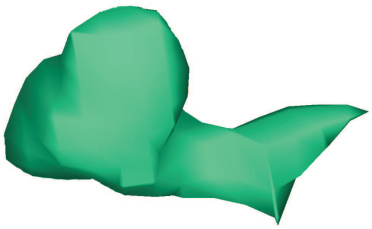

Figure 5.3: Amorphous (blob-like) strain-rate structure at a threshold of $S = 700$ s^{-1}.

A typical sheet-like vortical structure is shown in Fig. 5.2 at a threshold level of $\omega = 700$ s^{-1}. While sheet-like structures were apparent in the recorded data, they are not nearly as abundant as the tube bundles. However, this may be a consequence of the limited inertial range in this flow.

Structures of concentrated strain rate magnitude were also observed. At lower threshold levels, these structures existed as both amorphous blobs and interconnected assemblies of sheet-like structures as shown in Figs. 5.3 and 5.4. At higher thresholds the assemblies broke into simple sheet structures such as seen in Fig. 5.5. The amorphous structures remained amorphous even for higher threshold levels. All of these structures are very similar to the dissipation rate structures ($\varepsilon = 2\nu S_{ij}S_{ij}$) reported from DNS and experiments [10, 45, 75]. From these structures it is clear that the geometry of turbulence is far more complex than expressed by counter-rotating vortices.

5.2 Three-dimensional turbulence-flame interactions

The above turbulent structures illustrate a simple fact: the three-dimensional geometry of turbulence is very complex. As demonstrated in Chapter IV, even when planar cuts of the turbulence were considered, the geometry of the interactions did not commonly occur in simple configurations. Large groups of structures would often interact with the flame simultaneously or in sequence. Planar slices that resembled

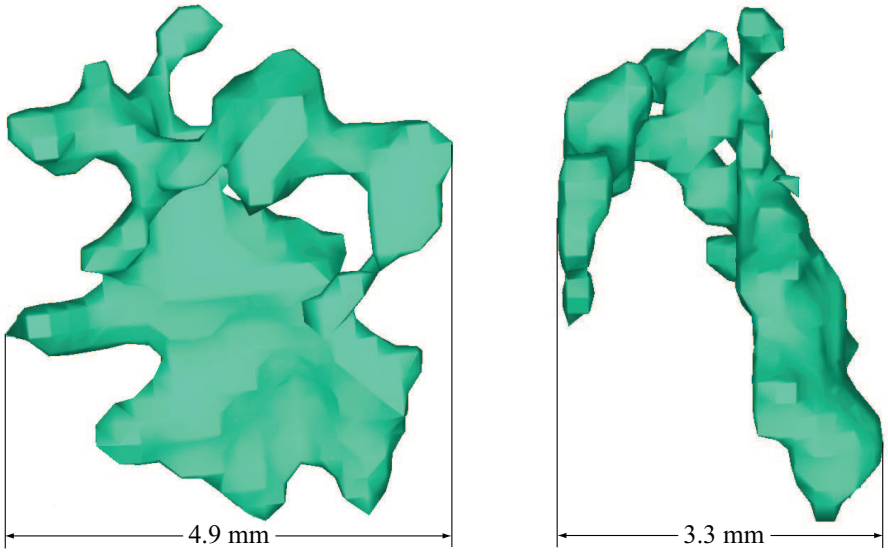

(a) Front view (b) Side view

Figure 5.4: Interconnected sheet-like strain-rate structures at a threshold of $S = 700\ \mathrm{s}^{-1}$.

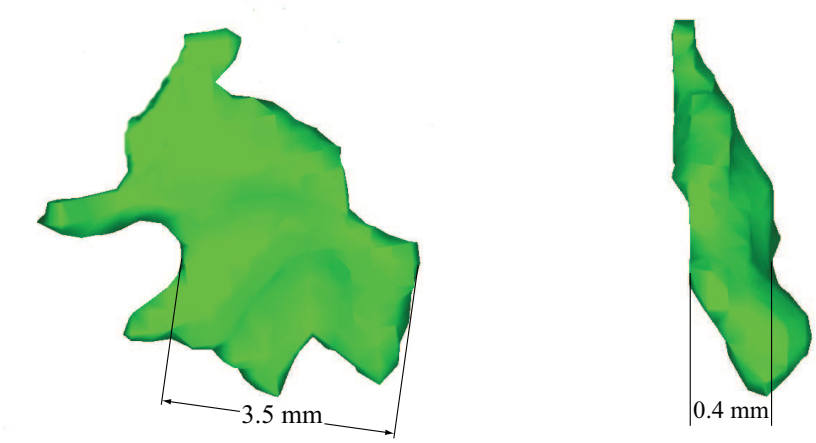

(a) Front view (b) Side view

Figure 5.5: Individual sheet-like strain-rate structure at a threshold of $S = 1000s^{-1}$.

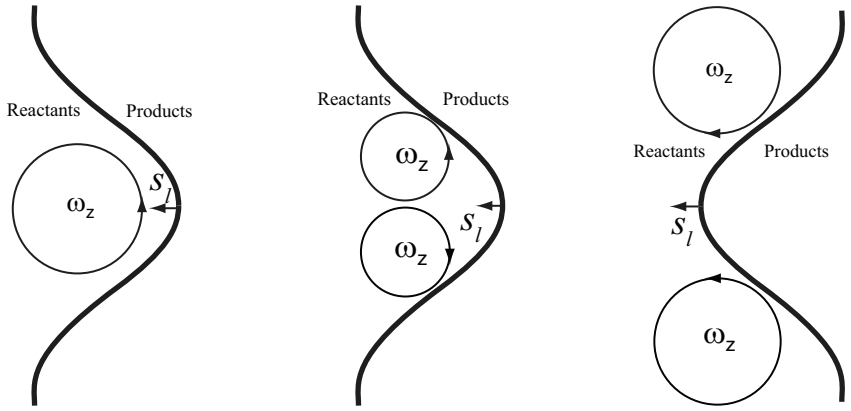

(a) Single vortex

(b) Outwardly rotating vortex pair

(c) Inwardly rotating vortex pair

Figure 5.6: Canonical configurations for turbulence-flame interactions.

the canonical counter-rotating vortex pair geometry were quite rare. However, even in the cases where the planar cuts were relatively simple, the three-dimensional turbulence could have possessed a complex geometry.

To demonstrate this, three simple planar geometries were considered. These are illustrated in Fig. 5.6 and correspond to three classically conceived configurations. In the first, a single vortical structure wraps the flame into a wrinkle. The second and third correspond to two configurations discussed in Chapter IV: the canonical counter-rotating vortex pair creating a negative curvature wrinkle and the counter-rotating vortex pair creating a positive curvature wrinkle. For each case, the Cinema-PIV component (C-PIV$_0$) of the OPCS-PIV diagnostic was first used to identify time sequences in which the vorticity fields in the vertical plane (image plane 2) resembled these configurations. The 3D turbulence-flame interactions were then reconstructed as described in §2.4.

The first interaction presented corresponds to the configuration shown in Fig. 5.6(a) and the planar visualization from the C-PIV$_0$ is shown in Fig. 5.7. In this interaction, what appears to be a single vortical structure wraped the flame surface into a simple wrinkle. The three-dimensional images of this interaction are presented

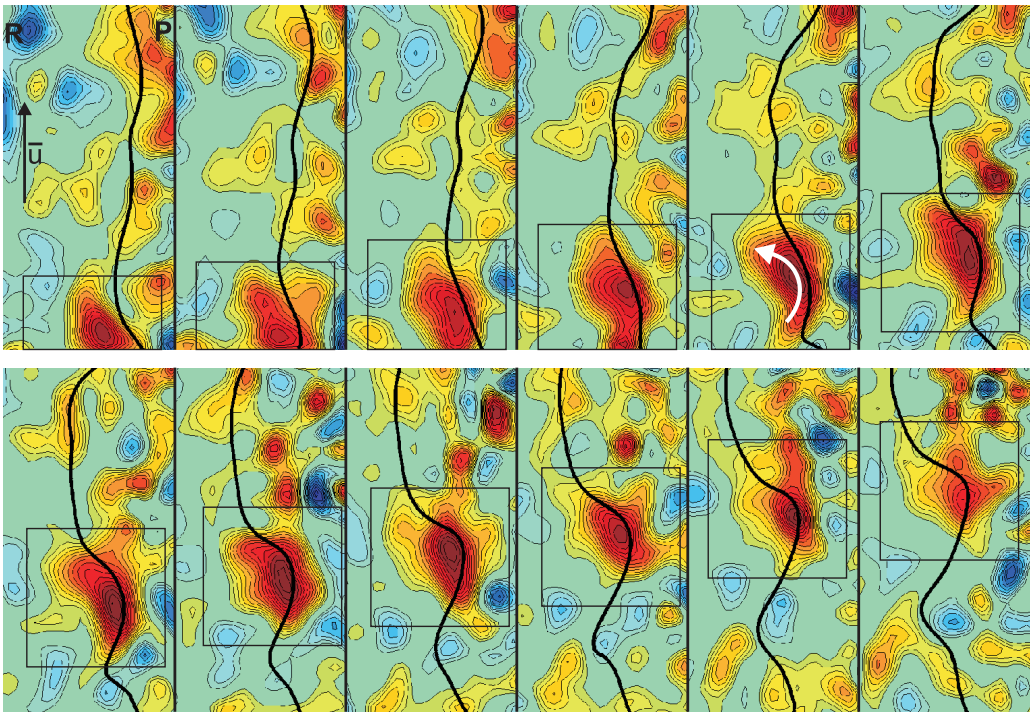

Figure 5.7: Planar measurement in image plane 2 from C-PIV. Interaction shows what appears to be a single vortical structure wrinkling the flame. Contours of ω_z between -1000 s^{-1} (blue) and 1000 s^{-1} (red). Flow is from bottom to top. Reactants are on the left. Field of view is 5 mm x 10 mm and the time between frames is 0.33 ms. The time sequence begins with the top left frame.

in Fig. 5.8. The flame in both the vertical and horizontal planes is shown as the black lines. The boxed structure in Fig. 5.7 was extracted and evolved as it moved downstream. When reconstructed in 3D, the turbulence was clearly seen to have a horseshoe like shape; there were two counter rotating branches meeting at an end. The single structure visualized in the planar measurements was a cut through this common end. Hence, both the planar measurements and simple vortex interpretation do not reflect the complexity of this interaction.

In the second interaction, a counter-rotating pair of vortical structures interacted with the flame. The flame was strained in the center, producing flame surface. This flame surface was wrapped into a wrinkle by the vortices. The 2D and 3D visualizations of such an interaction are shown in Figs. 5.9 and 5.10. The planar

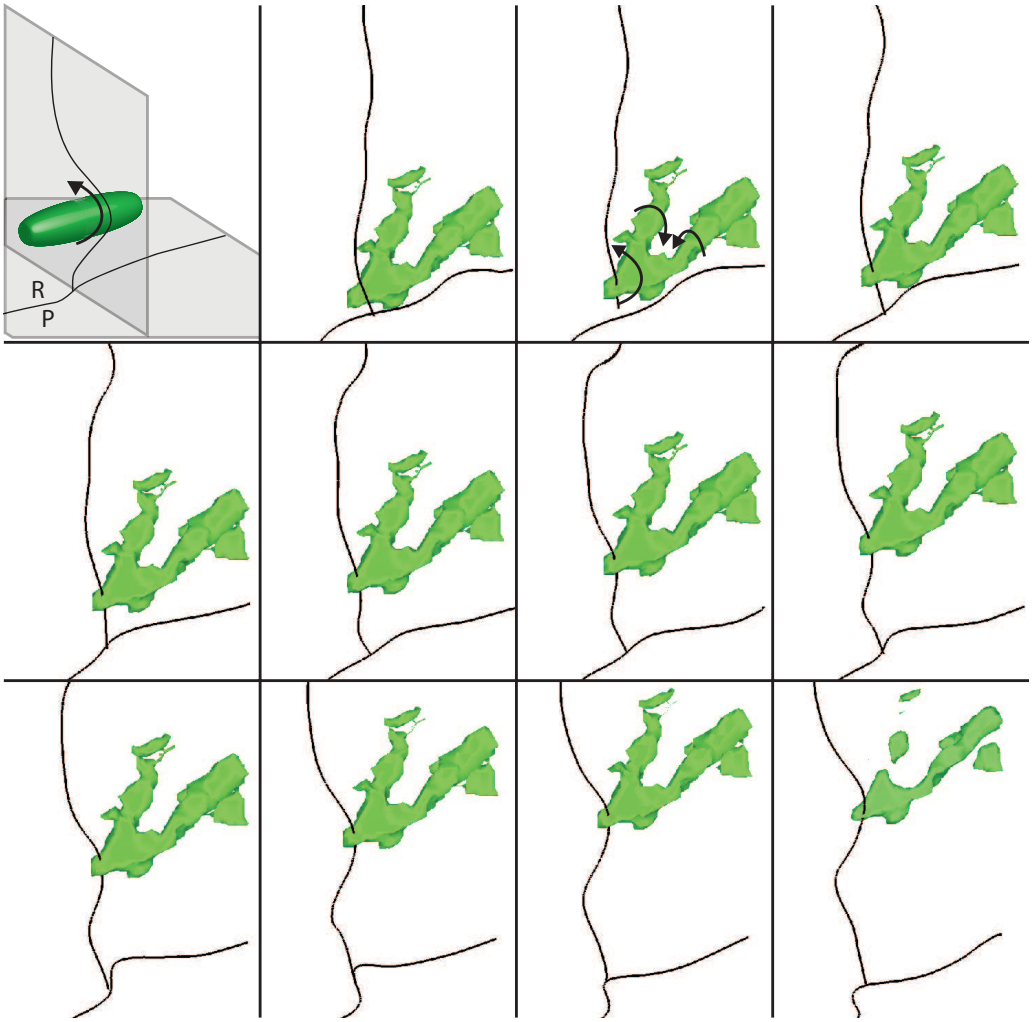

Figure 5.8: Measured images of a horseshoe shaped vortex interacting with the flame (the flame contour in each plane is indicated by the thick black lines). The first frame shows a schematic of the 3D canonical configuration for this interaction. The single structure observed from the planar measurement (Fig. 5.7) is actually the connected end of the horseshoe. Isosurface of $\omega = 700$ s^{-1} are shown. The flow is from bottom to top, the reactants are on the left, and the time between frames is 0.33 ms. The time sequence begins with the top left frame.

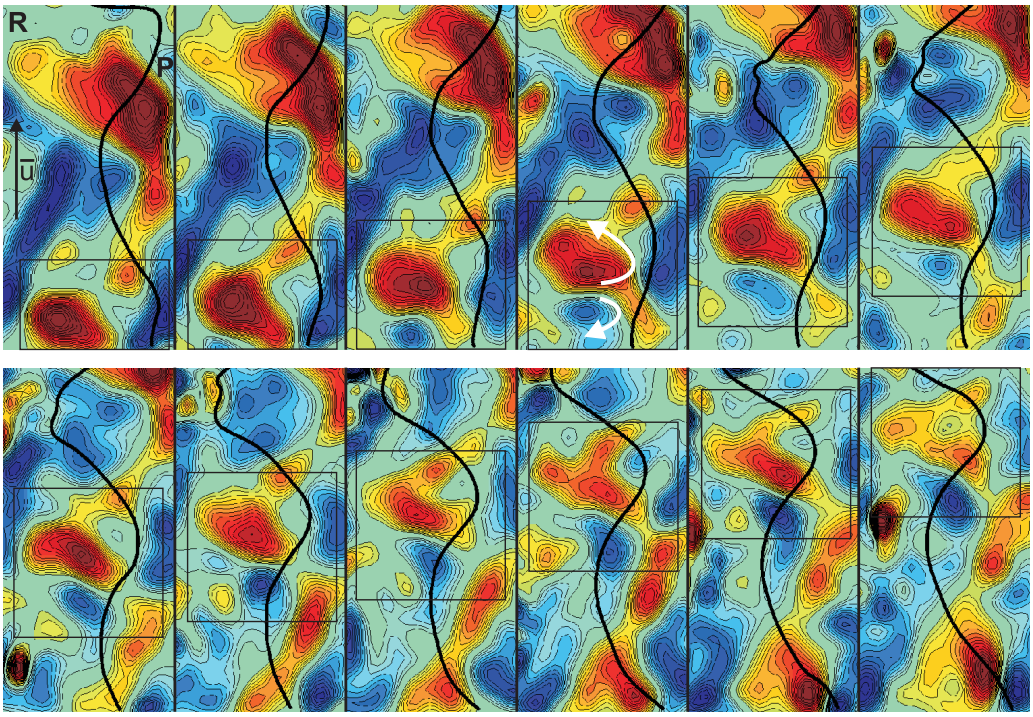

Figure 5.9: Planar measurement in image plane 2 from C-PIV. Interaction shows what appears to be a counter-rotating pair of vortical structures. The flame is strained between the structures and the flame surface is wrinkled. Contours of ω_z between -1000 s^{-1} (blue) and 1000 s^{-1} (red). Flow is from bottom to top. Reactants are on the left. Field of view is 5 mm x 10 mm and the time between frames is 0.33 ms. The time sequence begins with the top left frame.

cuts show a counter rotating vorticity field as expected. The 3D turbulence during this interaction did consist of a pair of counter rotating vortical structures. However, the geometry of the 3D structures was quite complex; their axes were angled with respect to each other and there were numerous bends in the structures; the lower structure had a horseshoe geometry. Also, the structures were pushed together in the center of wrinkle during the interaction. This was likely due to a hydrodynamic scale flow pattern created by the wrinkle and associated with the hydrodynamic instability. Such a flow pattern channels fluid into the negatively curved region of a flame wrinkle. Once again, interpreting this interaction by relating the planar measurements to the canonical geometry does not capture the complexity of the true 3D process.

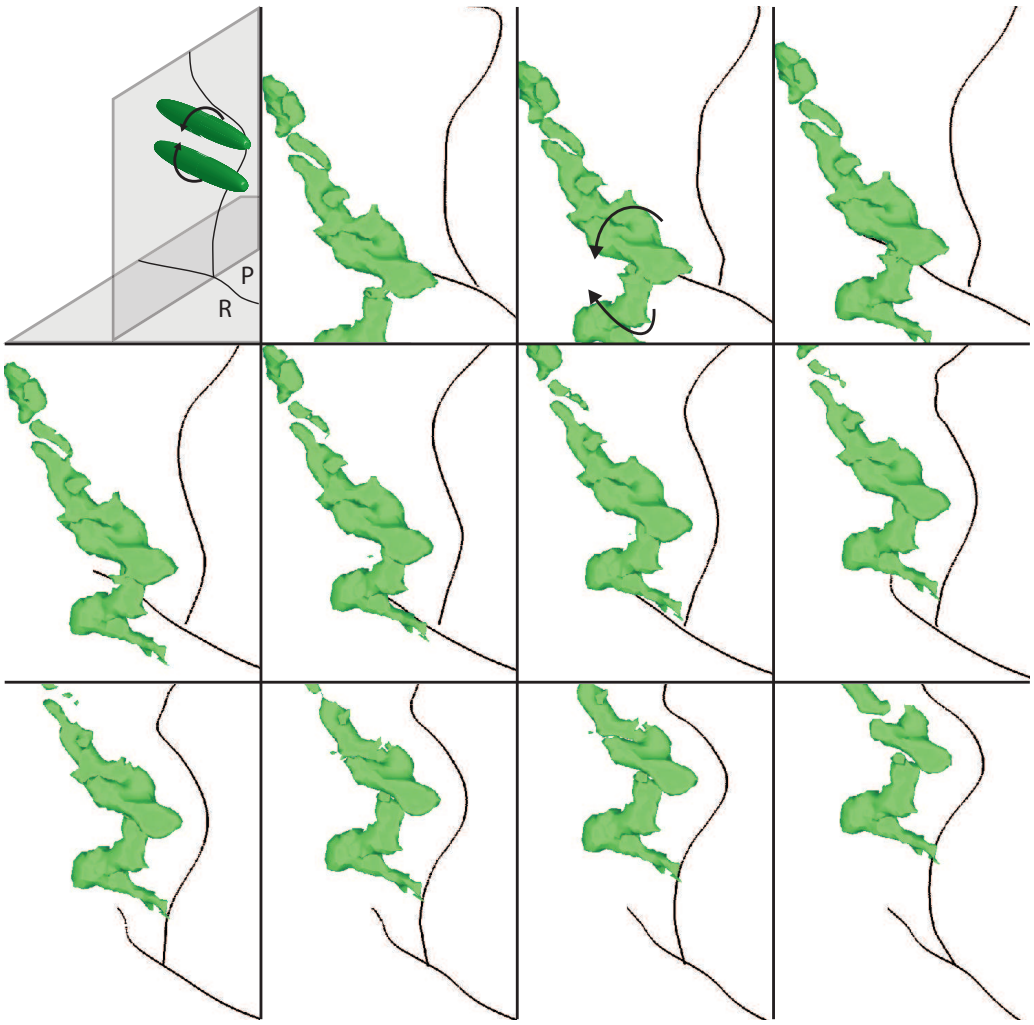

Figure 5.10: Measured interaction of two counter rotating vortical structures with the flame. The first frame shows a schematic of the 3D canonical configuration for this interaction. The geometry of the interaction and structures is much more complex than described by the canonical configuration (Fig. 5.6(b)) or planar measurements (Fig 5.9). Isosurfaces of $\omega = 700$ s^{-1} are shown. The flame contour in each plane is indicated by the thick black lines. The flow is from bottom to top, the reactants are on the left, and the time between frames is 0.33 ms. The time sequence begins with the top left frame.

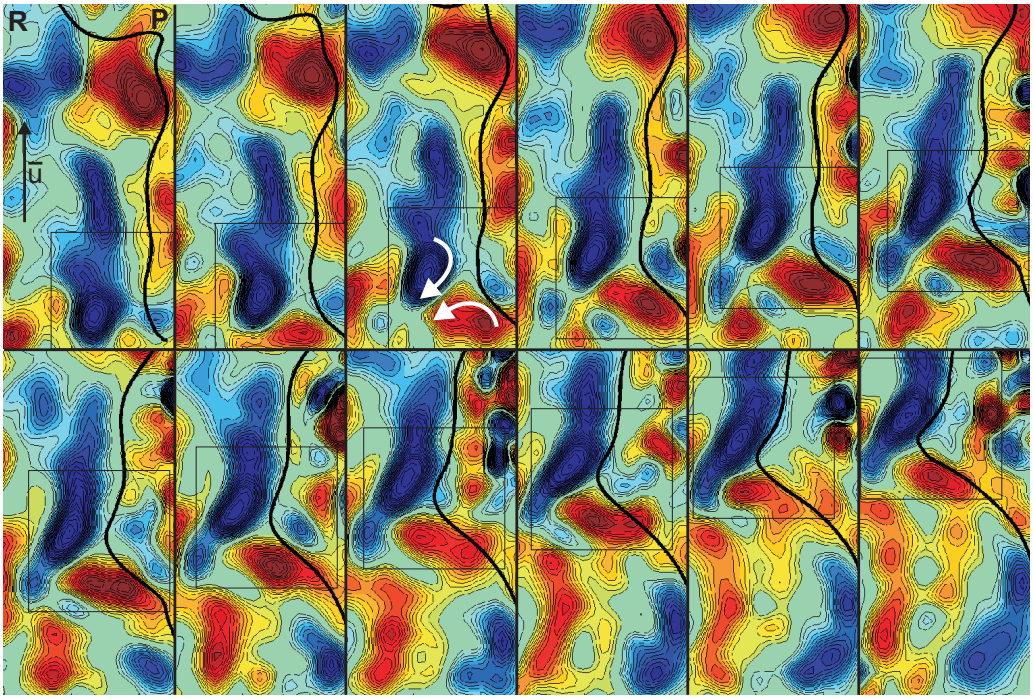

Figure 5.11: Planar measurement in image plane 2 from C-PIV. Interaction shows what appears to be a counter-rotating pair of vortical structures. The rotation is such that a positive curvature wrinkle is formed. Contours of ω_z between -1000 s^{-1} (blue) and 1000 s^{-1} (red). Flow is from bottom to top. Reactants are on the left. Field of view is 5 mm x 10 mm and the time between frames is 0.33 ms. The time sequence begins with the top left frame.

The complex geometry of the turbulence-flame interactions is further shown in the third configuration. This configuration consisted of a counter-rotating vorticity field creating a positive curvature wrinkle. The 2D and 3D visualizations of this interaction are shown in Figs. 5.11 and 5.12. The 2D slice clearly shows the classically conceived vorticity field. However, the geometry of the turbulence in 3D was once again very complex. There did exist two counter-rotating vortical structures, but the structures were intertwined. Furthermore, each individual structure was of a complex shape and oriented differently in space.

The above interactions illustrate a simple point: the geometry of turbulence-flame interactions is very complex. This poses a problem for stretch rate models based on the canonical configuration. Namely, these models assume that the stretching of the

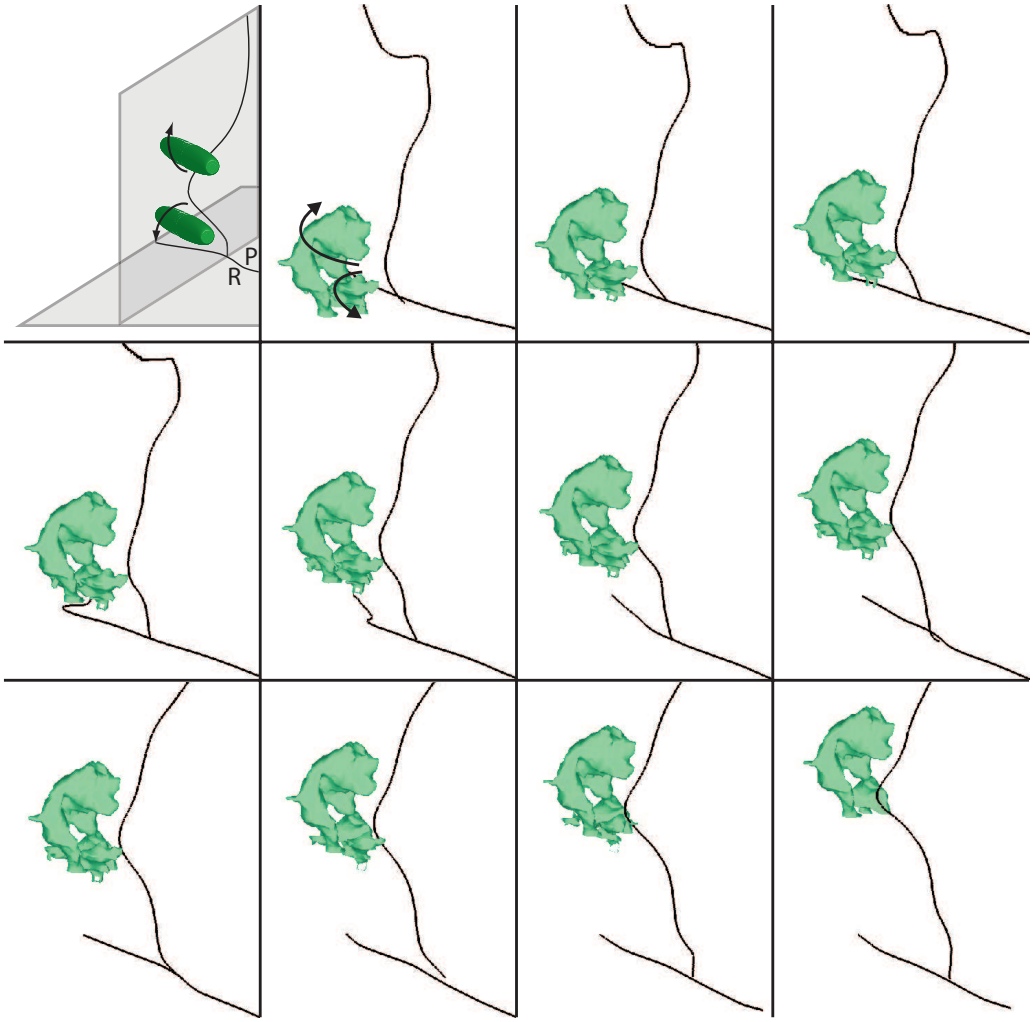

Figure 5.12: Measured interaction of two vortical structures generating a positive curvature wrinkle in the flame. The first frame shows a schematic of the 3D canonical configuration for this interaction. The geometry of the interaction and structures is much more complex than described by the canonical configuration (Fig. 5.6(c)) or planar measurements (Fig. 5.11). Isosurfaces of $\omega = 700$ s^{-1} are shown. The flame contour in each plane is indicated by the thick black lines. The flow is from bottom to top, the reactants are on the left, and the time between frames is 0.33 ms. The time sequence begins with the top left frame.

flame surface caused by turbulence at a particular scale and strength is described by a single interaction geometry. The stretch rate is characterized by simple properties of the turbulence and any turbulence having these properties is assumed to exert the same stretch rate. However, this is clearly not the case. Different turbulent structures of the same 'scale' and 'strength' would exert vastly different stretch rates on the flame depending on their orientation and geometry.

5.3 The orientation of $\vec{\omega}$, $\underline{S}$, and $\hat{n}$

From the above discussion, it is apparent that the geometry of individual turbulence-flame interactions is not well described by simple counter-rotating vortex ideas. The statistical accuracy of such a description can also be assessed using the OPCS-PIV. To do so, the orientation of $\vec{\omega}$ and $\underline{S}$ with respect to $\hat{n}$ in the vicinity of the flame was considered.

The canonical flame-vortex configuration implies a particular orientation of the vorticity field with respect to the flame. Since such a flow field is two dimensional, the vorticity vector is always normal to the flame sheet. In Fig. 5.6, $\vec{\omega} = \omega_z \hat{k}$ points out of the plane. The flame is planar and $n_z = 0$. Hence, $\vec{\omega} \cdot \hat{n} = 0$.

Furthermore, the canonical configuration implies a particular orientation of the strain rate field with respect to the flame. Consider the strain rate field associated with the counter-rotating Burgers' vortices in §4.4. As the strain-rate structure interacts with the flame, the strain rate along the centerline is always aligned either parallel or perpendicular to the flame surface. This can be shown by considering the eigenvectors of the strain rate tensor. As described in §1.10, the eigenvalues of $\underline{S}$ (ζ_i) represent the principal strain rates. The eigenvectors ($\vec{e}_i$) represent the directions in which these are exerted. In all cases the magnitude of the eigenvectors will be

normalized to unity. For this discussion, the eigenvalues will be order such that $\zeta_1 > \zeta_2 > \zeta_3$. Hence, the most extensive principal strain rate is listed first and the most compressive is listed last.

For the interaction of the strain rate structure in Fig. 4.23, the flow field is 2D and the most extensive and compressive principal strain rates balance ($\zeta_1 = -\zeta_3$). The intermediate eigenvalue is zero. The eigenvectors associated with ζ_1 and ζ_3 are perpendicular and lie in the $x-y$ plane. For the extensive and compressive principal strain rates along the centerline these eigenvectors are always $\vec{e}_1 = [0 \quad 1 \quad 0]^T$ and $\vec{e}_3 = [1 \quad 0 \quad 0]^T$ respectively. The flame orientation is $\hat{n} = [-1 \quad 0 \quad 0]^T$. Hence, $|\vec{e}_1 \cdot \hat{n}| = 0$ and $|\vec{e}_3 \cdot \hat{n}| = 1$. The magnitude of the inner product must be considered as the normalized eigenvectors are indeterminant to within a factor of ± 1. While these inner product deviate from zero off the centerline, they still remain close to zero and unity in magnitude due to the distinct orientation of the strain rate structure with respect to the flame. Hence, according to the simple interaction geometry, the inner product, $|\vec{e}_1 \cdot \hat{n}|$, should generally be around zero and $|\vec{e}_3 \cdot \hat{n}|$ should generally be around one.

The validity of these conditions ($\vec{\omega} \cdot \hat{n} = 0$, $|\vec{e}_1 \cdot \hat{n}| \approx 0$, and $|\vec{e}_3 \cdot \hat{n}| \approx 1$) in real turbulence-flame interactions were assessed at the intersection point of the two OPCS-PIV image planes. As described in §4.2.2, the complete 3D velocity gradient tensor and flame surface orientation were known at this location. From the velocity gradient tensor, both the vorticity vector and strain rate tensor were computed. The eigenvectors of the strain rate tensor adjacent to the flame were then calculated. These were ordered as indicated above and normalized to have a magnitude of unity. The necessary inner products were then computed from the eigenvectors, vorticity vector, and flame surface normal. Furthermore, the same procedure was performed

using the velocity field at a point along the centerline. This provided information about the natural orientation of this turbulence field away from the flame. Data from 10000 vector fields were used for the statistics.

Figure 5.13 present the PDFs of these inner products. The vorticity vector has been normalized to unit length, indicating the orientation of the vorticity. As can be seen, the orientation of all quantities was distributed over a range. However, there did appear to be some preferential orientation of the turbulence. Furthermore, the presence of the flame had an effect on the orientation of the strain rate field.

The orientation of the vorticity field showed a slight preferential alignment towards $|\omega_z \cdot \hat{n}| = 0$. However, there were many cases when the exact opposite was true and the vorticity vector was aligned parallel to the flame sheet. The preferential orientation may have been due to the mechanism with which the turbulence was generated; the 2D slot burner and slot grating likely created vorticity aligned with the z-axis. The wire mesh and natural evolution of the turbulence may not have completely removed this at the measurement volume. Nevertheless, the orientation of the vorticity field was not well described by the canonical geometry. Furthermore, it did not appear that the flame front effected the orientation of the vorticity field.

The most extensional principal strain rate axis essentially had no preferential orientation with respect to the flame; the PDF was generally flat. However, there was a slight difference between the statistics away from the flame (at the burner centerline) and at the flame. Away from the flame, $\vec{e}_1$ had a slight preferential alignment normal to the flame surface. Near the flame, it developed a slight preferential alignment parallel to the flame surface. The intermediate principal strain rate axis had a distinct preferential alignment parallel to the flame. This was increased when adjacent to the flame. The most compressional principal strain rate axis preferentially aligned

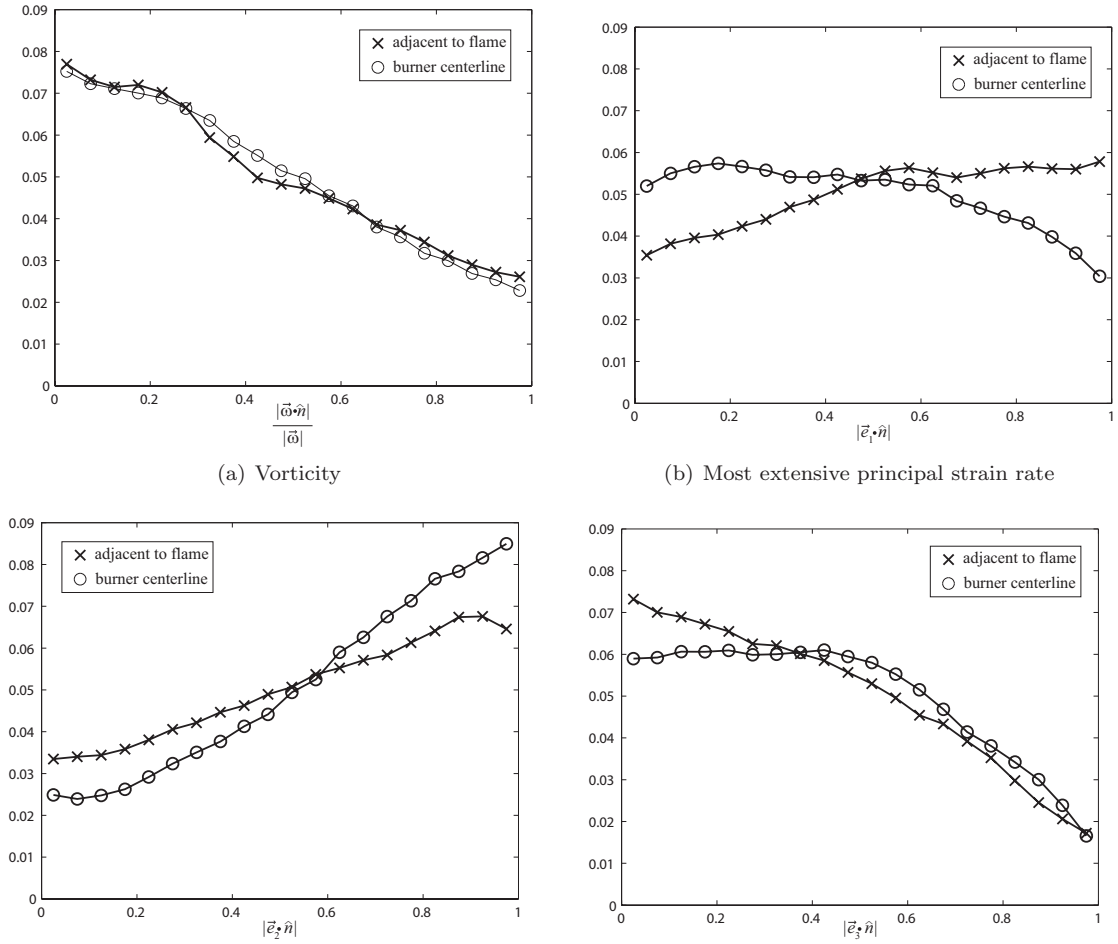

(a) Vorticity

(b) Most extensive principal strain rate

(c) Intermediate principal strain rate

(d) Most compressive principal strain rate

Figure 5.13: Probability distribution functions showing the orientation of the turbulence with respect to the flame surface normal.

normal to the flame surface. Once again, the preference was increased in the vicinity of the flame.

While the particular orientation statistics are not a general result, it is nevertheless apparent that the 3D turbulence field was not aligned as predicted by 2D canonical model. All eigenvectors of the strain rate tensor were oriented in a distributed manner with respect to the flame. Furthermore, the preferential orientations of the strain rate were not as would be expected from the canonical model. Hence, even in this simple flame, the canonical configuration is a poor description of the turbulence orientation.

5.4 Conclusions

This Chapter has demonstrated the complex geometry of turbulence-flame interactions. The geometry of non-reacting turbulence educed by the OPCS-PIV was shown to agree well with predictions from DNS. The interaction between such structures and the flame was also observed. Interactions that, in their planar slices, resembled three simple configurations were presented. However, the 3D measurement of these events indicated a very complex geometry that would not otherwise have been predicted. The geometry of turbulence-flame interactions was also studied statistically by considering the orientation of the turbulence field with respect to the flame normal. It was found that the orientation of the vorticity and principal strain rate axes were widely distributed with respect to the flame normal.

From these observations, an important (yet somewhat obvious) conclusion may be drawn: the geometry of turbulence and its interaction with a flame is very complex. Direct observation of the turbulence field produced by modern DNS also indicate this conclusion (see for example Ref. [115]). As a consequence, models for the strain rate and curvature based on simple geometries are unlikely to adequately described the effect of turbulence on a flame. This is not only true for the canonical counter-rotating vortices, but any individual or group of geometries; the spectrum of possibilities is too rich. When curved, intertwined, and randomly oriented structures are considered, the stretch exerted on the flame will depend highly on the particular configuration of the turbulence.

Furthermore, the evolution of the local turbulence field will be highly dependant on the specific geometry of the turbulence and interaction. The transport of vorticity and strain rate are dependant on the surrounding turbulence field as described

by Eqs. 1.58 and 1.59. Hence, different configurations will evolve differently and exert different influences on the flame. As was seen in Figs. 5.8-5.12, the strengths and paths of the turbulent structures evolve as they interact with the flame. It is not difficult to imagine that the flame would also affect the local geometry of the turbulence, which cannot be measured from the employed diagnostics.

These conclusions present a large problem for turbulent combustion simulations. If the true interaction between turbulence and a flame is too complex to be described as the ensemble of simple interactions, models based on such interactions are inherently inaccurate. Models for the stretch rate should not explicitly dictate a particular geometry for the turbulence but instead be based on statistical analysis of real turbulent flames. When considering the large scales of turbulence, this implies a difficulty because the large scales are not universal and the statistics of these scales will vary from flow to flow. However, the geometry dependent large scales are explicitly calculated in LES. The subgrid scales, associated with the inertial and dissipative ranges, are generally assumed to be universal. If properly characterized, these scales should be statistically universal and statistical subgrid models feasible. Such models are discussed in the next Chapter.

CHAPTER VI

Modeling subgrid terms in LES

This Chapter describes the analysis and development of subgrid models for use in LES. First, a new method for experimentally investigating turbulence-flame interactions is presented. This method directly measures the processes that must be modeled in the subgrid of an LES. Using this methodology, the subgrid strain rate, curvature stretch rate, and turbulent burning velocity were investigated. In each case, previous models and modeling paradigms were analyzed. In general, these required significant modification to accurately reflect true turbulence-flame interaction. The measured data, combined with concepts from Chapters IV and V, were used to make the appropriate modifications.

6.1 Analysis method for subgrid processes

In a Large Eddy Simulation, the large scales of the turbulence are explicitly resolved and the effects of small scales are modeled in the subgrid. That is, the flow field is filtered at some scale, Δ, and fluctuations below this scale are not directly computed. In combustion simulations, the flame also is typically too thin for explicit resolution. Hence, some form of filtered flame front is considered. Simulations compute the filtered velocity field, flame front position, and some other properties of the flow (e.g. temperature, composition). However, the small scale details of the

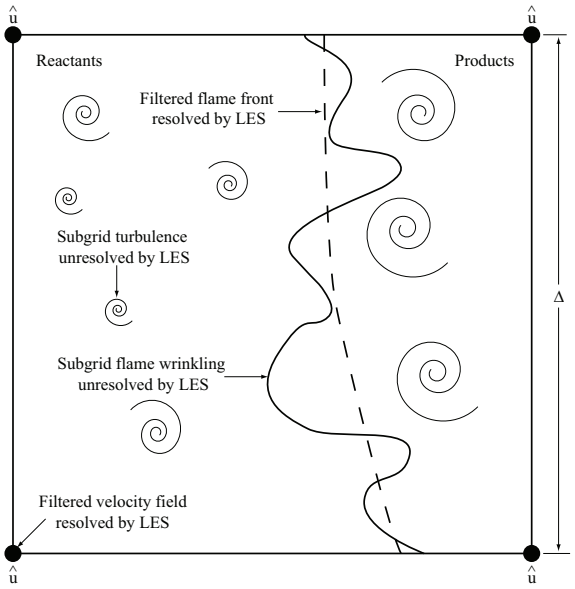

Figure 6.1: Theoretical control volume containing a wrinkled turbulent flame. The boundary of this volume can be considered to be an LES cell. The LES computes the filtered velocity field and flame front, but not the subgrid details. These details were resolved in the present measurements.

flame and flow are not resolved. Hence, any turbulence-flame interaction processes occurring at subgrid scales must be modeled.

Consider a theoretical control volume containing a wrinkled flame as is shown in Fig. 6.1. The boundary of the volume can be considered to be the boundary of an LES cell. At the corners of the volume, there are points that represent the LES nodes. At these locations, a simulation would contain explicit information about the filtered quantities, $\tilde{q}$ or $\hat{q}$ (e.g $\hat{\vec{u}}$, $\hat{\underline{S}}$, and $\tilde{c}$). Recall that, $(\tilde{\cdot})$ and $(\hat{\cdot})$ represent standard and density weighted filtering operations, which are given by Eqs. 1.31 and 1.32 respectively. The mean filtered flame front position is represented by an iso-surface of some variable (e.g. $\tilde{c} = 0.5$ or $\breve{G} = G_0$). Internal to the volume there are subgrid fluctuations of the filtered quantities, q', where:

$$q' = q - \tilde{q} \tag{6.1}$$

or

$$q' = q - \hat{q} \tag{6.2}$$

As the flame propagates over the reactants in the control volume, the effect of the subgrid terms need to be modeled. These models must be parameterized by properties that can be computed using LES. Of particular interest are the subgrid strain rate ($a_{t,sg}$), curvature stretch rate ($\kappa_{c,sg}$), and turbulent burning velocity $s_{t,sg}$. These terms are defined below.

6.1.1 Definition of subgrid terms

As the flame interacts with the flow it is strained by the turbulent velocity fluctuations. The strain rate on the flame can be decomposed into the components that are due to the resolved ($a_{t\Delta}$) and subgrid ($a_{t,sg}$) flow contributions. A model for $a_{t,sg}$ must accurately predict the strain rate exerted by the unresolved component of the velocity field. Note that $a_{t\Delta}$ is not equivalent to applying a filtering operation to a_t; the strain rate exerted by the filtered flow on the filtered flame is not strictly equivalent to the filtered strain rate. That is, filtering the strain rate yields:

$$\hat{a}_t = \delta_{ij}\hat{S}_{ij} - \widehat{n_i n_j S_{ij}} \tag{6.3}$$

However, decomposing the velocity field and flame normal into their filtered and fluctuating components and substituting into the strain rate equation yields:

$$a_t = \delta_{ij}\hat{S}_{ij} - \tilde{n}_i\tilde{n}_j\hat{S}_{ij} + a_{t,sg} = a_{t\Delta} + a_{t,sg} \tag{6.4}$$

where $a_{t,sg}$ contains all terms involving subgrid fluctuations of the flame surface normal or velocity field. The normal of the filtered flame surface is designated as $\tilde{n}$ and appropriate filtering of the flame will be handled below. Equation 6.4 can be regarded as a definition of $a_{t,sg}$. Furthermore, it clearly can be seen that $a_{t\Delta} \neq \hat{a}_t$.

Similarly, the curvature stretch rate of the filtered flame is not identical to the filtered curvature stretch rate. That is, the resolved and subgrid components are related to the actual flame curvature stretch rate by:

$$\kappa_c = s_{l\Delta}\frac{\tilde{x}'_f\tilde{y}''_f - \tilde{x}''_f\tilde{y}'_f}{\left(\tilde{x}'^2_f + \tilde{y}'^2_f\right)^{3/2}} + s_{l\Delta}C_{sg} = s_{l\Delta}C_\Delta + s_{l\Delta}C_{sg} = \kappa_{c\Delta} + \kappa_{c,sg} \tag{6.5}$$

where $x_f(\vartheta)$ and $y_f(\vartheta)$ are the parametric space curves defining the flame and $s_{l\Delta}$ is the mean propagation speed of the flame in the cell. C_Δ represents the curvature of the filtered flame and is not identical to $\tilde{C}$. Equation 6.5 can be regarded as the definition of $\kappa_{c,sg}$.

The subgrid turbulent burning velocity requires a different definition than the stretch rate components. In the laminar flamelet regime, $s_{t,sg}$ is largely determined by the subgrid flame surface area. Variations in the local flame propagation speed (i.e. $s_{l\Delta}$) are a minor effect and will be treated using the laminar theory described in §1.5.2. The flame surface area ratio is defined as the area of the true wrinkled flame (A_t) divided by the area of the filtered flame (A_Δ) in the control volume. That is:

$$\frac{s_{t,sg}}{s_{l\Delta}} = \frac{A_t}{A_\Delta} = \Xi \tag{6.6}$$

This is essentially the turbulent burning velocity defined in §1.5, with the laminar flame area replaced by the area of the filtered flame.

6.1.2 Filtering of the measured flow field

Consider the measured flame and flow field shown in Fig. 6.2(a). This instant can be considered the beginning of the interaction between the existing flame surface and the fluid in the reactants. This is defined as $t = 0$. At this instant, a coarse scale grid can be superimposed on the flow field, shown by the dotted lines. Each cell and node of this coarse grid is representative of an LES cell and node. The goal

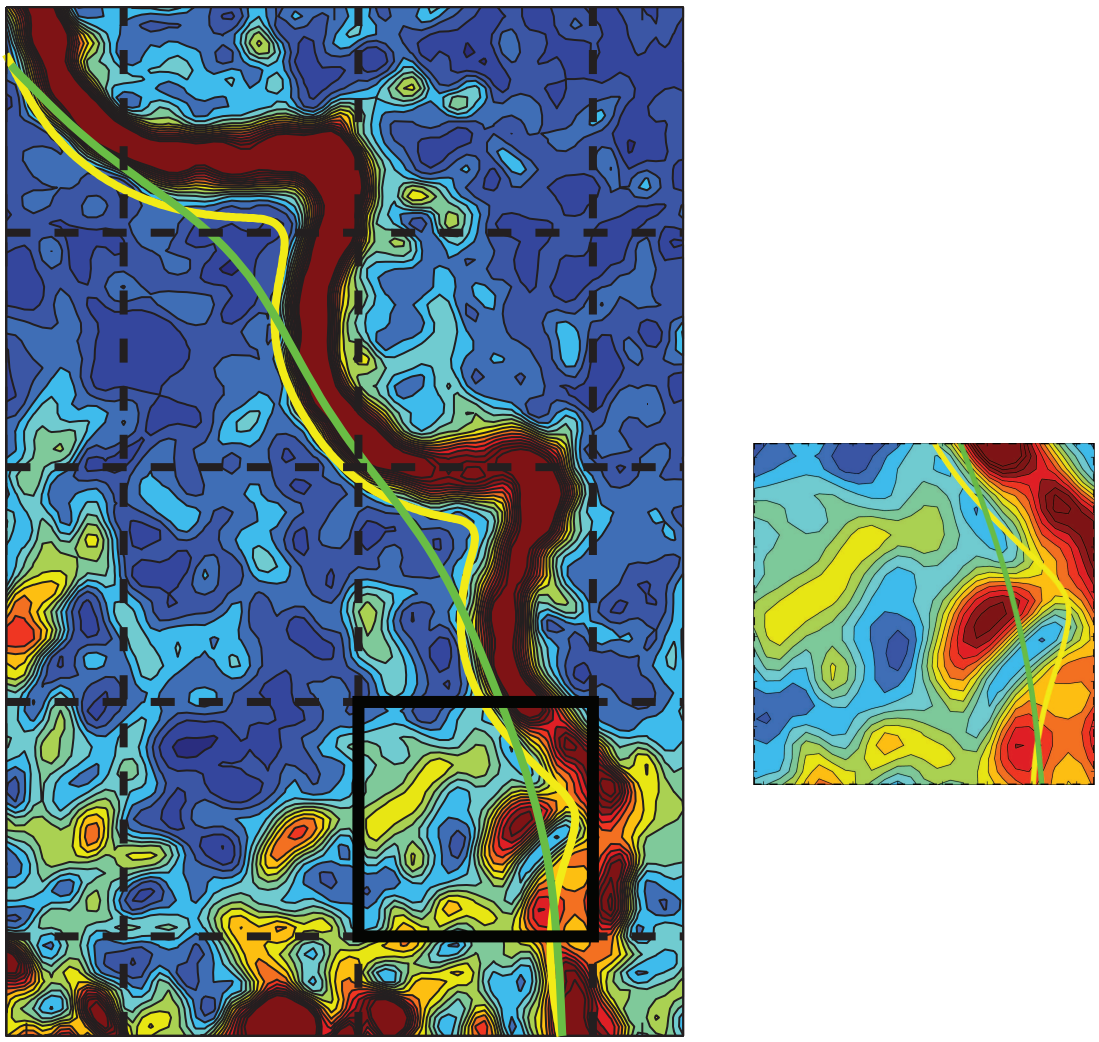

(a) Entire field

(b) Individual Cell

Figure 6.2: Measured strain rate field and flame front (yellow line) overlaid with an artificial LES grid (dotted lines) and filtered flame front (green line). The measurements resolve the subgrid details required for model development. Contours of strain rate magnitude (S) between 0 s^{-1} (blue) and 1500 s^{-1} (red).

of subgrid models is to determine the effects of the subgrid processes occurring in these cells over a theoretical LES time step.

To analyze and develop such models, the filtered information that would be computed by LES had to be determined. Typical LES employs an implicit filter. In such a scheme, the filter width is set by the computational grid size and the filter kernel is set by the numerical method used to determine the derivatives. Alternatively, an explicit filter scheme can be used. This involves filtering the flow field at some scale larger than the computational grid. Explicit filtering allows the filter kernel to be tailored to have desired characteristics, but requires greater computational resolution for an equivalent filter size. Hence, implicit filtering is commonly used. However, in the current experiment, the resolution of the measurements was such that explicit filtering was possible. Explicit filtering was found to provide several advantages. Firstly, implicit filtering did not provide an accurate representation of the $\tilde{c}$ field; the flame front was too thin to be resolved on an LES scale grid. Some form of explicit filtering was therefore required to determine the filtered flame. Secondly, the computational methods used to compute the turbulence properties and strain rate on the flame were more suited to an explicitly filtered field. For example, the circulation method used to compute the vorticity and shear strain rates would not be appropriate on a coarse-grid with implicit filtering of the flow field. Finally, explicit filtering has the potential to reduce numerical errors that are associated with the finite difference schemes used as implicit filters. [8, 9, 46, 60].

The LES velocity field therefore was determined by explicitly filtering the measured velocity field according to Eq. 1.32. For the majority of the analysis, a Gaussian kernel with a standard deviation of $\frac{\Delta}{3}$ was used. However, the effect of varying the filter was studied and is discussed in §6.5. It was found that the results were

essentially independent of the filtering method.

The filtered flame front position was determined by explicitly filtering the c field. Consistent with the laminar flamelet concept, the reaction progress variable was treated as a Heaviside function; all fluid on the reactant side of the c^* isocontour was treated as reactants ($c = 0$) and all fluid on the product side was treated as products ($c = 1$). This field then was filtered using a standard (non-density weighted) filter as given by Eq. 1.31. The filtered flame front position was defined as the $\tilde{c} = 0.5$ isocontour and is shown in Fig. 6.2(a) as the thick green line.

6.1.3 Subgrid turbulence-flame interactions

To study the relevant subgrid processes, the interaction between the fluid and flame in a particular cell was considered. Such a cell is shown in Fig. 6.2(b). From this point on, only the fluid contained in this cell at $t = 0$ was considered for the interaction. Hence, the control mass of fluid for this interaction was defined as the fluid contained in the cell at $t = 0$. A control mass was required since the fluid expanded as it interacted with the flame.

In order to analyze the interaction of this fluid with the flame, the control mass was tracked in time in a Lagrangian manner and the flame front properties in the control mass were determined. Consider the fluid comprising the control mass in Fig. 6.3(a). At each point there was a velocity associated with the local fluid element. In the next frame of the interaction, each element had convected a distance based on these velocities. That is, every point in the control mass, $(x_i(t), y_j(t))$, had convected such that:

$$(x_i(t + \Delta t), y_j(t + \Delta t)) = (x_i(t), y_j(t)) + \vec{u}(x_i, y_j, t)\Delta t \tag{6.7}$$

This identified the location of the fluid element in the next frame and therefore

(a) $t = 0$ ms (b) $t = 0.9$ ms (c) $t = 1.8$ ms (d) $t = 2.7$ ms (e) $t = 3.6$ ms

Figure 6.3: Evolution of a control mass of fluid (shown in white) as it interacts with the flame. Each fluid element is tracked in a Lagrangian manner according to Eq. 6.7. Field of view is 6.4 mm x 7.2 mm.

tracked the control mass as it interacted with the flame. The process could be repeated until there was no flame remaining within the control mass, indicating that all the reactants had been consumed. In practice, it was repeated until less than 10% of the original reactants remained as shown in Figs. 6.3(b)-6.3(e). Since the flow was turbulent, the shape of the mass deformed during this evolution. Furthermore, since the surface contained a flame, some fluid expanded during each time step. Hence the volume increased. By tracking the interaction of a particular mass of fluid with the flame, the strain rate, curvature, and turbulent burning velocity associated with this fluid was determined.

Note that this process considers the interaction between a specific mass of fluid and the flame. This is different than considering the interaction between a specific section of flame surface with some fluid. The latter interaction is not well defined since flame surface is created and destroyed (mass is not). Furthermore, studying the control mass interaction focuses the analysis on the effect of fluid on the flame, not flame on the fluid.

For each quantity $a_{t,sg}$, $\kappa_{c,sg}$, and $s_{t,sg}$, a subgrid model should predict the filtered value over the computational time step (i.e. the interaction). For the first two quantities, this should be spatially filtered over the flame surface in the control mass and temporally filtered over the time of the interaction. For the latter quantity,

the spatial filter does not have meaning. At any time the spatially filtered value of any flame front property q in the control mass with volume $V_m(t)$ in terms of the parametrically defined planar flame is:

$$\langle q(t)\rangle = \frac{1}{\vartheta_2(t) - \vartheta_1(t)} \int_{\vartheta_1(t)}^{\vartheta_2(t)} q(\vartheta, t) d\vartheta \tag{6.8}$$

where the ϑ_i indicate the values of the parameter where the flame enters and exits the control mass. The overall value for the interaction is then:

$$\overline{\langle q\rangle} = \frac{\int_0^{t_f} A_t(t)\langle q(t)\rangle dt}{\int_0^{t_f} A_t(t) dt} \tag{6.9}$$

The area of the flame (i.e. the length of the flame in the planar measurements) in the control mass is given by:

$$A_t(t) = \int_{\vartheta_1(t)}^{\vartheta_2(t)} \sqrt{[x'_f(\vartheta)]^2 + [y'_f(\vartheta)]^2} d\vartheta \tag{6.10}$$

The area of the filtered flame, A_Δ, also is given by Eq. 6.10 with x_f and y_f replaced by $\tilde{x}_f$ and $\tilde{y}_f$ respectively.

6.1.4 A typical interaction

To demonstrate the above analysis procedure, the results from a typical interaction are presented. The filter size was $\Delta/\delta_l^0 = 40$. Figure 6.4 shows the temporal evolution of the strain rate and curvature fluctuation profiles versus distance along the flame surface (φ) in the control mass. As the interaction evolved, different turbulent structures influenced the flame, creating pulses of strain rate. For example, at $t = 0$, there were two extensively straining turbulent structures interacting with the flame near the edges of the domain. The one at $\varphi \approx 0$ mm generated a negatively curved wrinkle while the one at $\varphi \approx 3.5$ mm was associated with a wrinkle that was partially out of the domain. During the interaction history, the flame was positively

stretched, resulting in a longer flame segment after the interaction. This is indicated by the increasing maximum values of φ at later times. The expected wrinkle shape (which is that of strong negative curvature surrounded by weaker positive curvature) also was observed.

The temporal evolution of the spatially averaged fluctuations is shown in Fig. 6.5. Some important traits are evident. Firstly, while $\langle a_{t,sg} \rangle$ in this interaction tended to be positive, it was occasionally negative and was significantly lower in magnitude than the peak local strain rates. This indicates that at any given time in the subgrid, the extensive and compressive strain rates exerted by the subgrid turbulence balanced to a certain extent. This effect is even more pronounced in the mean curvature. While $\langle C_{sg} \rangle$ tended to be negative, it was an order of magnitude smaller than the local peaks. These plots further indicate that the canonical image that turbulence only creates positive strain rate and negative curvature are inaccurate.

6.1.5 Model evaluation and development

Using the CS-PIV data, the various subgrid terms (e.g. $\overline{\langle a_{t,sg} \rangle}$, $\overline{\langle \kappa_{c,sg} \rangle}$, and $\overline{\Xi}$) were evaluated for thousands of real turbulence-flame interactions, representing thousands of subgrid processes. The statistics of these quantities then were related to properties that could be computed in LES, providing the necessary data for model evaluation and development. The remainder of this Chapter provides these statistics, evaluates previous modeling paradigms, and proposes new models where appropriate. Additionally, since the filter was artificially imposed on the data, the effects of varying Δ were explicitly determined.

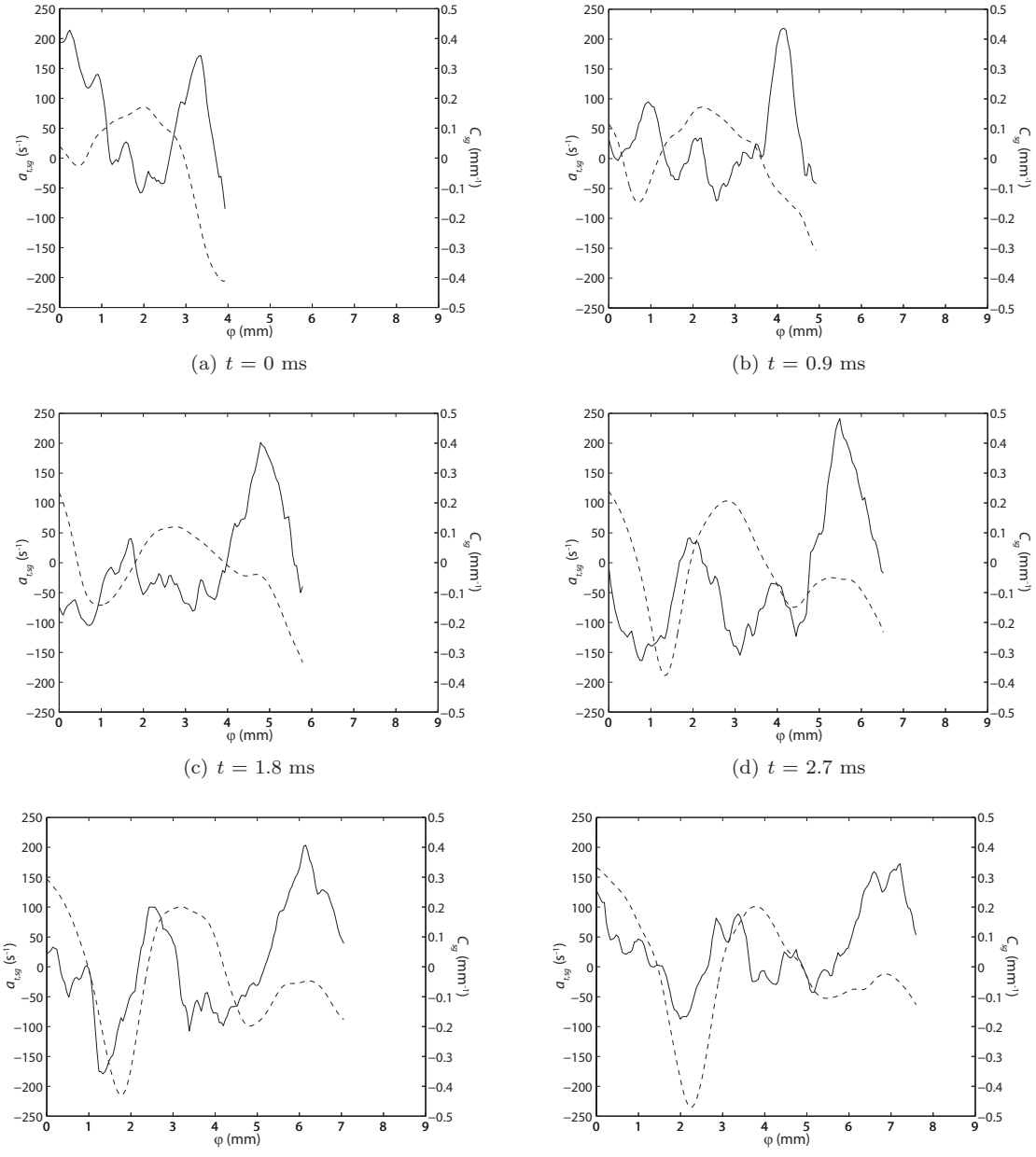

(a) $t = 0$ ms

(b) $t = 0.9$ ms

(c) $t = 1.8$ ms

(d) $t = 2.7$ ms

(e) $t = 3.6$ ms

(f) $t = 4.5$ ms

Figure 6.4: Profiles of the subgrid strain rate on the flame and flame curvature at various times during a typical control mass interaction. (–) - strain rate, (- -) - curvature.

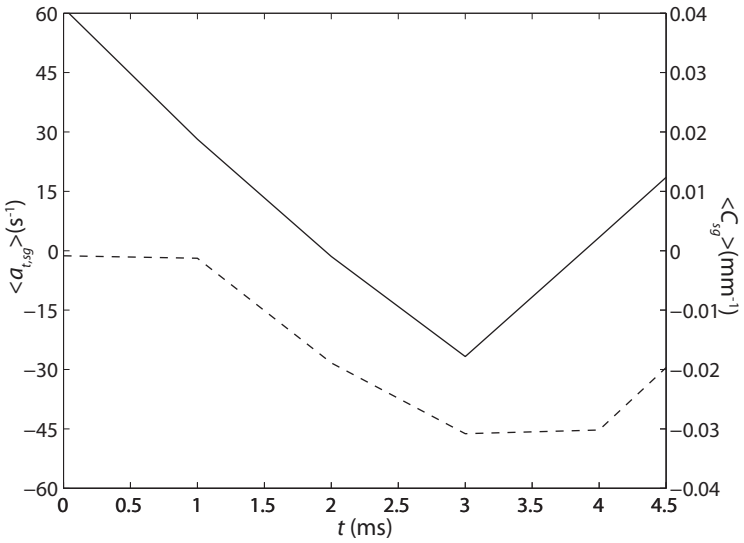

Figure 6.5: Temporal profiles of the spatially averaged subgrid strain rate and curvature during the interaction of Fig. 6.4. (–) - strain rate, (- -) - curvature.

6.2 Modeling the subgrid strain rate

In this Section, the previous model for the strain rate is evaluated and a new model developed. To do so, the data from Case 2 was used. While data from Cases 1 and 3 were also available, only the Case 2 data were tractable for the current analysis. The Case 2 flame was oriented more perpendicular to the flow than the others. Hence, fluid control masses passed through the flame in the field of view. The Case 1 and 3 flames were oriented much more parallel to the bulk flow direction as seen in Chapter III. Measuring the interaction between fluid control masses and these flames was difficult as the interactions rarely took place entirely within the field of view. Converged statistics were therefore not obtained for these Cases.

6.2.1 Previous model

The previously employed modeling paradigm for the subgrid strain rate first will be analyzed. As described in §1.6, this has been previously modeled as:

$$\overline{\langle a_{t,sg} \rangle} = \Gamma_\kappa \left(\frac{\Delta}{\delta_l^0}, \frac{u'_\Delta}{s_l^0} \right) \frac{u'_\Delta}{\Delta} \tag{6.11}$$

The stretch efficiency function employed in such models, Γ_κ, is determined as described in §1.7 and is based on the canonical vortex pair configuration. In this relation, u'_Δ is the subgrid root-mean-squared velocity fluctuation in the cell, averaged over the computational time step. Since the strength of the turbulence used to derive Γ_κ was characterized in the unburnt reactants, u'_Δ should be conditioned on the reactants. Hence, in the present notation:

$$u'_\Delta = \overline{\langle u'_i u'_i \rangle_u^{1/2}} \tag{6.12}$$

Recall that subscript u indicates the unburnt reactants. The parameters in Eq. 6.11 are slightly reorganized in different versions of the model, but are equivalent [22, 28, 51, 74]. It is noted that u'_Δ must be modeled in LES. However, in the present analysis it can be directly computed from the data.

As described in §1.7, there are various forms of the stretch efficiency function that have been implemented in models. Colin et al. [28] represent their stretch efficiency function as:

$$\Gamma_\kappa \left(\frac{\Delta}{\delta_l^0}, \frac{u'_\Delta}{s_l^0} \right) = 0.75 \exp \left[- \frac{1.2}{\left(u'_\Delta / s_l^0 \right)^{0.3}} \right] \left(\frac{\Delta}{\delta_l^0} \right)^{2/3} \tag{6.13}$$

This is plotted in Fig. 6.6. Figure 6.6(a) shows the function over a wide range of turbulence intensities, while Fig. 6.6(b) shows it over a range comparable to that of the current measurements. While the specific curves for Γ varied slightly in previous studies, they all follow the general trend shown: the stretch efficiency increases with the turbulence intensity and filter size [22, 28, 74].

Formulations such as these are based on the assumption that turbulence only consists of counter-rotating vortices, which may lead to problems in the models. To investigate the implications of this assumption, the joint PDFs (JPDFs) of the measured flame strain rate and turbulence intensity were calculated. These are shown

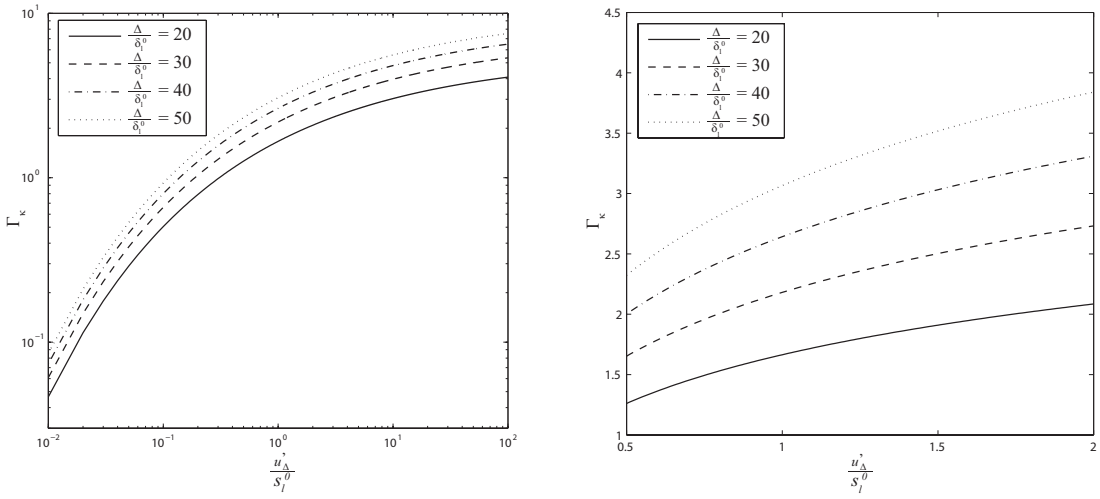

(a) Logarithmic axes

(b) Linear axes in the range of the current experiment

Figure 6.6: Computed stretch efficiency function of Colin et al. [28] at the CS-PIV test condition.

in Fig. 6.7. The strain rate was normalized by $\frac{u'_\Delta}{\Delta}$ and for each sub-plot a single value of $\frac{\Delta}{\delta_l^0}$ was considered. Rearranging Eq. 6.11 yields:

$$\Gamma_\kappa\left(\frac{\Delta}{\delta_l^0}, \frac{u'_\Delta}{s_l^0}\right) = \overline{\langle a_{t,sg}\rangle}\frac{\Delta}{u'_\Delta} \tag{6.14}$$

Hence, the vertical axis of the JPDFs provide the distribution of the strain efficiency. Between 5000 and 8000 interactions were considered for each JPDF.

As can be seen, there was a large distribution of strain rates for any given turbulence strength and filter size. While visual inspection does not reveal any distinct correlation between the efficiency function and turbulence intensity, there is in fact a positive correlation. To demonstrate this, the correlation coefficient (χ) of Γ_κ and $\frac{u'_\Delta}{s_l^0}$ was computed for each case:

$$\chi\left(\Gamma_\kappa, \frac{u'_\Delta}{s_l^0}\right) = \frac{\mathrm{Cov}\left(\Gamma_\kappa, \frac{u'_\Delta}{s_l^0}\right)}{\sqrt{\mathrm{Var}(\Gamma_\kappa)\,\mathrm{Var}\left(\frac{u'_\Delta}{s_l^0}\right)}} \tag{6.15}$$

In this equation, Cov and Var indicate the covariance and variance of the arguments respectively. The computed correlations are listed in Table 6.1 for filter sizes. As can be seen, there is a distinct positive correlation between the two quantities.

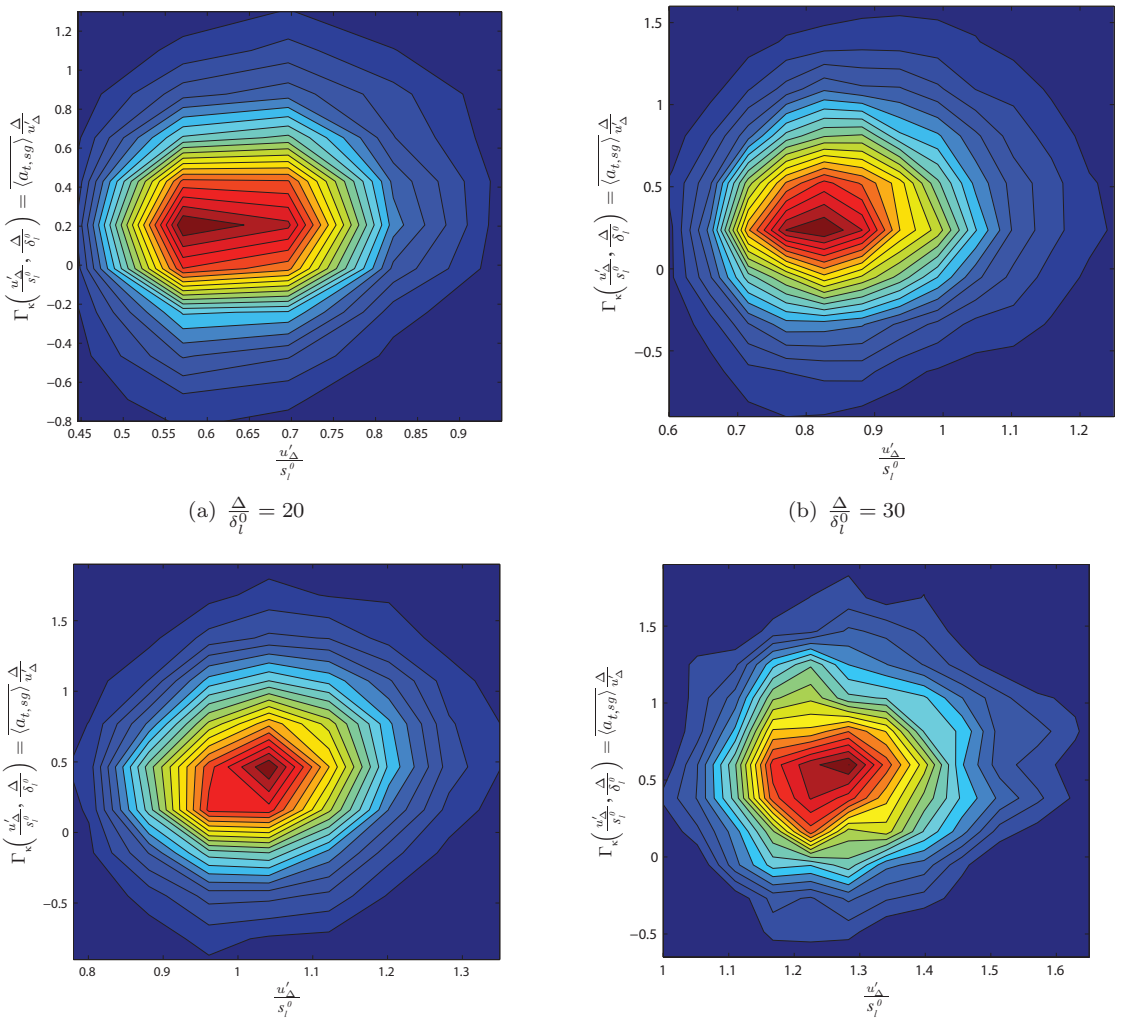

(a) $\frac{\Delta}{\delta_l^0} = 20$

(b) $\frac{\Delta}{\delta_l^0} = 30$

(c) $\frac{\Delta}{\delta_l^0} = 40$

(d) $\frac{\Delta}{\delta_l^0} = 50$

Figure 6.7: Joint PDFs of the normalized subgrid tangential strain rate and turbulence intensity at various filter sizes. The vertical axis is the stretch efficiency, Γ_κ (Eq. 6.11).

$\frac{\Delta}{\delta_l^0}$	20	30	40	50
$\chi\left(\Gamma_\kappa, \frac{u'_\Delta}{s_l^0}\right)$	0.11	0.10	0.12	0.10

Table 6.1: Measured values of the stretch efficiency function-turbulence intensity correlation. Γ_κ is defined by the previous model of Eq. 6.11.

The positive correlation coefficients in Table 6.1 indicate that the mean straining efficiency of the turbulence increased with stronger turbulence. Models for the strain rate exerted on a flame therefore must predict the mean efficiency ($\overline{\Gamma}_\kappa$) as function of the flow properties. To determine the measured mean efficiency curves, the abscissa in Fig. 6.7 was divided into ten equal segments. The mean $\overline{\Gamma}_\kappa$ and $\frac{u'_\Delta}{s_l^0}$ in each segment then was determined. In reference to the efficiency function ($\bar{\cdot}$) refers to the ensemble, not temporal average. The results are shown in Fig. 6.8. Only data points for which there were sufficient interactions to achieve statistically meaningful results are shown. For each data point, the expected standard deviation in the computed mean values ($\sigma_{\overline{\Gamma}_\kappa}$) was calculated:

$$\sigma_{\overline{\Gamma}_\kappa} = \frac{\sigma_{\Gamma_\kappa}}{\sqrt{N}} \tag{6.16}$$

where σ_{Γ_κ} is the standard deviation of the measured efficiency for individual interactions and N represents the number of interactions used to compute the mean. Data points are shown only where:

$$\frac{\sigma_{\overline{\Gamma}_\kappa}}{\overline{\overline{\Gamma}}_\kappa} < 0.05 \tag{6.17}$$

For each filter scale, ten possible data points were available. However, the statistical restriction resulted in only three to five valid points at a given filter size. Nevertheless, some trends were apparent: the mean efficiency was positive and increased with the turbulence intensity and filter size. These trends are in agreement with the previous models.

However, by comparing Fig. 6.8 with Fig. 6.6(b), it is clear that there was a large discrepancy between the values measured in this experiment and those predicted by the previous model of Ref. [28]. In particular, the measured mean subgrid strain rates (and hence strain efficiency) were considerably lower than those predicted. This was

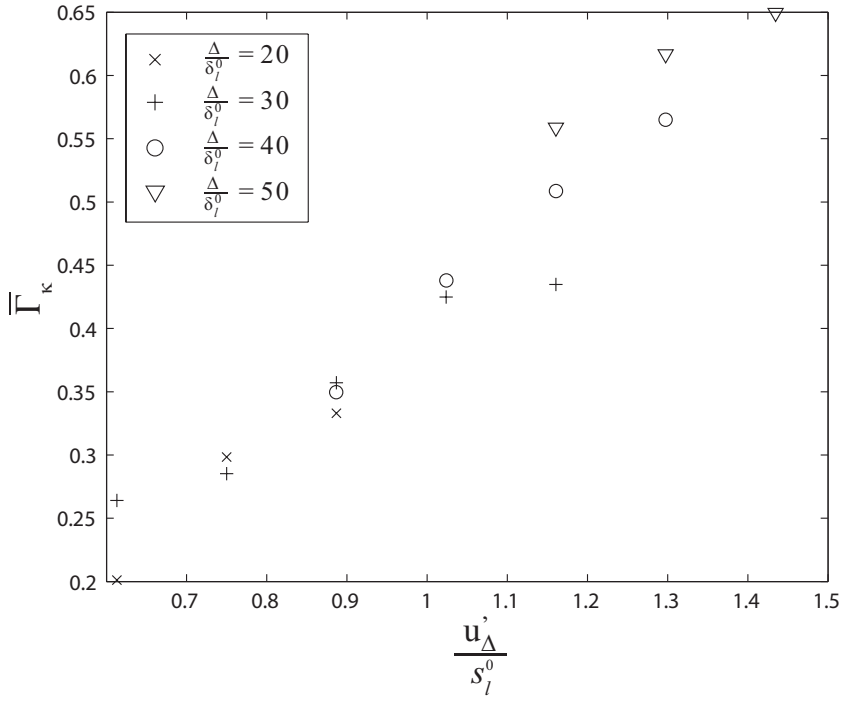

Figure 6.8: Measured values of the mean stretch efficiency function based on the definition of Eq. 6.11.

primarily caused by the canonical model neglecting turbulence that exerts negative strain rate. As has been shown several times (e.g. Fig. 6.4), such compressive strain rate is a significant portion of the total and must be considered. It is noted that the stretch efficiency function derived by Charlette et al. [22] includes an artificial cutoff, which prevents turbulence below a certain threshold from stretching the flame. This correction lowers the computed efficiency for weak turbulence and may produce more accurate results at low u'_Δ. However, the mechanism by which they reduce the efficiency is not representative compressive strain rate and will not provide the necessary correction at stronger turbulence.

Despite the observation that negative strain rate occurs in the experiment, it was found that the mean subgrid strain rate was always positive. This indicates that there is a difference between turbulence-flame interactions that exert positive and negative strain rate; if they were completely equivalent, the mean contributions

would balance and there would be no net strain rate. There also would be no change in the efficiency with increasing turbulence intensity; any changes in the efficiency of the positive strain rate would be balanced by those of the negative strain rate. Hence, the positive and increasing mean efficiency indicates that there are differences in the physical processes leading to positive and negative strain rate. This will be discussed further in §6.2.2.2.

There is one other fundamental difference between the measured efficiencies and those computed in Refs. [22, 28, 74] assuming the canonical vortex configuration. The traditional stretch efficiency function is derived based on the increase in *total* reaction rate during an interaction; it measures the overall stretch rate. However, in modeling applications, it is applied without modification to represent solely the strain rate. The measured data on the other hand, truly represents the *strain* efficiency. This difference is significant for two reasons. Firstly, it effects how the efficiency varies with scale. Many of the inefficiencies associated with stretching a flame by turbulence are associated with curvature effects. Small scale or weak vortical structures do not effectively *wrinkle* a flame. Hence the stretch efficiency of associated with small structures is low. However, this does not necessarily indicate that their strain efficiency is equally low. While the measured data in the current formulation does exhibit increasing efficiency with increasing filter size, this may not be the result of changes in the efficiency of individual turbulence-flame interactions. It may instead be intrinsic to the characteristic stretch rate employed in the definition (u'_Δ/Δ) as will be discussed in §6.2.2.1.

Secondly, assuming that the stretch efficiency function is equal to the strain efficiency in some ways reduces the error intrinsic to assuming turbulence-flame interaction is described by the canonical configuration. Since this configuration creates

positive strain rate and negative curvature, these two effects somewhat balance each other in the total stretch rate. Hence, the negative curvature stretch rate somewhat mimics the effects of the negative strain rate exerted by real turbulence. By applying the stretch efficiency function to represent solely the strain rate, the effects of the simplified turbulence were somewhat muted; two wrongs somewhat make a right. However, the differences in magnitude between the measured efficiencies and those computed from Eq. 6.13 indicate that this effect is insufficient to account for the measured negative component of the strain rate.

6.2.2 Proposed model

Based on the above observations, it is apparent that the previous model for the stretch efficiency function should be modified to better reflect real turbulence-flame interactions. This was done using the present measurements. A new formulation of the characteristic strain rate is first presented. The measured data are then used to determine the model.

6.2.2.1 The characteristic strain rate: $\frac{u'_\Delta}{\Delta}$ or S'_Δ?

The first step in formulating the model is to properly characterize the potential strain rate that could be exerted by the turbulence. That is, the characteristic strain rate of the turbulence in the LES cell (κ_Δ) must be determined. Previous models have typically assumed that the strain rate should scale as:

$$\kappa_\Delta = \frac{u'_\Delta}{\Delta} \tag{6.18}$$

The Kolmogorov cascade was then used to relate the subgrid velocity fluctuations to the resolved scale fluctuations.

However, as shown above, this formulation results in poor correlation between the measured values of Γ_κ and the turbulence intensity. Furthermore, as indicated

in §4.4, the strain rate exerted on the flame is characterized by a particular aspect of the velocity fluctuations: the fluid dynamic strain rate. Therefore, it is proposed that:

$$\kappa_\Delta = S'_\Delta = \overline{\langle S'_{ij} S'_{ij} \rangle}_u^{1/2} \tag{6.19}$$

Here, S'_Δ is subgrid strain rate magnitude in the reactants of an LES cell. In simulations, this quantity can be computed from the subgrid energy transfer model. In order to accurately simulate the energy in the subgrid turbulence, LES methods must determine the transfer of energy from the resolved to the subgrid scales. This is equivalent to determining the subgrid dissipation rate:

$$\varepsilon_{sg} = 2\nu \overline{\langle S'_{ij} S'_{ij} \rangle} \tag{6.20}$$

Hence, in LES S'_Δ can be inferred from the subgrid scale dissipation rate, which is modeled. For example, the Smagorinsky model states that [101]:

$$\varepsilon_{sg} = 2C_s^2 \Delta^2 \left(\hat{S}_{ij} \hat{S}_{ij} \right)^{3/2} \tag{6.21}$$

where C_s is the Smagorinsky constant. However, in the present analysis S'_Δ was determined directly from the data in the same manner as u'_Δ.

Both S'_Δ and u'_Δ/Δ are measures of the characteristic strain rate and are intrinsically linked; increasing the velocity fluctuations will increase the fluid dynamic strain rate. However, use of the strain rate has several advantages. Firstly, it is a more direct measure of the straining potential of the flow. The exact relationship between $\frac{u'_\Delta}{\Delta}$ and the characteristic strain rate of the flow is not always clear. As will be seen below, characterizing $\overline{\langle a_{t,sg} \rangle}$ using S'_Δ results in significantly better correlation.

Additionally, the use of S'_Δ allows for a more typical definition of the efficiency. The strain rate exerted on the flame is a fraction of S'_Δ determined by the physics

of the interaction process and orientation of the strain rate field with respect to the flame. Hence, the efficiency function should be less than unity. As shown in Fig. 6.6, the efficiency function characterized by u'_Δ/Δ may be around 10. For these reasons, the subgrid strain rate on the flame in the following analysis will be characterized by S'_Δ such that:

$$\overline{\langle a_{t,sg} \rangle} = \Gamma_a(\vec{\xi}) S'_\Delta \tag{6.22}$$

This equation may be treated as a definition of the strain efficiency function, $\Gamma_a(\vec{\xi})$, which will be determined below. At present, the parameter set $(\vec{\xi})$ is left unspecified.

However, the above definition of the efficiency function involves a dependance on the filter scale that does not reflect a dependence on the physical scale of the turbulence-flame interaction. This also is intrinsic to the previous formulations of Γ_κ such as in Eq. 6.13. To illustrate the dependence, consider a single turbulence-flame interaction that is filtered at two different scales, $\Delta_1 > \Delta_2$ and imagine that the subgrid strain rate exerted on the flame was independent of the filter size. The traditional model would then yield:

$$\overline{\langle a_{t,sg} \rangle}_1 = \Gamma_{\kappa 1} \frac{u'_{\Delta 1}}{\Delta_1} \tag{6.23}$$

$$= \Gamma_{\kappa 1} \frac{u'_L}{L} \left(\frac{L}{\Delta_1} \right)^{2/3} \tag{6.24}$$

It is assumed that:

$$\frac{u'_\Delta}{u'_L} = \left(\frac{\Delta}{L} \right)^{1/3} \tag{6.25}$$

based on the Kolmogorov cascade. This is the standard approach used to derive Γ_κ [28, 74].

If the strain rate exerted on the flame was independent of the filter size:

$$\overline{\langle a_{t,sg}\rangle}_1 = \overline{\langle a_{t,sg}\rangle}_2 \tag{6.26}$$

$$= \Gamma_{\kappa 2}\frac{u'_L}{L}\left(\frac{L}{\Delta_2}\right)^{2/3} \tag{6.27}$$

and therefore:

$$\frac{\Gamma_2}{\Gamma_1} = \left(\frac{\Delta_2}{\Delta_1}\right)^{2/3} \tag{6.28}$$

Therefore, even if the strain rate exerted on the flame was independent of filter size, the efficiency function would increase as $\Delta^{2/3}$. This is exactly the relationship indicated in Ref. [28] and Eq. 6.13. Hence, the explicit dependance on the filter size in the traditional models is somewhat a result of the choice of characteristic strain rate, not a physical process. Note that this does not imply that the scale of the subgrid turbulence is not a parameter that affects the strain efficiency. Variations beyond the intrinsic dependence were apparent in the measurements and will be included in the final model.

Similarly, the proposed model for the strain efficiency involves an intrinsic negative power law relationship between the strain efficiency and filter size. Once again, consider a turbulence-flame interaction filtered at two different scales. If the same subgrid strain rate was exerted independent of the filter, the proposed model would yield:

$$\overline{\langle a_{t,sg}\rangle}_1 = \Gamma_{a1}S'_{\Delta 1} \tag{6.29}$$

$$= \Gamma_{a1}\left(\frac{\varepsilon}{2\nu}\right)^{1/2}\left(\frac{\Delta_1}{L}\right)^{1/3} \tag{6.30}$$

$$= \overline{\langle a_{t,sg}\rangle}_2 \tag{6.31}$$

$$= \Gamma_{a2}\left(\frac{\varepsilon}{2\nu}\right)^{1/2}\left(\frac{\Delta_2}{L}\right)^{1/3} \tag{6.32}$$

$$\frac{\Gamma_2}{\Gamma_1} = \left(\frac{\Delta_2}{\Delta_1}\right)^{-1/3} \tag{6.33}$$

Therefore, if the actual strain rate was independent of the filter size, the model would yield a strain efficiency that decreased with increasing filter size as $\Delta^{-1/3}$. This dependance could be removed by defining the characteristic strain rate as:

$$\kappa_\Delta = S'_\Delta \left(\frac{\Delta}{\delta_l^0} \right)^{-1/3} \tag{6.34}$$

However, in the present formulation it was chosen to include the Δ dependance in Γ_a, which is consistent with the traditional models; Eq. 6.22 will be used.

6.2.2.2 Determination of the strain efficiency function

Figure 6.9 show the JPDFs of Γ_a and fluid dynamic strain rate calculated from the data for Case 2. These are identical in form to those seen in Fig. 6.7, but with the strain rate characterized by S'_Δ. Also, the abscissa has been changed to $S'_\Delta \frac{\delta_l^0}{s_l 0}$. This is the characteristic fluid dynamic strain rate normalized by the reaction rate of the flame and is analogous to $\frac{u'_\Delta}{s_l^0}$ in the previous formulations. The quantity $\frac{s_l^0}{\delta_l^0}$ is proportional to mean reaction rate of the flame as shown by the classical premixed flame analysis of Mallard and Le Chatelier, which yields [68]:

$$s_l^0 \sim \sqrt{\alpha_u \overline{\dot{w}}_r} \tag{6.35}$$

$$\delta_l^0 \sim \sqrt{\frac{\alpha_u}{\overline{\dot{w}}_r}} \tag{6.36}$$

As can be seen, the JPDFs of Γ_a in Fig. 6.9 possess the same general properties as those of Γ_κ in Fig. 6.7. However, the positive correlation between efficiency and turbulence intensity is more apparent. To demonstrate this, Table 6.2 contains the strain efficiency-S'_Δ correlation coefficients for this formulation of Γ_a at all filter sizes. As can be seen, these values are greater than those in the traditional formulation (Table 6.1).

The mean values of the strain efficiency were calculated in the same manner as in §6.2.1 and are presented in Fig. 6.10. These data exhibit a few interesting

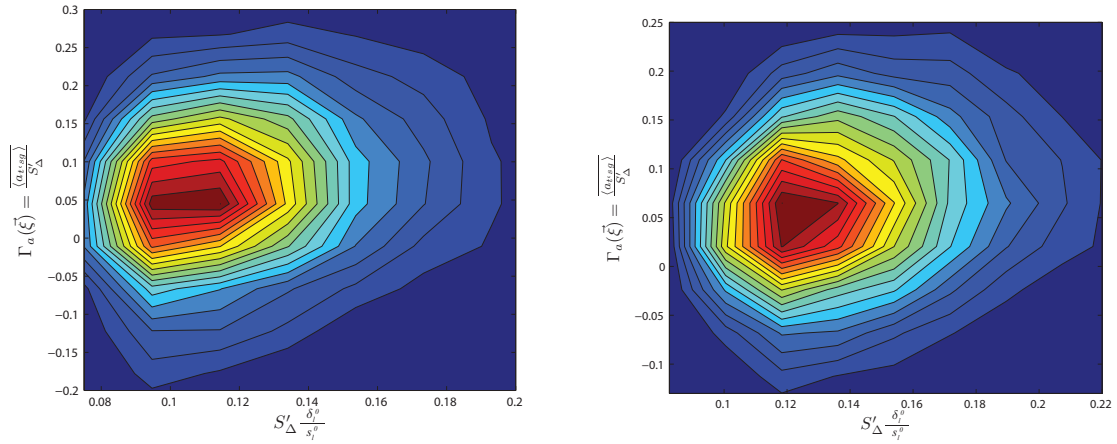

(a) $\frac{\Delta}{\delta_l^0} = 20$ (b) $\frac{\Delta}{\delta_l^0} = 30$

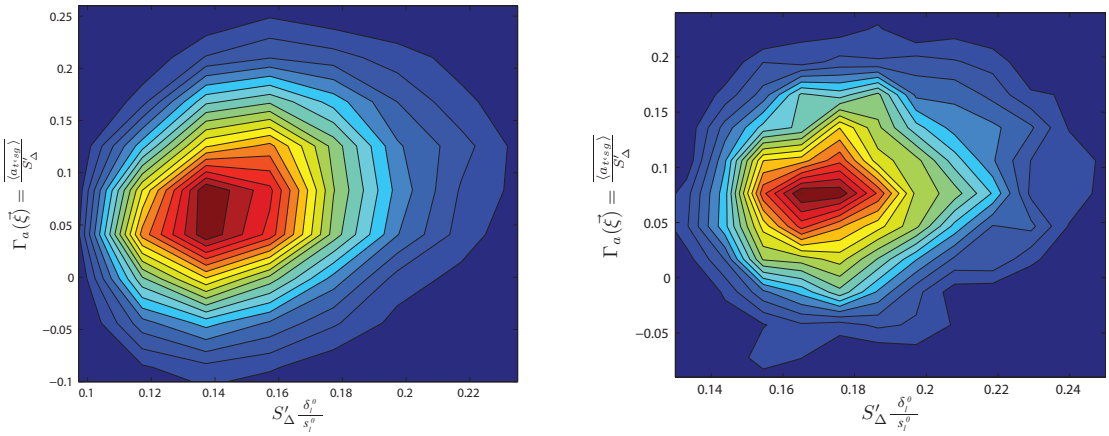

(c) $\frac{\Delta}{\delta_l^0} = 40$ (d) $\frac{\Delta}{\delta_l^0} = 50$

Figure 6.9: Joint PDFs of the normalized subgrid tangential strain rate and fluid dynamic strain rate at various filter sizes. The vertical axes are indicative of the newly formulated strain efficiency, Γ_a (Eq. 6.22).

$\frac{\Delta}{\delta_l^0}$	20	30	40	50
$\chi\left(\Gamma_a, S'_\Delta \frac{\delta_l^0}{s_l^0}\right)$	0.15	0.15	0.16	0.15

Table 6.2: Measured values of the new strain efficiency function-turbulence intensity correlation for proposed formulation in Eq. 6.22.

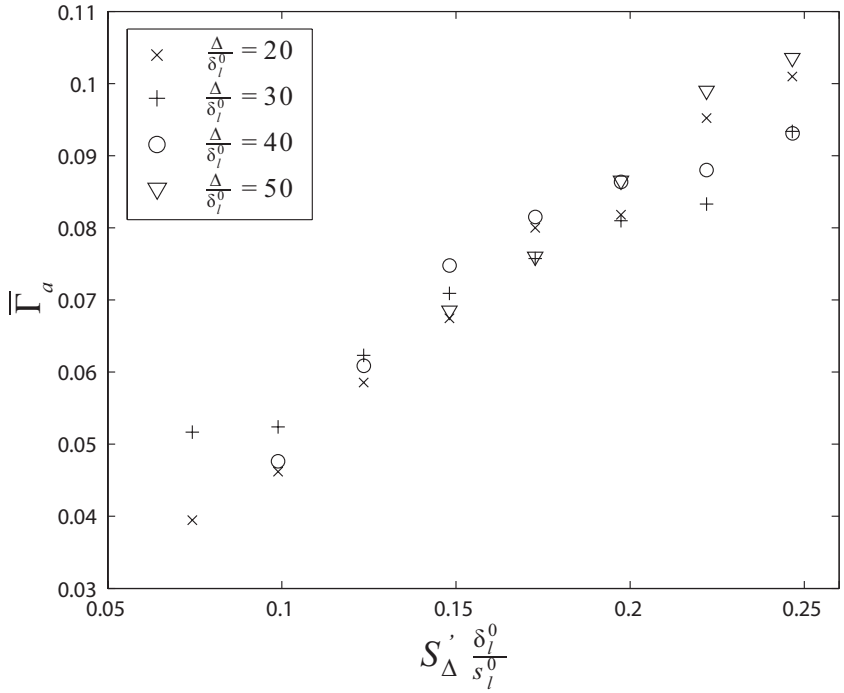

Figure 6.10: Measured mean strain efficiency function determined from the proposed modeling paradigm (Eq. 6.22).

traits. Firstly, the data statistically converged better when the parameter S'_Δ was used rather than u'_Δ; the number of converged data points more than doubled. This confirms that the strain rate on the flame is better characterized by the fluid dynamic strain rate than by u'_Δ, as was discussed in Chapter IV. Secondly, there was little dependance of the $\overline{\Gamma}_a$ values on the filter scale. All the data in Fig. 6.10 followed essentially the same line. However, as described in §6.2.2.1 there still exists a physical dependence on the filter scale. If the strain rate exerted on the flame was independent of the filter scale the strain efficiency function would posses a $\Delta^{-1/3}$ dependance. Thirdly, in the range of values studied, the strain efficiency appeared to increase linearly. However, it is expected that these curves would asymptote to a constant value at some turbulence intensity as discussed in §6.2.2.3. Finally, the magnitude of the efficiency function formulated in this manner was considerably less than when formulated based on u'_Δ.

The data in Fig. 6.10 could now be used directly to determine a fit for the strain efficiency function. However, several observations can be made that lead to a more insightful form of $\overline{\Gamma}_a$:

1. At any instant, the strain rate exerted on the flame varied between positive and negative values as seen in Fig. 6.4. If the contributions from each balanced, there would be no net strain rate on the flame surface.

2. The net strain rate on the flame surface was positive. While there were some particular interactions where the net strain rate was negative, the ensemble mean for any strength and scale of turbulence was always positive. Hence, the efficiency associated with the generation of positive strain rate on the flame is different than that associated with negative strain rate.

3. The mean strain efficiency varied with the strength of the turbulence. The dependence of the positive and negative strain efficiencies on turbulence intensity must therefore be different. If they varied in the same manner, increases in each would be proportional and the total strain efficiency would not be a function of the turbulence intensity.

A formulation for $\overline{\Gamma}_a$ based purely on the data in Fig. 6.10 would not explicitly identify the different behaviors of compressive and extensive strain rate with changing turbulence intensity that must occur. Furthermore, it would assume that the distribution between positive and negative strain rates is independent of the flow and model parameters. However, this was not the case as is demonstrated in Fig. 6.11. This plot shows the mean probability of finding positive strain rate ($\overline{P}_p^a$) at all filter sizes. The data were computed in the same manner as $\overline{\Gamma}_a$ and the solid lines represent a fit to the data that is described in §6.2.2.3. As can be seen, the

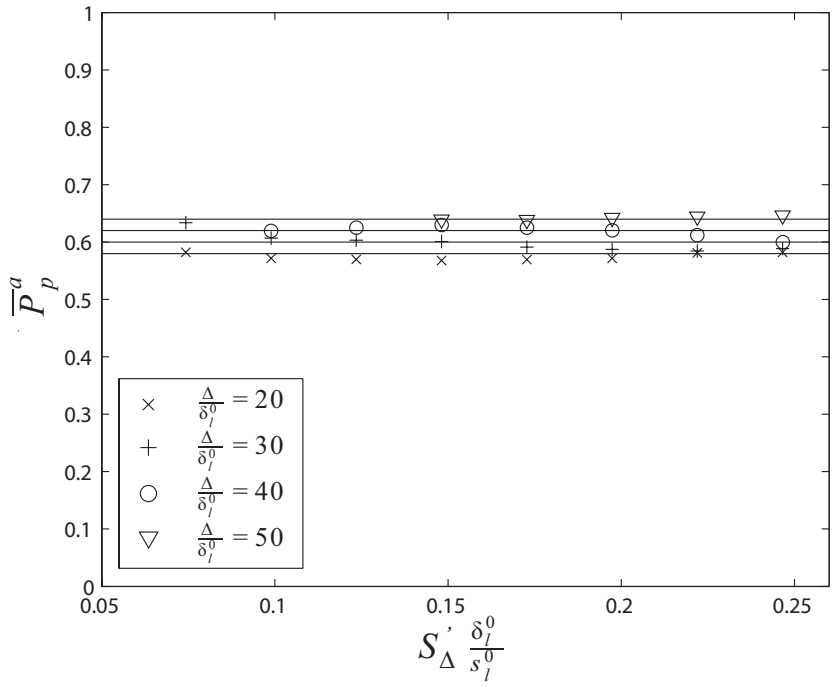

Figure 6.11: Measured mean probability of finding positive strain rate. Solid lines represent the fits from §6.2.2.3.

probability of finding positive strain rate varied with the filter size; increased filter sizes corresponded to increased probability of positive strain rate. This indicates that positive strain rate was associated with larger scales than negative strain rate; as the filter size was increased, more positive strain rate was contained in the subgrid. However, for each filter size, $\overline{P}_p^a$ was fairly constant and independent of the turbulence intensity. Nevertheless, the formulation of $\overline{\Gamma}_a$ must be able to account the observed different distributions and different behaviors of positive and negative strain rate.

Based on these observations, the following form is proposed for the strain efficiency function:

$$\overline{\Gamma}_a = \overline{\Gamma}_p \overline{P}_p^a - \overline{\Gamma}_n \left(1 - \overline{P}_p^a\right) \tag{6.37}$$

That is, the overall strain efficiency is comprised of two parts: the efficiency when the turbulence is exerting positive strain rate multiplied by the probability of exerting

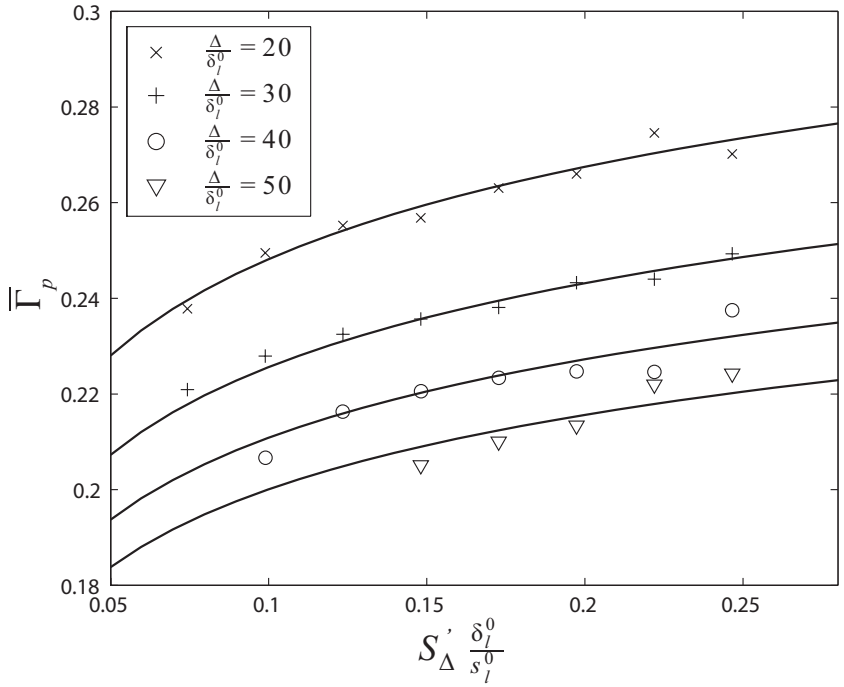

Figure 6.12: Measured mean strain efficiency function associated with extensive (positive) strain rate. Solid lines represent the fit from §6.2.2.3.

positive strain rate, and the efficiency when it is exerting negative strain rate multiplied by the probability of exerting negative strain rate. The efficiency functions are therefore defined as:

$$\Gamma_p = \frac{\left\{\overline{\langle a_{t,sg}\rangle}; a_{t,sg} > 0\right\}}{S'_\Delta} \tag{6.38}$$

$$\Gamma_n = \frac{\left\{|\overline{\langle a_{t,sg}\rangle}|; a_{t,sg} < 0\right\}}{S'_\Delta} \tag{6.39}$$

This formulation accounts for all of the aforementioned observations.

It now remains to determine $\overline{\Gamma}_p$, $\overline{\Gamma}_n$ as a function of the turbulence and flame properties. Figures 6.12 and 6.13 show the measured positive and negative strain efficiency functions. The solid lines in these plots represent fits to the data, which are described in §6.2.2.3. As can be seen, $\overline{\Gamma}_p$ increased with the turbulence intensity. Conversely, the negative strain efficiency function decreased with increasing turbulence intensity. However, both $\overline{\Gamma}_p$ and $\overline{\Gamma}_n$ exhibited similar dependance on the filter

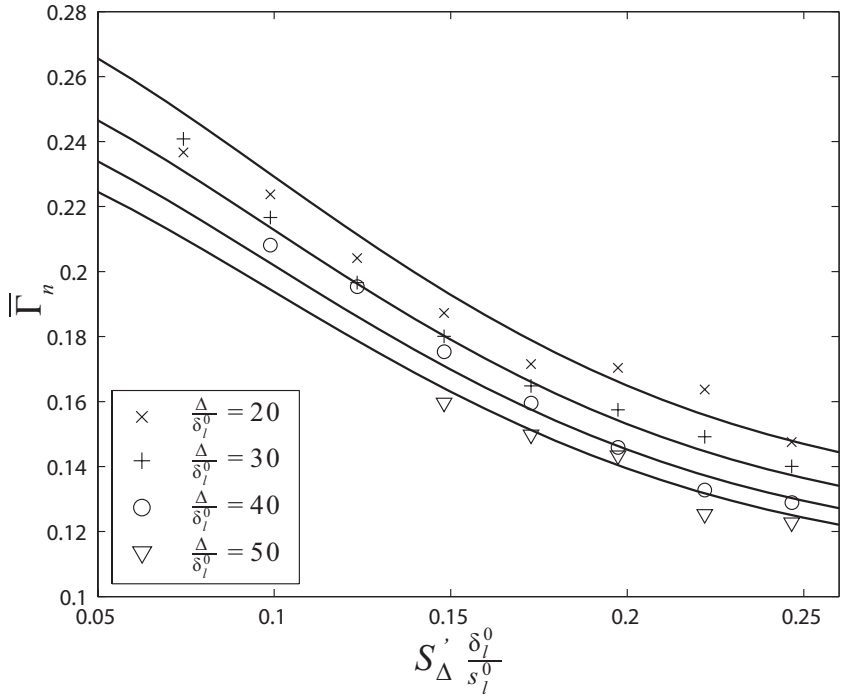

Figure 6.13: Measured mean strain efficiency function associated with compressive (negative) strain rate. Solid lines represent the fit from §6.2.2.3.

size: smaller filter sizes resulted in higher strain efficiency.

The different behaviors of the strain efficiency functions with increasing turbulence may be somewhat understood by considering simple counter-rotating vortex configurations combined with hydrodynamic scale flow patterns set up by the flame wrinkling. These hydrodynamic scale flows are associated with the hydrodynamic instability as described in §1.11. First consider the canonical configuration of outwardly rotating vortices, positive strain rate, and a negative curvature wrinkle. In such an interaction, flow is channeled into the wrinkle (e.g. Fig. 5.10). This tends to push the vortical structures together and may increase the strain rate (relative to if the flame remained planar). Stronger turbulence would create larger wrinkles and enhance this channeling. Hence, the creation of large negative curvature wrinkles should have no detrimental effect on the strain rate and may enhance it. The increasing efficiency may also be simply associated with common observation that

stronger turbulence is more effective at stretching the flame [22, 28, 74].

If, on the other hand, negative strain rate is exerted on the flame, this is associated with inwardly rotating vortical structures and a positive curvature wrinkle. Such a wrinkle creates a diverging flow field in the reactants, which tends to push the vortical structures apart and weaken the strain rate (e.g. Figs. 4.36 and 4.37). Hence, negative strain rate is associated with a wrinkling process that tends to attenuate the strain rate. The stronger the turbulence, the larger the wrinkle and the more significant the attenuation. Therefore, when stronger turbulence is associated with negative strain rate, it tends to attenuate the strain rate faster, resulting in a lowered efficiency.

These simple ideas illustrating the difference between negative and positive strain efficiency are, of course, an oversimplification of the turbulence-flame interaction. However, DNS studies have shown that the strain rate and curvature are negatively correlated in real turbulent flames; negative strain is associated with positive curvature and vice versa [18]. These phenomenological ideas are therefore applicable regardless of the particular turbulence configuration. Furthermore, they clearly indicate the need to consider the fluid dynamic strain rate when describing turbulence-flame interactions. The vortical structures in such interactions may remain essentially unchanged, but the strain rate field associated with them is greatly affected.

The filter scale dependence exhibited by the strain efficiency also requires consideration. The independence of the overall strain efficiency with respect to filter size displayed in 6.10 and the inverse dependance displayed in both Figs. 6.12 and 6.13 appear at first to be in conflict with the standard observation of increasing stretch efficiency with increasing filter size. However, this is not the case. As described in §6.2.2.1, the definition of the strain efficiency function based on S'_Δ intrinsically

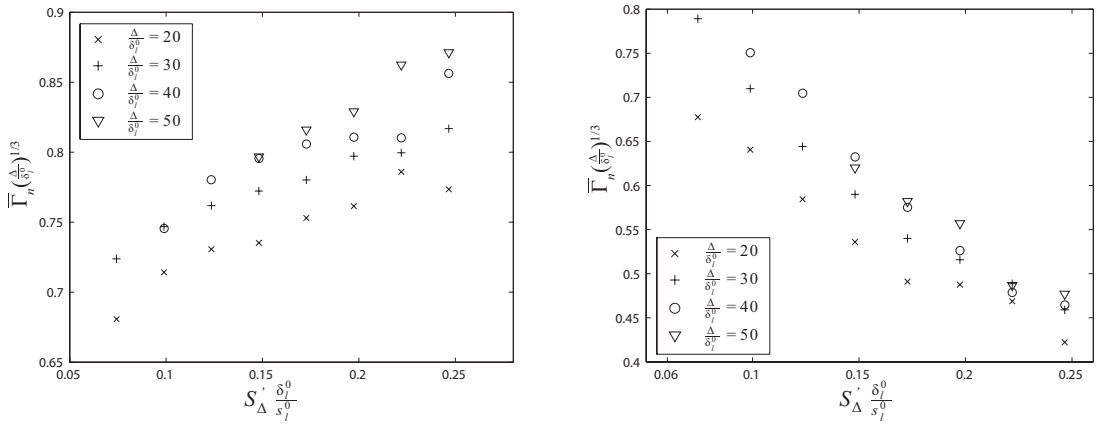

(a) $\overline{\Gamma}_p$ (b) $\overline{\Gamma}_n$

Figure 6.14: Measured strain efficiency functions with the intrinsic $\frac{\Delta}{\delta_l^0}$ dependence removed. The efficiency of the turbulence in straining the flame increases with increasing filter size.

includes a $\Delta^{-1/3}$ dependence; if the actual efficiency of the turbulence was independent of scale the efficiency function would still show this relationship. The actual physical dependence of strain efficiency on turbulence scale is displayed when this is accounted for. Figure 6.14 shows the various strain efficiency functions normalized by $(\Delta/\delta_l^0)^{-1/3}$. As can be seen, larger filter sizes resulted in a larger normalized strain efficiency in all cases. Hence, larger scale turbulence was more efficient in generating strain rate on the flame than smaller scale turbulence.

6.2.2.3 Some useful fits

During the above analysis, the parameters that control the strain efficiency functions and $\overline{P}_p^a$ have become apparent. Namely:

$$\overline{\Gamma}_p = \overline{\Gamma}_p\left(S'_\Delta\frac{s_l^0}{\delta_l^0}, \frac{\Delta}{\delta_l^0}\right) \tag{6.40}$$

$$\overline{\Gamma}_n = \overline{\Gamma}_n\left(S'_\Delta\frac{s_l^0}{\delta_l^0}, \frac{\Delta}{\delta_l^0}\right) \tag{6.41}$$

$$\overline{P}_p^a = \overline{P}_p^a\left(\frac{\Delta}{\delta_l^0}\right) \tag{6.42}$$

In order to implement the proposed model, fits to the measured data are required. Due to hardware limitations, the range of turbulence studied herein does not en-

compass the entire range of turbulence encountered in practical combustion devices. Hence, direct fits to the measured data may not reflect the actual trends at higher turbulence intensities. For example, the positive strain efficiency cannot continuously increase in the nearly linear manner indicated by the data. This curve must asymptote to some limiting value that is strictly less than unity; the data in Fig. 6.12 appears to begin this behavior in the measured range. Similarly, the negative efficiency cannot decrease to zero. The measured data in Fig. 6.13 indicate that $\overline{\Gamma}_n$ also approaches a constant lower limit.

This section provides fits for the measured data that behave in the expected manner at higher turbulence intensities. That is, curves for $\overline{\Gamma}_p$ and $\overline{\Gamma}_n$ are sought that asymptote to some constant value. The validity of these fits outside of the measured range must be evaluated in a future research effort. Also, a simple fit for $\overline{P}_p^a$ will be presented.

The following form is proposed to fit $\overline{\Gamma}_p$:

$$\overline{\Gamma}_p = \left[b_1 \exp\left(-\frac{b_2}{\left(S'_\Delta \frac{\delta_l^0}{s_l^0} \right)^{b_3}} \right) \left(\frac{\Delta}{\delta_l^0} \right)^{b_4} \right] \left(\frac{\Delta}{\delta_l^0} \right)^{-1/3} \tag{6.43}$$

This function contains several components and is similar in form to Eq. 6.13. The constant b_1 scales the magnitude of the efficiency, while b_2 and b_3 determine the growth rate of the curve. These parameters describe the effect of varying the turbulence intensity. The effect of varying the filter scale is represented by the power law terms. Firstly, the intrinsic effect of varying the filter scale is given by the -1/3 power law as described in §6.2.2.1. The second power law, characterized by b_4 indicates the actual changing efficiency of the strain field with varying filter size. Figure 6.14 indicates that the efficiency increases with filter size. Hence, b_4 is expected to be positive.

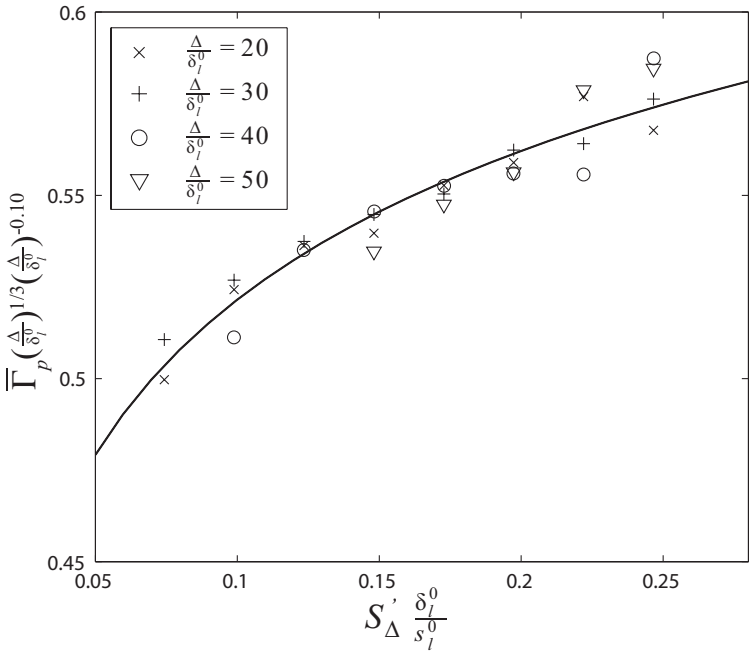

Figure 6.15: Positive strain efficiency function normalized by Δ power law scaling. Solid line is the fit of Eq. 6.45.

This formulation assumes that the dependence on filter scale can be completely encompassed by the power law terms. Hence, when $\overline{\Gamma}_p$ is normalized by these terms, all the data should fall on a single curve. To test this, b_4 was varied over a range and the value resulting in the lowest mean standard deviation of the data determined. It was found that $b_4 = 0.10$ provided the minimum scatter. Figure 6.15 shows $\overline{\Gamma}_p$ normalized by the power law terms. As can be seen, the data collapses well. Hence, a fit was sought to the scaled data such that:

$$\overline{\Gamma}_p \left(\frac{\Delta}{\delta_l^0}\right)^{-0.10} \left(\frac{\Delta}{\delta_l^0}\right)^{1/3} = b_1 \exp\left(-\frac{b_2}{\left(S'_\Delta \frac{\delta_l^0}{s_l^0}\right)^{b_3}}\right) \tag{6.44}$$

In this form, b_1 is seen to be the filter independent asymptotic limit of the efficiency function; once the filter scale dependence is accounted for, this value indicates the maximum strain efficiency. However, it possesses no explicit physical meaning; it simultaneously encompasses the effect of straining inefficiencies from physical turbulence-flame interaction and the numerical effects of the power laws. The mea-

sured data did not reach large enough turbulence levels to experimentally observe this asymptote and good fits could be accomplished over a range $0.6 < b_1 < 18$.

To determine a reasonable value, the limiting case of $\frac{\Delta}{\delta_l^0} = 1$ was considered. In the thin flamelet regime, the flame thickness is smaller than any turbulence length scale. This limit therefore corresponds to an unfiltered turbulence field. If the interaction between a single turbulent structure and the flame is considered, the maximum possible efficiency would be unity and hence $b_1 = 1$. In reality, the value would likely be less than unity since not all fluid dynamic strain rate is converted to strain rate on the flame. However, $b_1 = 1$ is a limiting upper value. Furthermore, it was found that the residual (sum of the squares) error in the fit approached a minimum around this value as shown in Fig. 6.16(a). Hence, a value of $b_1 = 1$ was used. With this parameter set, the data was fitted with the constants $b_2 = 0.43$ and $b_3 = 0.18$, resulting in:

$$\overline{\Gamma}_p = \left[\exp\left(-\frac{0.43}{\left(S'_\Delta \frac{\delta_l^0}{s_l^0} \right)^{0.18}} \right) \left(\frac{\Delta}{\delta_l^0} \right)^{0.10} \right] \left(\frac{\Delta}{\delta_l^0} \right)^{-1/3} \tag{6.45}$$

This curve is shown as the solid lines in Figs. 6.12 and 6.15 and the dashed line Fig. 6.19. As can be seen, the fit closely matches the measured data.

A fit for the negative strain efficiency function was computed in a similar manner. For $\overline{\Gamma}_n$, a fit was sought such that:

$$\overline{\Gamma}_n = \left[\left(c_1 \exp\left(-\frac{c_2}{\left(S'_\Delta \frac{\delta_l^0}{s_l^0} \right)^{c_3}} \right) + c_4 \right) \left(\frac{\Delta}{\delta_l^0} \right)^{c_5} \right] \left(\frac{\Delta}{\delta_l^0} \right)^{-1/3} \tag{6.46}$$

Here, c_5 represents the power law effect of varying the filter size. This value was determined in the same manner as above and found to be $c_5 = 0.15$. Figure 6.17 shows $\overline{\Gamma}_n$ normalized by the filter scale relations. Once again, the data collapses well to a single curve.

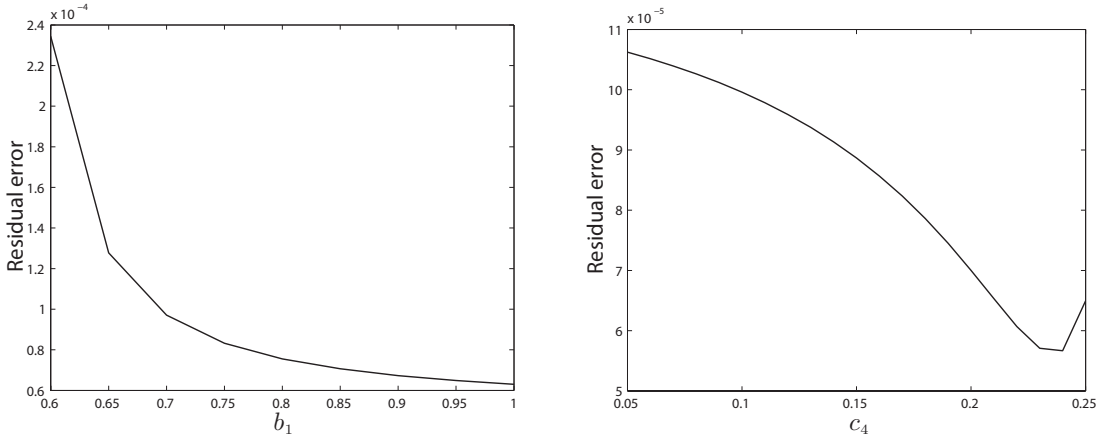

(a) $\overline{\Gamma}_p$ (b) $\overline{\Gamma}_n$

Figure 6.16: Residual error from varying the filter independent asymptotic limits.

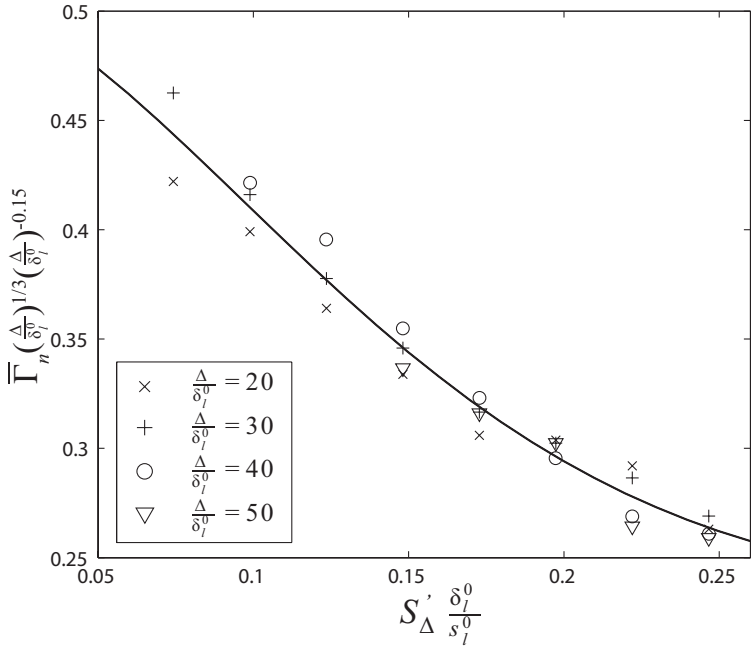

Figure 6.17: Negative strain efficiency function normalized by Δ power law scaling. Solid line is the fit of Eq. 6.47.

The filter independent asymptotic limit is described by c_4. Unlike $\overline{\Gamma}_p$, the data for $\overline{\Gamma}_n$ had begun to asymptote in the measured range and hence c_4 could somewhat be determined directly. To do so, c_4 was varied over values around the measured minimum in Fig. 6.17 and the resulting residual error determined. As can be seen from Fig. 6.16(b). This had a minimum at $c_4 = 0.23$. At this value, $c_1 = 0.28$, $c_2 = 23.7$ and $c_3 = -1.73$, which resulted in:

$$\overline{\Gamma}_n = \left[\left(0.28\exp\left(-23.7\left(S'_\Delta\frac{\delta_l^0}{s_l^0}\right)^{1.73}\right)+0.23\right)\left(\frac{\Delta}{\delta_l^0}\right)^{0.15}\right]\left(\frac{\Delta}{\delta_l^0}\right)^{-1/3} \tag{6.47}$$

This curve is shown as the solid lines in Figs. 6.13 and 6.17 and the dotted line in Fig. 6.19. Once again, the fit closely matches the measured data. It is noted that this curve approaches $c_1 + c_4$ as the turbulence intensity approaches zero. This behavior is unlikely since previous studies have shown that the overall efficiency approaches zero in this range. It is therefore possible that the data would drop to zero at lower turbulence levels. However, very few interactions occurred in this range and converged statistics were not available. Furthermore, such very weak turbulence does significantly contribute to the overall strain rate.

In order to determine a fit for the overall strain efficiency function, the above two fits and the probability of positive strain rate are needed. As shown in Fig. 6.11, this probability increased with the filter size. At a given Δ, it was essentially constant for all turbulence intensities. It was found that $\overline{P}_p^a$ increased linearly with Δ in the measured range. However, this trend could not continue for all filter sizes; there must be some limiting distribution of positive and negative strain rate at large and small enough filter scales. For example, as Δ approaches δ_l^0, $\overline{P}_p^a$ should not drop below 0.5. Similarly as Δ increases, $\overline{P}_p^a$ should approach a constant value representing the overall distribution of strain rate.

Unfortunately, these limiting values could not be determined from the data. Nev-

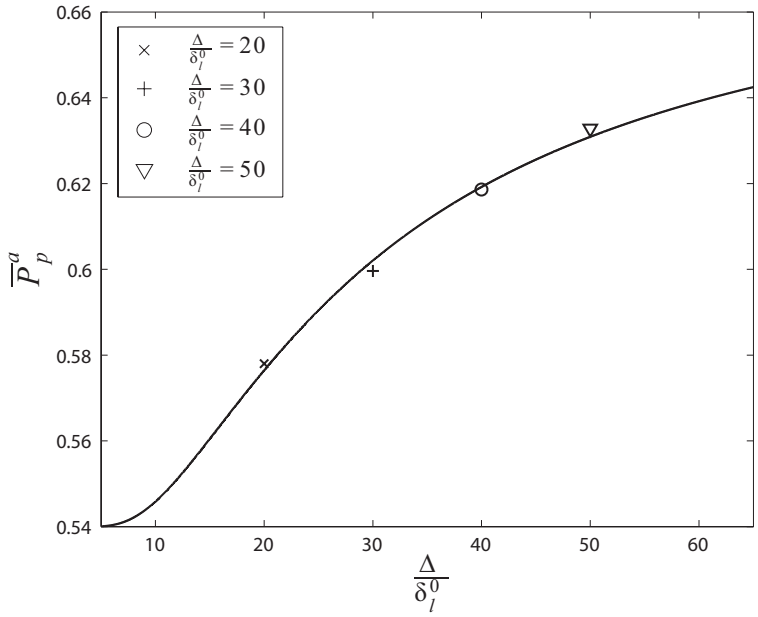

Figure 6.18: Mean measured probability of positive strain rate along with the fit of Eq. 6.49.

ertheless, it was decided to fit the results to a function that has the correct qualitative behavior and taking the form:

$$\overline{P}_p^a = p_1 \exp\left(-\frac{p_2}{(\Delta/\delta_l^0)^{p_3}}\right) + p_4 \tag{6.48}$$

In this equation, p_4 sets the lower limit and $p_1 + p_4$ sets the upper asymptotic limit. To determine p_4, the measured data was linearly extrapolated to $\frac{\Delta}{\delta_l^0} = 1$. This yielded $p_4 = 0.54$. However, using this value, the data could be accurately fit using a variety of upper limits. The value of $p_1 + p_4$ was therefore varied from the maximum measured $\overline{P}_p^a$ to unity and the value corresponding to the minimum residual error selected. This yielded an upper limit of $\overline{P}_p^a = 0.68$ and $p_1 = 0.14$. With these values, the data was fitted by:

$$\overline{P}_p^a = 0.14 \exp\left(-\frac{55}{(\Delta/\delta_l^0)^{1.2}}\right) + 0.54 \tag{6.49}$$

Figure 6.18 shows the fit of Eq. 6.49 and the mean probability of positive strain rate at each measured filter size. The fit values at the employed filter scales are also

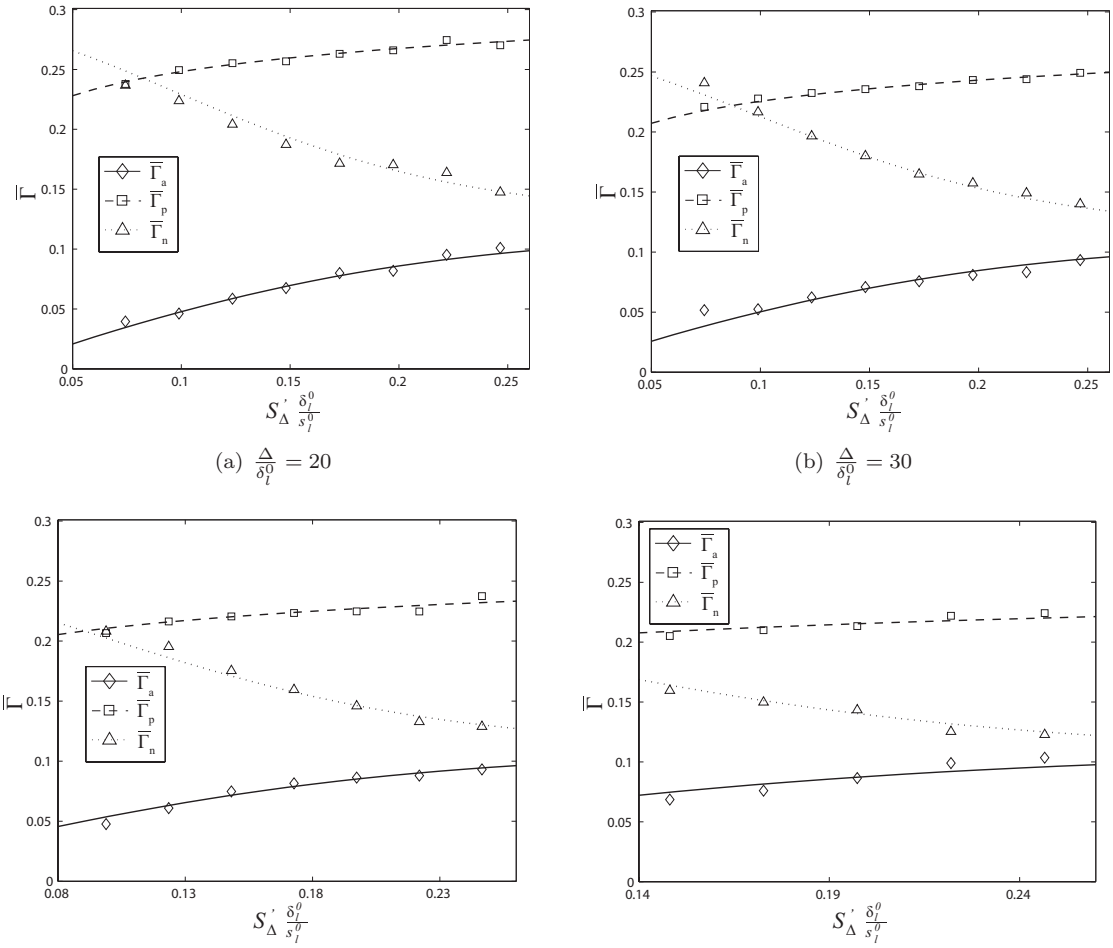

(a) $\frac{\Delta}{\delta_l^0} = 20$ (b) $\frac{\Delta}{\delta_l^0} = 30$

(c) $\frac{\Delta}{\delta_l^0} = 40$ (d) $\frac{\Delta}{\delta_l^0} = 50$

Figure 6.19: Measured and fitted strain efficiency functions.

shown as the solid lines in Fig. 6.11. As can be seen, the fit accurately follows the measured data.

The fit for $\overline{\Gamma}_a$ is given by Eqs. 6.37, 6.45, 6.47, and 6.49. The resultant curves are shown as the solid lines in Fig. 6.19. As can be seen, the proposed formulation for the overall strain efficiency function and the fits for its various components accurately predict the measured data.

6.2.2.4 Model summary and future work

Based on the above analysis, a new model has been proposed for the subgrid strain rate exerted on a turbulent premixed flame, given by Eq. 6.22. The model

was framed using the subgrid fluid dynamic strain rate to characterize the turbulence intensity, as this was shown to be a better parameter than the typically used $\frac{u'}{\Delta}$. Also, Eq. 6.22 incorporates many observations about real turbulent premixed flames that are not accurately described by the canonical flame-vortex interaction that has been used to develop previous models. Namely, Eq. 6.22 account for the fact that turbulence exerts both positive and negative strain rate and that these processes behave differently at different turbulence levels. The strain efficiency of extensive strain rate increased with the turbulence intensity, while that of negative strain rate decreased. The probability of finding positive strain rate remained approximately constant as the turbulence level varied. This resulted in a net strain efficiency that increased with the turbulence intensity. Also, the strain efficiency decreased with increasing filter size. This is contrary to previous models. However, it was shown that the definition of the characteristic strain rate caused an intrinsic dependence on the filter size. When this dependence was removed, the strain efficiency increased with the filter size. Fits to the measured data were provided that can be implemented in LES simulations.

This model should provide a better estimate for the subgrid strain rate exerted on a turbulent premixed flame. However, there are further developments that are required before it can be fully implemented. Most particularly, the range of turbulence intensities studied should be increased. With the current experiment, it was only possible to investigate low to moderate turbulence intensity due to hardware limitations. The asymptotic behavior of the positive and negative efficiency functions for large turbulence levels could not be explicitly measured. While the fits provided were designed to mimic an asymptotic approach to a constant, the accuracy of these curves at higher turbulence intensities should be investigated. Therefore, similar

experiments or DNS studies should be made at higher turbulence levels as diagnostics and computational capabilities advance. Similarly, the range of filter scales investigated must be expanded by investigating larger domains.

While the trends identified are expected to be qualitatively true in general, the universality of the quantitative results must be investigated. This should be done in a variety of burner configurations. Such studies may indicate that additional parameters are desirable in the strain efficiency function. For example, it is possible that the orientation of the large scale (i.e. background) fluid dynamic strain rate field may be important [10, 49, 54, 82]. Hamlington et al. [49] have shown that the local vorticity field preferentially aligns with the axis of the most extensive component of the background principal strain rate. The resulting fine scale strain-rate field locally aligns as dictated by the vorticity. Hence, in a flow with a strong mean shear, the subgrid strain rate field may be aligned differently relative to the flame than in the present measurements. A parameter characterizing this orientation could be used to improve the model.

Properties of the reactant mixture other than s_l^0 and δ_l^0 also may be significant. For example, differential diffusion may affect the strain transfer functions. To investigate this, mixtures of varying Lewis and Markstein numbers should be investigated. While data was taken at different Markstein numbers, only the Case 2 data was tractable for the current analysis. The remaining flames were oriented much more parallel to the bulk flow direction. Measuring the interaction between fluid control masses and these flames was difficult as the interactions rarely took place entirely within the field of view. Converged statistics were therefore not obtained. However, the same analysis can be applied to different burner configurations where the flame orientation would not be a problem. This would allow preferential diffusion effects

to be studied.

6.3 Modeling the subgrid curvature stretch rate

In §1.6, two models for the subgrid curvature stretch rate were described. One model, employed in Ref. [22], postulated that $\overline{\langle \kappa_{c,sg} \rangle}$ was negative and equal in magnitude to the subgrid strain rate. The second, employed in Refs. [51, 52], postulated that it was negative and proportional to $s_l \Sigma$. These ideas were analyzed using the measured data.

6.3.1 The curvature stretch rate-strain rate balance model

Since the previous model for $\overline{\langle a_{t,sg} \rangle}$ (Eq. 6.11) was found to inaccurately represent the measurements, the assumption:

$$\overline{\langle \kappa_{c,sg} \rangle} = -\overline{\langle a_{t,sg} \rangle} \tag{6.50}$$

also would produce inaccurate values values for the curvature stretch rate. However, the postulation that these terms locally balance was analyzed. To do so, the data from Case 2 was analyzed. As described in §4.3, the propagation speed of this flame was expected to remain at essentially the unstretched flame speed and the curvature stretch rate was given by:

$$\overline{\langle \kappa_{c,sg} \rangle} = s_l^0 \overline{\langle C_{sg} \rangle} \tag{6.51}$$

where C_{sg} is the subgrid curvature.

Shown in Fig. 6.20 are the PDFs of the ratio $\frac{\overline{\langle \kappa_{c,sg} \rangle}}{\overline{\langle a_{t,sg} \rangle}}$ at various filter sizes. If Eq. 6.50 was valid, these PDFs would be centered around -1. However, this is clearly not the case. This result is unsurprising since, as described in §4.8, this flame has regions in which flame surface is generated and destroyed in the mean; flame surface area is convected from the base to the tip. Hence, this balance could not hold locally

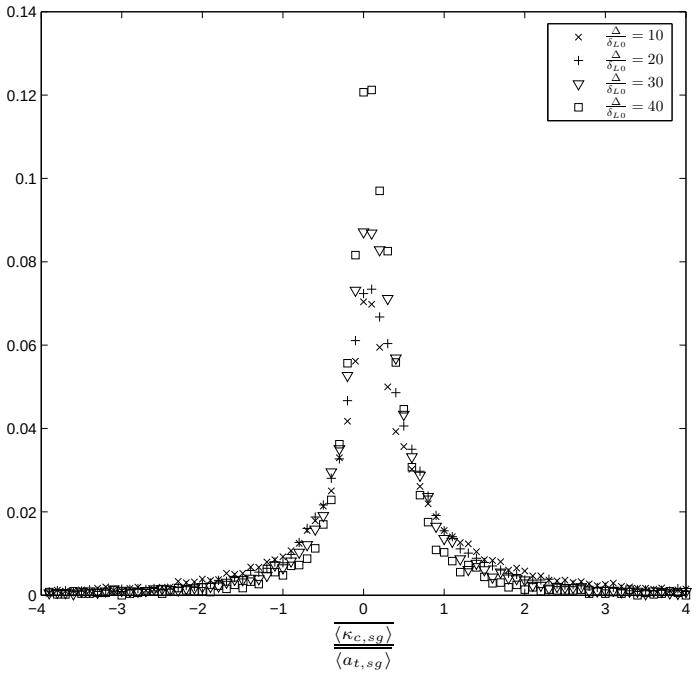

Figure 6.20: PDFs of $\frac{\overline{\langle \kappa_{c,sg} \rangle}}{\langle a_{t,sg} \rangle}$ at various filter sizes for Case 2. These indicate that the curvature stretch rate and strain rate do not balance.

for the overall flame surface (including the large scales). Figure 6.20 shows that it does not hold at the subgrid scales.

6.3.2 The curvature stretch rate-flame surface area model

The model of Hawkes and Cant [51, 52] is similar to that employed in RANS flame surface density approaches and states that the curvature stretch rate is negative and proportional to $s_l\Sigma$. This model is based on a geometric argument: in order for the flame surface area in a given volume to increase, the flame must become more wrinkled and therefore must become more curved. However, it does not account for the fact that an unwrinkled flame has flame surface density. The model would erroneously predict that a planar flame would be stretched due to curvature. This issue can be avoided by considering the *increase* in flame surface area relative to the unwrinkled flame. This is given expressly by the wrinkling factor, Ξ. Therefore, the

relationship between $\langle \kappa_{c,sg} \rangle$ and Ξ will be evaluated. This may be written as:

$$\langle \kappa_{c,sg} \rangle = \Upsilon(\vec{\zeta}) \frac{s_l^0}{\delta_l^0} \Xi \tag{6.52}$$

Note that there is no temporal averaging of the stretch rate in this equation. Since the model is based on a geometric argument, it should be valid at every instant and studying turbulence-flame interactions is unnecessary. In Eq. 6.52, $\Upsilon(\vec{\zeta})$ provides the relationship between the flame wrinkling and curvature stretch rate, which is analogous to the strain efficiency function. This function will be referred to as the 'wrinkling transfer function'. The standard model implies that Υ is a negative constant.

The characteristic curvature stretch rate in Eq. 6.52 is identified as $\frac{s_l^0}{\delta_l^0}$. That is, δ_l^0 is representative of the smallest scale wrinkle scale possible in the subgrid; the flame cannot be wrinkled at a scale finer than some multiple of the flame thickness. This ratio therefore gives an estimate of the maximum curvature stretch rate, which is associated with the small scale subgrid wrinkles. Alternatively, a large scale wrinkling length could be used, which would be related to Δ. However, such a definition would be less indicative of fine scale wrinkling occurring in the subgrid. Also, use of δ_l^0 provides a characteristic stretch rate that is independent of the filter size.

To begin the analysis, profiles of $\overline{\Upsilon}$ were computed in the same manner as those of $\overline{\Gamma}$. Once again, Case 2 was used and s_l was assumed to equal the unstretched value of s_l^0 everywhere. The profiles of $\overline{\Upsilon}$ are shown in Fig. 6.21 for all filter sizes studied. As can be seen, the wrinkling transfer function follows a complex shape with a few common properties: it is positive for low Ξ, decreases with increasing Ξ (sometimes becoming negative), and then begins to level off. Also, the transfer function appears to decrease with the filter size. It therefore does not appear that the overall curvature stretch rate always negative and proportional to the amount of wrinkling as predicted

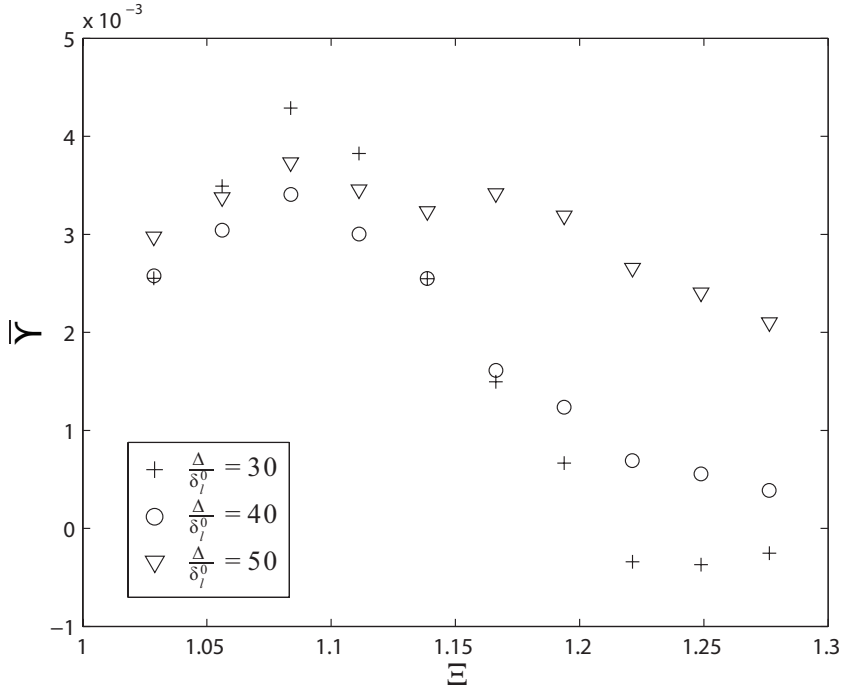

Figure 6.21: Measured mean wrinkling transfer function ($\overline{\Upsilon}$) as a function of the wrinkling factor.

by the traditional model. It is noted the smallest filter considered was $\Delta = 30\delta_l^0$ (as opposed to $\Delta = 20\delta_l^0$ in §6.2). Smaller filter scales approached the order of the thermal thickness of the flame (recall that δ_l^0 is the reaction zone thickness). The thermal thickness limits the minimum wrinkle dimension and considering filters of this scale produced inaccurate results.

While the values in Fig. 6.21 indicate the overall transfer function, they do not directly indicate how curved the flame was; they simultaneously account for the amount of wrinkling and the distribution between positive and negative curvature. As the flame became more wrinkled it necessarily became more curved. This is demonstrated in Fig. 6.22, which shows profiles of the mean of the transfer function magnitude, $\overline{|\Upsilon|}$. These data increased quickly at low Ξ and then leveled off. This confirms a basic idea of the model: as the flame wrinkling increased, the transfer function magnitude approached a constant and the curvature of the flame increased

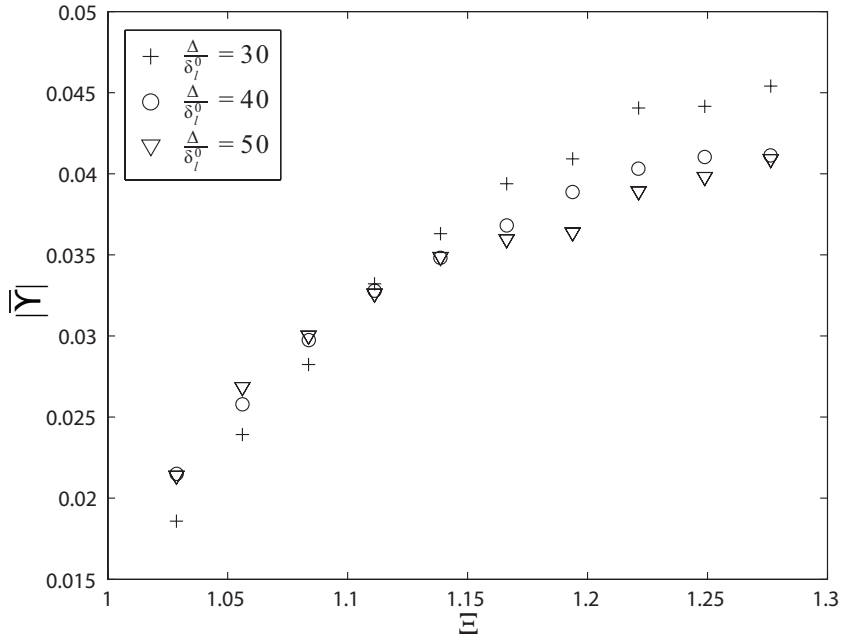

Figure 6.22: Measured mean wrinkling transfer function magnitude.

in proportion to the flame wrinkling. The complex shapes of the $\overline{\Upsilon}$ curves therefore indicate that the distribution of positive and negative curvature (both in magnitude and probability) varied as the flame became more wrinkled. It is noted that the maximum wrinkling factor studied is in the range of 1.3, which is relatively low. Therefore $\overline{|\Upsilon|}$ was proportional to Ξ for relatively low wrinkling factors.

Since the transfer function magnitude increased in a regular manner but its value varied in a complex manner, there must have been competing effects from the positive and negative components of the curvature stretch rate. This argument is similar in nature to that used to propose Eq. 6.22 for the strain rate model. Therefore, the subgrid curvature stretch rate was modeled as:

$$\langle \kappa_{c,sg} \rangle = \Upsilon(\vec{\zeta}) \frac{s_l}{\delta_l^0} \Xi = \left[\overline{\Upsilon}_p \overline{P}_p^c - \overline{\Upsilon}_n \left(1 - \overline{P}_p^c \right) \right] \frac{s_l^0}{\delta_l^0} \Xi \tag{6.53}$$

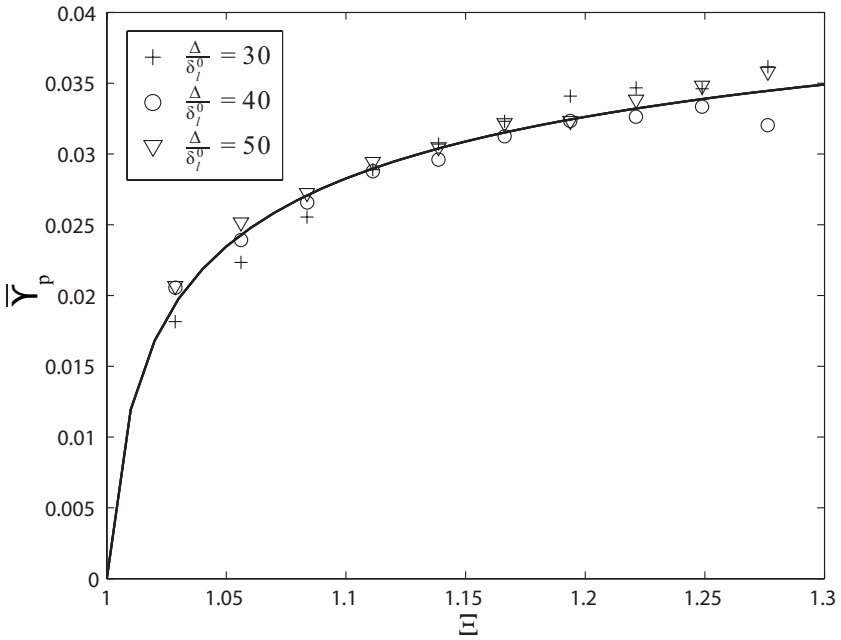

Figure 6.23: Measured mean positive wrinkling transfer function. Solid lines represent the fits described in §6.3.2.1.

where

$$\Upsilon_p = \{\langle \kappa_{c,sg} \rangle ; \kappa_{c,sg} > 0\} \frac{\delta_l^0}{s_l^0} \tag{6.54}$$

$$\Upsilon_n = \{\langle |\kappa_{c,sg}| \rangle ; \kappa_{c,sg} < 0\} \frac{\delta_l^0}{s_l^0} \tag{6.55}$$

and $\overline{P}_p^c$ is the probability of finding positive curvature at a given wrinkling factor.

Profiles of the measured positive and negative wrinkling transfer functions are provided in Figs. 6.23 and 6.24. The solid lines represent fits to the data, which are described in §6.3.2.1. As can be seen, the negative transfer function always was greater than the positive transfer function. This was expected since a wrinkled flame tends to form small regions of intense negative curvature and large regions of diffuse positive curvature. Hence, at a particular wrinkling factor the negative transfer function should be greater. By the same argument, the probability of positive curvature should be greater than the probability of negative curvature. Figure 6.25 shows this probability for the measured data. For all cases, $\overline{P}_p^c$ was greater that 0.5

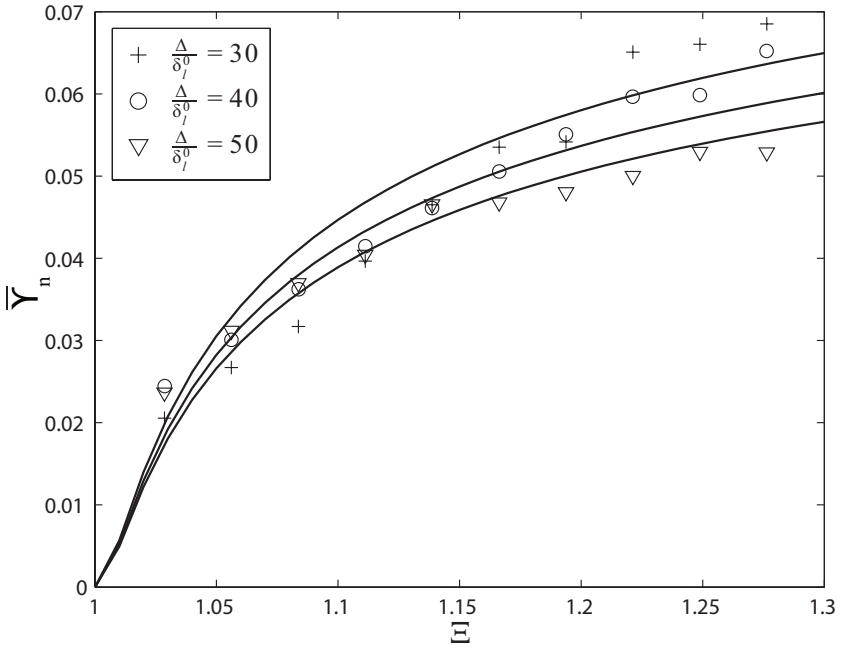

Figure 6.24: Measured mean negative wrinkling transfer function. Solid lines represent the fits described in §6.3.2.1.

and approached a constant value with increasing Ξ. At very low wrinkling factors it was less than its asymptotic value but still greater than 0.5. Hence, $\overline{\Upsilon}_p$, $\overline{\Upsilon}_n$, and $\overline{P}_p^c$ had qualitatively the behavior expected from the kinematics of a wrinkled flame.

The transfer functions also exhibited some of the behavior predicted by the traditional model [51]. That is, they approached a constant as Ξ increased. While the constant was not reached in the measured range, this indicates that the stretch rate associated with both positive and negative curvature in a highly wrinkled flame will be proportional to the wrinkling factor.

The data for the positive transfer function did not exhibit a filter scale dependence. However, one was apparent for the negative transfer function; decreasing filter sizes resulted in increasing transfer functions. The different dependencies were caused by the different length scales of positive and negative wrinkles. Once again, the wavelength of positive curvature wrinkles is much larger than those of negative

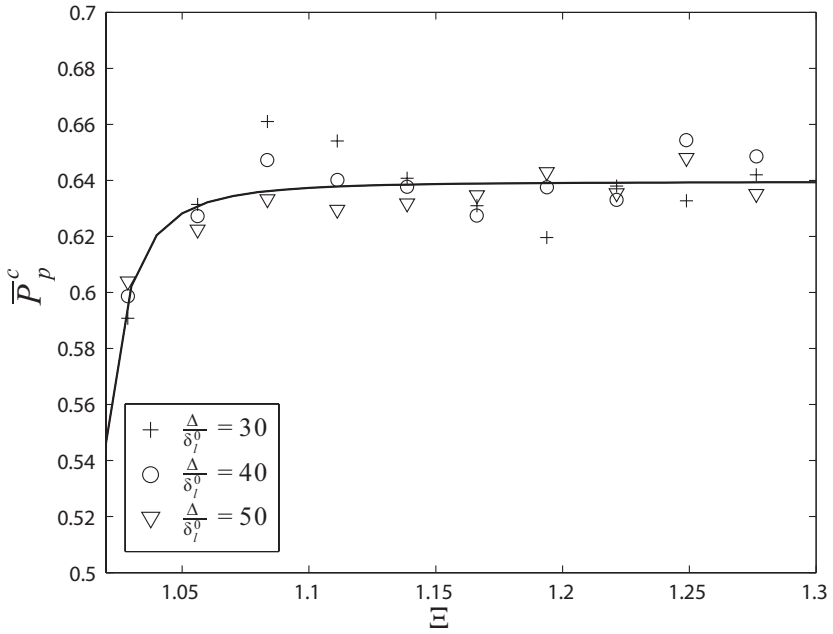

Figure 6.25: Measured mean probability of finding positive curvature. Solid lines represent the fits described in §6.3.2.1.

curvature. In the range of filter scales studied, positive curvature wrinkles were often similar in length to the maximum filter size. Negative curvature wrinkles were considerably smaller. Hence, decreasing the filter size did not greatly effect the former, while retaining more of the later in the subgrid. This resulted in the Δ dependencies shown. However, if the filter size was increased further, $\overline{\Upsilon}_p$ would likely exhibit some dependence. This effect was not studied because of the limited field of view.

6.3.2.1 Useful fits

The above analysis has indicated the parameters that control the wrinkling transfer functions and $\overline{P}_p^c$. Namely:

$$\overline{\Upsilon}_p = \overline{\Upsilon}_p\left(\Xi, \frac{\Delta}{\delta_l^0}\right) \tag{6.56}$$

$$\overline{\Upsilon}_n = \overline{\Upsilon}_n\left(\Xi, \frac{\Delta}{\delta_l^0}\right) \tag{6.57}$$

$$\overline{P}_p^c = \overline{P}_p^c\left(\Xi, \frac{\Delta}{\delta_l^0}\right) \tag{6.58}$$

In this section, fits for these functions are determined.

While the filter scale dependence of $\overline{\Upsilon}_p$ was not experimentally observed, it may occur for larger filter sizes as discussed above. Hence, while is in included as a parameter, it will not be addressed in the fits. A fit for $\overline{\Upsilon}_p$ was therefore sought of the form:

$$\overline{\Upsilon}_p = d_1 \exp\left(-\frac{d_2}{(\Xi-1)^{d_3}}\right) \tag{6.59}$$

This is a similar functional form to the fits for $\overline{\Gamma}$, with a shift of the coordinate axis. The asymptotic roll off of the data in Fig. 6.23 was significant enough for the limit, d_1, to be determined directly from the data. This resulted in:

$$\overline{\Upsilon}_p = 0.053 \exp\left(-\frac{0.26}{(\Xi-1)^{0.38}}\right) \tag{6.60}$$

This curve is shown as the solid line in Fig. 6.23 and the dashed lines in Fig. 6.27.

The negative transfer function exhibited a filter scale dependence. Hence, a power law was included in the fit:

$$\overline{\Upsilon}_n = e_1 \exp\left(-\frac{e_2}{(\Xi-1)^{e_3}}\right)\left(\frac{\Delta}{\delta_l^0}\right)^{e_4} \tag{6.61}$$

The exponent e_4 was determined in the same manner as for $\overline{\Gamma}$ and found to be -0.27. The measured data normalized by this filter scale dependence is shown in Fig. 6.26. As can be seen, the data collapsed well to a single curve. However, the asymptotic roll off had not occurred as clearly as compared with the data for $\overline{\Upsilon}_p$. The fit parameter e_1 was therefore varied over an appropriate range and the overall fit corresponding to the minimum residual error selected. This resulted in:

$$\overline{\Upsilon}_n = 0.27 \exp\left(-\frac{0.24}{(\Xi-1)^{0.54}}\right)\left(\frac{\Delta}{\delta_l^0}\right)^{-0.27} \tag{6.62}$$

This is shown as the solid lines in Figs. 6.24 and 6.26 and the dotted lines in Fig. 6.27.

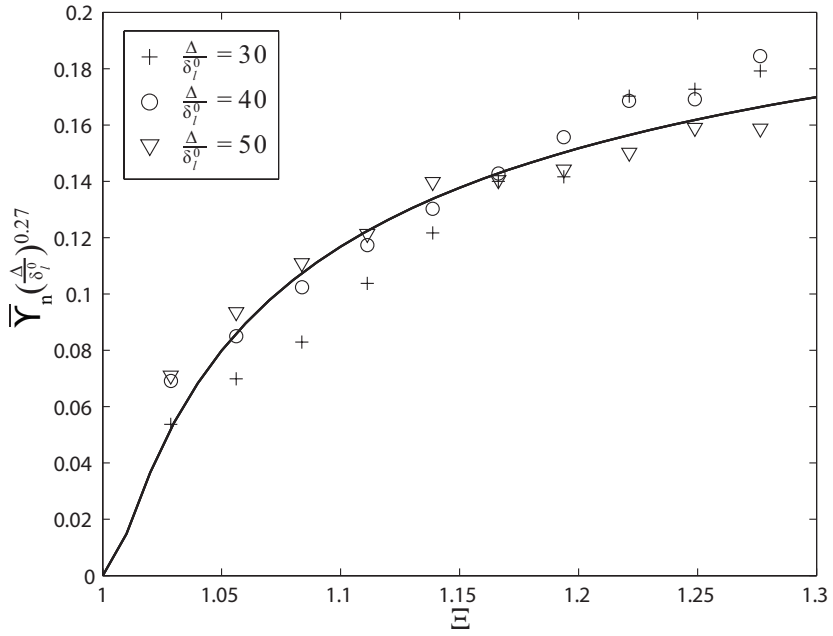

Figure 6.26: Negative wrinkling transfer function normalized by Δ power law scaling. Solid line is the fit of Eq. 6.62.

Finally, a fit was needed for $\overline{P}_p^c$. While the values quickly approached a constant of approximately 0.65, they were considerably lower at small Ξ. Using a constant severely over predicted $\overline{\Upsilon}$ in this range. Hence, $\overline{P}_p^c$ was fitted to a curve of the now familiar form, resulting in:

$$\overline{P}_p^c = 0.65 \exp\left(-\frac{1.4e-5}{(\Xi-1)^{2.4}}\right) - 0.016 \tag{6.63}$$

The resultant overall transfer function is plotted as the solid lines in Fig. 6.27. As can be seen, the fit follows the data quire well. There are some discrepancies at low Ξ, but these are associated with low curvature stretch rate and are therefore unlikely to be significant.

6.3.2.2 Effects of varying Markstein number

The CS-PIV cases studied allowed the effect of varying the Markstein number on the wrinkling transfer function to be observed. Unlike the strain rate model, only the geometry of the flame (not the turbulence-flame interaction) needed to be

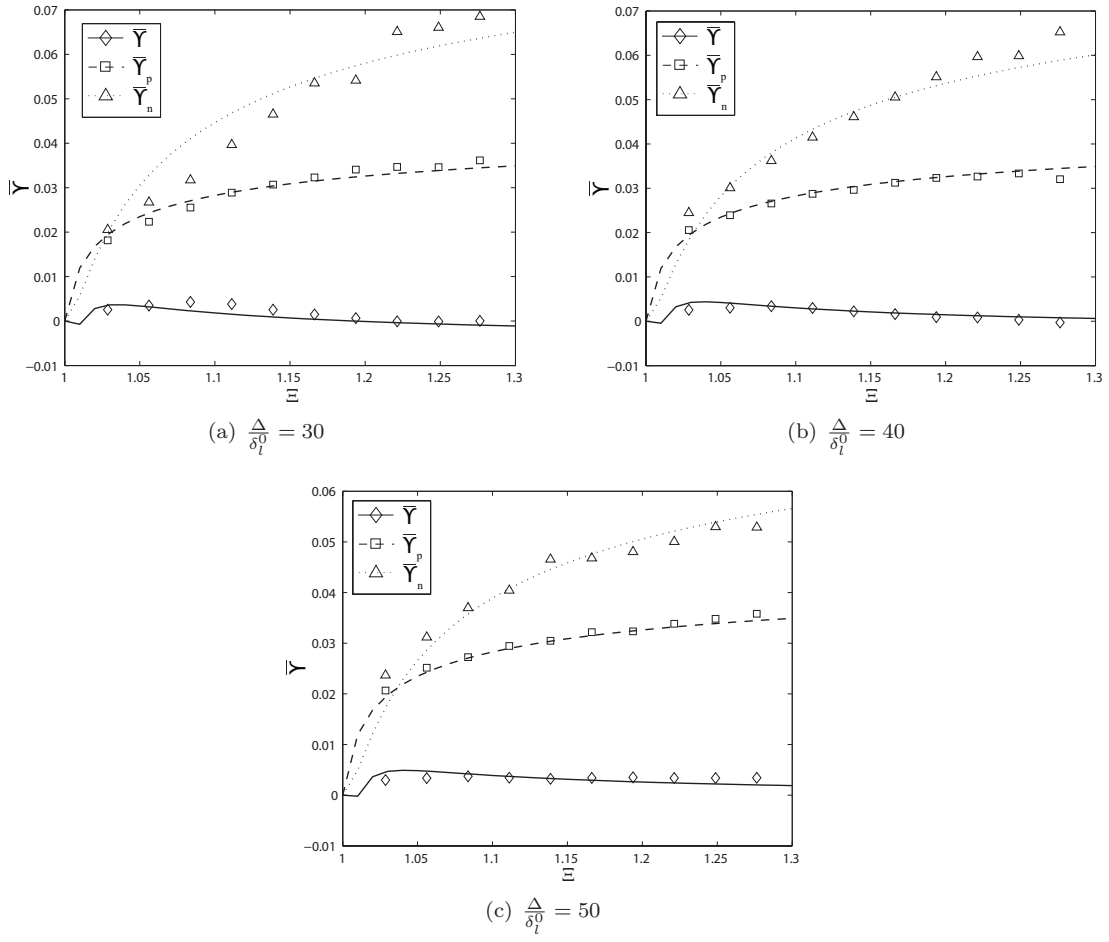

(a) $\frac{\Delta}{\delta_l^0} = 30$

(b) $\frac{\Delta}{\delta_l^0} = 40$

(c) $\frac{\Delta}{\delta_l^0} = 50$

Figure 6.27: Measured and fitted wrinkling transfer functions.

considered. Hence, the difficultly in obtaining strain rate data for Cases 1 and 3 mentioned in §6.2.2.4 did not apply. However, quantitative analysis was not possible since the Markstein number is not a well defined quantity. For the mixtures studied, experimental results have indicated a wide range of Markstein numbers [78]. Various studies have indicated that several of Markstein numbers may be needed for a single reactant mixture. That is, one may be required for each of positive and negative strain rate and curvature stretch rate. However, qualitative observations of the effects of Markstein number could be made. Additionally, Case 1 ($\phi = 0.60$) was not used in this discussion. This flame was considerably thicker than either Case 2 ($\phi = 0.70$) or Case 3, ($\phi = 1.35$). Filtering the field for Case 1 at scales considerably larger than the flame thickness and contained in the field of view did not result in sufficient data for statistical convergence.

Cases 2 and 3 correspond to Markstein numbers of approximately zero and greater than zero respectively, while possessing nearly identical flame speeds and thicknesses. Hence, variations in the wrinkling transfer functions should therefore be due to Markstein number effects. According to Eq. 1.29, the flame speed in a negative curvature winkle with positive Markstein number should increase; the flame speed in a positive curvature wrinkle should decrease. This acts to attenuate the wrinkle. However, given a wrinkling factor, the effect of Markstein number on the positive and negative transfer functions not so clear.

Figure 6.28 shows the wrinkling transfer functions for Cases 1 and 2 at $\frac{\Delta}{\delta_l^0} = 50$. As can be seen, the positive and negative transfer functions were nearly identical between the cases. However, the total transfer function was lower for Case 3. This is because, as shown in Fig. 6.29, the probability of positive curvature decreased.

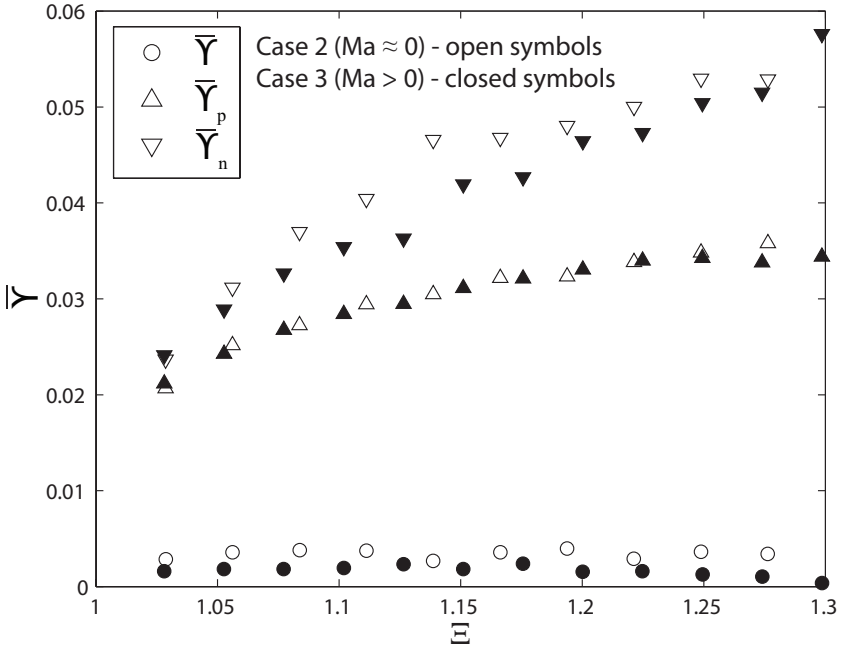

Figure 6.28: Measured mean wrinkling transfer functions for Cases 2 and 3. Varying the Markstein number did not significantly alter $\overline{\Upsilon}_p$ or $\overline{\Upsilon}_n$. However, $\overline{\Upsilon}$ decreased.

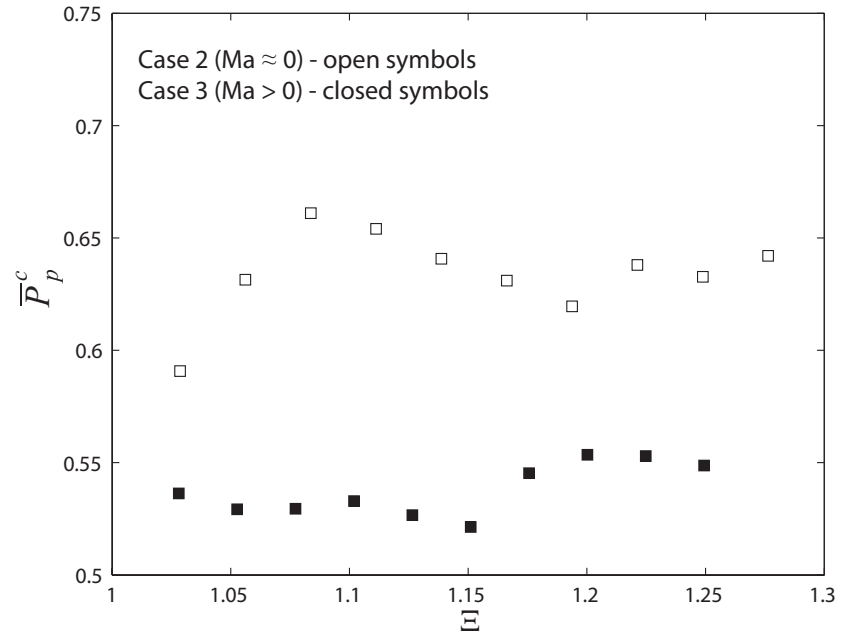

Figure 6.29: Measured probability of positive curvature for Cases 2 and 3. Increasing the Markstein number reduced the probability of positive curvature.

6.3.2.3 Model summary and future work

Based on the analysis described in this Section, a model for the subgrid curvature stretch rate was developed. The basic premise for the model was based on the observation that, as the flame surface becomes more wrinkled, it must also become more curved. Hence, a wrinkling transfer function was proposed that relates the flame wrinkling to the curvature stretch rate. In the traditional model, the transfer function would be a negative constant. However, it was found that the overall curvature stretch rate was not strictly negative did not increase in magnitude proportionally to the flame wrinkling; the transfer function was not a negative constant. This discrepancy was due to a complex balance between positive and negative curvature as the wrinkling increased. A model was therefore proposed in the form of Eq. 6.53, which accounts for these differences; separate transfer functions for positive and negative curvature were employed.

As the flame became more wrinkled, the wrinkling transfer functions for both positive and negative curvature wrinkles approached constants. Those for negative curvature had larger magnitude at the same filter scale and turbulence intensity. However, the probability of positive curvature was greater than for negative curvature. This was due to the kinematics of a wrinkled flame, which creates small regions of high negative curvature and large regions of low positive curvature. There therefore was a balance between the higher negative transfer function and higher probability of finding positive curvature that resulted in a complex form for the overall transfer function. It also was found that negative transfer functions increased with decreasing filter size, while the positive transfer function was independent. Fits to the measured data were presented that account for these observations. These fits can be used as a model for the subgrid curvature stretch rate in turbulent combustion

LES.

The effects of varying Markstein number also were observed. It was found that increasing the Markstein number did not significantly change the positive or negative transfer functions. However, it did result in a decreased probability of positive curvature. The overall transfer function and curvature stretch rate were therefore reduced.

It is expected that this model should be quite general; the relationship between the flame wrinkling and curvature is geometric and should have little to do with the specific configuration of the flame. However, for useful implementation of this model it is necessary to extend the range on wrinkling factors studied; studies of more highly wrinkled flames are needed. This is similar to the need to study higher turbulence levels for the strain rate model development in §6.2.2. Fortunately, since this is an instantaneous geometric relationship, neither temporally resolved diagnostics nor velocity measurements are needed. All that is required is high resolution imaging of the flame surface topography. Such diagnostics have been used to study fractal characteristics of the flame surface and may now be used to further develop this model [47, 48].

Also, further studies are needed to evaluate the effects of differential diffusion. That is, a wider variety of Markstein and/or Lewis numbers must be studied. Since these parameters effect how the flame speed responds to wrinkling, it is likely that they will effect the flame topography and consequentially the wrinkling transfer function.

6.4 Models for the subgrid turbulent burning velocity

Direct evaluation of subgrid turbulent burning velocity models is difficult. Firstly, there are many proposed models (eg. Refs. [22, 36, 58, 85, 87]). Secondly, they often include a wide range of model constants and sub-functions (for example Eq. 1.55). Evaluation of such a model can be quite ambiguous if these terms are likewise ambiguous or model dependant. Hence, the approach taken is not to evaluate particular models, but to ask if an algebraic relationship for the local turbulent burning velocity is reasonable. That is, can the local wrinkling of a flame be related solely to the turbulence characteristics immediately upstream of the flame during the turbulence flame interaction? For this analysis the Case 2 data is once again used. Hence, $s_l \approx s_l^0$, which is the simplest case. For an algebraic relationship to hold, there must be some function, Ψ, such that:

$$\frac{\overline{\langle s_t \rangle}}{s_l^0} = \Xi = \Psi\left(\frac{u'_\Delta}{s_l^0}\right) \tag{6.64}$$

According the traditional models described in §1.5.1, the turbulent burning velocity should increase with the turbulence intensity.

Figure 6.30 shows the profiles of the measured wrinkling factor versus the turbulence intensity at various filter scales. As can be seen, there is no clear relation between the two quantities. At $\Delta/\delta_l^0 = 40$ and 50, the turbulent burning velocity was essentially independent of the turbulence intensity. At $\Delta/\delta_l^0 = 30$, it decreased slightly. However, all of the observed variations were quite small and on the order of the expected statistical error (Eq. 6.17). Essentially, the observed turbulent burning velocity was not correlated with the strength of the turbulence immediately upstream of the flame during the local turbulence flame interaction. Furthermore, this lack of correlation could not be due to a balance between positive and negative aspects

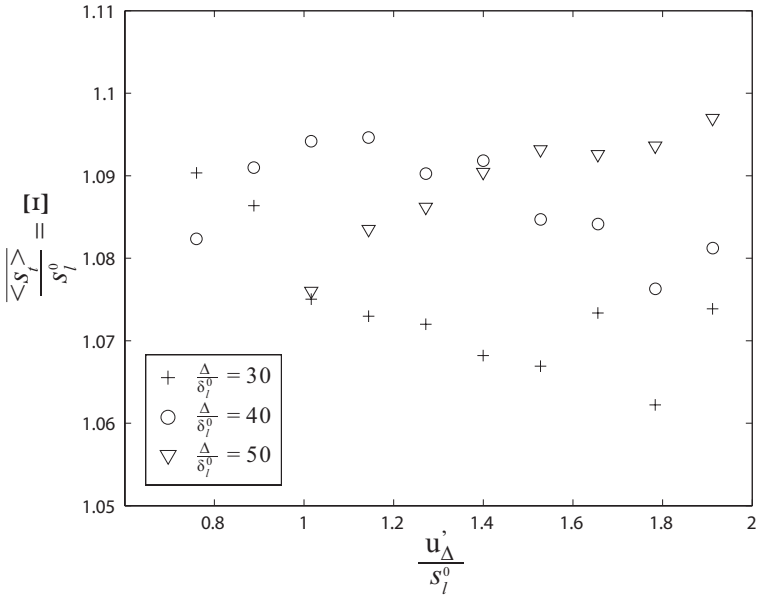

Figure 6.30: Variation of turbulent burning velocity with turbulence intensity.

as was the case for the strain rate and curvature stretch rate; there is no negative component of area. It is however possible that a positive correlation may be found in cases with stronger turbulence. As the local turbulence intensity increased it would have a more direct effect on the local flame surface area.

6.4.1 Implications for modeling

It therefore appears that the local turbulent flame surface area is not entirely set by the local turbulence; the transport of flame surface must be considered. Therefore, in the context of subgrid models for the turbulent burning velocity in the laminar flamelet regime, a model that takes into account this transport is necessary. This can be achieved using the flame surface density or wrinkling factor transport equations. However, it appears that models that predict the flame surface area based on algebraic relationships with the turbulence intensity will not be accurate based on Fig. 6.30. Therefore, modification to the subgrid models employed in typical G-equation simulations would be necessary.

However, the above result does not imply that algebraic relationships are not useful in the context of all turbulent flames. The analysis considered the increase in turbulent burning velocity to be directly related to the flame surface area. This is true in the thin flamelet regime. It is also possible that the role of small scale turbulence may be to locally enhance the propagation speed of the flame by increasing the turbulent transport of heat and reactants. This would be the case in the 'thin reaction zone' regime identified in §1.3. In such a case, the local increase in the propagation speed should be set by the local turbulence and algebraic relationships may hold.

Furthermore, algebraic relationships have been shown to give good estimates of the overall turbulent burning velocity as long as they are applied in a consistent manner [36]. That is, relationships developed based on specific flame geometry should only be used for such a geometry. However, such relationships are not appropriate for general subgrid models.

6.5 Independence of the filter

As mentioned in §6.1.2, the quantitative results of this analysis may be somewhat dependant on the particular filter used. That is, the filtered quantities in Eqs. 6.4, 6.5, and 6.6 will depend on the filter kernel. So will the resultant fluctuations. For an implicitly filtered field, the differences represent the choice of a specific numerical scheme to compute the derivatives. For the explicit filtering method used here, they represent the choice of a specific filter kernel. However, in either case, changing the filter not only changes the flame surface conditioned fluctuations, but also the fluid dynamic fluctuations used to characterize the interaction. Ideally, changing the filter should affect both of these quantities in a similar manner. Hence, the resultant

relationships for $\overline{\Gamma}$ and $\overline{\Upsilon}$ would be largely unchanged.

The effects of changing the filter kernel are also mitigated if the majority of the turbulence is in the subgrid. In such cases, the filtered quantities are small in comparison to the fluctuation magnitudes. This is true regardless of the particular filter kernel. In such cases, subtracting a slightly different small number from the fluctuations would not significantly affect the results. As can be seen from Fig. 6.2(a), the majority of the turbulence in this experiment was contained in the subgrid. This was because of the limited range of scales mandated by the limited temporal and spatial resolution of the diagnostics. However, a beneficial consequence was that the effect of varying the particular filter kernel should be reduced.

To determine the effect of the filter, the above analysis was repeated using a different kernel. Recall that the previous filter was a Gaussian with a standard deviation of $\Delta/3$. This will be designated as H_1. The second filter selected was chosen as a worst case scenario; a square filter was used. This will be designated as H_2. Therefore, at every point, the filtered value was simply the average (or density weighted average) of all the points within the filter volume. While this is physically a poor choice of filter, it represents an extreme effect.

Both the strain rate and curvature stretch rate analyzes were performed using this filter for Case 2 at $\Delta/\delta_l^0 = 40$. Figure 6.31(a) shows the positive, negative, and total strain efficiency functions for each filter kernel. As can be seen, the results are nearly identical. The same is true for the probability of positive strain rate shown in Fig. 6.31(b). The curvature stretch rate model was also found to be essentially independent of the filter. The wrinkling transfer functions and probability of positive curvature are shown in Fig. 6.32. Once again, the results are nearly identical for the Gaussian and square filter. It therefore appears that the results

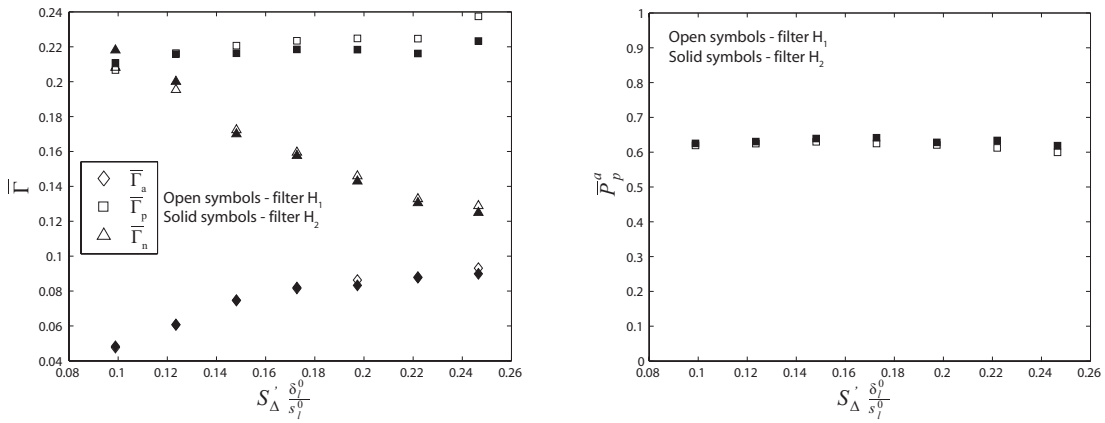

(a) Strain efficiency functions

(b) Probability of positive strain rate

Figure 6.31: Effects of varying the filter on the strain rate model. H_1 is a Gaussian filter, H_2 is a square filter.

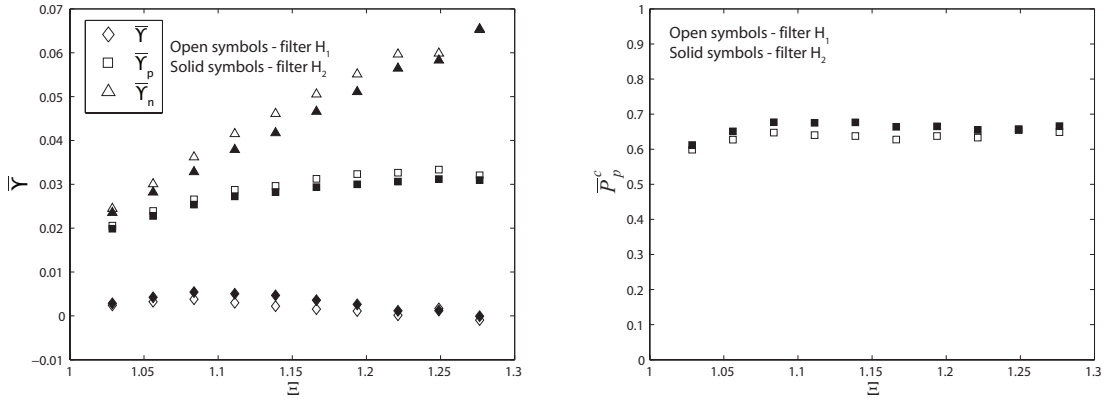

(a) Wrinkling transfer functions

(b) Probability of positive curvature

Figure 6.32: Effects of varying the filter on the curvature stretch rate model. H_1 is a Gaussian filter, H_2 is a square filter.

herein are virtually independent of the particular filter used. However, this may be somewhat a consequence of the restricted range of turbulence scales. The filter kernel independence should be reconfirmed when studies are made at higher Reynolds numbers.

6.6 Conclusions

The goal of this analysis was to evaluate and develop models and modeling paradigms for several important quantities in turbulent combustion LES. An anal-

ysis method was developed that measures the processes that must be modeled in the subgrid scales of an LES. Control masses of fluid, in which all turbulence scales were resolved, were tracked as they interacted with the flame. After the turbulence field was filtered, the resultant effects on the flame surface were analogous to the processes occurring in the subgrid scales of an LES. Based on the statistics of these interactions, models for the subgrid strain rate, curvature stretch rate, and turbulent burning velocity were analyzed and developed.

The traditional model for the subgrid strain rate related $\overline{\langle a_{t,sg} \rangle}$ to a stretch efficiency function Γ. This function was based on the canonical flame-vortex interaction and therefore assumed that the turbulence only generates extensive strain rate. However, the measurements showed that this was not the case; significant compressive strain rate occurred. This resulted in the traditional model greatly over-predicting the measured strain rate. Furthermore, it was found that the traditional characteristic fluid strain rate, based on the subgrid RMS velocity fluctuations, resulted in significant noise.

A new model was proposed in which the effects of extensive and compressive strain rate were explicitly differentiated and the fluid strain rate was characterized by S'_Δ. It was found that this characterization resulted in significantly better correlation with the experiment, confirming the analysis of Chapter IV. It was also found that the efficiency of extensive and compressive strain rates varied in different manners with changing turbulence intensity: the former increased while the latter decreased. Hence, separate efficiency functions for each were required. The effect of varying the filter size was also observed. The characteristic strain rate implied an inherent dependence of the efficiency on the filter scale. When this was accounted for, the strain efficiency increased with increasing filter size. This indicates that large scale

turbulence is more effective at straining the flame than small scale turbulence.

Two models for the curvature stretch rate were also analyzed. The first assumed that the subgrid strain rate and curvature stretch rate locally balanced. However, this was found not to be the case. In general, flame surface was either produced or destroyed during a particular interaction. Hence, the balance did not hold and models should account for the transport of flame surface area.

The second model assumed that the curvature stretch rate could be related to the amount of flame surface present via the flame surface density. However, this formulation would predict a curvature stretch rate for unwrinkled flames. The model was therefore recast in terms of the flame wrinkling factor. It was once again found that the positive and negative components contributed significantly and somewhat canceled each other out. A model was therefore developed based on a similar paradigm to the strain rate. This related the wrinkling factor to the curvature stretch rate using separate transfer functions for the positive and negative components. It was found that these transfer functions allowed the total stretch rate to be predicted.

The idea that the increase in flame surface area (and therefore the turbulent burning velocity) can be related to the turbulence immediately upstream of the flame was analyzed. Based on global results and the Damköler paradigm, the local burning velocity should increase with the turbulence intensity via an algebraic relation. However, it was found that there was no correlation between these quantities during specific turbulence-flame interactions over the measured range. This is because the amount of flame surface in a given control mass was not set entirely by the turbulence in that mass. Wrinkles that had been generated elsewhere and convected to the region being considered greatly influenced the local burning velocity. This is consistent with the previous observations that flame surface transport is signifi-

cant. Hence, algebraic relationships for the turbulent burning velocity based on the local turbulence parameters do not provide an accurate prediction of the local flame surface area.

CHAPTER VII

Conclusions

This dissertation has provided a new look at the dynamics of turbulent premixed flames at low Reynolds number. To do so, high-speed laser diagnostics were designed, mechanistic descriptions of the turbulence-flame interaction determined, and models for important subgrid terms in LES developed. Each of these aspects is summarized below.

7.1 Development of CS-PIV and OPCS-PIV diagnostics

In order to investigate turbulence-flame interactions, measurement of the temporally evolving turbulent flow field and flame surface topography were required. The experiment was carried out on a premixed slot Bunsen flame burning methane-air mixtures at various equivalence ratios. Tracking the dynamics of the turbulence and flame necessitated the development of two new high-speed laser diagnostics. The first technique, Cinema-Stereoscopic PIV (CS-PIV), provided temporally resolved three-component vector fields in a plane parallel to the flow. This diagnostic operated a rates of 1111 kHz with a vector spacings of 140 μm and accurately resolved the viscous scale of the turbulence. Due to its high accuracy, the CS-PIV was used for the majority of the quantitative analysis.

The second technique, Orthogonal-Plane Cinema-Stereoscopic PIV (OPCS-PIV),

allowed reconstruction of the full three-dimensional velocity gradient field. It operated at 3 kHz with a vector spacing of 190 μm. Using a 'modified Taylor's hypothesis', the full 3D velocity gradient tensor and turbulence geometry were determined in a plane perpendicular to the flow. Data from an additional plane, parallel to the flow, then was used to determine the trajectory and strength of particular turbulent structures as they interacted with the flame. This allowed the true geometry of 3D turbulence-flame interactions to be studied. Furthermore, it allowed the orientation of the turbulence field with respect to the flame to be investigated. These diagnostics represent the first application of temporally resolved PIV to the study of turbulent flame dynamics and the first application of OPCS-PIV in general.

7.2 Phenomenological analysis of turbulence-flame interactions

The CS-PIV and OPCS-PIV were used to phenomenologically investigate the interaction between a turbulent flow and a flame. The results of this investigation were as follows:

1. **The strain rate exerted on a flame surface is not characterized by vorticity.** This is contrary to the method typically used to develop models for turbulence-flame interactions. These models generally consider the interaction between a counter-rotating vortex pair and the flame. However, the analysis indicated the interaction of vortical structures with the flame gives neither an accurate picture of the strain rate on the flame or flame wrinkling.

2. **The interaction of turbulence with a flame does not occur in counter-rotating vortex pairs.** In reality, turbulence-flame interactions resembling the simple canonical geometry occurred very rarely. Instantaneous images containing an interaction of this geometry occurred in less than 20% of the recorded

data. Within these frames, the canonical geometry only accounted for a portion of the total turbulence-flame interaction. Vorticity fields involving large groupings of structures were found to interact with the flame. Under the canonical description, each vortex pair in the group would create a single wrinkle having a size set by the pair. However, this did not occur and single large wrinkles were usually formed around the entire group.

3. **The strain rate and wrinkling of a flame surface are characterized by the fluid dynamic strain rate and vorticity fields respectively.** Based on the above observations, an analysis of the strain rate equation was performed. This indicated that the strain rate on the flame surface is determined by the fluid dynamic strain rate field in the reactants. Wrinkling of the flame is associated with redistribution of the surface by vortical structures. Hence, coherent structures associated with both fluid strain rate and vorticity must be considered. These ideas were confirmed using the measured interactions.

4. **The curvature stretch rate and flame strain rate were distributed amongst positive and negative values.** This also is in contrast to the predictions based on the canonical vortex geometry, which states that the sole effect of turbulence on the flame is to exert positive strain and generate negative curvature. Furthermore, various other modeling paradigms also assume that the curvature stretch rate always is negative. However, large regions of positive curvature were observed. Since positive curvature wrinkles grew with time, they accounted for a significant amount of the curvature stretch rate. Negative curvature wrinkles formed cusps and became smaller in time. The mean curvature at some locations was found to be positive. Furthermore, significant regions of

negative strain rate were observed. While the mean strain rate was positive at all locations in the flame, it was considerably less than would occur if there was no negative strain rate.

5. **The transport of flame surface density must be accounted for.** There were regions where the mean strain rate and curvature stretch rate were positive. Hence, these are regions in which flame surface is produced. Since the flames were statistically stationary in time, there was no temporal change overall surface area. The flame surface produced in these regions must therefore have been transported to the tip of the flame where the large negative curvature (i.e. negative stretch rate) destroyed surface area. This means that the curvature stretch rate and strain rate do not necessarily balance locally, which is assumed in some models. Furthermore, the local flame wrinkling, curvature, and turbulent burning velocity are not determined solely by the local turbulence, but are dependant on the transport of flame surface area from other locations. This transport must be accounted for in models. The often-used algebraic relations for turbulent burning velocity do not account for this transport and therefore are inadequate.

6. **The geometry of turbulence-flame interactions cannot be described by simple geometries.** The interaction of 3D turbulent structures and the flame were observed to occur in very complex geometries. This involved structures that were multiply curved, intertwined, and oriented in various manners with respect to the flame. Furthermore, the statistical orientation of the $\underline{S}$ and $\vec{\omega}$ fields with respect to the flame were distributed over all possible directions. Hence, it is not possible to describe the expected effect of turbulence on a flame

surface as the ensemble of simple interactions. The actual effect will be highly dependent on the particular shape, orientation, and evolution of the turbulence involved. Models should therefore be developed that are based on the statistics of real interactions and do not explicitly dictate a geometry.

7.3 Modeling turbulent premixed flames

From the above observations, it was concluded that models based solely on the canonical flame-vortex configuration could not describe real turbulence-flame interactions. Nor so could models that assume a balance between strain rate and curvature stretch rate, or those that use an algebraic relationship for the turbulent burning velocity. Nevertheless, such models were assessed. New models then were developed. Both the analysis and development were performed using a new method that tracks the interaction between fluid control masses and the flame front. This allowed measurement of the subgrid processes the must be modeled in LES. Using this method, thousands of control mass-flame interactions were studied, representing thousands of subgrid processes. The resultant data allowed for the desired model assessment and development, which are summarized below.

7.3.1 Modeling the subgrid strain rate

The previous model relates the subgrid strain rate to the stretch efficiency function, which is derived from simulations of canonical flame-vortex interactions [74]. The concepts of the previous model were analyzed, yielding the following observations:

1. **The turbulence in a given control mass exerted regions of both positive and negative strain rate.** The turbulence in a given control mass could exert regions of both positive and negative strain rate on the flame surface.

Consequentially, the overall strain efficiency function for a particular interaction could be positive or negative.

2. **The ensemble mean strain rate on the flame (and strain efficiency) at any turbulence intensity was positive, but considerably less than predicted by the model.** Despite the fact that individual turbulence-flame interactions could exert positive or negative strain rate, the mean strain rate for any strength of turbulence was positive. Hence, turbulence exerting positive strain rate was more effective than turbulence exerting negative strain rate. However, due to the negative components, the net strain rate was considerably less than predicted by the standard models.

3. **The strain efficiency increased with increasing turbulence intensity and filter size.** Not only did the mean strain rate on the flame increase with increasing turbulence intensity, but so did the mean strain efficiency. This further indicates there are differences between turbulence that exerts positive and negative strain rate. The strain efficiency increased with increasing filter size. Both of these observations are in qualitative agreement with the previous models.

4. **The strain efficiency was poorly correlated with the subgrid velocity fluctuations.** When the characteristic strain rate of the fluid was taken to be u'_Δ/Δ, the measured strain rate on the flame was poorly correlated with the turbulence intensity.

Based on these observations, a new model for the strain rate was proposed, which is summarized below:

1. **The strain rate on the flame should be characterized by the fluid dynamic strain rate.** It was shown that the strain rate exerted on the flame by turbulence is best characterized by the fluid dynamic strain rate in the reactants ahead of the flame. Hence, the magnitude of the subgrid strain rate tensor should be used in the formulation of the strain efficiency function. The subgrid strain rate is computed by LES as part of the energy transfer model. The measured strain rate on the flame was well correlated with the subgrid fluid strain rate in the reactants.

2. **The net strain efficiency function is positive and it increases with turbulence intensity.** When characterized by the fluid dynamic strain rate tensor, the strain efficiency function was still positive and increased with increasing turbulence intensity.

3. **The strain efficiency function should be represented in terms of an extensive and compressive component.** The strain efficiency represents a balance between the extensive and compressive strain rate. Since the overall efficiency changes with the turbulence intensity, so must this balance. This implies that the overall efficiency function must reflect both changes in the efficiency as well as the probability of positive and negative strain rate. A form of the strain efficiency function that explicitly accounts for all of these effects was presented. It was found that the positive strain efficiency increased with increasing turbulence intensity, while the negative strain efficiency decreased. The probability of finding positive strain rate was relatively independent of the turbulence intensity.

4. **The effectiveness of turbulence in exerting strain increased with increasing filter size. However, the strain efficiency function decreased.** The definition of the characteristic strain rate used in this (and the previous) model implies a certain intrinsic dependance on the filter scale. That is, even if the strain rate on the flame was independent of the filter size, the strain efficiency function would still exhibit a dependence. Because of this, the strain efficiency functions measured appeared to decrease with increasing filter size. However, when the intrinsic dependence was accounted for, the actual effectiveness of the turbulence was found to increase when larger scales were included.

The measured data were used to determine the quantitative relationship between the turbulence intensity, filter size, and strain rate exerted on the flame. By decomposing the strain rate into its positive and negative components, relatively simple dependencies could be obtained that reflected all of the observations. Some useful fits to the data were provided that could be easily implemented in LES modeling applications.

7.3.2 Modeling the subgrid curvature stretch rate

Two general modeling ideas were investigated. The first assumed that a balance exists between the subgrid strain rate and the curvature stretch rate. However, it was found that this balance did not hold either for individual interactions or on the mean. This was unsurprising as transport of flame surface was previously shown to be important.

The second idea related the curvature to the amount of flame surface in the cell. That is, the curvature stretch rate was assumed to be proportional to the flame surface density. While the previous formulation of this model possessed some

problems, it was found that this general paradigm could be used to predict the curvature stretch rate. This is summarized below.

1. **The curvature of the flame surface should be related to the wrinkling factor, not the flame surface density.** Using a relationship between flame surface density and curvature would predict that an unwrinkled flame undergoes stretch due to curvature, which is incorrect. On the other hand, relating the wrinkling factor to the curvature describes the increase in flame surface area relative to the unwrinkled case.

2. **The local instantaneous flame curvature could be either positive or negative.** The positive regions tended to be larger in area and possess a lower magnitude curvature than the negative regions. This is the behavior expected from the kinematics of a propagating flame surface.

3. **In the mean, the curvature stretch rate could be either positive or negative.** The mean stretch rate varied with both wrinkling factor and filter size between positive and negative values. This indicates a varying balance between the positive and negative curvature components that must be reflected in the model.

Based on these observations, the model for the curvature stretch rate was developed based on a form that is similar to that for the strain rate.

1. **A wrinkling transfer function can be used to relate the wrinkling factor to the curvature stretch rate.** This function is analogous to the strain efficiency function.

2. **The wrinkling transfer function should be represented in terms of positive and negative transfer functions.** Since the total stretch rate is

comprised of a negative and positive component, separate transfer functions are needed to reflect differences in how these components behave with increased wrinkling. It was found that the positive transfer function was everywhere lower than the negative and both asymptotically approached constant values. The probability of positive curvature was greater than that of negative curvature. Once again, these traits were consistent with the kinematics of a flame surface.

The measured data were then used to construct the positive and negative wrinkling transfer functions and the probability of positive curvature. Data fits were determined that easily could be implemented in simulations employing the flame surface density or wrinkling factor transport equations.

7.3.3 Modeling the turbulence burning velocity

The idea that the turbulent burning velocity could be related to the local instantaneous turbulence through an algebraic relationship was analyzed. It was found that there was no clear relationship between these two quantities. This is because the flame surface area in a particular cell was not entirely determined by the turbulence interacting with the flame at that time. It also depended on all of the winkling that had previously occurred and convected to that location. That is, it depended on the transport of flame surface.

Hence, simulation methods that require the turbulent burning velocity (such those employing the G-equation), must in some way account for this transport in their models. It is expected that at least a convective flame surface term will be needed to accurately predict the burning velocity. Alternatively, a hybrid scheme may be necessary. That is, the flame surface density transport equation may be used to determine the subgrid flame surface area. The subgrid burning velocity thus deter-

mined may then be applied to the G-equation to provide an accurate propagation speed for the $G = G_0$ surface.

Such a hybrid scheme would address significant issues in both the G-equation and Σ transport equation methods. Unlike algebraic relations, it would provide an accurate propagation speed for the G-field. This is necessary for the flame to have accurate dynamics. Also, the transport equation would only be used to determine the local flame surface area. Hence, the problems inherent in filtering the progress variable field (c) in the standard Σ transport methods are avoided. That is, instead of employing Σ_{sg} to close the $\tilde{c}$ transport equation (Eq. 1.30) it would be employed implicitly in the G transport equation (Eq. 1.42). Since G is smooth on the LES grid (unlike c), no expensive or complicated schemes would be necessary to handle its filtering. However, the numerical consequences of such a scheme would have to be addressed.

7.4 Future work

While this study has provided new insight and modeling guidelines for many important processes occurring in turbulent premixed combustion, there is still considerable work that must be done. Firstly, the range of turbulence intensities and scales must be expanded. Presently these parameters were restricted by hardware limitations. However, even during the course of this research new imaging capabilities have become available. Such technology would allow higher turbulence intensities and a greater range of scales to be studied. Additionally, there are still some modeling terms required for LES that need to be investigated. For example, in the flame surface density equation the effects of the resolved scales on the subgrid transport terms must be determined. Such terms could once again be investigated if a larger

range of scales were studied.

The analysis procedure used here could also be applied to DNS data sets. Modern DNS is reaching the point that realistic flames can be simulated in 3D. While such data are generally also restricted in Reynolds number, they have the potential to accurately extend the analysis into the third dimension. However, caution must be used to ensure adequate resolution of the flame front and turbulence.

Either using the provided data fits or new fits resulting from the extended studies, the models provided should be implemented into LES codes. In particular, they are appropriate for LES employing the flame surface density transport equation. Such codes may then be run for the test cases in this study and the global results compared. This would allow direct assessment of the applicability of the flame surface density transport model to LES.

Finally, this study focused on the thin flamelet regime. However, as higher turbulence intensities are reached, the flame may transition into the thin reaction zone regime. That is, micro-scale turbulence may enter the preheat zone and effect its structure. This would have a large effect on the propagation speed of the flame. Combining the high speed velocimetry diagnostics developed in this study with high speed spectroscopy or temperature measurements would allow such processes to be studied experimentally for the first time.

APPENDICES

APPENDIX A

Derivation of strain rate transport equation in a reacting flow

A general transport equation for the strain rate components in a reacting flow can be derived by taking the spatial derivative of the equations for the conservation of momentum:

$$\frac{\partial}{\partial x_j}\frac{\partial u_i}{\partial t} + \frac{\partial}{\partial x_j}\left(u_k\frac{\partial u_i}{\partial x_k}\right) = \frac{\partial g}{\partial x_j} - \frac{\partial}{\partial x_j}\left(\frac{1}{\rho}\frac{\partial p}{\partial x_i}\right) + \frac{\partial}{\partial x_j}\left(\nu\frac{\partial^2 u_i}{\partial x_k \partial x_k}\right) \tag{A.1}$$

Setting $A_{ij} = \partial u_i/\partial x_j$, this can be expanded as:

$$\frac{\partial A_{ij}}{\partial t} + u_k\frac{\partial A_{ij}}{\partial x_k} = -A_{ik}A_{kj} - \frac{1}{\rho}\frac{\partial^2 p}{\partial x_i \partial x_j} + \frac{1}{\rho^2}\frac{\partial p}{\partial x_i}\frac{\partial \rho}{\partial x_j} + \nu\frac{\partial^2 A_{ij}}{\partial x_k \partial x_k} + \frac{\partial \nu}{\partial x_j}\frac{\partial^2 u_i}{\partial x_k \partial x_k} \tag{A.2}$$

Recognizing that $S_{ij} = 1/2(A_{ij} + A_{ji})$, the appropriate forms of Eqn. A.2 can be summed to yield:

$$\begin{aligned}\frac{\partial S_{ij}}{\partial t} + u_k\frac{\partial S_{ij}}{\partial x_k} = &-\left(\frac{A_{ik}A_{kj} + A_{jk}A_{ki}}{2}\right) - \frac{1}{\rho}\frac{\partial^2 p}{\partial x_i \partial x_j} + \nu\frac{\partial^2 S_{ij}}{\partial x_k \partial x_k} \\ &+ \frac{1}{2\rho^2}\left(\frac{\partial p}{\partial x_i}\frac{\partial \rho}{\partial x_j} + \frac{\partial p}{\partial x_j}\frac{\partial \rho}{\partial x_i}\right) + \frac{1}{2}\left(\frac{\partial \nu}{\partial x_j}\frac{\partial^2 u_i}{\partial x_k \partial x_k} + \frac{\partial \nu}{\partial x_i}\frac{\partial^2 u_j}{\partial x_k \partial x_k}\right)\end{aligned} \tag{A.3}$$

The first term on the right can be written in terms of $\underline{S}$ and $\vec{\omega}$ by recognizing that $A_{ij} = S_{ij} - \Omega_{ij}$ and equating the terms of $\underline{\Omega}$ with the various vorticity components.

This yields the final transport equation:

(A.4)

$$\frac{\partial S_{ij}}{\partial t} + u_k \frac{\partial S_{ij}}{\partial x_k} = -S_{ik}S_{kj} - \frac{1}{4}\left(\omega_i\omega_j - \delta_{ij}\omega_k\omega_k\right) - \frac{1}{\rho}\frac{\partial^2 p}{\partial x_i \partial x_j} + \nu\frac{\partial^2 S_{ij}}{\partial x_k \partial x_k} + \frac{1}{2\rho^2}\left(\frac{\partial p}{\partial x_i}\frac{\partial \rho}{\partial x_j} + \frac{\partial p}{\partial x_j}\frac{\partial \rho}{\partial x_i}\right) + \frac{1}{2}\left(\frac{\partial \nu}{\partial x_j}\frac{\partial^2 u_i}{\partial x_k \partial x_k} + \frac{\partial \nu}{\partial x_i}\frac{\partial^2 u_j}{\partial x_k \partial x_k}\right)$$

APPENDIX B

Index of refraction effects in a PIV target medium

The dual-forward-scatter mode employed in the PIV diagnostics forced at least one camera to view the calibration grid through the target material. This material had a different index of refraction than air, causing the light to deflect slightly at the air/target interface according to Snell's Law:

$$n_a \sin\alpha = n_t \sin\beta \tag{B.1}$$

where n_a and n_t are the indices of refraction of air and the target respectively. The angles α and β are as shown in Fig. 2.1(b).

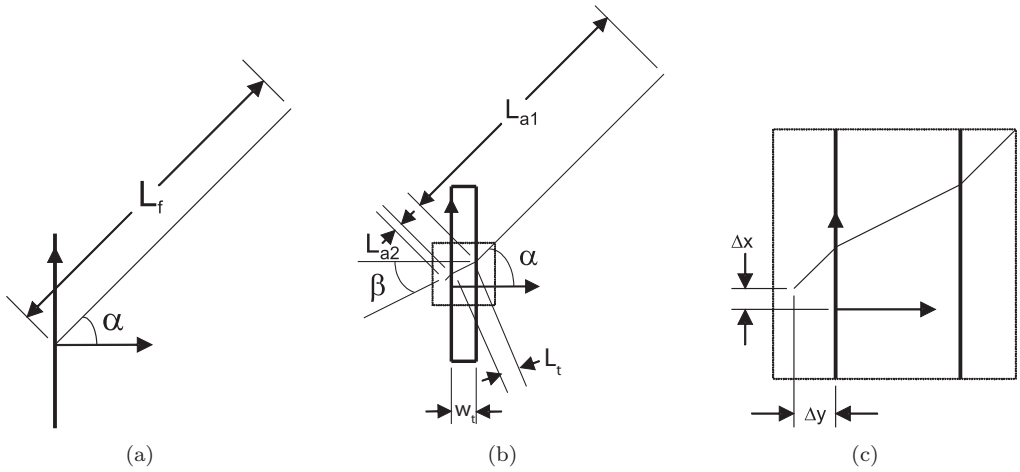

Figure B.1: Geometric parameters in Snell's Law

Figure 2.1(a) shows an ideal lens focused on an infinitely thin plane. The length L_f is the working focal distance of the lens. The practical system is shown in Fig.

2.1(b). Here, the light bends at the target such that the plane of focus is beyond the calibration grid. The total working distance of the lens remains constant such that:

$$L_f = L_{a1} + \frac{w_t}{\cos\alpha} = L_{a1} + L_g + L_{a2} \tag{B.2}$$

where L_{a1} and L_{a2} are the light path lengths before and after the air/target interfaces, L_g is the path length within the target, and w_t is the width of the target.

The path length in the glass is related to target thickness and light angle by:

$$\frac{L_t}{w_t} = \cos\beta \tag{B.3}$$

and the path length in the air opposite the lens is:

$$\frac{L_{a2}}{w_t} = \frac{\cos\beta - \cos\alpha}{\cos\beta\cos\alpha} \tag{B.4}$$

The resultant displacements of the image plane, Δx and Δy as shown in Fig. 2.1(c), are thus:

$$\Delta x = (L_{a2} + L_t)\sin\alpha - (L_{a2}\sin\alpha + L_t\sin\beta) \Rightarrow \tag{B.5}$$

$$\frac{\Delta x}{w_t} = \frac{\sin\alpha}{\cos\beta} - \tan\beta \tag{B.6}$$

$$\Delta y = L_{a2}\cos\alpha \Rightarrow \tag{B.7}$$

$$\frac{\Delta y}{w_t} = 1 - \frac{\cos\alpha}{\cos\beta} \tag{B.8}$$

Plots of $\Delta x/w_t$, $\Delta y/w_t$, and the total displacement magnitude ($\delta_t = \sqrt{\Delta x^2 + \Delta y^2}/w_t$) versus lens angle are provided in Fig. B.2 for $\frac{n_t}{n_a} = 1.5$. This index of refraction ratio is typical for glass in air. For the system to be practical, the out-of-plane displacement (Δy) should be approximately one order of magnitude smaller than the depth of focus, which was found to be approximately 500 μm for the CS-PIV system. This ensures that the target can be traversed through the sheet while keeping both cameras in focus. For the chosen angular displacement of 35^o, $\Delta y = 0.11 w_t$. Hence,

a maximum target thickness of about 450 μm was allowed. The photographic film used as the target was 130 ± 5 μm thick. The glass flats used to sandwich the film were 85 ± 5 μm thick each. The target therefore induced out-of-plane shifts that significantly less than a tenth of the depth of focus.

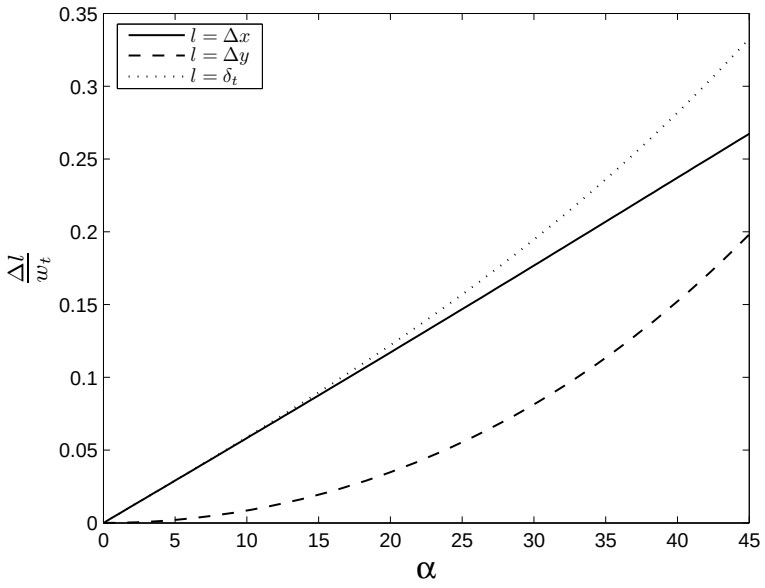

Figure B.2: Displacements due to light bending at various input angles with $n_t/n_a = 1.5$.

Associated with the out-of-plane shift is the in-plane shift component, Δx. Essentially, this is an artificial displacement between the calibration target images taken by each camera. Hence, the deviation of the light path through the target results in a slight discrepancy between the location of velocity vectors determined by each camera. However, since the target was symmetric, this shift was equal for each camera and did not result in a calibration error. Minor asymmetries in the target were compensated for by the DaVis software self-calibration algorithm.

BIBLIOGRAPHY

BIBLIOGRAPHY

[1] R. G. Abdel-Gayed and D. Bradley. A two-eddy theory of turbulent premixed flame propagation. *Philos. Trans. R. Soc. Lond., A*, 301:1–26, 1981.

[2] I. Amidror. Scattered data interpolation methods for electronic imaging systems: A survey. *J. Electron. Imaging*, 11:157–176, 2002.

[3] J. B. Bell, M. S. Day, J. F. Grcar, M. J. Lijewski, J. F. Driscoll, and S. A. Filatev. Numerical simulation of a laboratory-scale turbulent slot flame. *Proc. Combust. Inst.*, 31:1299–1307, 2007.

[4] M. Boger, D. Veynante, H. Boughanem, and A. Trouve. Direct numerical simulation analysis of flame surface density concept for large eddy simulation of turbulent premixed combustion. *Proc. Combust. Inst.*, 27:917–925, 1998.

[5] O. N. Boratav and R. B. Pelz. Structures and structure functions in the inertial range of turbulence. *Phys. Fluids*, 9:1400–1415, 1996.

[6] I. Boxx, C. Heeger, R. Gordon, B. Böhm, M. Aigner, A. Dreizler, and W. Meier. Simultaneous three-component PIV/OH-PLIF measurements of a turbulent lifted, C3H8-Argon jet diffusion flame at 1.5 kHz repetition rate. *Proc. Combust. Inst.*, 32:905–912, 2009.

[7] D. Bradley, P. H. Gaskell, A. Sedaghat, and X. J. Gu. Generation of pdfs for flame curvature and for flame stretch rate in premixed turbulent combustion. *Combust. Flame*, 135:503–523, 2003.

[8] T. Brandt. A priori tests on numerical errors in large eddy simulation using finite differences and explicit filtering. *Int. J. Numer. Meth. Fluids*, 51:635–657, 2006.

[9] T. Brandt. Usability of explicit filtering in large eddy simulation with a low-order numerical scheme and different subgrid-scale models. *Int. J. Numer. Meth. Fluids*, 57:905–928, 2008.

[10] J. G. Brasseur and W. Lin. Kinematics and dynamics of small-scale vorticity and strain-rate structures in the transition from isotropic to shear turbulence. *Fluid Dyn. Res.*, 36:357–384, 2005.

[11] K. N. C. Bray, P. A. Libby, and J. B Moss. Flamelet crossing frequencies and mean reaction rates in premixed turbulent combustion. *Combust. Sci. Tech.*, 41:143–172, 1984.

[12] K. A. Buch and W. J. A. Dahm. Experimental study of the fine-scale structure of conserved scalar mixing in turbulent shear flows. Part 1. Sc $\ll$1. *J. Fluid Mech.*, 317:21–71, 1996.

[13] K. A. Buch and W. J. A. Dahm. Experimental study of the fine-scale structure of conserved scalar mixing in turbulent shear flows. Part 2. Sc $\approx$ 1. *J. Fluid Mech.*, 364:1–29, 1998.

[14] P.C. Bueno, B. Ganapathisubramani, N. T. Clemens, and D. S. Dolling. Cinematographic planar imaging of a Mach 2 shock wave/turbulent boundary layer interaction. In *43th AIAA Aerospace Sciences Meeting and Exhibit. Reno, NV*, 2005.

[15] V. Bychkov. Importance of the Darrieus-Landau instability for strongly corrugated turbulent flames. *Phys. Rev. E*, 68:066304, 2003.

[16] P. Cambray and G. Joulin. Length-scales of wrinkling of weakly-forced, unstable premixed flames. *Combust. Sci. Technol.*, 97:405–428, 1994.

[17] S. M. Candel and T. Poinsot. Flame stretch and the balance equation for the flame area. *Combust. Sci. Technol.*, 70:1–15, 1990.

[18] N. Chakraborty and R. S. Cant. Unsteady effects of strain rate and curvature on turbulent premixed flames in an inflowoutflow configuration. *Combust. Flame*, 137:129–147, 2004.

[19] N. Chakraborty and M. Klein. A priori direct numerical simulation assessment of algebraic flame surface density models for turbulent premixed flames in the context of large eddy simulation. *Phys. Fluids*, 20:085108, 2008.

[20] N. Chakraborty and N Swaminathan. Influence of the Damköler number on turbulence-scalar interaction in premixed flames. I. Physical insight. *Phys. Fluids*, 19:0451003, 2007.

[21] P. Chakraborty, S. Balachandar, and R. J. Adrian. On the relationships between local vortex identification schemes. *J. Fluid Mech.*, 535:189–214, 2005.

[22] F. Charlette, C. Meneveau, and D. Veynante. A power-law flame wrinkling model for LES of premixed turbulent combustion. Part 1: non-dynamic formulation and initial tests. *Combust. Flame*, 131(2):159–180, 2002.

[23] F. Charlette, C. Meneveau, and D. Veynante. A power-law flame wrinkling model for LES of premixed turbulent combustion. Part 2: Dynamic formulation. *Combust. Flame*, 131(1):181–197, 2002.

[24] J. H. Chen and H. G. Im. Correlation of flame speed with stretch in turbulent premixed methane/air flames. *Proc. Combust. Inst.*, 27:819–826, 1998.

[25] J. H. Chen and H. G. Im. Stretch effects on the burning velocity of turbulent premixed hydrogen/air flames. *Proc. Combust. Inst.*, 28:211–218, 2000.

[26] Y. Cho, J. H. Kin, T. Cho, I. Moon, Y. Yoon, and C. Lee. Analysis of turbulent premixed flame structure using simultaneous PIV-OH PLIF. *J. Visualization*, 7(1):43–54, 2004.

[27] P. Clavin and F. A. Williams. Effects of molecular diffusion and thermal expansion on the structure and dynamics of premixed flames in turbulent flows of large scales and low intensity. *J. Fluid Mech.*, 116:251–282, 1982.

[28] O. Colin, F. Ducros, D. Veynante, and T. Poinsot. A thickened flame model for large eddy simulations of turbulent premixed combustion. *Phys. Fluids*, 12(7):1843–1863, 2000.

[29] S. Correa. A review of nox formation under gas-turbine combustion conditions. *Combust. Sci. Technol.*, 87:329–362, 1992.

[30] R. Cucitore, M. Quadrio, and A. Baron. On the effectiveness and limitations of local criteria for the identification of a vortex. *Eur. J. Mech. B*, 18:261–282, 1999.

[31] W.J.A. Dahm, C. M. Scheil, and G. Tryggvason. Dynamics of vortex interaction with a density interface. *J. Fluid Mech.*, 205:1–43, 1989.

[32] G. Damköhler. Der Einfluβ der Turbulenz auf die Flammengeschwindigkeit. *Z. Elektrochem*, 46:601–652, 1940.

[33] G. Darrieus. Propagation d'un front de flamme. In *La Technique Modern (Paris)*, 1938.

[34] P. A. Davidson. *Turbulence*. Oxford University Press, 2004.

[35] S. K. Dhanuka. *An Experimental Study of the Stable and Unstable Operation of an LPP Gas Turbine Ccombustor*. PhD thesis, University of Michigan, 2008.

[36] J. F. Driscoll. Turbulent premixed combustion - flamelet structure and turbulent burning velocities. *Prog. Energy Combust. Sci.*, 34:91–134, 2008.

[37] Y. Dubief and F Delcayre. On coherent-vortex identification in turbulence. *J. Turbulence*, 1:1–22, 2000.

[38] J. M. Duclos, D. Veynante, and T. Poinsot. A comparison of flamelet models for premixed turbulent combustion. *Combust. Flame*, 95(1):101–117, 1993.

[39] F. Durst, A. Melling, and J. J. Whitelaw. *Principles and Practice of Laser-Doppler Anemometry*. Academic Press, 1976.

[40] G. Eggenspieler and S. Menon. Combustion and emission modelling near lean blow-out in a gas turbine engine. *Prog. Comput. Fluid. Dy.*, 5(6):281–297, 2005.

[41] J. R. Fanchi and K. W. Tjan. *Energy in the 21st Century*. Wold Scientific, 2005.

[42] S. A. Filatyev, J. F. Driscoll, C. D. Carter, and J. M. Donbar. Measured properties of turbulent premixed flames for model assessment, including burning velocities, stretch rates and surface densities. *Combust. Flame*, 141(1):1–21, 2005.

[43] S. A. Filatyev, M. P. Thariyan, R. P. Lucht, and J. P. Gore. Simultaneous stereo particle image velocimetry and double-pulsed planar laser-induced fluorescence of turbulent premixed flames. *Combust. Flame*, 150(3):201–209, 2007.

[44] B. Ganapathisubramani, K. Lakshminarasimhan, and N. T. Clemens. Determination of complete velocity gradient tensor by using cinematographic stereoscopic PIV in a turbulent jet. *Exp. Fluids*, 42(6):923–939, 2007.

[45] B. Ganapathisubramani, K. Lakshminarasimhan, and N. T. Clemens. Investigation of three-dimensional structure of fine scales in a turbulent jet by using cinematographic stereoscopic particle image velocimetr. *J. Fluid Mech.*, 598:141–175, 2008.

[46] S. Ghosal. An analysis of numerical errors in large-eddy simulations of turbulence. *J. Comput. Phys.*, 125:187–206, 1996.

[47] F. C. Gouldin. An application of fractals to modeling premixed turbulent flames. *Combust. Flame*, 68:249–266, 1987.

[48] Ö. L. Gülder. Turbulent premixed combustion modelling using fractal geometry. *23rd Sypmosium (International) on Combustion*, 23:835–842, 1990.

[49] P. E. Hamlington, J. Schumacher, and W. J. A. Dahm. Local and nonlocal strain rate fields and vorticity alignment in tubulent flows. *Phys. Rev. E*, 77:026303, 2008.

[50] C. Hasse and N. Peters. A two mixture fraction flamelet model applied to split injections in a di diesel engine. *Proc. Combust. Inst.*, 30:2755–2762, 2005.

[51] E. R. Hawkes and R. S. Cant. A flame surface density approach to large eddy simulation of premixed turbulent combustion. *Proc. Combust. Inst.*, 28:51–58, 2000.

[52] E. R. Hawkes and R. S. Cant. Implications of a flame surface density approach to large eddy simulation of premixed turbulent combustion. *Combust. Flame*, 126:1617–1629, 2001.

[53] J Jeong and F Hussain. On the identification of a vortex. *J. Fluid Mech.*, 258:69–94, 1995.

[54] J. Jiménez. Kinematic alignment effects in turbulent flows. *Phys. Fluids A*, 4:562, 1992.

[55] J. Jiménez, A. A. Wray, P. G. Saffman, and R. S. Ragallo. The structure of intense vorticity in isotropic turbulence. *J. Fluid Mech.*, 255:65–90, 1993.

[56] S. Kadowaki and T. Hasegawa. Numerical simulation of dynamics of premxied flames: flame instability and vortex-flame interaction. *Prog. Energy Comust. Sci.*, 31:193–241, 2005.

[57] K. C Kim, S. Y. Yoon, S. M. Kim, H. H. Chun, and I. Lee. An orthogonal-plane PIV technique for the investigations of three-dimensional vorticial structures in a turbulent boundary layer flow. *Exp. Fluids*, 40:876–883, 2006.

[58] E. Knudsen and H. Pitsch. A dynamic model for the turbulent burning velocity for large eddy simulation of premixed combustion. *Combust. Flame*, 154:740–760, 2008.

[59] A. N. Kolmogorov. A refinement of previous hypotheses concerning the local structure of turbulence in a viscous incompressible fluid at high Reynolds number. *J. Fluid Mech.*, 13:82, 1962.

[60] A.G. Kravchenko and P Moin. On the effect of numerical errors in large eddy simulations of turbulent flows. *J. Comput. Phys.*, 131:310–322, 1997.

[61] L. D. Landau. On the theory of slow combustion. *Acta Physicochim. (USSR)*, 1944.

[62] P. Lavoie, G. Avallone, F. De Gregorio, G. P. Romano, and R. A. Antonia. Spatial resolution of PIV for the measurement of turbulence. *Exp. Fluids*, 43:39–51, 2007.

[63] C. K. Law. *Combustion Physics*. Cambridge University Press, 2006.

[64] C. K. Law and C. J. Sung. Structure, aerodynamics, and geometry of premixed flamelets. *Prog. Energy and Combust. Sci.*, 26:459–505, 2000.

[65] N. J. Lawson and J. Wu. Three-dimensional particle image velocimetry: error analysis of stereoscopic techniques. *Meas. Sci. Technol*, 8:894–900, 1997.

[66] N. J. Lawson and J. Wu. Three-dimensional particle image velocimetry: experimental error analysis of a digital angular stereoscopic system. *Meas. Sci. Technol*, 8:1455–1464, 1997.

[67] J. L. Lumley. Interpretation of time spectra measured in high-intensity shear flows. *Phys. Fluids*, 8:1056–1062, 1965.

[68] E. Mallard and H. L. Le Chatelier. *Annals of Mines*, 4:379–568, 1883.

[69] F. E. Marble and J. E. Broadwell. The coherent flame model for turbulent chemical reactions. Technical Report TRW-9-PU, Project Squid, 1977.

[70] G. H. Markstein. *Nonsteady Flame Propagation*. Macmillan Co., 1964.

[71] M. Matalon. On flame stretch. *Combust. Sci. Technol.*, 31(3):169–181, 1983.

[72] M. Matalon, C. Cui, and J. K. Bechtold. Hydrodynamic theory of premixed flames: effects of stoichiometry, variable transport coefficients and arbitrary reaction orders. *J. Fluid Mech.*, 487:179–210, 2003.

[73] M. Matalon and B. J. Matkowsky. Flames as gas-dynamic discontinuities. *J. Fluid Mech.*, 124:239–59, 1982.

[74] C. Meneveau and T. Poinsot. Stretching and quenching of flamelets in premixed turbulent combustion. *Combust. Flame*, 86(4):311–332, 1991.

[75] F. Moisy and J. Jiménez. Geometry and clustering of intense structures in isotropic turbulence. *J. Fluid Mech.*, 513:111–133, 2004.

[76] H. C. Mongia. A 4th generation propulsion combustor technology for low emissions. *AIAA paper*, 2003-2657, 2003.

[77] C. J. Mueller, J. F. Driscoll, D. L. Reuss, M. C. Drake, and M. E. Rosalik. Vorticity generation and attenuation as vorticies convect through a flame. *Combust. Flame*, 112(3):342–358, 1998.

[78] U. C. Müller, M. Bollig, and N. Peters. Approximations for burning velocities and Markstein numbers for lean hydrocarbon and methanol flames. *Combust. Flame*, 108(3):349–356, 1997.

[79] J. A. Mullin. *A Study of Velocity Gradient Fields at Intermeadiate and Small Scales of Turbulent Shear Flows via Dual-Plane Stereoscopic Particle Image Velocimetry.* PhD thesis, Univeristy of Michigan, 2004.

[80] J. A. Mullin and W. J. A. Dahm. Dual-plane stereo particle image velocimetry measurements of velocity gradient tensor fields in turublent shear flow. Part ii. Experimental results. *Phys. Fluids*, 18:1–28, 2006.

[81] K. K. Nomura and P. J. Diamessis. The interaction of vorticity and rate-of-strain in homogeneous sheared turbulence. *Phys. Fluids*, 12:846, 2000.

[82] K. K. Nomura and G. K Post. The structure and dynamics of vorticity and rate of strain in incompressible homogeneous turbulence. *J. Fluid Mech.*, 377:65–97, 1998.

[83] K. L. Pan, J. Qian, C. K. Law, and W. Shyy. The role of hydrodynamic instability in flame-vortex interaction. *Proc. Combust. Inst.*, 29:1695–1704, 2002.

[84] R. N. Paul and K. N. C. Bray. Study of premixed turbulent combustion including Landau-Darrieus instability effects. *Proc. Combust. Inst.*, 26:259–266, 1996.

[85] N. Peters. *Turbulent Combustion.* Cambridge University Press, Cambridge, UK, 2000.

[86] S. Pfadler, M. Löffler, F. Dinkelacker, and A. Leipertz. Measurement of the conditioned turbulence and temperature field of a premixed Bunsen burner by planar laser Rayleigh scattering and stereo particle image volocimetry. *Exp. Fluids*, 39(2):375–384, 2005.

[87] H. Pitsch. A consistent level set formulation for large-eddy simulation of premixed turbulent combustion. *Combust. Flame*, 143(4):587–598, 2005.

[88] H. Pitsch. LES of turbulent combustion. *Annu. Rev. Fluid Mech.*, 28:453–482, 2006.

[89] A Pocheau. Front propagation in a turbulent medium. *Europhys. Lett.*, 20:401–406, 1992.

[90] T. Poinsot and D. Veynante. *Theoretical and Numerical Combustion.* Edwards, Philadelphia, PA, 2 edition, 2005.

[91] T. Poinsot, D. Veynante, and S. Candel. Quenching processes and premixed turbulent combustion diagrams. *J. Fluid Mech.*, 228:561–606, 1991.

[92] S. B. Pope. The evolution of surfaces in turbulence. *Int. J. Eng. Sci.*, 26(5):445–469, 1988.

[93] S. B. Pope. *Turbulent Flows.* Cambridge University Press, 2000.

[94] M. Raffel, C. Willert, and J. Kompenhans. *Particle Image Velocimetry: A Practical Guide.* Springer, Berlin, Germany, 1998.

[95] C. C. Rasmussen. *An Experimental Study of Flame Stability in a Directly-Fueled Wall Cavity With a Supersonic Free Stream.* PhD thesis, University of Michigan, 2006.

[96] P.-H. Renard, D. Thevenin, J.C. Rolon, and S. Candel. Dynamics of flame/vortex interactions. *Prog. Energy Combust. Sci.*, 26:225–282, 2000.

[97] C. J. Rutland and A. Trouve. Direct simulations of premixed turbulent flames with nonunity Lewis numbers. *Combust. Flame*, 94:41–57, 1993.

[98] K. I. Schelkin. Tech. memo no. 1110. Technical report, NACA, 1947.

[99] J. O. Sinibaldi, C. J. Mueller, A. E. Tulkki, and J. F. Driscoll. Suppression of flame wrinkling by buoyancy: the baroclinic stabilization mechanism. *AIAA J.*, 36(8):1432–1438, 1998.

[100] G. I. Sivashinsky. Instabilities, pattern formation, and turbulence in flames. *Annu. Rev. Fluid Mech.*, 15:179–199, 1983.

[101] J. Smagorinsky. General circulation experiments with the primitive equations: I. The basic equations. *Mon. Weather Rev.*, 91:99–164, 1963.

[102] A. Stella, G. Guj, J. Kompenhans, H. Richard, and M. Raffel. Three-components particle image velocimetry measurements in premixed flames. *Aerosp. Sci. Technol.*, 5:357–364, 2001.

[103] C. J. Sung, J. S. Kistler, M. Nishioka, and C. K. Law. Further studies on effects of thermophoresis on seeding particles in LDV measurements of strained flames. *Combust. Flame*, 105(1):189–201, 1996.

[104] C. J. Sung, C. K. Law, and R.L. Axelbaum. Thermophoretic effects on seeding particles in LDV measurements of flames. *Combust. Sci. Technol.*, 99:199–132, 1994.

[105] N. Swaminathan and R. W. Grout. Interaction of turbulence and scalar fields in premixed flames. *Phys. Fluids*, 18:045102, 2006.

[106] Z. C. Tan and R. C. Reitz. An ignition and combustion model based on the level-set method for spark ignition engine multidimensional modeling. *Combust. Flame*, 145(1):1–15, 2006.

[107] M. Tanahashi, S. Murakami, G. Choi, Y. Fukuchi, and T. Miyauchi. Simultaneous CH-OH PLIF and stereoscopic PIV measurements of turbulent premixed flames. *Proc. Combust. Inst.*, 30:1665–1672, 2005.

[108] A. Trouve and T. Poinsot. The evolution equation for the flame surface density. *J. Fluid Mech.*, 278:1–31, 1994.

[109] A. Upatnieks, J. F. Driscoll, S. L. Ceccio, and C. C. Rasmussen. Liftoff of turbulent jet flames - Assessment of edge flame and other concepts using cinema-PIV. *Combust. Flame*, 138(3):259–272, 2004.

[110] L. Vervisch, E. Bidaux, K. N. C. Bray, and W. Kollmann. Surface density function in premixed turbulent combustion modeling, similarities between probability density function and flame surface approaches. *Phys. Fluids A*, 10:2496–2503, 1995.

[111] F. Williams. *Combustion Theory, 2nd ed.* Addison-Wesley, Reading, USA, 1985.

[112] F. Williams. *The Mathematics of Combustion.* Society for Industrial & Applied Mathematics, ed. Buckmaster, J. D., 1985.

[113] J. C Wyngaard and S. F. Clifford. Taylor's hypothesis and high-frequency turbulence spectra. *J. Atmos. Sci.*, 34:922–929, 1977.

[114] V. Yakhot. Propagation velocity of premixed turbulent flames. *Combust. Sci. and Tech.*, 60:191–214, 1988.

[115] M. Yokokawa, K. Itakura, A. Uno, T. Ishihara, and Y. Kaneda. 16.4-tflops direct numerical simulation of turbulence by a fourier spectral method on the Earth Simulator. Online. Available: http://www.sc-2002.org/paperpdfs/pap.pap273.pdf. Accessed: 12/2008, 2005.

[116] J. Yuan, Y. Ji, and C. K. Law. Effects of turbulence and flame instability of flame front evolution. *Phys. Fluids*, 18(10), 2006.